Toroidal Optical Microresonators as Single-Particle Absorption Spectrometers

By

Kevin D. Heylman

A Dissertation submitted in partial fulfillment

of the requirements for the degree of

Doctor of Philosophy

(Chemistry)

At the

UNIVERSITY OF WISCONSIN-MADISON

2016

Date of final oral examination: November 21, 2016

The dissertation is approved by the following members of the Final Oral Committee:

Randall Goldsmith, Assistant Professor, Chemistry

Gilbert Nathanson, Professor, Chemistry

John C. Wright, Professor, Chemistry

Deniz Yavuz, Professor, Physics

Martin T. Zanni, Professor, Chemistry

Abstract

Single-particle and single-molecule measurements are invaluable tools for characterizing structural and energetic properties of molecules and nanomaterials. Photothermal microscopy in particular is an ultrasensitive technique capable of single-molecule resolution. In this thesis I introduce a new form of photothermal spectroscopy involving toroidal optical microresonators as detectors and a pair of non-interacting lasers as pump and probe for performing single-target absorption spectroscopy. The first three chapters will discuss the motivation, design principles, underlying theory, and fabrication process for the microresonator absorption spectrometer. With an early version of the spectrometer, I demonstrate photothermal mapping and all-optical tuning with toroids of different geometries in Chapter 4. In Chapter 5, I discuss photothermal mapping and measurement of the absolute absorption cross-sections of individual carbon nanotubes. For the next generation of measurements I incorporate all of the advances described in Chapter 2, including a double-modulation technique to improve detection limits and a tunable pump laser for spectral measurements on single gold nanoparticles. In Chapter 6 I observe sharp Fano resonances in the spectra of gold nanoparticles and describe them with a theoretical model. I continued to study this photonic-plasmonic hybrid system in Chapter 7 and explore the thermal tuning of the Fano resonance phase while quantifying the Fisher information. The new method of photothermal single-particle absorption spectroscopy that I will discuss in this thesis has reached record detection limits for microresonator sensing and is within striking distance of becoming the first single-molecule room-temperature absorption spectrometer.

Table of Contents

Table of Figures

Acknowledgments

In the spring of 2011 I made the fateful decision to attend the University of Wisconsin for graduate school. Before visiting, I was not expecting to attend here. In fact I mostly agreed to come for the visit weekend at the urging of one of my undergraduate advisors, who was a former student of Fleming Crim. My mind was completely changed by my brief visit to Madison. The climate of the department seemed to be one of enthusiasm, fraternity, and dedication to science. I am happy to say that my time here has not dimmed that impression at all. If I had to go back and choose again, I would make all of the same decisions. The UW-Madison Chemistry Department truly is a wonderful place for graduate students.

More than most graduate students I have leaned on staff members in the department for assistance. I want to especially thank the following members of the department for their invaluable help at all stages of my Ph.D.

I spent many hours in the student machine shop with Kendall Schneider and Rick Pfeiffer. Kendall and Rick have, again and again, guided me in the process of building all the parts that go into the two microresonator setups. They have been more than patient with my mistakes, ignorance, and incessant questions. We would not have a functioning single-particle spectrometer without them. I have learned a great deal about how to operate a milling machine, how to select the right material or geometry for the job, and how to navigate the complex world of machining. Likewise Steve Myers, Jerry Stamn, Ed Vasiukevicius, Jim Mallarkey, and Matt Martin in the main shop have made all of this work possible, and have always made time when I or someone from my group needed something. I have greatly appreciated Jerry and Steve's time when I needed advice on how to build or assemble something. The machine shop has been vital to the functioning of our research group and to my project in particular.

Bill Goebel and Craig Trewartha In the electronics shop have helped greatly with RF electronics. Bill taught me how to connectorize BNC cable, how to design a transimpedance amplifier, and the cause

of popcorn noise in the earliest photodetector. Their creativity and experience has been a treasure that I was lucky to take advantage of. Tracy Drier in the glass shop helped us design and assemble the taper pulling setup. Moreover, his detective work when we were sold a bad batch of wafers allowed us to identify the type of glass and why it exploded in the deposition furnace.

Chad Skemp (and all of the other staff helping him) in the purchasing office has endured my frequent requests with more professionalism than I deserve, and I thank him (as well as apologize) for everything. Mike Bradley taught me everything I know about shipping and receiving, and I'm always happy when I have an excuse to go visit him. I will miss his competence and sense of humor. As one of the first students in the Goldsmith group, I've worked more than most with the building managers Jeff Nielsen and Kyle LeRoux. Both men have been resourceful and prompt about getting things done, and I suspect my requests have been stranger and more difficult than most. Rob McClain in the instrument facility has always been a resource for us when we needed his expertise on a question of instrumental analysis. His creativity and experience is a valuable resource. The department secretaries keep the department functioning. Sue Martin, April Leslie, and Kristi Heming have all been very helpful and friendly to me as I fumbled my way through reimbursements or scheduling. Finally, Alan, Paul, and all of the 9th floor guys helped me solve endless IT problems as I put together our group's computer and backup systems. They always had time for my silly questions.

Graduate students in other research groups have also enabled much of this work. Aaron Ledvina in Joshua Coon's group helped us test out their CO_2 laser on our early toroids, guiding us down a more productive path and letting us realize that we needed to purchase a more powerful laser. Nick Myllenback and Greg Eyer in Trisha Andrew's group were extremely accommodating when I needed to sublimate CoPc at ridiculous temperatures in one of their hoods. I enjoyed working with them. Likewise, Yuelin Peng in the same group helped me with thermal evaporation of CoPc, patiently explaining how each step of the process worked. Matt Stolt in the Jin group, as well as being a stalwart comrade on the frisbee field and

dodgeball court, helped me out in a pinch with a variety of characterization techniques. Not only did he show me how to take high-quality SEMs of nanoparticles, he made time immediately to take TEM images of our suspicious gold nanorods. Meng-Yin Wu in Mike Arnold's group repeatedly prepared solutions of dispersed SWCNTs for me, and I thank him. I also thank Xiaomeng Lu in Regina Murphy's group for assistance with DLS (dynamic light scattering). Thanks to Denise Femia and Mark Thompson at USC for making the fused porphyrin:pyrene molecules discussed in Appendix 2, especially given the grant deadline we were working under. I think this molecule has an exciting future on the resonator project.

Christine Suzanne Miller at Argonne National Laboratories helped us early on with XeF_2 etching. We mailed samples to her repeatedly, and then in the summer of 2012 I went down for a couple of days and worked directly at the Center for Nanomaterials. The staff at Argonne were very helpful and considerate of my limited time, and Christine as well as Il Woong Jung and Valentina Kutepova quickly trained me and assisted me in fabrication.

The WCAM staff were all vital to the success of this project: Hal, Quinn, Kurt, Becky, Dan. Dan keeps the lights on, even when things are going haywire. Becky trained me on my first tools, ranging from oxidation furnaces to lithography. Quinn trained me on a wide variety of process steps in etching and lithography. I've learned a great deal from his training sessions and examinations, and I will miss his grim sense of humor. Quinn always made sure that not only did we know what a process tool was doing, we knew how it operated. I enjoyed training with Kurt as well, since his mixture of professionalism and accessibility makes for a great teacher. I'm also grateful to all the cleanroom staff for their rapid response to my requests for training, advice, or process modifications. Finally, I've really appreciated the gusto with which Hal has taken to our strange requirements and offered increasingly daring ideas to make the microstructures we needed. I also apologize for the ABEL trap packaging process, during which Hal replaced no less than 5 broken blades on the silica saw while I was dicing wafers.

I want to thank Gil Nathanson and John Wright for serving on my TBO, RP, and dissertation

committees. One of my favorite memories of the past five years was the closed session to my TBO. Your eager questions and keen insight actually predicted many of the challenges that Randy and I stumbled upon, and I wish we had listened more closely! Whenever I meet someone who is nervous about their TBO, I tell them to relax because I had a great time. I also thank Marty Zanni and Deniz Yavuz for serving on my dissertation committee.

As an affiliate member of the Zanni group, I want to thank Marty and his group for letting me join summer canoe trips and spring cooking parties. Zanni group events are fun and leave you with lasting memories—especially the year we were the only group to make it down an unnavigable river for the whole summer. I'll never forget the dinner parties, where we assembled in a tiny kitchen, wearing our finest clothes, partnered up with a stranger, and all 20 of us simultaneously tried to make gourmet meals. I'm also grateful for the people I've spent time with having fun outside of lab. Wyatt, Danny, Brandon, Cherry, Tristan, Erik, Kayla, J.J., Kale, Alice, Sudheer, Giri, Heejun, Somenath, Wenting, Randy, and Ann are just some of the awesome people who've made time for me. I will miss watching Champions' League Finals or classic movies at Danny's apartment, and talking philosophy and playing obscure board games over a beer at Wyatt's place.

I played with the Huckel's Rule and HammersOnly.com MUFA teams for three seasons, and only wish that I'd played for more seasons. My frisbee teammates made every game fun, both when we were doing really well and when we weren't. I learned a lot about frisbee and about teamwork from my time on the MUFA fields. I will miss you guys. I also am glad I had the chance to play for the Buckyballs dodgeball team for two seasons. I'm especially grateful to the founding members who went along with my initial fumbling attempts to found the Chemistry Department dodgeball team. I was privileged to see some truly heroic plays by my chemistry colleagues on the middle school gym court, including an unmatched 6 vs. 1 comeback victory by Danny Tabor.

I have been fortunate enough to be a member of the most friendly research group in the world. Angela, you keep bringing in delicious food, and you've always patiently answered my stupid questions about synthetic and safety issues. Alex, I really enjoy your sense of humor, your commitment to understanding chemistry, and your taste in music. I've learned a lot about Labview from you, even though you joined the group much later than I did. I'm glad that being my prospective during visit weekend didn't scare you away. Andrew, I regret not having spent more years with you. Whenever you talk I learn something interesting, and we'll definitely have to become friends on Spotify. I'm glad that someone from the DC area will stick around to keep the Goldsmith group hip. Danny, I've picked up more music from you than anyone else in the group, and your group meeting fun fact about being snakebitten is the story by which I judge all other personal stories. David, I've never met anyone with better public speaking skills and you have a way of making fields I don't know much about—proteins and stuff—and making them fascinating. James, you've always made time for my strange questions about electronics or software and I will miss your self-deprecating sense of humor. Katie, I admire your dedication and enthusiasm for research and your ability at trivia. Maitreya, you were my only fellow graduate student for a long time and you took me under your wing, and I'm grateful for that. Ryan, thanks for all the help in the machine shop. You picked up on that kind of stuff far faster than I did. Lydia, your organizational skills and general neatness are skills that I hope to learn from your example. Sharla, you helped me constantly both personally and professionally and the world is a better place with you in it. Megan, Nicholas, Kyle, Mike, Tyler, Daniel, and Emily: I didn't work with any of you in the lab, but all of you were a positive presence in the group and made the working environment a better place. I wish you all the best in your future careers. Sudheer, you joined in my last year and I wish you had joined earlier. I've really enjoyed our time together, both in the lab working with electronic or Labview and our time on Friday nights going to the grocery. I really admire your easy laugh and your dedication to your research. Sunil, you were a rock in the lab. I always knew I could go to you for help with anything I was doing in the synthetic lab. You taught me how

to handle air-sensitive reagents, how to setup a reaction, and generally how to avoid hurting myself in lab. I think you even taught me once how to correctly pour a corrosive reagent from a bottle (a skill most children master before they start kindergarten). I will always miss how you not only offered some of your lunch to us everyday, you practically forced us to try you and your wife's delicious Indian cooking. In many different ways all of you have been role models to me, giving me unintentional lessons that I will carry with me as I leave here.

Last but not least are the members of Team Toroid. Until my 3rd year, I was the sole member of Team Toroid. Now it has expanded greatly and I am excited to be handing off the project to a hand-picked team of expert scientists.

Kasie you were the first person to join me on Team Toroid, and we'll always be K-Dawg and K-Slyce. In short order you became far more skilled in the cleanroom than I ever was, and the way you've pushed through the fabrication of the all-glass toroids is nothing short of remarkable. The way that the cleanroom staff adore you is a testament to your fabrication street smarts and conscientiousness about leaving the bench better than you found it. I will miss your funny stories about your family members and your well-timed sarcasm. Now that I'm gone, I don't know who will let you into lab when you forget your keys. Your patience and flexibility are traits that I hope to develop in my own professional life.

Erik, you are the person I've worked with the closest in graduate school (besides Randy). It only took you a few months to know more about toroids than I managed to pick up in three years, which is a testament to your relentless intelligence. But even more than your raw intellectual firepower, I have deeply appreciated your humility and sense of humor. You always deflect praise with good humor, and we've cracked endless jokes as we work together on solving problems with the alignment, or Labview, or the electronics, or any of the other million things that can go wrong on the microscope. Every day you come into work at some ridiculously early hour and dive into something or other, whether it's jaw-

dropping renderings or complicated Labview code. Despite being smarter than me, you always pay attention when I try to teach you something, even if I'm the one who ends up learning more. I admire your easygoing nature and focused intelligence, and will try to emulate them myself.

Morgan, you joined Team Toroid recently but have already proven yourself indispensable. When I came to you with a desperate need for help taking data, you dived into it without a thought for whether the demands it placed on your time were reasonable, because you were committed to getting the job done I know you will thrive on this project, just as you have with your earlier research projects as an REU student and a graduate student. I was very impressed during your REU at the way you picked up things so quickly—one week doing synthesis, another designing circuit boards, and another building simulations. Your diverse skillset is invaluable to working on this project. Your work ethic and eagerness to learn new skills are traits that I admire and hope to emulate.

Levi, you've joined the project only days ago so I can't comment on your past. But I know in the future you will be a great asset to Team Toroid.

I want to thank my parents for the unending patience and dedication to my intellectual, social, and moral education. They made me a person, and in addition to raising me they gave me the best education they could possibly put together. Everything I have accomplished in my life comes from their hard work. Every metaphorical paper I write in my life has them as the last authors. In return, they have had endure being around me for 27 years. And not just my parents, but my whole family, in fact, has made me who I am today and I am deeply grateful. And I will miss being close to my sister and Bill in Chicago. I'm also blessed with the most patient and kind parents-in-law in the world. 妈妈，爸爸，你们总是对我很好。我感觉非常幸福。我是你们的儿子， 你们是我的父母。

I met two people in Madison who shaped my life in far-reaching ways. Randy Goldsmith and I met during visit weekend and I soon began bombarding him with questions. I continued to do so until he

accepted me into his fledgling research group in 2011. I was given the task of building the resonator setup. This experience, the subject of this dissertation, has taught me so many more things than I could have ever imagined. I am profoundly grateful for the endless hours that Randy has devoted to teaching me. He is the finest master that an apprentice could ask for and the best confidante a graduate student could want. Throughout these years he has kept an ever-present eye on my well-being, guiding my professional development and even allowing me to take a month off to visit my family in China right before my graduation. As I write this paragraph I am saddened by the thought that we will never have another off-the-wall discussion of ways to tackle the problems in our research. Randy and I have entertained crazy ideas, argued about scientific and engineering facts, shared music recommendations, and confided in each other. I'm going to miss working for the best boss ever.

The other person I met in Madison was my wife Tianqi. Forgive me for saying this, but chemistry has always bonded us together. Although we met on the 4 bus, our first real conversation involved a quantum mechanics problem set (thanks Professor Schmidt!). Over the years we grew closer together and we were married in Madison in 2014. She has always listened when I shared my thoughts and feelings, even when they weren't very interesting. Because she is the reason I get up and go to work in the morning and the reason I come home every night, the thesis you are reading would not exist if I had not met her. She is not only my best friend but also the love of my life. I dedicate my thesis to Tianqi Zhang and hope that she will always have a place in her heart for me.

Chapter 1

1. Introduction

1.1 Absorption spectroscopy

Absorption spectroscopy is one of the oldest parts of the chemist's toolkit, dating back to the mid-1800s. The inventors of absorption spectroscopy, Robert Bunsen and Gustav Kirchoff, discovered rubidium and cesium after realizing that the dark lines present in flame spectra could be used as fingerprints of elemental compounds.[1] Absorption spectroscopic measurements later proved that the sun was made of elements found on Earth and were a major instigator for the quantum revolution. Since then absorption spectroscopy has remained one of the most important characterization tools in physics, biology, material science, astronomy, and chemistry. Absorption spectroscopic measurements usually probe electronic transitions in atoms, molecules, and bulk materials. One of the most important modern applications is the identification of diverse elements and molecules in an unknown sample. In its three-minute-long working lifetime, a spaceborne absorption spectrometer recently proved that, contrary to all expectations, vast amounts of water and volatile hydrocarbons are found in the lunar polar regions.[2] In more terrestrial experiments, absorption spectroscopy can inform about chemical changes as molecules cycle through oxidation states or coordination environments. Further information comes from adding different modalities of sensing, including polarization, ultrafast transient absorption, spatial dependence, and nonlinear absorption. Molecular absorption spectra in particular are sensitive to the local environment, including electric fields, temperature, and pressure. Absorption spectroscopists have investigated systems at an enormous range of length scales, from single molecules at cryogenic temperatures[3] to the atmosphere of entire planets.[4] Our goal in this thesis is to push back the frontier in

yet another direction. We aim to determine the absorption spectrum of single molecules under ambient conditions.

Why would we want to make our lives difficult by trying to measure molecules one at a time? Single-molecule (SM) studies are valuable on systems where substantial heterogeneity exists. This comes in two flavors: static and dynamic. Static heterogeneity is variation in electronic or conformational structure within an ensemble of chromophores. For example, a conjugated polymer molecule with over 200 chromophores can absorb light through any chromophore and will primarily emit light through the single site with the lowest energy.[5] Since this molecule in particular is frequently the active component of organic light-emitting devices, the fact that ensemble absorption and ensemble emission measurements are probing different chromophores is a problem. Dynamic heterogeneity is often seen in catalytic cycles, where the molecules of interest cycle through several distinct states. Within an ensemble, the phase of every catalyst is random, so the ensemble spectroscopic signal is a mélange of all the different parts of the catalytic cycle. Short-lived steps in the catalytic cycle will be particularly hard to characterize. As a further example of heterogeneity, SM fluorescence measurements have demonstrated that the rate constant of a single catalyst fluctuates over time.[6] However, as this chapter will explore, existing methods of absorption spectroscopy have not reached the single-molecule limit in a way that allows exploration of these kinds of systems.

While the goal of extending absorption spectroscopy to the room-temperature, single-molecule limit is exciting in its own right, let us consider some practical applications. The first would be any systems where existing single-molecule techniques (primarily fluorescence) cannot be applied. Fluorescence fails in the presence of charge carriers, so conducting molecular materials are an unexplored territory. An important conducting polymer is PEDOT:PSS (Polydiethoxythiophene:Polystyrene sulphonic acid), which is widely used[7] in organic photovoltaics[8] and thermoelectrics[9] because of its rare combination of visible transparency and electrical conductivity. The polymer's morphology upon deposition is hideously

complicated,[10] with significant uncertainty about the secondary, tertiary, and quaternary structure. This is important to understand better because the electrical conductivity is strongly affected by intra and intermolecular orientation and aggregation.[11,12] Since electronic properties are measurable via absorption spectroscopy, and single-polymer conformation/structure is accessible through polarization-dependent absorption (as previously demonstrated via fluorescence excitation),[13] this is an important system to learn more about.

A very different field is the characterization of working catalysts, whether organometallic water-splitting or metalloenzymes. Metal-containing catalysts typically possess visible absorption features from metal-ligand charge transfer, and these absorption peaks are a strong function of oxidation state (as well as the coordination environment and identity of ligands). A fluorescent label, which will necessarily be at some distance for the metal center to avoid changing the catalyst's performance, will not be all that sensitive to the behavior of the catalyst itself. Studying unsynchronized dynamics of metallocatalysts at the single-molecule level in a non-perturbative but informative manner would provide powerful mechanistic insight that is not available through existing means.

1.2 Existing techniques: single-particle absorption spectroscopy and single-molecule fluorescence

How far forward to we have to push the frontier to realize our goal of studying such single-molecule systems? State-of-the-art micro-absorption spectrometers can record the absorption spectrum of single nanoparticles.[14] Single-particle detection with high signal to noise is possible via a wide range of optical methods, including far-field extinction,[15,16] scattering,[17,18] interference,[19] near-field methods,[18 17] or photothermal microscopy.[20-22] However, there is a large difference between the absorption cross-section of nanoparticles and of single molecules. Gold nanorods (AuNRs) are frequently targets of single-

particle absorption spectroscopy, both as a proof of principle[22-24] and as systems of interest in their own right.[25,26] Single AuNRs have an absorption cross-section of $\sigma_{abs} \approx 1 \times 10^{-10}$ cm^2 .[27] Single-particle absorption measurements are enabled largely by exciting with a laser focused to a diffraction-limited spot. Unfortunately, diffraction limits light from being focused to a spot with a diameter smaller than the wavelength. More quantitatively, consider a red laser (λ = 638 nm) focused with a large numerical aperture (NA) air objective (NA = 0.95). The Abbe diffraction limit is given by

$$D = \frac{\lambda}{NA} \quad so \quad A = \pi\left(\frac{\lambda}{2NA}\right)^2 \qquad 1.1$$

At the focus the spot diameter (D) for this laser is D = 672 nm, corresponding to an area A = 3.5 x 10^{-9} cm^2 (let us round to 10^{-9} cm^2 for convenience). A commercial UV/Vis/NIR absorption spectrometer has an excitation spot of order 10^0 cm^2. The difference between these two approaches is emphasized by considering the fractional absorption of a single AuNR in both instruments. The fractional absorption by the nanoparticle is $10^{-10}/10^{-9} = 0.1$ in the hypothetical single-particle microscope, or $10^{-10}/10^0 = 10^{-10}$ in the commercial UV/Vis/NIR spectrometer. One of these measurements is possible even the presence of substantial background absorption, while the other is impossible under any circumstances. The same type of comparison illustrates how difficult it is to measure absorption from single molecules. Molecular absorption cross-sections are $\sigma_{abs} \approx 1 \times 10^{-16}$ cm^2.[28] The several orders of magnitude difference between the size of the diffraction-limited focused excitation beam spot (10^{-8}-10^{-9} cm^2) and the molecule's absorption cross-section means that the largest extinction possible from a single molecule is only 10^{-8} to 10^{-7}, under ideal conditions. Reaching the single-molecule limit of ΔT = 0.000001 % with a transmission measurement requires heroic efforts to minimize all sources of noise after focusing the beam to a diffraction-limited spot, and although technically possible,[29] is not practical.

A major exception to this 10^{-8} extinction rule of thumb is that at temperatures near absolute zero the freezing out of phonons will cause molecular electronic peaks to collapse into a far narrower zero-

phonon line. Zero-phonon lines have a sharp peak (on the order of 10 MHz) with a maximum absorption cross-section 10^4- 10^5 larger than the molecule's homogeneously-broadened absorption peak at room temperature. The very first optical single-molecule experiment[3] exploited zero-phonon lines. This result used frequency-modulation spectroscopy to enhance detection limits; the same technique will be applied in our research, albeit in a somewhat different manner, and will be discussed in the second chapter of this thesis. In this first report and in later experiments a molecule can be made to absorb a significant fraction of the excitation beam, for example 30% in contemporary work.[30] However, little chemistry or biology happens at 4 K, putting a grievous limitation on the possible types of samples that can be analyzed. In order to maintain our focus on chemistry under ambient conditions, we will not consider any experimental configurations that require cryogenic temperatures or ultrahigh vacuum.

In response to the difficulties associated with single-molecule (SM) absorption spectroscopy, SM fluorescence spectroscopy has emerged over the previous two to three decades as a major area of research in chemistry and especially biochemistry. Although the very first report[31] of SM fluorescence involved cryogenic temperatures, the overwhelming majority of experiments since then have been at room temperature. The key concept that enables SM fluorescence is the Stokes shift.[28] Because the rate of vibrational relaxation to the ground vibrational level of the electronic excited state is extremely fast (10^{-12} s) compared to the rate of fluorescence decay for a typical chromophore (10^{-9} s), emitted photons are at significantly redder wavelength than excitation photons. Scrupulous optical filtering of the light collected from the excitation volume allows for isolation of the weak SM fluorescence from the much stronger excitation beam. This technique is so successful that single molecules can be seen with the unaided eye; in fact, this is a demo that our research group routinely performs. The combination of long-pass optical filters with extremely potent stopbands and low-noise single-photon-counting detectors has made possible the single-molecule sensitivity enabled by fluorescence spectroscopy. Single-molecule fluorescence spectroscopy possesses a powerful combination of non-invasiveness (far-field optical

method at ambient temperature/pressure) combined with high signal-to-noise (enabling real-time tracking, polarization anisotropy, FRET, etc.) As a result the Nobel Prize in Chemistry in 2014 was awarded to Moerner, Betzig and Hell for the development of super-resolution microscopy, of which single-molecule fluorescence spectroscopy plays a significant role.

However, there are several drawbacks to using fluorescence as a readout. The vast majority of molecules are not fluorescent because the rate of non-radiative relaxation dominates over the fluorescence emission rate. In most experiments the molecule or protein of interest has to be covalently labeled with a fluorescent dye, complicating the experimental procedure and potentially perturbing the functionality of the system. Fluorescent molecules under optical excitation spend a lot of time in the excited state, and are thus highly vulnerable to oxidation and to intersystem crossing into long-lived triplet states. The former problem (photobleaching) results in irreversible and complete quenching of the single-molecule signal. This limits the total number of detected photons in an optimized dye to about 10^6.[32] The latter problem of "blinking" results in erratic periods of zero emission. An unfortunate compromise has to be reached between signal-to-noise (optimized with high fluorescence fluence and thus high excitation intensity) and observation time (optimized with low excitation intensity). Another complication is fluorescence quenching. On example where quenching is particularly damning is in the study of conjugated polymers, where the injection of a single charge carrier will quench fluorescence within a substantial radius.[33] As a result conducting polymers, a rich set of molecules with complicated nanoscale structure and polaron energetics, have never been studied with single-molecule spectroscopy.

Another pressing issue in single-molecule spectroscopy is the need to learn useful information about the targeted molecule. SM fluorescence techniques can provide a wealth of information about conformation and dynamics.[28] However, information about electronic states of the target molecule is complicated by interpretation of the relaxation dynamics of the molecule. Emission spectroscopy (excitation with a fixed wavelength and collection with a spectrometer) enables identification of the

distribution of LUMO levels in single molecules at cryogenic temperatures.[34,35] However, the already weak fluorescence signal has to be divided over the number of points in the spectrum, hurting the achievable signal-to-noise. Signal-averaging away this problem doesn't work because of photobleaching. Fluorescence excitation spectroscopy (excitation with a tunable laser and colorblind detection) is more technically challenging, only being achieved at room temperature quite recently,[36,37] and provides information about any excited states that decay to an emissive state. The heterogeneity of individual molecules is immediately apparent in the huge range (>100 nm) in differences in excitation spectra maxima.[36] This approach is a less direct method to determining a molecule's absorption spectrum; for example, any state that decays non-emissively is missed in this approach.

Of the thousands of papers published on single-molecule spectroscopy under ambient conditions, all but a handful have used fluorescence. There are so few reports of non-fluorescent single-molecule spectroscopy at room temperature that we can briefly discuss them all here. Figure 1 illustrates the optical transitions involved in these various techniques. Sandoghdar and coworkers detected[29] single dye molecules on a clean surface in a transmission measurement (Figure 1a) through balanced detection. This approach essentially scales down a conventional double-beam absorption spectrometer to use a diffraction-limited laser beam. Fractional transmission is detected by a pair of balanced photodetectors, and each of the four detectors images at a different, fixed wavelength or optical path. Single absorbing molecules are readily imaged, with contrast most notable by probing at two different wavelengths simultaneously. However, even strong dye molecules with σ_{abs} >10 x 10^{-16} cm^2 require some signal averaging to reliably detect and the experiment is already shot-noise-limited. Using balanced detection and probing changes on the order of 10^{-6} to 10^{-7} in $\Delta T/T$ makes it really hard to tune the wavelength. Further, tuning polarization will also affect the balancing ratio making this method a non-robust tool for characterizing molecules. While this result is profoundly impressive and elegantly simple, it does not appear to be a viable route to a general-purpose single-molecule absorption spectrometer.

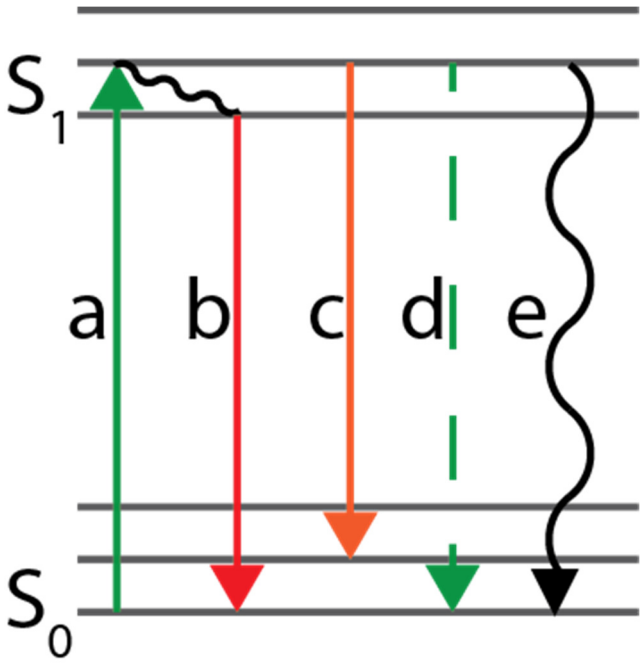

Figure 1: Energy-level diagram of single-molecule spectroscopic methods.

(a) Extinction. Measurement of extinction of the excitation beam by excitation from S_0 to S_1 (or other states). (b) Fluorescence. Rapid non-radiative relaxation to the ground excited S_1 state followed later by radiative emission. (c) Raman. Inelastic scattering of an excitation beam results in emission of light with a wavelength longer (Stokes) or shorter (anti-Stokes) than that of excitation light. (d) Interferometric scattering (iSCAT). Elastic scattering of incident light is detected after heterodyning with the scattering background. (e) Photothermal. Non-radiative relaxation results in a local temperature increase that is detected optically. (not shown) Ground state depletion microscopy.

Xie and coworkers[38] detected single molecules through ground state depletion, using a pump beam to keep the molecule in the excited state a substantial fraction of the time. The transmission of a second probe beam is monitored to detect absorption. The pump beam is modulated at low MHz frequencies, allowing for lock-in amplification of the probe beam transmission through modulation transfer. The depth of modulation for a single dye molecule at λ_{max} (~ 1×10^{-7}) is actually less than the shot noise from a single linescan (2.1×10^{-7}) although signal averaging for 1300 ms recovers a signal to noise (S/N) ratio of 3. This experiment used a strong dye ($\sigma_{abs} = 5 \times 10^{-16}$ cm^2) with a long excited-state lifetime. For a more representative chromophore, consider the humble industrial dye cobalt phthalocyanine

(CoPc)[39] with an extinction coefficient of σ_{abs} = 1 x 10^{-16} cm^2 and excited-state lifetime of τ_{exc} ~ 3 ps.[39] Metal phthalocyanines, and their close cousins metal porphyrins, are ubiquitous in living organisms.[40] In Xie's experiment, this typical molecule would give a probe beam contrast of 1.2 x 10^{-10}, requiring 1,380 minutes of continuous excitation to achieve a S/N ratio of 3. Increasing the probe and pump powers 100x (to 35 mW each) suggests a contrast of ~ 1 x 10^{-8}, still requiring 120 s of averaging and absorption of >10^{12} photons to achieve 3:1 SNR. This ground state depletion technique, while an impressive technical achievement, does not appear to be a fruitful route forward for non-emissive molecules.

Another competing SM technique is iSCAT (interferometric Scattering), recently pioneered by Kukura and Sandoghdar.[41-43] In this approach (Figure 1d), the weak scattered field from a single protein interferes with the much stronger field reflected at the surface of the substrate (a glass microscope coverslip). The intensity of the scattered field contains an interference term proportional to the product of the molecule's reflectivity (extremely small) and the air-glass interface reflectivity (significant). Not only detection but high-speed tracking of single protein motion has been demonstrated.[44] Nonetheless, there remain some serious challenges. While all single-molecule experiments must deal with impurities and contamination, these issues are particularly grave when detecting scattered light as the signal. Every molecule scatters light, so it is hard to envisage how this technique will ever be applied to specifically detect small molecules. There is also very little information obtained about the analyte. Lacking spectral characterization, the only information that can be extracted is the particle's polarizability, which can be related to the mass of the particle with some assumptions. Finally, scattering is proportional to the sixth power of a nano—object's radius, making it harder to scale down to small molecules than absorption.[21] While interferometric scattering can be very useful for label-free tracking of single molecules, it is not a replacement for single-molecule absorption spectroscopy.

Near-field scanning optical microscopy (NSOM) is a technique that was very popular in the first years of single-molecule spectroscopy.[45] While the ability to focus light to a spot far smaller than the Abbe

diffraction limit is invaluable for single-molecule spectroscopy, the other experimental complications are serious. First, only the surface of a system can be probed with NSOM. Second, the spot size is very dependent on the focus, requiring nanometer stability and approach distance.[46] Light transmission through the narrow tip aperture is also quite low and the material being investigated needs to be quite flat given the proximity of the tip to the surface. Contrast is a function of topography, adding further complication to interpretation of data. Single-molecule resolution in Raman spectroscopy (Figure 1c) is possible through a near-field probe (TERS) or through surface-enhanced Raman spectroscopy (SERS). While the spectral fingerprint from a Raman spectrum is a powerful tool for characterization, the huge plasmonic enhancement required to achieve single-molecule SERS is only found with random clusters of silver nanoparticles interacting with organic dyes.[47-50] This intense plasmonic field, necessary to reach SM resolution, is potentially quite perturbative. Finally, Raman measurements are complementary to absorption measurements, largely probing different aspects of the molecule's structure and energetics.

A rather different approach was taken by Orrit, Lounis and coworkers.[21,51] In fealty to the law of conservation of energy, a nonluminescent nanoparticle or molecule must dissipate energy from optical excitation as heat. This heat flow, on the order of nW for a strongly pumped single molecule and significantly larger for a metallic nanoparticle, creates a localized hotspot in the surrounding material. In photothermal (Figure 1e) microscopy this hotspot can be measured with a second laser focused onto the same spot. The second laser, referred to as the probe beam, is scattered from the hotspot because of the change in refractive index of the material with temperature. In 2002 Orrit et al. reported detection of single gold nanoparticles (σ_{abs} = 8 x 10^{-14} cm^2) with a 3-beam photothermal technique.[20] Lounis et al. provided a key improvement in 2004 by intensity modulating the pump beam and measuring the resulting frequency sidebands on the probe beam, simplifying the experiment and improving detection limits to near single-molecule levels(σ_{abs} = 10^{-15} cm^2).[52] In 2010, Orrit et al. made the final leap and obtained high S/N in detection of dye molecules at room temperature,[51] and photothermal imaging of several different

molecules is shown in the SI of that work. However, the authors acknowledge a few critical drawbacks. The incident optical intensity has to be quite high, 5 x 10^6 W/cm^2 for exciting single molecules of BHQ1 and 3.5 x 10^7 W/cm^2 to probe the resulting photothermal hotspot. Each molecule must cycle through excitation and dissipation in just 25 ps (15 nW /(3.9 x 10^{-19} J/photon)), so that upon dissipating excitation energy the molecule immediately absorbs another photon. The authors do not attempt to record an absorption spectrum, and this would be quite difficult in practice because the two laser beams need to remain tightly coaligned over the wavelength range of interest.[22] Chromatic aberration in both microscope objectives would be an issue here. Most importantly, the experiment requires immersion in glycerol to maintain a sufficiently high dn/dT. Water, for example, is not usable because of the low dn/dT at room temperature. Yet in contrast to the other techniques described above, the problems in this experiment sound tractable. Glycerol immersion of the sample is only necessary because of signal/noise considerations. Acquiring an absorption spectrum is difficult in this geometry, but would be far easier if the photothermal hot spot was detected in a different way. It is with these thoughts in mind that we set out to build our single-molecule absorption spectrometer.

1.3 In search of the ideal SM thermometer

Taking the experiments of Orrit and Lounis as a jumping-off point, let us discuss the requirements for a single-molecule absorption spectrometer. Most importantly, the detection limit of the photothermal transduction step must be greatly enhanced. Further, the new detection scheme should be adaptable to different systems: molecules in air, molecules in films, and molecules in aqueous solution. To achieve single-molecule resolution, Orrit et al. needed to immerse molecules in glycerol, which motivates us away from using this photothermal scattering technique for our spectrometer. Instead, we will rely on a very different sort of detector, which maintains extreme temperature sensitivity despite a relatively small

dn/dT. To detect a tiny heat flow from a single molecule, the detector must have a small detection volume, to maximize the temperature change from the minuscule single-molecule heat source. To summarize, we need an exquisitely sensitive microscale thermometer that functions under ambient temperature and pressure.

What are the most impressive thermometers currently available? The most sensitive thermometer known employs SQUID (Superconducting QUantum Interference Device) magnetometry to reach sub-nanoKelvin sensitivity, but only operates at liquid helium temperatures (~4 K)[53,54]. Recently, at room temperature, Luiten and coworkers[55] used the shift of resonance frequencies in millimeter-sized optical resonators to reach 80 $\mathrm{nK}/\sqrt{Hz}$ sensitivity. In this sensor, a change in 80 nK corresponds to a shift in the optical cavity's resonant wavelength of 1 attometer (10^{-18} m) with a probe wavelength of 1 μm, giving a noise floor of 1 part in 10^{-12}. However, this particular optical resonator confines light to a volume of 4 x 10^{-6} cm^3, making it too large to be an effective single-molecule detector. The apparatus needed to reach such a detection limit is quite complicated as well. It requires simultaneous locking of two different laser wavelengths to the resonator and pre-stabilization of the resonator temperature with a macroscopic heater before locking the resonator temperature by adjusting the power of the coupled probe beam. Juggling four simultaneous feedback loops is not trivial. The experiment of Luiten and coworkers does serve to illustrate the extreme sensitivity possible with optical resonators, a development exploited recently in the first detection of gravitational waves with a kilometer-scale optical resonator.[56] To measure single nanoparticles and molecules we chose to miniaturize the WGM optical resonator, exploiting microscale WGM optical resonators which have been used for a variety of thermal sensing experiments.[57,58]

1.4 Sensing with optical resonators

This thesis will discuss the successful deployment of these microscale WGM optical resonators for single-particle spectroscopy. Our ultimate aim is a general-purpose single-molecule absorption spectrometer, although we came just short of this goal during my thesis. The use of optical microresonators as single-particle spectrometers motivates a discussion of their properties. An optical microresonator is any optical configuration that confine light for multiple passes to a one-cycle path length of 10-1000 μm. Resonance occurs when the round trip path length of the resonator is equal to a whole number of wavelengths. Resonators are used to build up optical intensity, acting as a sort of light bucket, with the most familiar example being laser cavity resonators. Indeed, some of the lowest threshold lasers on record are made from the exact type of microresonator used in this thesis.[59-61]

Microresonators are often used for sensing because light passes through the resonator volume for many roundtrips, allowing repeated sampling of a proximal analyte. Sensing occurs when a physical property of the resonator is affected by the analyte, which might be a single protein or the local humidity. The two most common resonator configurations are a Fabry-Perot resonator (Figure 2) and a ring resonator (Figure 2). Monolithic ring resonators are referred to as Whispering-Gallery Mode (WGM) resonators after the acoustic phenomenon with the same origins.[62] A whispering gallery is a circular (or semi-circular) wall where sound waves propagate with low losses along the inside edge of the circle, allowing for one person to whisper and another to hear across a great distance. As in other types of waveguides, light confinement in WGM resonators is achieved through total internal reflection (TIR). Light can be confined to a region of higher refractive index as long as the propagation vector maintains a sufficiently small angle relative to the interface between media. The most familiar type of waveguide is the humble fiber optic cable, which is so heavily optimized that it can transmit light with losses as low as 0.2 dB per kilometer.[63] In a fiber optic cable, light is confined to a core layer of doped glass surrounded by

a cladding layer of glass with slightly lower refractive index. The cladding layer can also be air, as in the air-guided optical fiber tapers and WGM resonators used in this thesis. Coiling a fiber optic cable into a loop produces a simple optical resonator. The simplest ring resonator, made from a length of optical fiber coiled into a loop, can be used for sensing.[64] WGM resonators, the monolithic analog of the fiber loop resonator, come in a variety of shapes and size (Figure 2). The choice of materials, size, and geometry depends on the application. The first dielectric optical ring resonator was proposed theoretically in 1939,[65] many decades before fabrication techniques suitable for optical frequencies became available.[66,67] WGM microresonators find important applications in cavity optomechanics,[68-71] and single-particle or single-molecule sensing.[56,72-75] Given the immense variety of optical microresonators available, how do we know which type will be most suited to our needs?

The simplest figure of merit is Q/V, where Q is the Q-factor and V is the mode volume. The Q-factor determines the average photon lifetime in the resonator, and can be experimentally characterized by the sharpness of the coupling efficiency as a function of wavelength. The Q-factor is defined by $Q = \lambda_0 / \lambda_{FWHM}$ where λ_0 is the resonant wavelength and λ_{FWHM} is the full-width at half-maximum of the resonance. This integer multiple condition enforces constructive interference between successive reflections inside the cavity. How strictly this condition is met is determined by the number of roundtrips for the average photon. Conversely, wavelengths that are not integer multiples of the optical path length will grow

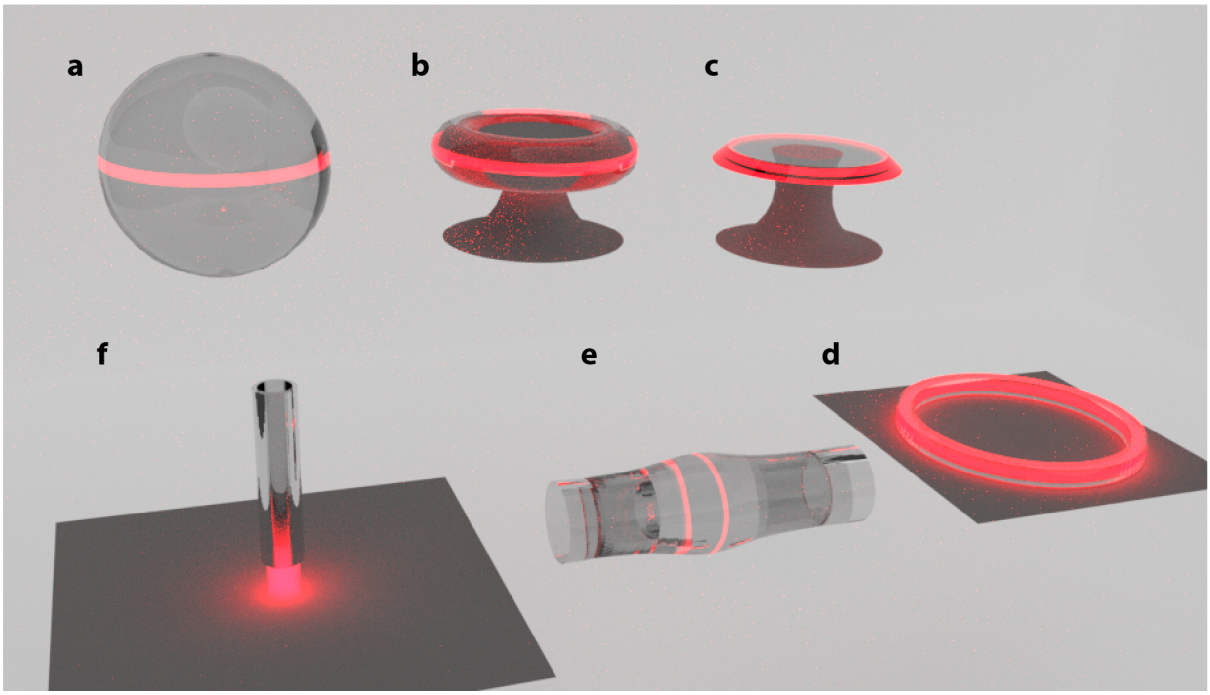

Figure 2 : Types of optical microresonators.

This figure shows the most common varieties of optical microresonators. (a) Microsphere. (b). toroid. (c) microdisk. (d) Fabry-Perot cavity. (e) microbottle. (f) microring.

increasingly out of phase and begin to destructively interfere with themselves. The reader can convince themselves by adding up two sine waves of slightly different frequencies and noting how many cycles it takes for them to grow out of phase as a function of frequency detuning. Propagating for only a few cycles results in the two waves being largely still in phase and constructively interfering regardless of frequency difference; this is analogous to the broad spectral linewidth of a resonator with a low Q-factor. By contrast, if the two waves propagate for a vast number of cycles, then eventually even two very similar frequencies that are initially in phase will end up with a random phase relationship and average just as much in-phase as out-of-phase, resulting in no net constructive interference. Therefore a low-loss resonator (high Q-factor) can only be coupled to when the probing laser is tuned within a very narrow range of wavelengths centered on the resonant wavelength. The higher the Q-factor, the more precisely λ_0 can be determined, making the Q-factor a critical contributing factor to the detection limit of any WGM-based sensor. Finally,

the mode volume V is simply the volume occupied by light resonant inside of a microresonator. A smaller mode volume is better, all other things being equal, by decreasing the volume of material that must be heated by the single-molecule photothermal heat source in our experiment in order to see a measureable response.

To better understand our requirements, we will first discuss the possible mechanisms for sensing with optical resonators. Broadly speaking, there are four methods of sensing with optical microresonators. The most widely-used sensing modalities is change in refractive index. The resonance wavelength is linearly proportional to the refractive index of the material where the light is resonating:

$$m\lambda = nL \quad (m\lambda = 2\pi Rn \; for \; WGM) \tag{1.2}$$

where L is the roundtrip length, m a positive integer, n the refractive index, and R the physical radius of the resonator. Refractive index is a material property, and can inform on change to the composition of a resonator or more commonly to the immediate environment of the resonator. This is because microresonator resonant modes either propagate through the sensing medium, so-called open-access microcavities,[76,77] or have an evanescent tail extending some hundreds of nm into the surrounding medium. An analyte that enters the microresonator's mode volume will almost surely have a higher refractive index than the surrounding medium. The resulting increase in effective refractive index of the resonator changes the resonance wavelength by an amount proportional to the excess polarizability of the analyte compared to the pristine microresonator. This effect is referred to as the reactive mechanism. Refractive index is also sensitive to temperature, and in certain materials to the presence of electric fields.[78] The shift in WGM wavelength upon binding of an analyte is typically rather small. For example, a large protein like BSA (bovine serum albumin) will shift a microresonator by approximately 40 attometers (5 kHz).[79,80] Given that microresonators are typically probed at an optical frequency of 1550 nm (192 THz), this is an extremely subtle shift of 10^{-11} of the resonance wavelength. Detection of such events would not

be possible without the exceptionally high Q-factors of WGM resonators; and even then, detection requires plasmonic enhancement[80-83] or optomechanical coupling.[84]

The flip side to having extremely high sensitivity for resonance shift is that various sources can appear and complicate the measurement of the desired property, including exotic issues like ponderomotive noise and radiation pressure noise.[85] A lot of active research in the WGM sensing community involves different methods of measuring small resonance shifts in various elegant ways. Recent advances include self-referencing by using a second microresonator not exposed to the analyte,[86-88] interferometry with light not coupled into a microresonator but experiencing a similar path length,[87,89,90] variation in the beatnote frequency between two lasing modes,[75] differential shift of TE and TM modes to shift in refractive index[91-93], shifts in mechanical resonance frequency,[84] Pound-Drever-Hall wavelength locking,[94] detection of backscattered light,[95] and heterodyning of the probe laser.[96]

In addition to the refractive index, the optical path length of the microresonator is determined by the geometrical size. A change in the physical dimensions of the resonator will cause a shift in the resonance wavelength, an effect that helped spawn the field of cavity optomechanics. For example, polymer microspheres are deformable, a property exploited for magnetic sensing.[97] With few exceptions,[98] solid-core silica microresonators are rarely used to sense deformation caused by external forces because of low compressibility in silica. However, the coherent electrostriction induced by radiation pressure of circulating light has been fertile ground for cavity optomechanics.[69-71] Given that (to my knowledge) there have been no reports of single particle or single molecule detection resulting primarily from a change in size of the resonator, we did not consider using this method of sensing in our photothermal experiments.

Another common method of optical sensing, especially in the mid-IR, is cavity ringdown absorption spectroscopy. The presence of an absorbing analyte is deduced from the decrease in cavity Q-factor. This idea has been extended to work with WGM optical microresonators.[76,99,100] In a resonator, the

losses may come from absorption or from increased scattering losses by a binding nanoparticle.[86] Q-spoiling can be measured in the time domain (as cavity ringdown time) or frequency domain (through changes in the resonance linewidth). Although this was originally suggested to be a viable route to near-single-molecule absorption spectroscopy,[101] subsequent work has generally shown this approach to be less successful than the reactive mechanism.

A final sensing modality involves a property that is more or less unique to optical microresonators. Because of the small mode volume compared to macroscopic resonators, it is often possible to observe splitting between a pair of otherwise degenerate modes in WGM microresonators. Specifically, any particular WGM mode is actually two modes that are either symmetric or antisymmetric with respect to the largest source of dielectric perturbation in the mode volume (Figure 3b,c). This might be a fabrication defect,[102] with a splitting energy of only a few MHz. The WGM with an antinode on top of the defect will experience either higher or lower optical path length, depending on whether material is missing or added. One method is to measure the change in splitting frequency, which is shifted by deposition of single nanoparticles.[103] Another method is to make the toroid lase, and the resulting beatnote between the two non-degenerate symmetric and anti-symmetric frequencies is both measurable (at MHz frequencies) and a means of sensitively detecting single nanoparticles.[104] A final quirk is the potential for thermal bistability caused by the high Q-factor achievable with silica WGM microresonators. Thermo-optic shifts induced by absorption of coupled light are very sensitive to absorption losses in the resonator, and the degree of this thermo-optic effect at constant input power has been used to calculate the thickness of a ~ 1 monolayer coverage of water.[105]

Are we any closer to picking out a microresonator and a sensing mechanism? We know that small mode volume (small V) will help us by decreasing the heat capacity of our thermometer. The most well-established sensing mechanism looks for change in the refractive index. The ultrasensitive macroscopic WGM thermometer of Luiten et al.[92] used this mechanism. The ratio of the thermo-optic coefficient

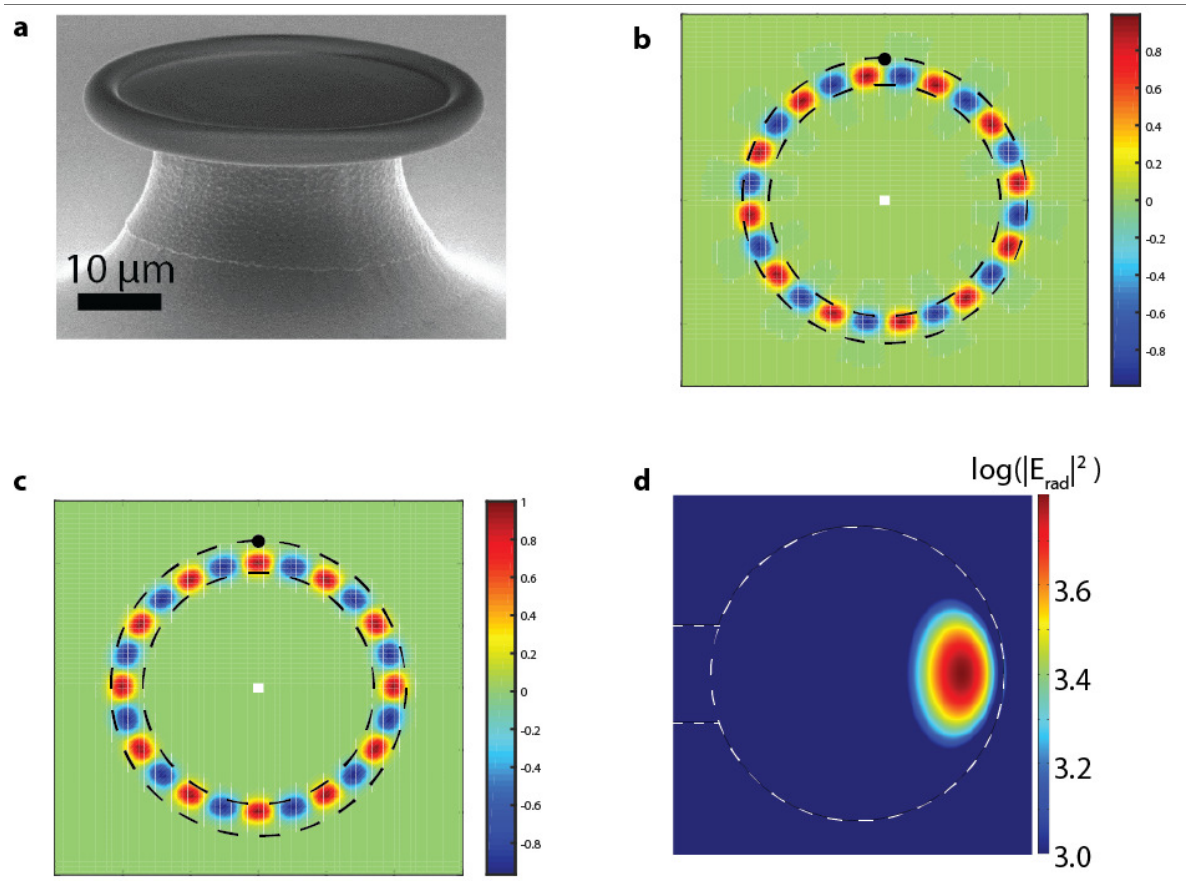

Figure 3: Toroid Microresonators and WGMs.

(a) SEM (scanning electron micrograph) of a toroidal optical microresonator of typical dimensions used in this work. The dark region is silica (thermal oxide) and the lighter region is silicon. (b) Cartoon of whispering gallery mode electric-field amplitude. The rim of the toroid is shown with black dashed lines. A nanoparticle is shown as black dot at top. This mode is antisymmetric. (c) Symmetric WGM mode. (d) Finite-element simulation of the fundamental WGM propagating in the rim of the toroid.

(dn/dT) to the thermal expansion coefficient (dL/dT) for a given material tells us whether we should monitor changes in n or L. In practice, it is difficult to measure these two changes distinctly, so we most likely don't have to worry about the distinction. The other two methods—Q-spoiling and mode splitting—are not really affected by a local heat source, especially if the heat source is very small. Further, these methods are much less popular in the literature and so there are fewer published techniques that can be used to enhance detection limits. Detection of the photothermally-induced shift in the resonator's

refractive index is therefore the best strategy. Therefore, we also know that optimizing the Q-factor is important. We need to have as high a resolution as possible for changes in refractive index. Measuring small changes in λ_0 is required, and a major factor in doing this is the linewidth of the resonance at λ_0. This is the Q-factor. So, our sensitivity is proportional to Q/V. Further, a material with high dn/dT is optimal. Finally, because molecular absorption cross-sections are very small, the material of the resonator must be extremely transparent to any wavelengths we want to do spectroscopy at. Which type of microresonator fits all of these requirements?

1.5 Previous sensing experiments with toroidal microresonators

On-chip, toroidal microresonators[106] are one of the most widely employed types of WGM sensors, owing to the their combination of ultrahigh (>10^8) optical Quality factor (Q-factor) and low mode volume (~ 3 x 10^{-10} cm^3). The ratio of Q/V (where V is mode volume) allows the buildup of exceptionally high circulating power, allowing observation of striking effects like Raman lasing in undoped silica,[74,75] phonon lasing[69] and laser cooling of a mesocopic resonator to nearly the quantum ground state.[107] A thermal reflow process (Chapter 3) ensures a nearly-atomically-smooth surface, minimizing surface losses, while the high transparency of fused silica[108] minimizes absorption losses. Radiation losses do not limit Q-factors for toroids with R > 15 μm in air[109] and R = 40 μm in water.[110] In fact, the limiting factor for the Q-factors of toroidal optical microresonators under ambient conditions is O-H overtone absorption by a surface monolayer of water to 2-4 x 10^8.[111,112] In practice Q-factors are more typically 1-2 x 10^7, limited by fabrication or contamination. These resonant linewidths at 1550 nm are 8 fm (Q = 2 x 10^8) and 80 fm (Q = 2 x 10^7). As we will show in later chapters, even a much lower Q-factor can be used for sensing given the right detection setup.

The virtues of toroid microresonators for single-molecule sensing has not gone unnoticed by the community. In the past 4 years, single-molecule detection of unlabeled proteins has been demonstrated by three different research groups using WGM optical microresonators.[72,73,84] Using either plasmonic enhancement or optomechanical transduction to reach this detection limit, researchers were able to detect binding from single proteins or DNA oligomers. There is a fundamental limitation with this approach, though. In all of the experiments, the only observable is the reactive shift caused by excess polarizability from the binding molecule. On top of that, the highly nonlinear dependence of resonance shift on binding location makes the molecule's polarizability a fuzzy number. Binding kinetics can be inferred, and with some assumptions, a loose estimate of the macromolecule's mass from the polarizability. In contrast, our method obtains an absorption spectrum, potentially permitting identification and characterization of individual nanoparticles and ultimately molecules.

Silica, the material toroids are composed of, is unfortunately, not the best material for photothermal sensing. The temperature dependence of the refractive index is both weak and linear, and so we can use a Taylor expansion to calculate the resonance shift as a function of temperature:

$$\Delta\lambda = \left(\frac{\lambda_0}{n_0}\right) * \Delta n = \left(\frac{\lambda_0}{n_0}\right) * \Delta T * \frac{dn}{dT} \qquad 1.3$$

λ_0 and n_0 are constants (typically 1.55 μm and 1.44, respectively) while dn/dT for fused silica is 8.6 x 10^{-6} K^{-1}.[113] The thermal expansion coefficient of fused silica is small[114] compared to the thermo-optic coefficient, contributing only 8% to the temperature dependence of resonance wavelength shift. We typically neglect this thermal expansion from calculations of resonance shift, a common practice in this field.[89,112,115] The toroid will change resonance frequency in response to temperature with a tuning slope of 9.3 fm/mK. Increasing dn/dT is one avenue to improving the possible detection limit of this experiment. Comparing to the SM work of Orrit et al.[51], silica is 158x less sensitive than glycerol. Glycerol has a higher refractive index than that of fused silica, so that toroids will not function when immersed in glycerol. In

passing, I note that WGM microresonators made entirely from droplets of glycerol were first demonstrated during the writing of this thesis.[116]

Toroid microresonators also satisfy our other figures of merit. A typical toroidal microresonator (Figure 3) has a major radius of 25 μm, minor radius of 2 μm, and a mode volume of ~ 300 μm^3 as determined from the finite-element simulations of Oxborrow.[117] Independent confirmation of the mode volume is obtained from directly imaging WGMs.[118-120] The other types of resonators with similar Q-factors are microspheres (Figure 2) and macroscopic microdisks. Microspheres have mode volumes roughly an order of magnitude larger,[121] because WGM modes are not confined in the polar dimension (Figure 2). Millimeter size CaF_2 disk resonators possess unbeatable[122] Q-factors exceeding 10^{11} but the huge increase in mode volume renders them impractical for our purposes. Lastly, let's consider the material choice. Toroids are made from silica, a material with transparency from ~ 400 nm-2000 nm. Losses at near-infrared wavelengths are particularly low with a minimum near 1500 nm.[108,123] A complication is that the microresonator is supported by a silicon pillar and a silicon substrate, a material with notoriously strong absorption of visible and near-IR light. This potentially crippling issue has two solutions, both of which will be discussed in later chapters. The photothermal sensitivity of silica is also not ideal. An ideal material would have a much higher thermo-optic coefficient without sacrificing optical transparency, a requirement that is difficult to satisfy in practice. Further, the fabrication and use of toroidal optical microresonators had already been demonstrated widely before the beginning of this project, and for the reasons outlined above the toroid became the heart of our proposed single-molecule absorption spectrometer.

1.6 Putting it all together

We should begin the discussion of building the toroid microresonator absorption microscope with the most basic question: How are we exciting the targeted molecule or nanoparticle, and how are we measuring the heat it dissipates? Perhaps the simplest scheme would be to excite the molecule by coupling light into the microresonator via tapered fiber. This design has the virtue of simplicity (we had to couple into the microresonator anyway to probe resonance wavelengths) and the transverse confinement of the fundamental whispering gallery mode (Figure 3d) is nearly diffraction limited. Loock and coworkers[100] used this method to measure thin films of ethylene diamine by simultaneously probing the amplitude and phase shift of backscattered light as well as the phase of transmitted light. Rosenberger et al. used taper excitation with a tunable microsphere-derived WGM resonator to trace out a single rotational absorption line in various gases.[124] There are drawbacks to extending this approach to absorption spectroscopy, however. For one, the entire mode volume is excited simultaneously, making it impossible to localize absorbers by their spatial dependence and confirm that only one molecule is being measured at a time. For another, only a tiny fraction of the power coupled into the resonator is available for excitation, because the fraction of light propagating outside the silica is less than 1% (Chapter 9). The free spectral range (FSR) of a toroidal microresonator is later shown to be of order 1-10 nm, limiting the achievable spectral resolution. At the same time, the coupled laser must be narrow-linewidth (sub-MHz) and widely tunable (several THz) with very high tuning resolution (kHz precision) AND be continuous-wave because pulsed lasers strongly perturb toroids[125] and have a very low duty cycle ($< 10^{-5}$). I am not aware of any light sources in existence that satisfies all of these requirements. Additionally, the polarization of a WGM cannot be tuned, a grave loss because polarization offers a lot of information; for example, characterizing the structure individual conjugated polymers[13] and locating single absorbers.[126] The combined limitations to our three primary tools of spatial, wavelength, and polarization characterization conspire to make WGM excitation impractical for our single-particle or single-molecule experiments.

This suggests that free-space excitation is highly preferable. A number of previous experiments have involved interaction between a focused free-space laser and toroid or microsphere microresonator. The taper can be used to collect light resonantly scattered into the toroid by single scattering nanoparticles.[127] Ganta and Rosenberger[128] used an unfocused laser to heat a microsphere located inside of a vacuum chamber. Benson et al.[129,130] physically coupled a single nanodiamond onto a plastic microsphere and monitor the free-space excited, free-space collected luminescence intensity. Sandoghdar et al.[131] used a confocal laser scanning microscope to excite single luminescent nanoparticles on a microsphere's surface. It should be noted that we were not aware of any of these works during the initial development of our instrument, which was a mixed blessing. However, none of these reports involved a tunable excitation source; further, none of them aimed at measuring absorption by the target. Most importantly, none of these techniques used photothermal dissipation to decode information about an absorber on the microresonator's surface and measure the resulting heating of the mode volume.

Throughout the course of this thesis I will discuss the design, construction, and results of our toroid microresonator absorption spectrometer. The experimental setup is briefly discussed here. Figure 4 is a rendering of the apparatus. Resonant wavelengths of the toroid are monitored with a fiber-coupled laser, referred to hereafter as the probe laser. This beam does not significantly interact with any analytes on the surface of the toroid, due to the location, low coupled power (~ 1 μW) and long wavelength (~ 1.55 μm). Light is evanescently coupled into the toroid via this tapered optical fiber (Figure 4a) (see Chapter 2 and 3 for more details). Simultaneously, a free-space beam is focused down onto the top surface of the microresonator (Figure 4b) and used to excite single analytes. The position, polarization, and wavelength of this beam is tuned until absorbing nano-objects are found. This beam is hereafter referred to as the pump beam. Spectra are recorded by tuning the wavelength of the pump beam while monitoring the toroid resonance wavelength with the probe beam. If the targeted nano-object is transparent to the pump wavelength (Figure 4b), then nothing happens when the pump beam is focused on it. Conversely, if the

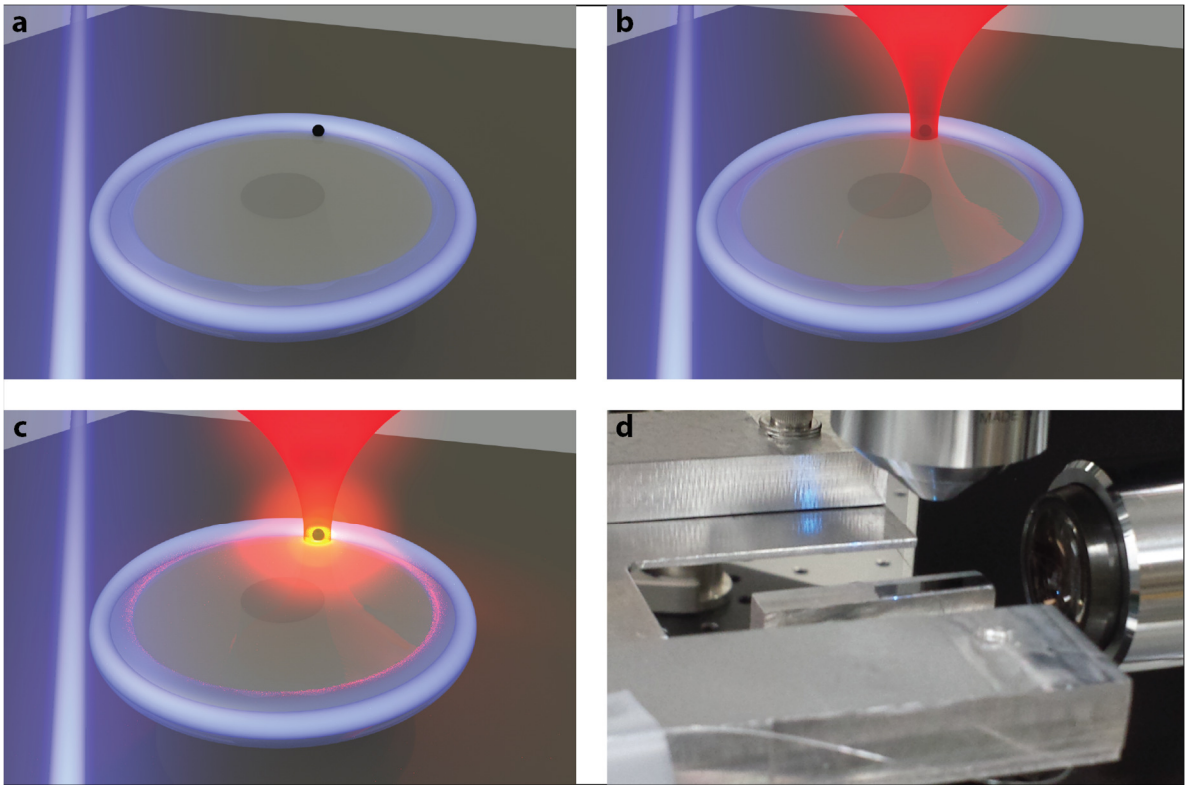

Figure 4: Rendering of microresonator absorption spectrometer.

(a) A fiber-coupled probe beam (blue) is evanescently coupled into the toroid. A single nano-object (black sphere) is randomly deposited onto the toroid surface by spincoating. (b) The nano-object is pumped with a focused free-space laser (red). (c) If the nano-object absorbs light from the pump laser, it dissipates heat into the toroid in proportion to its absorption coefficient at the pump wavelength. (d) Micrograph of the setup. The pump objective (top) is pulled back from the chip, which is resting on a 3-axis piezostage. The sideview objective is visible at right, as is the tapered optical fiber that straddles the silicon wafer chip.

target absorbs pump photons, then heat is dissipated by nonradiative relaxation (Figure 4c) and the toroid resonance wavelength shifts. The experimental observable is a shift in λ_0, and the desired variable is $\sigma(\lambda)$. A Micrograph of the coupling setup is shown in Figure 4. Details of the coupling setup will be given in Chapter 2.

Converting the amount of light absorbed by a target nano-object into a temperature change of the toroid is not trivial. Heat produced by a point source on the surface of the resonator will diffuse through the somewhat complicated geometry of the microresonator, at a rate that rapidly increases in

the regions composed of silicon. In fact the silicon support pillar and substrate act as a heatsink, making the equilibrium temperature of the resonator depend strongly on the distance of the heat source from the silicon pillar. We have developed numerical simulations (COMSOL Multiphysics) to treat this problem, and verified them by focusing a visible laser onto the microresonator. Chapter 4 discusses the results of this important calibration experiment.[132] Chapter 5 offers further validation of the finite-element numerical simulations with characterization of the absorption cross-section of multiwalled carbon nanotubes (MWCNTs).[133] Ultimately the simulation is used to convert the observable (average resonator temperature via resonance shift) to the desired parameter (absorption cross-section) by determining the effect of a given amount of dissipated heat on the microresonator temperature. The following equation calculates the absorption cross-section:

$$\sigma_{abs} = \frac{P_{thermal}}{I_{optical}} * \frac{1}{1 - \phi_{luminescence}} \qquad 1.4$$

where $P_{thermal}$ is the dissipated heat calculated from the resonance shift by COMSOL simulations, $I_{optical}$ is the intensity of the pump beam and is easily measured, and the fluorescence quantum yield $\phi_{luminescence}$ is ~ 0 for all systems measured in this thesis. Fortunately the photothermal effect is linear over multiple orders of magnitude[132] (Chapter 0) and so the simulation does not have to be rerun for every experimental data point, since it can be simply scaled to the observed resonance shift.

It is important to calculate the expected single-molecule photothermal signal. Early in this chapter we derived the fractional extinction as ~ (1 x 10^{-16} cm^2)/(~5 x 10^{-9} cm^2). Increasing excitation power will increase the dissipated heat until optical saturation is reached, as calculated by Equation 1.5

$$I_s = \frac{h\nu}{2\sigma\tau} \qquad 1.5$$

where I_s is saturation intensity, h is Planck's constant, ν is optical frequency, σ is absorption cross-section, and τ is excited-state lifetime. For our representative molecule cobalt phthalocyanine, I_s = 6 x 10^8 W/cm^2.

This requires an excitation power of 1 W, which is rather high. In this scenario the molecule will dissipate 60 nW of heat. Although much higher peak intensities are used in two-photon absorption or transient absorption experiments, we will proceed with a more reasonable excitation intensity of 1 x 10^8 W/cm^2, giving 10 nW of dissipated heat. COMSOL simulations indicate that a 10 nW heat source will cause a typical toroid microresonator to equilibrate at a resonance shift 2 fm redder. Immersion in water will suppress the predicted single-molecule resonance shift to approximately 0.5 fm, still well within the range of being measurable.

Achieving the diffraction-limited spot size used in these calculations is crucial. Most of the experiments performed in this thesis were taken with a spot size of 2.4 μm diameter, which reduces the photothermal SM signal for a given power by a factor of 28x compared to the optimized case just described. At the lower pump intensity levels available during my thesis (maximum of 3 x 10^5 W/cm^2), a strong dye molecule will only produce ~ 50 am of resonance shift. This is quite small compared to a typical resonance linewidth of >100,000 am. Detecting a small fraction of a linewidth shift will be crucial to the success of this project, absent a currently unknown means of boosting the single-molecule photothermal signal. How well can we do? Previous sensing experiments have demonstrated resonance shift detection limits that approach 100 am from stochastic binding of single nano-objects.[75,84] The optimized SM photothermal signal of 2 fm is well above this level, but requires high optical intensity with correspondingly high levels of background absorption from the resonator itself. Matching and exceeding the sensitivity of these other results will require a technique for measuring shifts of tiny fractions of a resonator linewidth and an additional means of narrowing the measurement bandwidth. While saving the

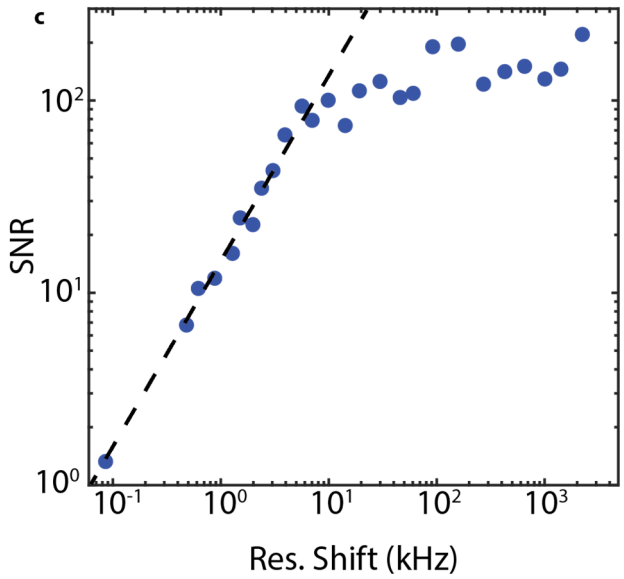

Figure 5: SNR at low-kHz resonance shift.

The signal to noise ratio is linear with signal below ~ 45 attometers of resonance shift for this particular WGM. Since the photothermal signal is always linear, the noise must be constant (additive). This indicates it is technical, not a fundamental source like shot noise, thermorefractive noise, or Johnson noise in the photocurrent. This data was taken with a WGM Q-factor of 2 x 10^7, for a linewidth of 78 femtometers. At this wavelength, 1 kHz = 8.33 am.

details for later discussion, we have developed a combination of phase-sensitive detection of the probe beam with an additional phase-sensitive, modulated detection of the excitation source. This allows us to reach a detection limit of less than 10^{-5} of a linewidth or ~ 1 am (Figure 5). A key feature of this achievement that will be discussed in Chapter 2 and Chapter 6 is bandwidth-narrowing. Because our photothermal signal occurs as long as the pump beam is turned on, and is otherwise zero, we can implement amplitude modulation and lock-in amplification. At the same time, we have room to decrease the focused spot size by improving the choice of optical equipment. Increasing the pump intensity at constant power will allow for improvement of the signal/noise ratio, while leaving the signal/background ratio unchanged. Shifting from SWIR to visible wavelengths (Chapter 8) will also significantly improve the signal/noise and signal/background by decreasing the excitation volume by a factor of ~8.

1.7 Roadmap to this thesis

The course of this thesis can be divided into three parts. First, we will examine in detail the microresonator single-particle spectrometer, particularly the optical and electronic subsystems and how they came to be in Chapters 2 and 3. Next, we will present the milestone experiments demonstrating photothermal mapping (Chapter 4), single-nanoparticle imaging (Chapter 5), and high-resolution, high-sensitivity single-particle absorption spectroscopy (Chapter 6). We will close by discussing photothermal tuning and Fisher information of Fano-resonant hybrid photonic-plasmonic resonators (Chapter 7) and suggest future directions for the project (Chapter 8), most particularly the road to single-molecule detection and characterization. Appendix 1 (Chapter 9) discusses the details of the finite element simulations used to support the research in Chapters 4-8. Appendix 2 (Chapter 10) examines unsuccessful experiments for their future potential. Appendix 3 (Chapter 11) covers back-scatter detection and compares it to the method of resonance shift detection used in the rest of this thesis. Finally, Appendix 4 (Chapter 12) covers photothermal imaging of individual carbon nanofibers.

Chapter 2

2. Design Questions, Quirks, and Quandaries

2.1 Overview

In this chapter I will lay out the design considerations for building a toroid microresonator single-particle absorption spectrometer. The overriding figure of merit will always be the detection limit. Other important figures of merit are the spectral range, time resolution, and experimental throughput. As discussed in Chapter 1, the single-molecule signal that we are ultimately driving towards is quite weak. The absorption background must consequently be suppressed enough to make possible robust single-molecule characterization. We must be capable of measuring a resonance shift from the toroid commensurate with that expected from the single-molecule. Second, we must know that this signal is only coming from our desired analyte.

How can we distinguish our signal of interest from background absorption? We have three tools at our disposal: polarization, position and wavelength. If the absorption is truly coming from impurities or defects in the silica, then it should be independent of azimuthal position, wavelength (within the range of the pump laser and to an imperfect extent), and polarization. A single-molecule signal, by contrast, should have strong wavelength dependence, 100% polarization dependence, and spatial dependence characteristic of an infinitesimally-small point. Our ideal spectrometer will have a pump laser that is continuously tunable through the visible and near-IR, focused to a diffraction-limited spot on top of the toroid, with fully adjustable linear polarization. Realizing all of these properties while maintaining the

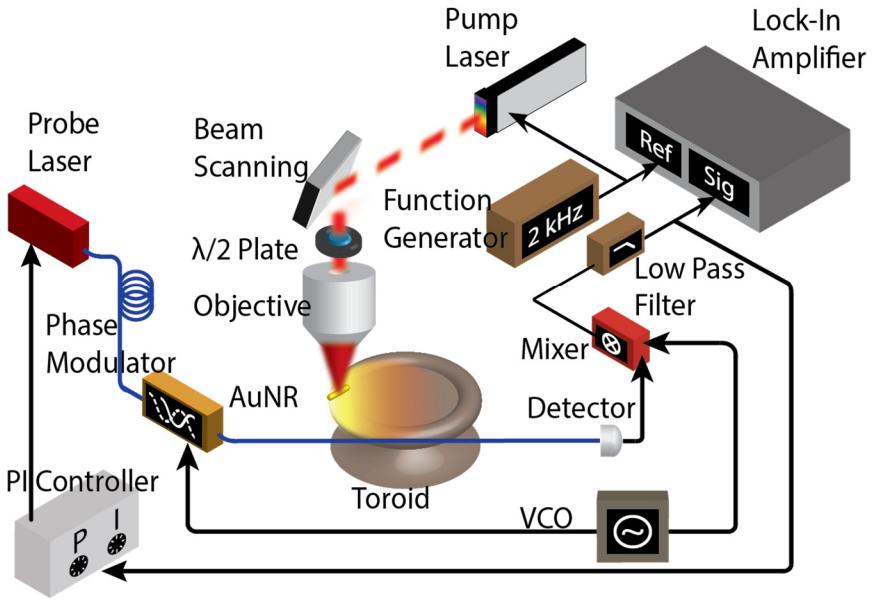

Figure 6: Block diagram of microresonator spectrometer.

The fiber-coupled probe laser (blue) is coupled into a microresonator with an optical fiber taper. Probe light is phase-modulated and the resulting photocurrent is mixed with the local oscillator to produce a signed error signal. The error signal is used to lock the wavelength of the probe laser to the microresonator. Single nano-objects are optically pumped with a second free-space tunable laser (red), delivered to the microresonator surface with a high-NA microscope objective and galvo-scanning delivery system. Amplitude modulation of the pump beam modulates the transmitted probe light, and a lock-in amplifier is used to maximize the detection limit

necessary paraphernalia for evanescently coupling into toroid microresonators is the central challenge explored in this chapter.

The single-particle toroid absorption spectrometer is shown in schematic form in Figure 6. Each section will be explored in detail in the course of this chapter. To summarize, the probe beam (blue) is coupled to toroid microresonators (Section 2.2) with a tapered optical fiber (Section 2.7) and detected with a photodiode. A $LiNbO_3$ modulator phase-modulates the probe beam at RF frequencies, allowing subsequent phase-sensitive demodulation of the photocurrent to recover the detuning between the probe wavelength and the WGM resonance. This demodulation occurs electrically with a mixer, local

oscillator, and low pass filter (Section 2.8). Simultaneously, the pump beam (red) is focused onto an absorber on the surface of the toroid. A beam scanning system (Section 2.3) and motorized half-wave plate (Section 2.4) provide control over the wavelength-tunable pump beam. The demodulated PDH error signal is then fed to lock-in amplifier locked to the amplitude modulation frequency of the pump beam (Section 2.9). This final step is vitally important for reaching the detection limits exploited in Chapter 6.

2.2 Toroidal optical microresonators

Fabrication of toroidal microresonators will be discussed in Chapter 3. For now we will concern ourselves with their optical and thermal properties. The WGM mode is entirely confined to the silica layer, so the properties of the silicon substrate and pillar are less important than those of the silica. The important exception to this principle is the subject of Chapter 4. The silica is grown from wet thermal oxidation of single-crystal silicon, referred to as thermal oxide. Thermal oxide is a well-characterized material because of its importance in computer chip manufacturing. It is quite similar to fused silica, the material used to make fiber optic cables. In either case the silica in the toroid is amorphous, lacking birefringence or other anisotropic properties. It is also robust to high temperatures, possesses modest thermal conductivity (1.4 W/mK),[134] and has rather small nonlinear optical coefficients. Thermal oxide is transparent from ~ 0.4-2.0 μm, with the exception of OH overtone absorption from interstitial OH defects and trapped water at ~ 1.38 μm. Two properties are of overriding interest: the Q-factor at the probe wavelength and background absorption at the pump wavelength.

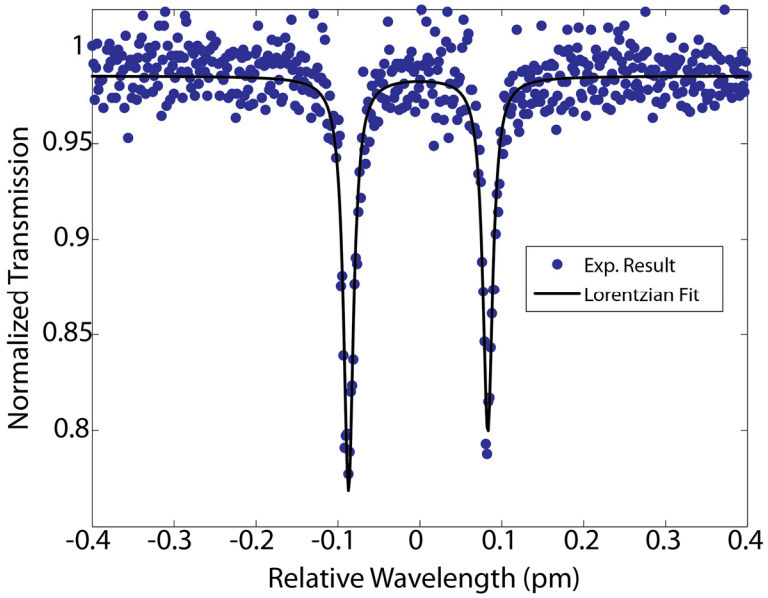

Figure 7: Ultrahigh-Q toroid WGM resonance.

Scanning the wavelength of the probe laser and measuring transmitted light (blue dots) allows for characterization of a WGM. This WGM is split into clearly-resolved symmetric and anti-symmetric modes. A pair of Lorentzian fits (black curve) is used to determine the Q-factor.

Q-factors are determined by the sum of losses, primarily bulk absorption, radiation loss, scattering, and surface absorption. Radiation loss is a function of resonator size, sharply decreasing as the dimensions of the resonator start to approach the wavelength of light.[135] Bulk absorption by the material of the resonator can be calculated from surface properties, and is rarely the limiting factor for dielectric WGM resonators (although silicon resonators may be limited). Immersing resonators in water exposes a substantial fraction of the optical mode to the much higher losses of water in the near-infrared, which may dramatically lower the Q-factor.[110,112] Scattering is determined by surface roughness, and the effect of scattering on the Q-factor can rarely be neglected. An important exception is surface-tension-induced reflowed resonators, which are the mostly commonly used in WGM sensing. The final source of limitation on the Q-factor is surface contamination, which may come from surface states,[136] water vapor,[111,112] or any other source of residue deposited on the surface. This last issue may be addressed by cleaning the

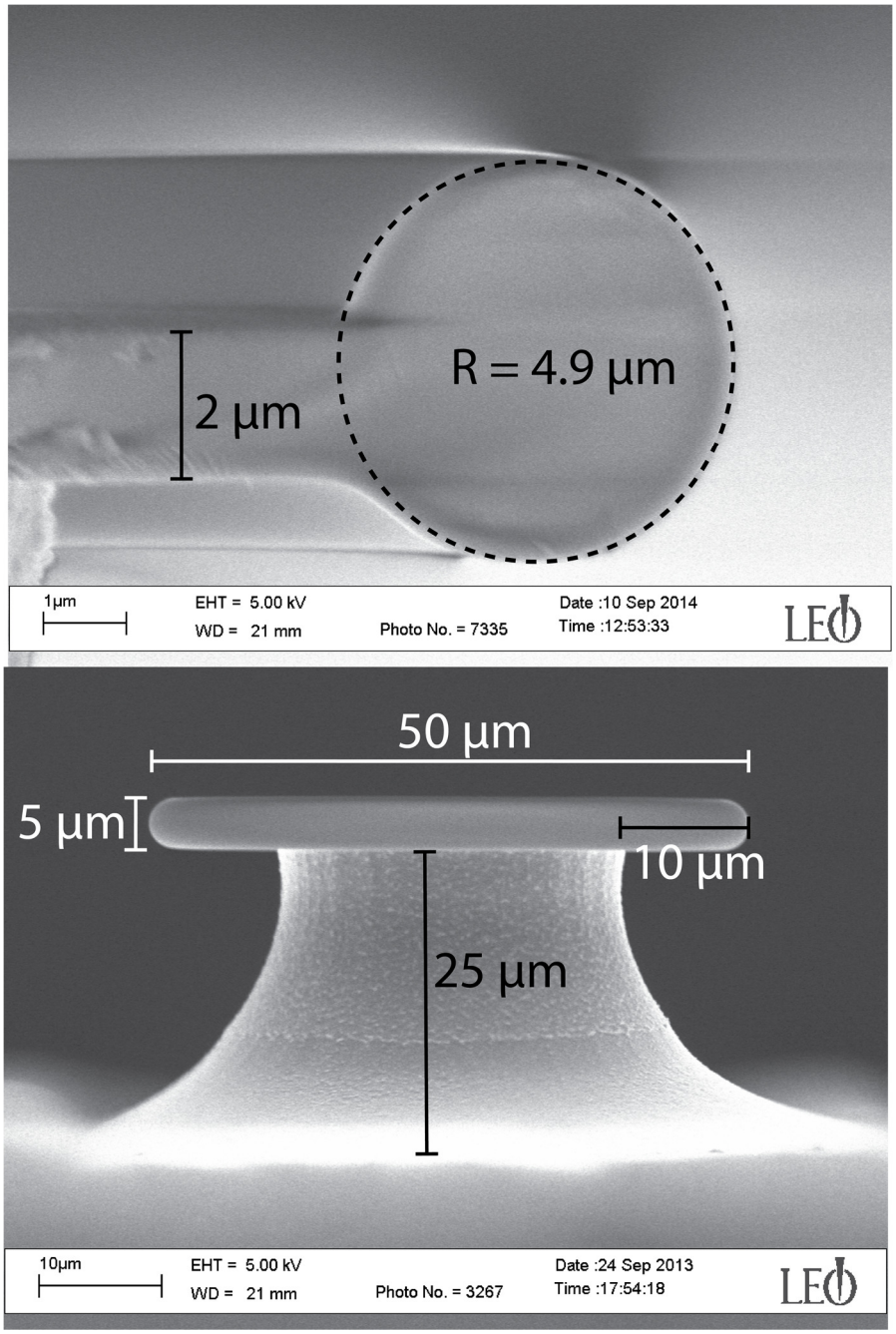

Figure 8: Dimensions of a typical toroid microresonator.

(a) A cross-sectional view taken from an accidentally fractured toroid. The minor diameter of 4.9 µm is typical for the toroids used in this work. The oxide thickness is 2 µm. (b) The major diameter is usually 42-50 µm, varying as a result of reflow power and undercut during etching. The silicon pillar height is approximately equal to 25 µm.

resonator, and is an area of active research in our group. Different classes of WGM sensors achieve

different Q-factors, owing to the various constraints imposed by material, geometry, fabrication, and size.

WGM resonances are fully described by three mode numbers, which can only take nonnegative integer values. In addition to the azimuthal mode number *m*, the number of radial (*q*) and axial (*l*) nodes can vary; the latter two indices refer to transverse component of the electric field. The fundamental mode, typically supposed to have the highest Q-factor, has $q = l = 0$. The first several transverse modes are plotted

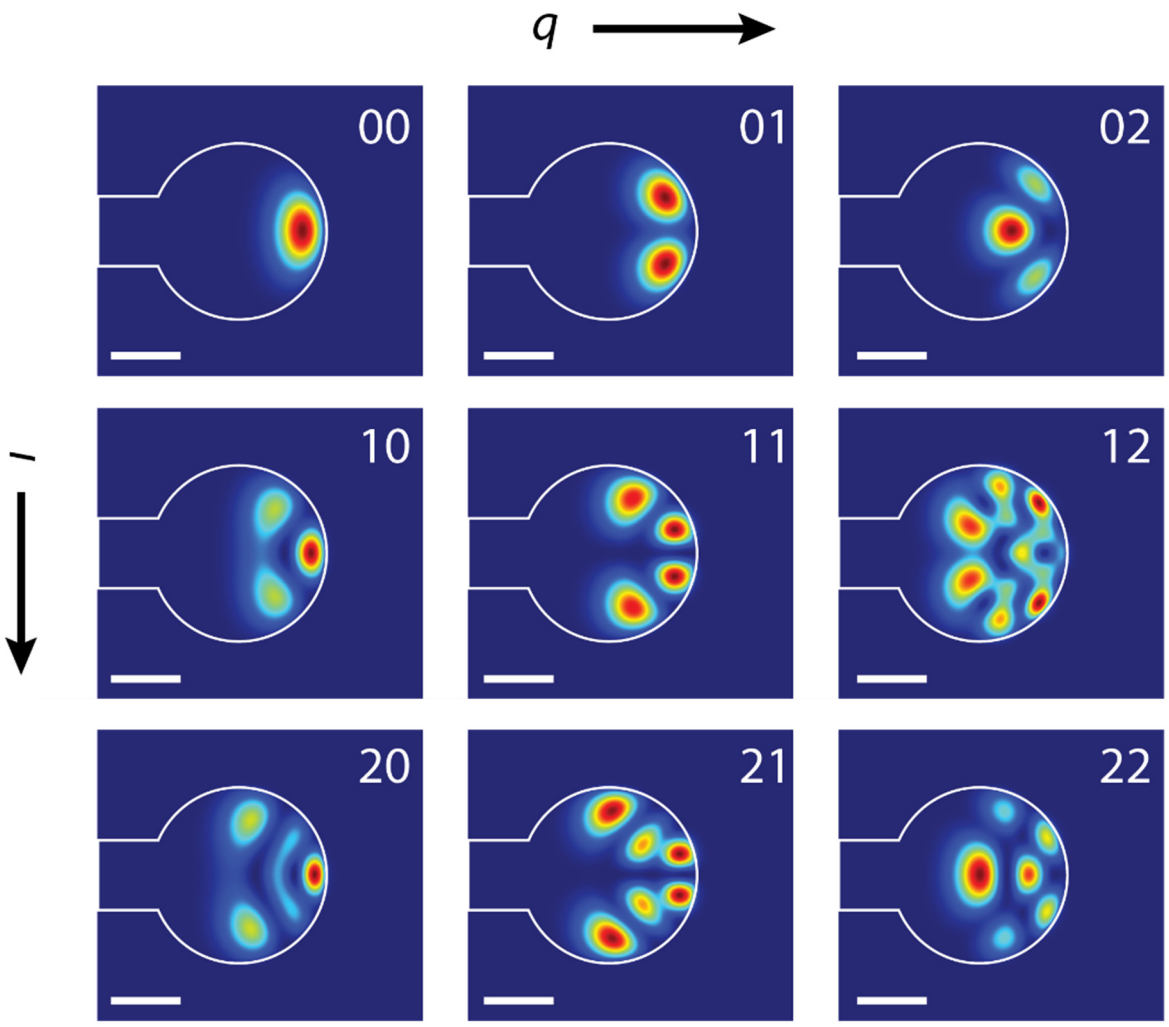

Figure 9: Finite-element simulation of the first nine transverse mode profiles for a given azimuthal mode number in a toroid.

The transverse mode profile is determined by two mode numbers (*q* and *l*) reporting the number of nodes in each direction. The scale bar is 2 μm and the color shows the optical intensity in arbitrary units. The geometry of the microresonator cross-section is marked by a solid white line.

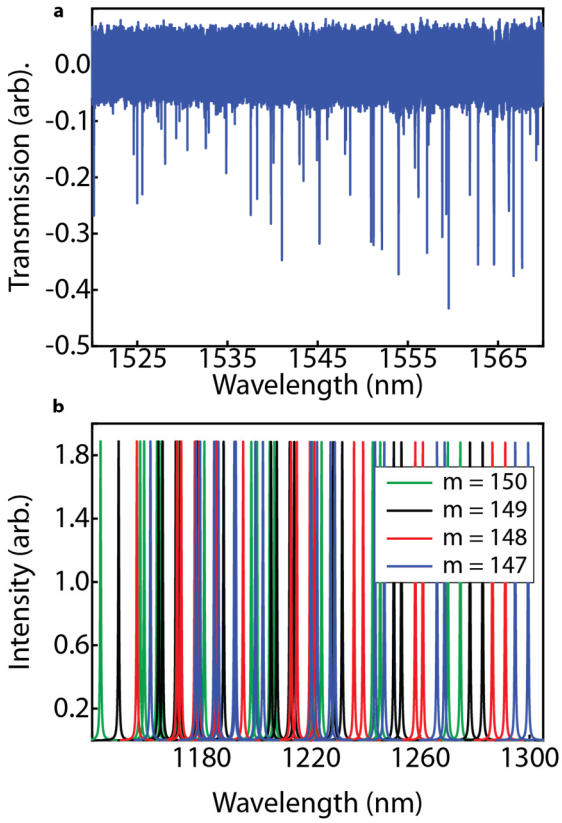

Figure 10: Mode spectrum of a toroid.

(a) The wavelength of the probe laser is tuned from 1520-1570 nm and the transmission through the fiber is measured (with phase modulation turned off). A large number of high-Q WGMs appear. Because the free spectral range for any single transverse mode in this toroid is approximately 11 nm in the probe laser wavelength band, the observed mode spectrum cannot be attributed solely to the fundamental mode. (b) Simulated WGMs are plotted as Lorentzians centered at the resonant wavelength of the WGM. A dense mode spectrum is observed using only four azimuthal mode numbers (colors) and the first nine transverse modes (including the fundamental mode).

in Figure 9. The range of resonant wavelengths covered by the nine lowest energy radial modes for a given azimuthal mode number is on the order of 50 nm (Figure 10), while the FSR (difference in wavelength between successive azimuthal mode orders) of any one of these higher order radial modes is of order 5 nm. The FSR of the resonator is found by taking the difference of two modes with successive *m*. In practice, the number of WGM resonances observable via taper coupling is far greater than the number predicted from the FSR, indicating that for each azimuthal mode number a large number of non-fundamental modes

are excited (Figure 10). Modes with identical azimuthal mode number are not degenerate, although the FSR is unmodified according to simulation in COMSOL Multiphysics. The observed mode spectrum can be thought of as a series of highly overlapping frequency combs, where each comb corresponds to a specific azimuthal mode number. This degree of overlap between sets of successive azimuthal modes greatly complicates the task of identifying individual modes. Consequently, we cannot confidently assign individual Fano resonances to corresponding WGMs identified by the probe beam in the 1520-1570 nm range of the probe laser.

There is a further degeneracy breaking for each WGM, into symmetric and anti-symmetric modes. There is a 90° phase shift between the two modes (Figure 3b,c). In a perfect toroid with no adsorbates or coupling fiber, these two modes would be degenerate. A single imperfection, either in the structure of the toroid or from an analyte binding, will cause the modes to shift. The mode with an antinode on the imperfection will shift to lower energy via the reactive mechanism, breaking the degeneracy of the two modes. In the more realistic case of multiple scatterers,[137] the degeneracy breaking still occurs. The splitting energy can be used to sense analytes;[104] more intriguingly, the beatnote from interference of the two modes is at detectable (~ 10 MHz) frequencies and can also be used for sensitive detection of single nanoparticles.[104,138] Although the doublet splitting is always present, it is often not observable, especially for a Q-factor below 10^7.

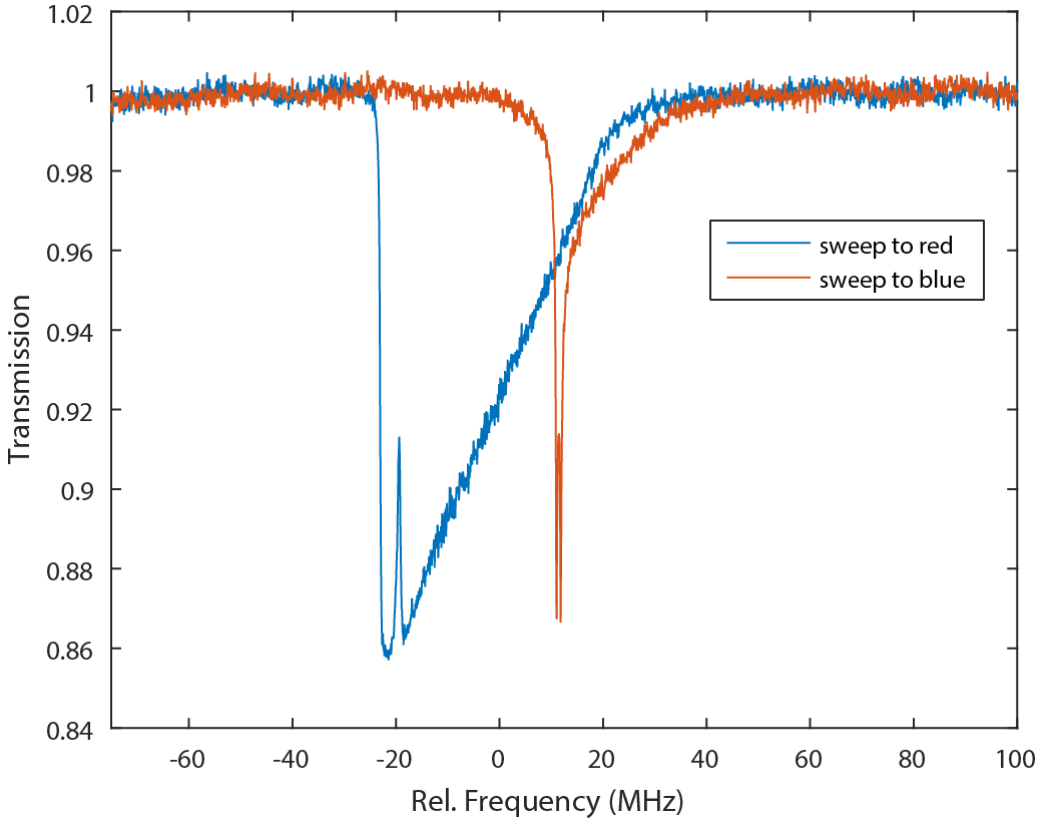

Figure 11: Thermal asymmetry in toroid resonances.

The scan direction causes thermal bistability that depends on the direction of wavelength scanning. Sweeping from redder to bluer wavelengths (orange) causes a narrowing of the resonance to produce unphysically high apparent Q-factors. Sweeping from bluer to redder wavelengths (blue) causes a linear decrease in transmission as the toroid heats up and the refractive index increases. Ultimately a saturation point is reached and the transmission suddenly rises again. This particular resonance is a doublet, and the splitting is apparent in both scan directions.

Another distinctive feature of optical microresonators is a consequence of the ultrahigh Q-factors. A modest coupled power into a 10^8 Q toroid will build up to an extreme circulating intensity. The cavity buildup factor is given by[139]

$$\frac{P_{circ}}{P_{input}} = \frac{\lambda Q_0 \kappa}{\pi^2 n R (1+K)^2} \qquad 2.1$$

where Q_0 is intrinsic Q-factor, P_{circ} is circulating power, P_{input} is the input power, and κ is $Q_0/Q_{coupling}$ where $Q_{coupling}$ is the Q-factor due to coupling. κ is equal to 1 at critical coupling; a critically-coupled toroid with $Q = 1 \times 10^8$ and a 45 um diameter has a buildup factor of 1.2×10^5. A launched power of 1 mW leads to 120 W inside the cavity. With a transverse mode area 2.1 μm^2 for the fundamental WGM, the steady-state optical power density is 5 GW/cm^2. Outside of STED microscopy, CW intensity this high is unheard of in spectroscopy. This intensity is so high that even through SiO_2 is extremely transparent, enough light is absorbed to noticeably heat up the cavity. Increasing temperature will redshift the cavity (Equation 1.3). This leads to an interesting behavior as the probe laser wavelength is tuned across the cavity.[66,112,140] If the laser is tuned from short to long wavelengths then the cavity begins to heat as light is brought to resonance (Figure 11). This heating causes the toroid resonance to shift to longer wavelengths, in effect "running away" from the probe laser. This continues until the cavity cannot heat up fast enough to compensate for wavelength scanning and the cavity "snaps back". The resulting observed resonance shape is triangular, with a linear tuning as the cavity heats up and an instantaneous change as it cools past the scanning laser. In the opposite scan direction, as the toroid begins to heat up the resonance moves in the opposite direction from the scan direction. This results in the resonance appearing approximately Lorentzian, but at a much higher Q-factor than experienced with a cold cavity. In this present work, we keep the input power low (1 μW) to stay well below the threshold for this behavior. It's easy to check for the presence of this effect by triggering off of the resonance peak on the oscilloscope, which causes the two scan direction peaks to superimpose, making for convenient visual identification of any thermally-induced asymmetry in peak shape. Overall this effect is unfortunate because it limits the probe power, and therefore reduces the slope of the error signal near the locking point.

2.3 Excitation light and beam scanning

As mentioned earlier, minimizing the excitation volume of the pump beam is a paramount concern. Tightening the radius of the beam's focused spot not only increases the single-particle absorption signal, it simultaneously decreases the volume of background excited, placing less stringent requirements on purification and cleaning of the microresonator. This means that excitation should be delivered with a high-NA microscope objective. Commercially-available refractive objectives have up to 0.95 NA (air) or 1.4 NA (oil immersion). Experimental reflective objectives have only recently reached NA this high.[141] Reflective objectives possess their own advantages (achromaticity and high near-IR transmission) as well as drawbacks (lower NA and complicated focus spot). Another type of optic, lensed fibers, are sometimes used with toroids.[127] Lensed fibers can deliver a theoretical spot size of 2.5 μm with a working distance of 14 μm at 1550 nm,[142] for an effective NA of 0.39. Further, the beam polarization is difficult to tune with respect to an object on the surface of the resonator. A final drawback is the need to mechanically scan the mount holding the fiber to move the excitation, a process that is slow and likely to cause jitter in the fiber's position. By contrast a free-space beam focused by an objective can be position scanned through a motorized mirror and a pair of relay lenses with extremely smooth and rapid motion, in the same manner as a persistence of vision display.

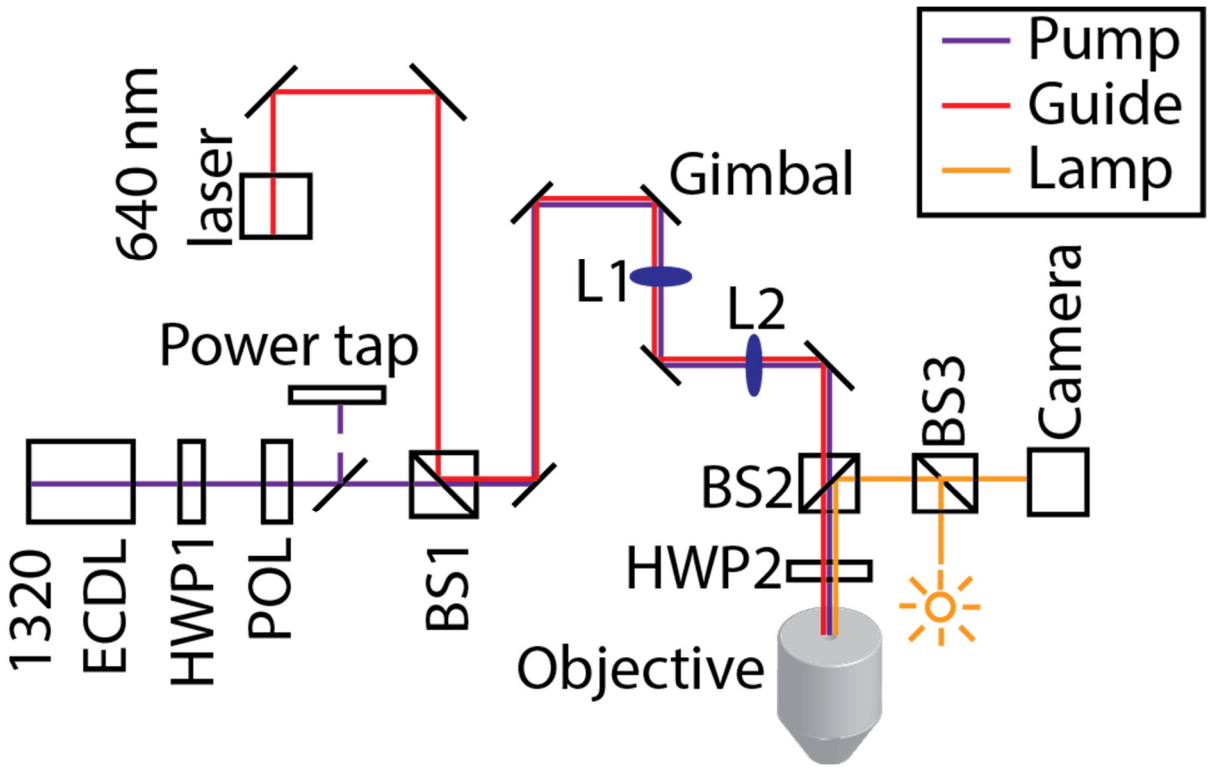

Figure 12: Optical path diagram.

A 640 nm guide laser (red) is coaligned with a 1320 nm ECDL (purple) with a dichroic beamsplitter (BS1). The ECDL power is adjusted with a half-wave plate (HWP1) and a polarizer (POL), and monitored in realtime with a pickoff mirror and a power meter (Power tap). Deflection on the gimbal-mounted motorized mirror is relayed by lenses (L1 and L2) to the back of the microscope objective. Imaging light is supplied by BS2 and B3 and a lamp (orange). The excitation half-wave plate (HWP2) is mounted immediately prior to the objective

The beam position in the sample plan is manipulated by changing the input parameters of the beam at the back aperture of the focusing objective. The objective lens, which can be approximated as a simple plano-convex lens, will convert angular displacement to spatial displacement and vice versa. It will also convert a collimated beam to a converging beam and vice versa. By varying the angle of a collimated beam input to the objective, we end up with a focused beam that propagates parallel to the optical axis but is displaced in proportion to the angular detuning of the incident beam. In practice it is difficult to place the beam-scanning mirror close enough to the objective, and the typical solution is to build a 4f-scanning microscope. In this configuration, a pair of lenses act as relays, allowing the tuning mirror to be placed far

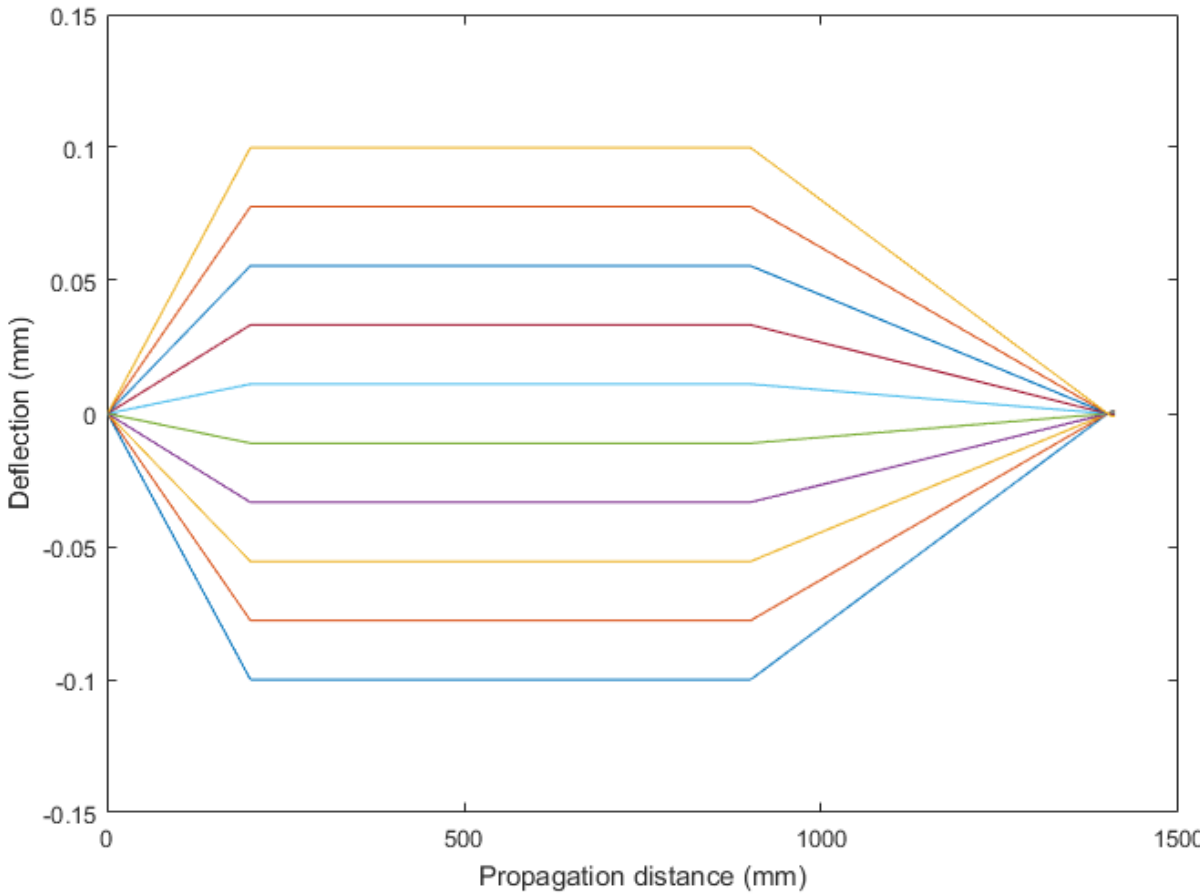

Figure 13: Raytracing plot of beam scanning.

A fan of rays spanning +/- 0.5 mrad optical angular deflection are shown. At distance 0 is the gimballed scanning mirror. The rays bend at lenses L1 and L2 (not pictured) as well as at the objective. The lens position and objective NA correspond to the values for the 1st-generation microresonator microscope (SCORPIO) as of November 2016.

away without "walking off" the back aperture of the objective. This position—4 focal lengths (f) away—is a conjugate plane to the back aperture of the objective. In our setup, more than 1 meter separates the scanning mirror from the objective and yet deflections in the sample plane of 100 nm or less must be reproducibly achievable.

I wrote a code in MATLAB to calculate how much deflection of the scanning mirror corresponds to deflection of the beam in the sample plane. This uses the 2x2 transfer matrix approach commonly found

in photonics textbooks. Figure 13 shows ray tracing applied to the toroid absorption spectrometer. Each colored ray represents a different angle of the scanning mirror. The most widely diverging angles correspond to +/- 0.5 mrad. A deflection of +/- 0.5 mrad in the angle of the beam reflected from the mirror (corresponding to a +/- 0.25 mechanical deflection of the mirror by the law of reflection) gives a theoretical lateral shift of +/- 1 μm in the sample plane. The scanning mirror mount is a U100-G with a pair of TRA12CC actuators (Newport). The actuator tip is 16 mm from the mirror face on axis and offset by 36 mm laterally. Using some basic trigonometry (chord length = $2R\sin[\theta/2]$ where θ = 0.25 mrad, R = 36 mm) a mechanical angular deflection of 0.25 mrad corresponds to 9 μm of actuator motion. In the actual setup I measure a deflection of 1 μm with actuator motion of 19.7 or 14.5 μm in the two mirror axes, which is reasonable agreement. The measured deflection is reproduced exactly even when the setup is realigned from scratch, and the cause of the discrepancy between x and y mirror axes is not known.

The earliest version of the experiment used a manually-actuated steering mirror, with 13 x 13 points per map (Figure 35). Each photothermal map took approximately 4 hours to acquire (pump beam blocked and unblocked for each of 169 mirror positions) and was obviously unpractical for further experiments. However, the data presented in Chapter 4 was acquired with this setup. We then upgraded the steering mirror with a pair of CONEX TRA12CC motorized actuators. Although this did not give us a true galvo-scanning setup, the leadscrew-driven motorized actuators vastly increased the data acquisition rate (approximately 1 minute for a fine-resolution photothermal map with 25 x 25 pixels). Whenever the setup is realigned, the position of the final two alignment mirrors is optimized until the beam can be scanned across the field of view of the camera without transmitted power dropping by more than 5%. This ensures that scanning the beam to different positions on the toroid doesn't vary the amount of excitation power being delivered.

Achieving the smallest possible spot size for the pump beam motivates the choice of microscope objective. The objective used for the vast majority of work in this thesis is a Nikon Plan Apo 60x objective

with a nominal 0.95 NA, near the theoretical maximum NA for an air objective. The diffraction-limited spot size is a function of wavelength and NA given by Equation 1.1**Error! Reference source not found.**. At 1320 nm a diffraction-limited spot size with 0.95 NA should be 1.39 μm diameter. We were never able to achieve a spot size this small, typically reaching a $1/e^2$ diameter of 2.35 to 2.45 μm whenever the 1320 nm pump laser was aligned. This is an effective NA of 0.55. Late in the course of my Ph.D. we discovered that this objective is designed to be used with a coverslip, explaining the discrepancy. While spatial resolution is not usually important in single-particle photothermal mapping because of the large distance between nearest-neighbor absorbers on the toroid, increased spot size leads to increased background signal. The cross-sectional area of the beam scales quadratically with NA, so the difference between nominal and actual NA leads to a 300% increase in background signal. Further, because the low power of the pump beam and the limited near-IR transmission of the objective limits us to peak power of 10 mW from the focused beam, the increased spot size leads to lower optical intensity and thus lower signal than desired. In the 2nd-generation microresonator photothermal microscope (Chapter 8), an oil-immersion (NA = 1.4) or water-dipping (NA ≥ 1) objective as well as a switch to visible wavelengths will result in an increase in signal to background excitation ratio of approximately a factor of 16, a huge improvement.

Most of the experiments presented in this thesis employed a tunable 1280-1365 nm pump laser. Not only is this beam impossible to observe visually, the silicon cameras used to align the relative position of the pump beam and the toroid are completely blind to the pump beam itself. To circumvent these difficulties we coaligned a visible laser to serve as a guide beam (Figure 12). This red beam (640 nm) is aligned onto the same path with a pair of steering mirrors. Co-alignment is tested crudely using an IR card (which does not work particularly well) and more precisely using an iris attached to an InGaAs power meter. The power meter has some sensitivity to 640 nm light, allowing us to sequentially block each of the two laser beams and optimize their alignment. Specifically, we first align the IR beam to the detector before using the two earliest steering mirrors to align near and far the 640 beam with the fixed location

power meter. Because the power of the 1320 nm beam is much more important, we choose dichroic mirrors (a total of 2 are necessary in the excitation path) that are optimized for 1320 nm, sacrificing almost all of the power in the 640 nm beam as a consequence. The power of the pump beam is monitored in real time with a beam sampler (Thorlabs BSF10-C), which is uncoated on the upstream side and AR-coated on the downstream side. The downstream surface is also wedged to eliminate etalon effects with the front surface, which plagued our earlier improvised power tap made from a simple microscope cover slip. An earlier version of the microscope included a wedged sample holder for the toroid chip that reflected pump beam light transmitted through the chip. This light was then collected with a lens and measured on a photodiode. The collection fraction (~ 10^{-5}) was too small to make this an effective means of power correction, largely because of the extremely fast divergence of the 60x-objective-focused beam. Accurate real time power measurements are important in our spectrometer because the absorption cross-section is proportional to the resonance shift divided by excitation power. By monitoring the pump laser power in real time, we can account for power fluctuations as well as automatically correcting for intentional attenuation of the beam. The 2nd-generation microresonator microscope (Chapter 8) was designed from the ground-up to collect transmitted light, highlighting the importance of monitoring excitation power.

On the imaging side (Figure 12) we collect light scattered from the resonator surface into two objectives. A side-view image is provided by a Mitutoyo 20x LWD Plan Apo objective on a Navitar Ultrazoom stereoscopic microscope. The ability to change the zoom by approximately a factor of 10 is helpful when aligning the fragile tapered optical fiber with the microresonator. In particular, the image on the Navitar camera allows for optimizing the height of the taper at the equator of the toroid, as well as keeping the 60x pump objective (working distance of only 0.18 mm) from crashing into the taper, toroid, or substrate. Light scattered off the top of the microresonator is collected by the 60x objective and passes through dichroic 2 (Figure 12) traveling upwards. The light then is split by a 50:50 non-polarizing beamsplitter, with half of the light reaching a camera. The other port of the beamsplitter is connected to

a fiber-coupled white light, which travels in the reverse direction to provide illumination on the toroid. Because Dichroic 2 is optimized to reflect 1320 nm light, and imaging light has to pass through going both down and up, the amount of light reaching the camera is limited. A much larger impediment to observation is the fact that the half-waveplate located right above the objective is AR-coated for SWIR light, and is quite reflective to visible light, causing substantial ghosting of the image unless it is tilted slightly out of plane; further, irises around both the camera and the white light lamp have to be closed partially, obscuring part of the image from the toroid plane but decreasing the intensity of ghost reflections on the camera. This imaging setup is an unhappy compromise, underscoring that spectroscopy is more important than alignment in this microscope.

We calibrate for wavelength transmission through the system by removing the pump objective and toroid chip holder, then placing the power meter head directly in the beam path where the objective typically resides. Tuning the pump wavelength and measuring the resulting spectrum, then dividing by the spectrum measured with the pickoff mirror near the laser head, gives the instrument's transmission function. In the work described in Chapter 6, Lorentzian lineshapes with a diversity of center wavelengths and no obvious distortions indicates that our calibration is good. Measurement of the toroid background (see Section 2.5) shows weak but sharply resolved water absorption peaks, further indication that we are accurately measuring absorption spectra. An attempt to lithographically define gold pads on the center of toroids (Figure 14a,b) and use their flat spectral response as a calibration target[22] did not succeed, however. With the help of Matt Stolt and Dong Liang in the group of Song Jin, I fabricated 10 μm diameter gold pads on finished toroids using electron-beam lithography. Photothermal mapping (Figure 14c) revealed no oddities, but the absorption spectrum (Figure 14d) varied stochastically (although reproducibly) between toroids. The extreme bumpiness (Figure 14b) of the surface of the center of the toroid, in comparison to the thickness of the film (15 nm), suggests that size-dependent plasmon

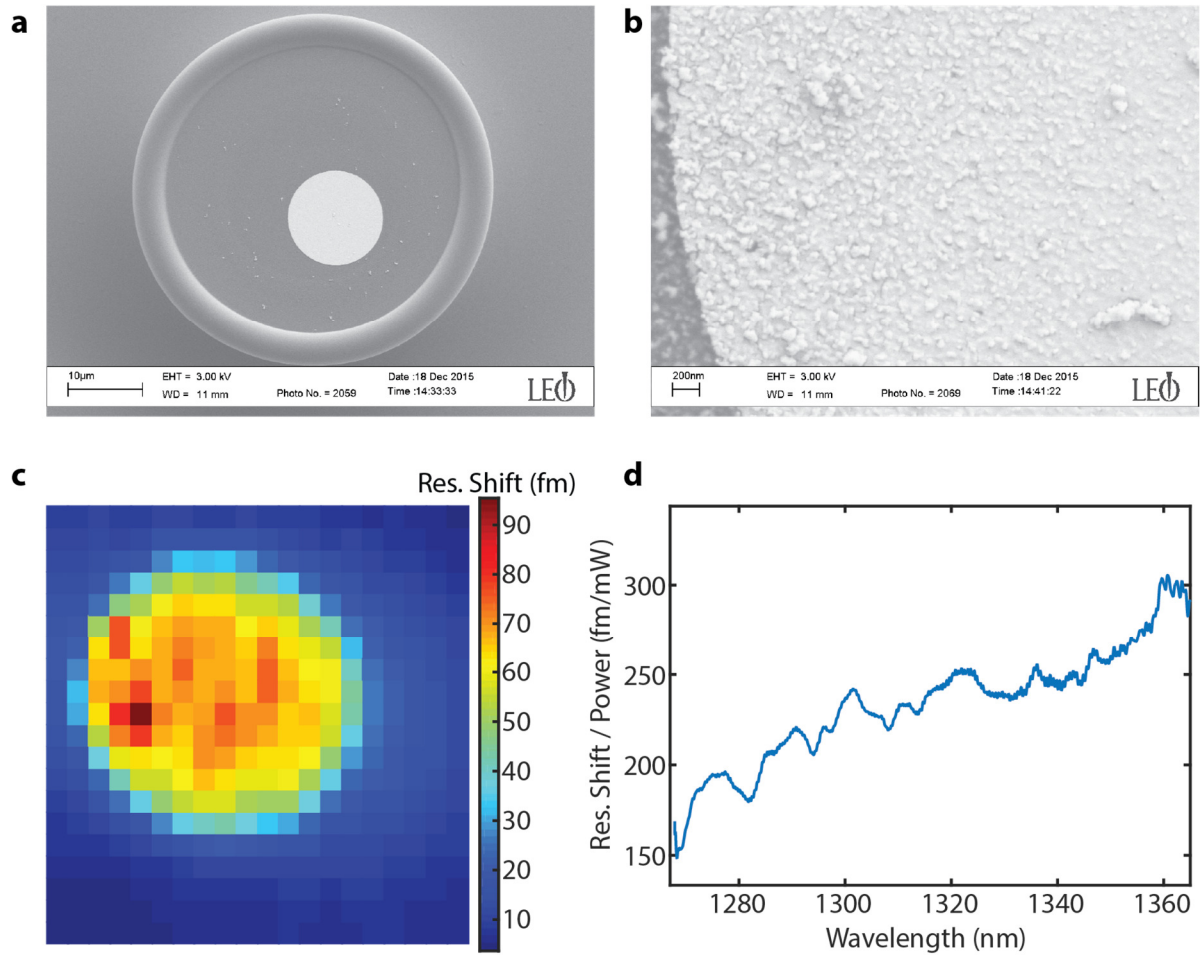

Figure 14: Lithographically-defined gold pad.

(a) SEM image of 10 µm diameter gold pad on a toroid. (b) zoomed-in SEM image of a gold pad, showing the high surface roughness. (c) Photothermal map of a gold pad, with 1 µm/pixel resolution. (d) Representative absorption spectrum of a gold pad. Fluctuations and the overall slope are reproducible on the same pad, but vary somewhat between different pads.

resonance effects may contribute. Later spectroscopic measurements on single AuNRs (Chapter 6) provided further reassurance of accurate wavelength calibration.

2.4 Polarization of the pump beam

Absorption of a photon by a single molecule involves a transition between discrete vibronic states with a probability proportional to the transition dipole moment. For example, a molecular ground vibronic state transitions to an excited vibronic state after absorption of a photon. In single molecules, the only transition moment with significant amplitude is the transition dipole moment μ. Conveniently, the electric field (E) of a laser beam is also dipolar, unless exotic optical elements are used to make it otherwise. When the two dipoles are aligned absorption occurs with a finite probability, and when the two dipole vectors are orthogonal the probability of absorption drops to zero. The absorption probability is proportional to the dot product squared:

$$\sigma_{abs} \sim (E \cdot \mu)^2 = |E|^2 |\mu|^2 \cos^2(\theta) \qquad 2.2$$

where θ is the angle between the two vectors. This curve, when plotted in polar coordinates as a function of θ, looks remarkably like an infinity symbol (Figure 15d). For a large ensemble of absorbers the contribution from each chromophore is summed and results in absorption that is independent of θ. For this reason, macroscopic absorption spectrometers don't normally bother with controlling the polarization of excitation light. In the intermediate case, where a small number of chromophores are being excited, the shape of the polarization curve can become quite interesting. In this case the tendency of chromophores to align is being probed by the ratio between the maximum and the minimum absorption. This angle-dependent depth of modulation (M) in absorption has been used to track changes in conformation of a single polymer molecule during solvent vapor annealing.[143]

Our instrument has been designed to allow complete control of the theta of the polarization beam relative to an arbitrarily oriented analyte. This allows us to accurately measure M values as long as the

polarization is linear over the full range of angles as well as being achromatic (linear at all wavelengths). This seems like a simple requirement, but was actually a nontrivial problem to diagnose and correct for. In the initial setup we had a half-wave plate far upstream, near the laser head, and tuned the orientation of this optic under the assumption that the polarization would stay linear all the way until the microscope objective.

While taking single-particle absorption spectra on plasmonic nanoparticles I observed unusual spectral features. Erik Horak figured out the source of the problem because it didn't make sense to him to tune the half-wave plate to maximize transmission through a polarizer placed right before the objective. By rotating the polarizer alone it was impossible to reach zero transmission; it was necessary to rotate both the polarizer and half-wave plate. That can't be explained if the polarization is linear, but can be explained if the half-wave plate orientation affects the ellipticity of the polarization. The light input to the half-wave plate was confirmed to be still as linear as it had been when we first aligned the system. After some consideration, we tried the simplest possible optical setup, with the pump laser, a half wave plate, a polarizer, and a power meter. This revealed textbook optical behavior (1000:1 extinction ratios at all half-wave plate orientations). Then we tried adding a single mirror between the waveplate and the polarizer, to more closely mimic the full optical setup. This immediately changed the achievable extinction ratios, which ranged from 1000:1 down to 12:1 depending on the relative angle between the linear polarization and the orientation of the mirror.

It is widely known among optical instrument builders that the reflectivity amplitudes of mirrors varies for *s* and *p* polarization states. It is less commonly realized that the phase of reflected light is also affected by the state of polarization. If linearly-polarized light is incident at purely *s* or *p* orientation, then the differential phase delay is irrelevant. However, at any other orientation, the differential reflected phase of *s* and *p* light will act to change the polarization state of the reflected light. This can be understood from the fact that the only difference between linear and circular polarization is the relative phase of the

s and *p* components. Further, this differential phase is a strong function of wavelength, both in our experience and as reported by manufacturers such as Semrock.[144] This leads to a wavelength-dependent and waveplate-orientation-dependent ellipticity in pump polarization. When exciting dipolar absorbers (e.g. gold nanorods or single molecules), it leads to anomalous peaks in the absorption spectrum because wavelength tuning also tunes the linearity of polarization. This is not good.

One attempt at mitigation involved using a quarter-wave plate and half-wave plate in tandem, shown in Figure 15a. Knowing that the mirrors in the optical path were depolarizing the pump beam, we tried pre-compensating for this deterministic elliptization using a quarter-wave plate and half-wave plate operating in tandem. Ideally this would result in high transmission for light parallel to the polarizer axis and zero transmission for light rotated by 90° (Figure 15b). However, we observed substantial transmission with orthogonally-polarized light, and the transmission varied strongly with wavelength (Figure 15c). This problem was ultimately resolved by simply moving the half-wave plate to right before the objective (Figure 12). Single gold nanorods are essentially perfect dipolar absorbers[24] and serve as a good test system for polarization linearity. Measurement of single nanorods with a variety of orientations gives perfect cosine^2(θ) dependence with extinction ratio reaching 2,500:1 (Figure 15d). Because the wave plate must be physically close to the excitation objective, it cannot be adjusted by hand without ruining taper-toroid coupling through coupled mechanical disturbance. A motorized optic holder (Thorlabs PRM1Z8) allows for rapid, remote-controlled rotation of the half-wave plate.

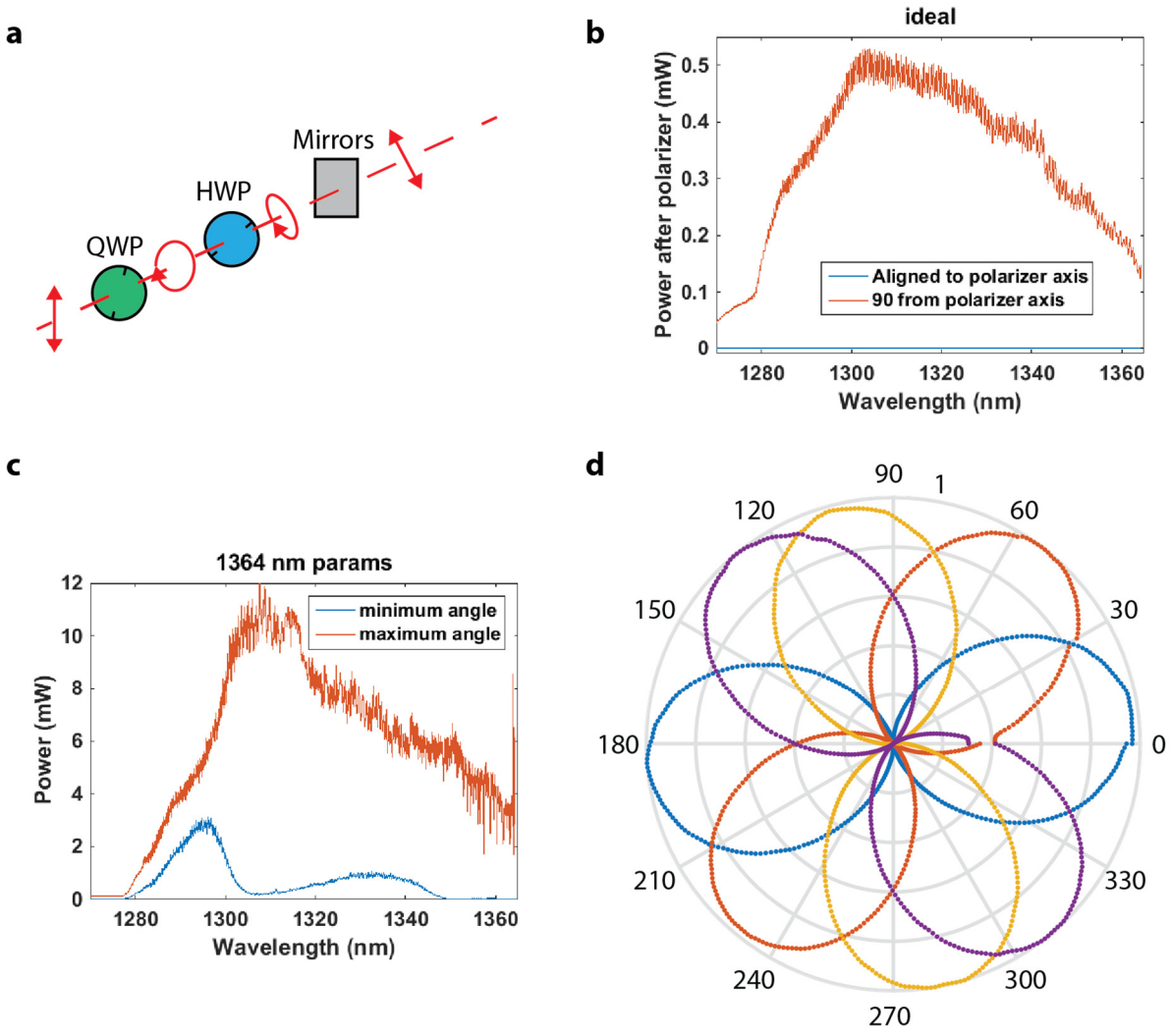

Figure 15: Polarization of the pump beam.

(a) Schematic of polarization pre-compensation scheme used in (b),(c). (b) Ideal result from this configuration. (c) Actual results using parameters optimized at 1364 nm. Optimizing at other wavelengths produced similar results. The orange curve is the angle that gave the highest transmission, and the blue curve is taken 90° apart. (d) Representative polarization curves for individual AuNRs using the modern setup with a half-wave plate immediately prior to the pump objective (Figure 12). Extinction ratios up to 2,500:1 are shown, and are equally high for AuNRs at any orientation.

2.5 Background absorption

Delivering excitation light via a free space laser, while offering the experimental advantages described earlier, requires some additional engineering. In particular, we want to minimize the spot size of the focused excitation beam, consequently maximizing the fraction of pump light absorbed by the target molecule. Just as important is minimizing the volume of silica that the pump beam travels through. Although the absorption of silica is quite small at the wavelength range typically described in this thesis (1280-1365 nm), the volume of silica excited by a beam passing through the rim of the toroid is so many orders of magnitude larger than the volume of a single molecule that it becomes a non-negligible component of the photothermal absorption signal. We can estimate the expected background signal by approximating the volume of silica excited as a cylinder as deep as the minor diameter of the toroid (5 μm) and as wide as the $1/e^2$ focused spot diameter (2.4 μm). The absorption losses in fused silica[108] are ~ 0.5 dB/km at 1 eV (11% per km). This means we expect 1.1 mW of photothermal background per km of fused silica with 10 mW of incident pump power. The actual 5 μm thickness should give 5.5×10^{-12} W. However, for visible light this will reach ~ 0.5 nW as silica is most transparent in the near-IR.

At a pump power of 10 mW, the actual background measured at the rim of the toroid is about 1 fm (150 kHz), Figure 16a. This is larger than the value estimated above. Having now discounted bulk silica absorption as the main source of background, we consider the other possible sources of photothermal background absorption in the current geometry.

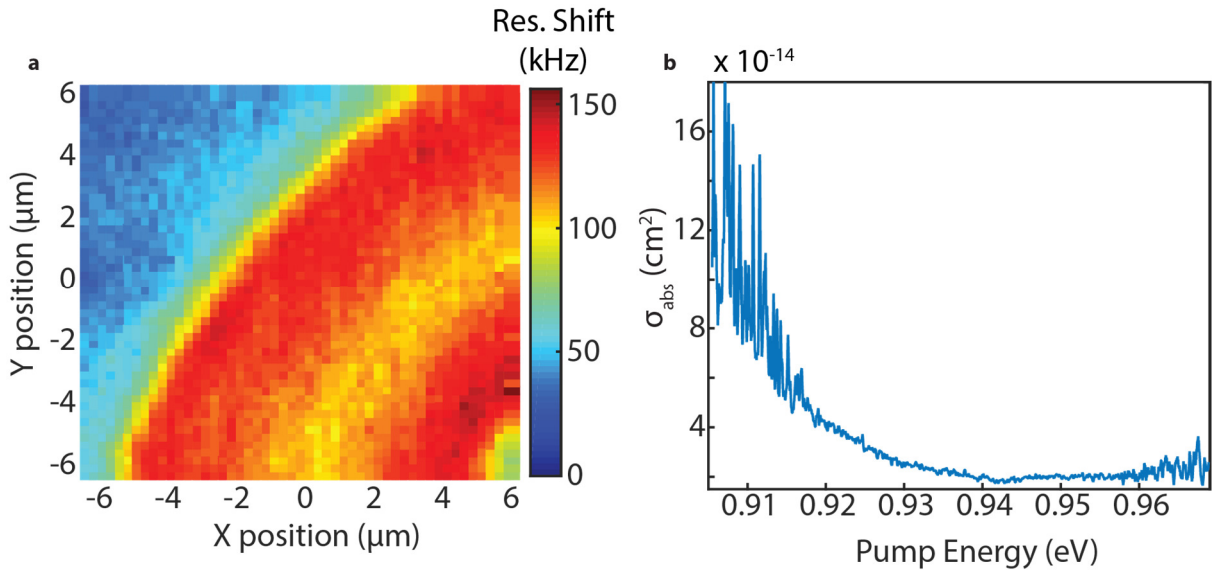

Figure 16: Background absorption by the toroid.

(a) Photothermal map on a clean toroid at 10 mW peak power, 1320 nm. The edge of the toroid is visible to the top left. At this wavelength, 1 kHz = 8.33 am of resonance shift. (b) Absorption spectrum taken at the center of (a), on the rim of the toroid. A sharp increase at longer wavelengths, with fine structure, is observable at left.

The spectral dependence of the background is conspicuously wavelength-dependent (Figure 16b). The sharp increase at wavelengths near 1370 nm (0.905 eV) is at the same energy as absorption by O-H overtone vibrations in fused silica.[145] Thermal oxide is grown through steam oxidation of silicon, and as a result it is not surprising that interstitial water becomes trapped in the oxide layer. Additional evidence comes from the fine structure visible on the peak in Figure 16b. These absorption lines are highly reminiscent of rotational fine structure on vibrational absorption peaks. We believe this to be the primary source of background absorption. O-H absorption can also result from water[146] adsorbed on the surface of the toroid. Adsorption is unlikely to be the source here, however. I tried purging the toroid setup under dry argon in the presence of fresh desiccant, and managed to lower the relative humidity near the toroid to ~ 2%. No change was observed in the amplitude or spectrum of background absorption. Water absorption drops by several orders of magnitude between 0.9 eV and the visible/NIR spectral range,

making this problem much less significant at the shorter wavelengths used in the 2nd-generation resonator setup. Surface contamination remaining after ozone cleaning and solvent rinsing is another possibility, if somewhat less likely. The spectral dependence of the background, and more importantly the spatial homogeneity of the background (Figure 16a-b) argue against this source. Chapter 8 will discuss the routes we are exploring to decrease background absorption or to improve contrast between the signal and background.

2.6 The Probe laser: fiber optics

Toroid microresonators are usually probed with a near-infrared tunable diode laser. We use a TLB-6728 external-cavity diode laser (ECDL) from New Focus, tunable from 1520 to 1570 nm. A widely-tunable laser is necessary because of the large FSR of toroids. The FSR of a toroid with 45 μm major diameter is given by Equation 2.3:

$$m\lambda = 2\pi Rn \quad and \quad (m+1)(\lambda - FSR) = 2\pi Rn \;\; so \;\; FSR = \frac{\lambda}{(m+1)} \qquad 2.3$$

With typical values being R = 22.5 μm, n = 1.44, λ = 1.56 μm, we have m = 130 and FSR = 11.9 μm. This FSR is somewhat conservative, because the TE and TM modes of the resonator are not degenerate (see Section 2.2) and we are not taking into account the many non-fundamental modes of the resonator (see Figure 9). In any event the tuning range of the probe laser is more than sufficient for our purposes, since we rarely need to use more than a single resonance per toroid. Conversely, it has been suggested that the size of the resonator be tuned to match the wavelength of a single-frequency laser. It is, at this time, impossible to fabricate a toroid (or even its unreflowed version, the microdisk resonator) to resonate at a specific wavelength.[147] Consider that a change of 1 nm in the major radius in Equation 2.3 leads to a change of 70 pm in the resonant wavelength. Fabrication tolerance for photolithography in an academic

cleanroom might be of order 500 nm, after taking into account resist reflow inconsistencies, which would give an enormous tolerance of 35 nm in resonant wavelength. The uncertainty in diameter only increases after including the stochasticity of the reflow process. This difficulty has motivated efforts to actively or passively tune the toroid resonant wavelength.[132,147-149]

1550 nm light is widely used in the telecoms industry for its extremely low propagation loss in silica optical fibers.[63] The 1550 nm region (C-band, L-band) is in fact a wavelength range where the transmission loss through silica (absorption + Rayleigh scattering) is at a global minimum. This light will propagate through Corning SMF28e+ fiber at a loss rate of 0.20 dB/km or less.[63] This enables us to use fiber optics for the entirety of the probe laser's path. Fiber-coupling the beam allows for us to divert light between the coupling setup and taper-pulling setup with no realignment, to easily keep room light from entering with the taper, to switch detectors or even detection scheme quickly, and most importantly to conveniently interact with the taper. Light from the probe laser is permanently pigtailed into polarization-maintaining fiber by the manufacturer. This fiber is first connected to a 60 dB two-stage isolator to attenuate back reflections. This is necessary because external-cavity diode lasers are vulnerable to back reflections and every splice or fiber connection is a potent source of back reflections owing to the change in reflective index at the air gap between fibers. The ECDL's vulnerability to back-reflections originates with the laser's design principle, whereby the lasing wavelength is determined by the wavelength of light back-reflected into the diode chip from the external grating. I have found that either a circulator (OZ Optics FOC-12N-111-9/125-SSS-1550-55-3A3A3A-1-1) or a two-stage isolator (Fiber Instrument Sales F209) provides sufficient isolation to keep etalon effects caused by back reflections to a minimum. I also found that a 2m length of singlemode fiber (but not 1m or 5m) helped to reduce etalon effects when tuning the probe laser. Currently, we have the fiber from the laser connected to a circulator, a paddle-based polarization controller (Thorlabs FPC560), the phase modulator used in PDH, then a hybrid patchcord with a FC/PC and FC/APC connector on different ends and the aforementioned 2m patchcord before reaching

a second polarization controller. The output from the polarization controller is connected to a tapered optical fiber using a bare fiber splice (FIS), and the output of the tapered fiber is collected by an avalanche photodiode (APD). The output of the taper is spliced into an APC patchcord whose output is collimated and then aligned inside of a lens tube onto the active area of the InGaAs APD. We have experimented with several different detectors for the probe beam. High bandwidth is needed because of the high phase modulation frequency (200 MHz), and substantial transimpedance gain is needed as well because of the low photocurrent (~ 1 μW). Low dark current is also important in our application. The optimal design of a photodiode detector is the subject of an entire chapter in Hobbs' magnificent instrument-building textbook.[150] Ultimately, gain and bandwidth are inversely related for any transimpedance amplifier, so a tradeoff between bandwidth and amplification is inevitable. APDs allow for partially overcoming this tradeoff because increasing the gain from avalanche multiplication is unrelated to transimpedance gain. Practical limitations keep avalanche gain for high-bandwidth APDs to gain of order 10^1. We have had good results with the APD430C from Thorlabs, which possesses sufficient bandwidth and (tunable) gain. Conveniently, unlike a single-photon-counting APD, this APD is not hyper-sensitive to room light and can be shielded with a simple lens tube and wrapping in tin foil, allowing for data acquisition with the room lights turned on.

Aside from the etalon effects already mentioned, there are other drawbacks to using fiber optics. Fiber optic cables are effective at sensing the presence of air currents or fluctuations in ambient temperature, whether intentionally or not. Additionally, the tight fabrication tolerances of fiber connectors makes them effective at backscattering light through the fiber to cause havoc upstream.[150] Essentially, every fiber patchcable is a low-Q Fabry-Perot resonator and acts as an interferometer. Because patch cables are of order 1m and the wavelength is of order 1 μm, they are quite sensitive to strain or temperature. A 1°C change in the temperature of a patchcord will change the length by close to half a wavelength. The FSR is approximately 2 pm, so a resonance shift of 1 pm will cause the patchcord to fully

modulate the probe beam. This resonance shift corresponds to a 0.2 K change in room temperature given thermo-optic coefficient of 8.6×10^{-6} K^{-1}. A lot of this effect can be ameliorated by switching to APC (angle-polished connector) patch cables. The endface of the fiber connector is polished at an 8° angle, causing light backscattered from connections to couple poorly into the fiber. A further problem is the degeneracy of polarization modes in fiber. Single-mode fiber, having a two-dimensional symmetric cross-section, has two polarization states that are nearly degenerate, split only by any residual birefringence in the fiber. It is difficult to maintain a launched polarization state in standard singlemode fiber because even small amounts of asymmetric pressure can couple the two nearly-degenerate polarization states. Polarization-maintaining fiber exists but is incompatible with the process of making tapered optical fibers. Unfortunately, coupling to WGMs in the toroid is a function of the probe beam polarization, as is the modulation depth of phase modulation. Occasional realignment of the state of polarization of the probe light before the taper junction is necessary. Nonetheless, the reconfigurability and low cost of fiber optics at 1.55 μm are powerful inducements for using them.

2.7 Tapered optical fibers

Coupling light into toroid WGMs is not as easy as coupling into a macroscopic Fabry-Perot resonator. Toroid WGMs are inherently difficult to couple into with far-field light because of their extremely low radiative loss rate. By time-reversal symmetry, low radiative losses implies low coupling efficiency to light incident from free space. Free-space coupling by end-firing at toroidal resonators requires distortion of the resonator shape to allow coupling of free-space radiation into WGMs;[86] by tunneling, high-Q modes can be excited from the initial low-Q free-space coupled mode.[86,151,152] Therefore, WGM microresonators generally must be coupled with the evanescent field of an air-clad waveguide or a

prism. Traditionally this has meant a prism operated above the critical angle, where light is totally internally reflected at the glass-air interface. This is still a popular method for microsphere resonators.[73] However, coupling to toroids[106,153,154] is impossible to accomplish with prisms because the toroid rises only ~20 μm from the surface of the substrate. Prisms are typically several thousand μm in size. Toroids are coupled into with tapered optical fibers (tapers) instead. A waveguide must be used instead.

Singlemode optical fiber is easily available at the telecom wavelengths used in this thesis (1.55 μm and 1.32 μm). However, a commercial optical fiber is unsuitable for coupling into an optical microresonator or indeed for any kind of evanescent coupling. The typical fiber used with 1550 nm light, SMF28e+, has a core diameter of 8.2 μm and a cladding diameter of 125.0 μm. Propagating light is confined to the core, with 58.4 μm of glass between the propagating mode and the outside world. To make this light available for evanescent coupling, the core and cladding have to be annealed together and thinned dramatically. Simply annealing the fiber without tapering, allowing dopant to diffuse and creating an air-guided optical fiber with 125 μm diameter would produce a highly multimode fiber. We require a singlemode fiber in order to efficiently phase-match to only the fundamental mode of the WGM microresonator,[153] which has the tightest confinement and consequently smallest mode volume. The number of supported transverse modes in a waveguide is proportional to thickness and quantified by the V-number:

$$V = \frac{2\pi a}{\lambda}\sqrt{n_{core}^2 - n_{clad}^2} \qquad 2.4$$

Where a is the core diameter, n_{core} the core refractive index, and n_{clad} the cladding refractive index. A waveguide is single-mode if V < 2.405. At a wavelength of 1.55 μm with an index of n_{core} = 1.468, a taper must have diameter less than 1.11 μm to be singlemode, dramatically thinner than the original fiber optic cable. Producing a single-mode, air-guided fiber comes at a cost. Because the protective coating is removed during taper fabrication and the glass fiber thinned dramatically by tapering, and strength of the

fiber varies with cross-sectional area, a tapered fiber is (245 μm/1.1 μm)^2 = 50,000 times more fragile than an unmodified singlemode fiber.

There are other reasons to use tapers. Prisms are not singlemode in the output,[155] while also making it difficult to spatially mode-match the microresonator. A taper can excite non-fundamental modes in toroids, but light can only couple back into a single mode in the taper. Instead of a taper, an integrated waveguide would be a powerful tool, and indeed has been demonstrated for thick resonators,[156] but is inherently difficult to integrate with the thermal reflow process necessary to give ultrahigh-Q factors in toroids. Because the waveguide and the microresonator retract when reflowed, the coupling distance is difficult to set. An additional drawback is the typically high propagation loss of planar waveguides.[155] By contrast fibers start at 0.2 dB/km attenuation, and can be pulled with < 0.05% additional loss.[157] The taper provides a means of probing individual WGMs with extremely high (and tunable) coupling efficiency. Further, the incident, back-scattered, and transmitted beams are already fiber-coupled for easy collection and measurement. Recently, welding of tapered fibers to toroids has been demonstrated as a means of creating a permanent stable coupling with the advantages of a tapered fiber waveguide.[158,159] However this method has not yet demonstrated complete coupling to the resonator or preservation of ultrahigh Q-factors.

The coupling physics between the taper and the toroid is well understood. When the taper is relatively far away, the overlap between the evanescent field of the taper and the toroid is minimal, and the intrinsic loss rate of photons inside the cavity (~ 1/Q) is greater than the rate of coupling to the resonator. As the taper is brought closer to the resonator, the amount of coupled light increases. At a certain distance the coupling rate into the cavity is exactly equal to the loss rate of photons in the cavity (which is now partially due to the presence of the tapered fiber). This condition is referred to as critical coupling. If the coupling parameters are optimized, then transmission through the fiber on resonance drops to zero. More than 30 dB of drop has been demonstrated.[160] As the fiber is further approached to

the toroid, the transmission begins to rise again, a phenomenon referred to as overcoupling (Figure 17). This is caused by the increased overlap between the WGM and the taper mode's evanescent field leading to a rising efficiency in out-coupling of resonant light back into the taper. A further interesting feature of the critical point is that the phase of transmitted light past the resonator shows a 180° phase change.[155] The light that transmits past the toroid and is collected by the detector has a very different origin on either side of the critical coupling point. In the undercoupling regime, transmitted light never coupled into the toroid. In the over-coupled regime, the only light transmitted past the toroid must have circulated through the toroid.

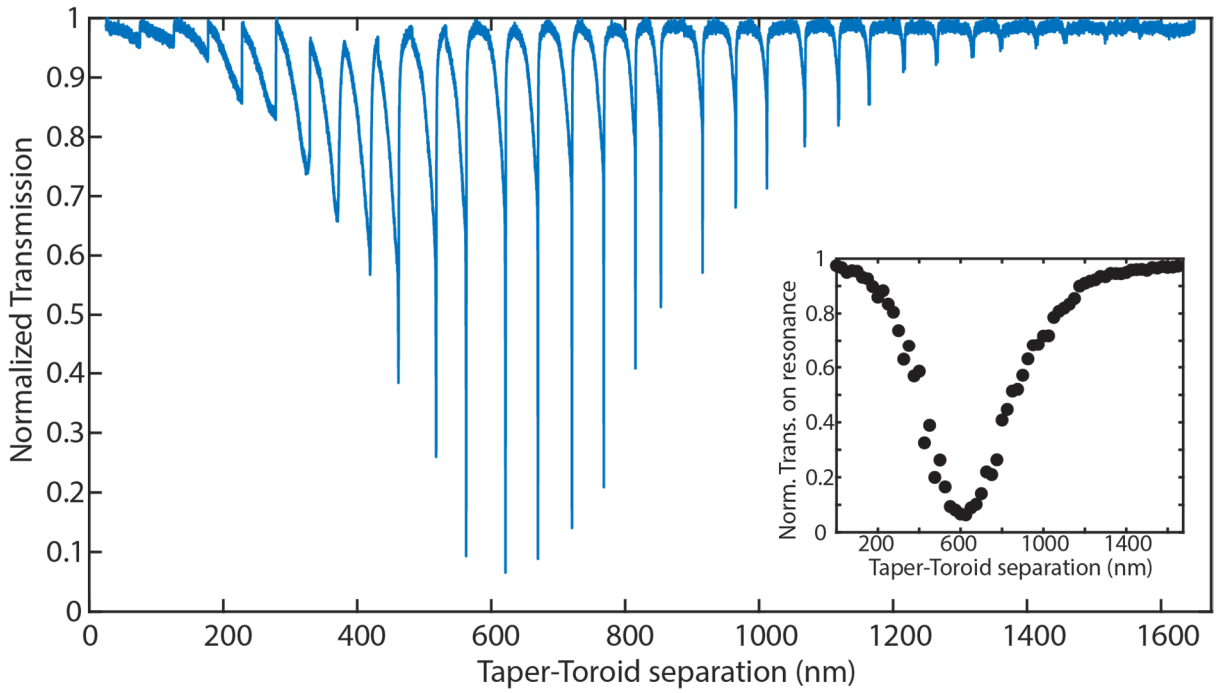

Figure 17: Taper stepping and effect on coupling and Q-factor.

A series of resonance scans where the position of the taper is stepped by 50 nm between each scan. Thermal bistability is clearly observed as the coupling rate is increased. (inset) Normalized transmission on resonance for the same approach curve, demonstrating the change in coupling efficiency in the transition from undercoupled to critically coupled to overcoupled. Imperfections in coupling conditions keep the critically coupled transmission to ~ 5%.

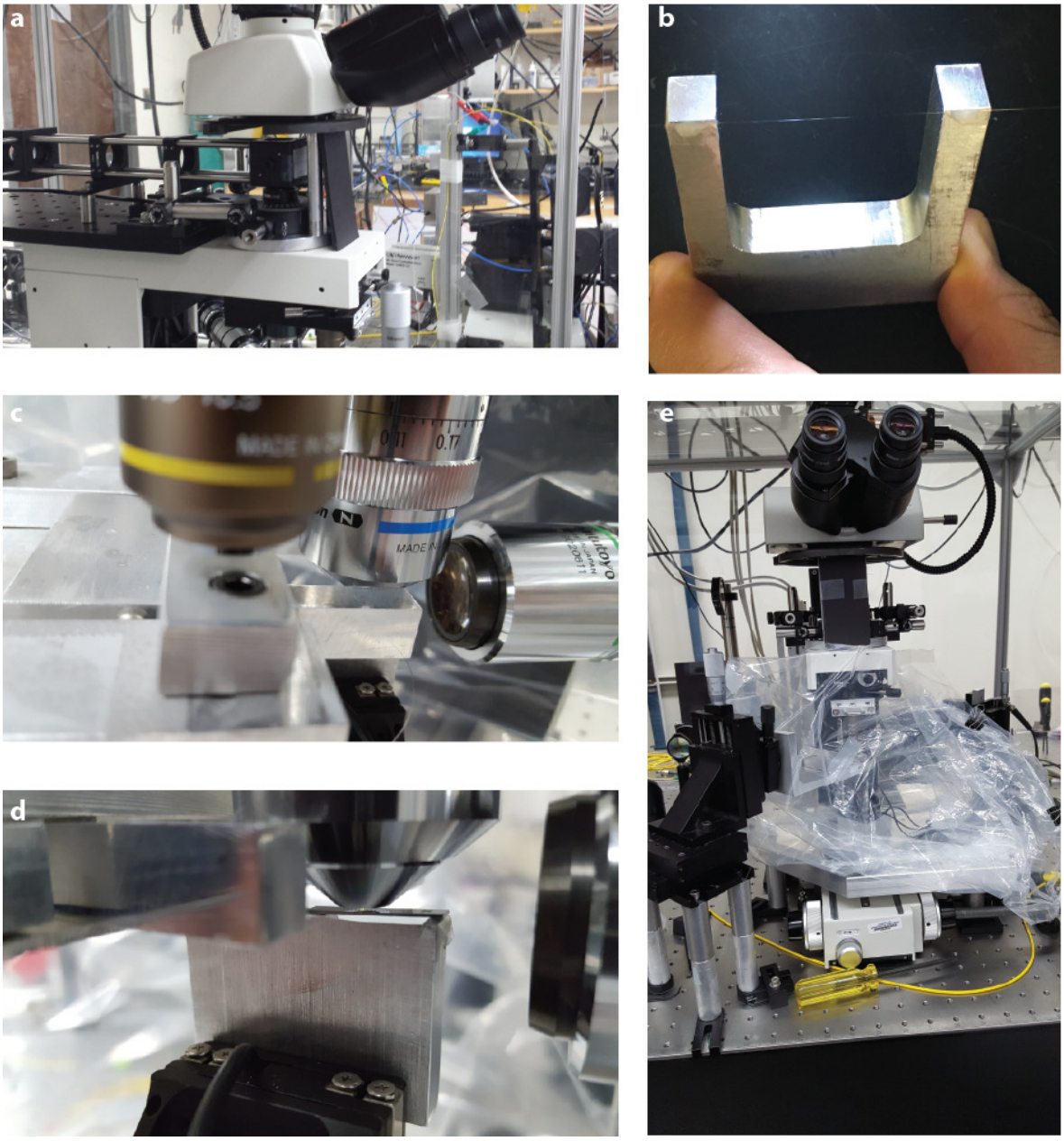

Figure 18: Current status of the 1st-generation microresonator spectrometer (SCORPIO).

(a) A breadboard is affixed to the shell of a Nikon FN1 microscope for mounting pump beam optics and the illumination system. (b) A taper glued into place in its U-shaped mount. This metal bracket is then affixed to a 3-axis translation stage. (c) Taper holder, 60x pump objective, and 20x objective aligned with toroid and taper. (d) Close-in view of the 60x objective focused onto a toroid while a taper is in coupling range. (e) View of the taper-toroid coupling setup. A transparent trash bag surrounds the coupling setup to keep out air currents. The polycarbonate/acrylic enclosure is opened to allow a view of the setup. The characteristic “pincers” holding the motorized waveplate are visible beneath the eyepiece.

The Q-factor also decreases tremendously as the taper is overcoupled. The *loaded* Q-factor, i.e. the Q-factor actually measured in the experiment, is lowered from the intrinsic Q-factor by the additional losses of photons re-coupled into the taper and scattered from the taper-toroid junction. Figure 17 demonstrates this; as the coupling rate is increased the peak gradually broadens until it is substantially broader than the scan range.

There are some significant drawbacks to using tapered optical fibers, and this has motivated continued interest in alternative methods of probing WGM modes. First, the taper has a tendency to drift. The taper is glued into place at two attachment points about 30 mm apart. With a central thickness of 1.1 μm or less, that's an aspect ratio of 27,300:1. This is analogous to a 2.1mm headphone cable being strung between the Petronas towers. As shown in Figure 17, coupling fluctuations of < 50 nm will cause significant changes in toroid-taper coupling. That would correspond to movement of < 100 μm by our hypothetical headphone cable by about the thickness of a human hair, displacement that is too small to see by eye. Unsurprisingly, air currents in the lab are not good for maintaining stable taper-toroid coupling. We ameliorate these partially with a polycarbonate box around the center part of the optical table and a transparent trash bag wrapped closely around the toroid coupling setup. The tight alignment tolerances and drift issues require an expensive 3-axis nanopositioning stage to hold either the taper or toroid. Because of the small mass of the toroid substrate compared to the taper holder, we elected to use a long-travel 3-axis piezostage (Attocube ECS3030 with ECC100 controller) to move the toroid relative to a fixed-position taper. A second problem with taper coupling is fragility and cleanliness. While possessing considerable compressional strength (tapers can be pulled by hand from both ends without breaking), tapers are quite fragile towards lateral force when under tension. Tapers sometimes break overnight, particularly in the first 24 hours after fabrication. A final issue is fouling.[73] In the tapered region, light is partially propagating in the air surrounding the fiber, giving rise to substantial optical intensity in the surrounding medium. This in turn causes optical trapping of nearby molecules or particulates onto the

taper, the most important part of the taper. This is bad for probe transmission, and also bad for our photothermal measurements because accumulated material will absorb light. Despite these drawbacks, the advantages of tapers and the lack of alternatives makes them our coupling method of choice.

2.8 PDH (Pound-Drever-Hall) wavelength locking

Resonance shifts in optical microresonators are typically detected by scanning the wavelength of the probe laser across the resonance, fitting a Lorentzian, and monitoring deviations in the peak position. Here we use a more sensitive and higher-bandwidth method for detecting the resonance spectral position, the Pound-Drever-Hall (PDH) wavelength locking technique.[161-164] In the 1940s RV Pound developed a method for stabilizing microwave oscillators[165] with a resonant cavity. At optical frequencies, stabilization of a laser with a resonant cavity by phase-sensitive locking was first demonstrated by Drever and Hall in 1983.[161] In our application, the degree of feedback needed to keep the probe laser resonant with a chosen toroid WGM is used to measure any deviations in the WGM resonance wavelength. Because WGMs are simple harmonic oscillators, the lineshape is Lorentzian and thus symmetric. From a control theory perspective,[162] this is a real problem. If the probe laser is matched to the peak of the WGM resonance, redshift or blueshift of the WGM resonance wavelength produces an equivalent change in transmission, making it impossible to calculate which direction the probe laser should be tuned to keep on resonance. It's possible to lock to the sloped regions on the side of the peak, but phase sensitivity is maximized at the peak for a Lorentzian resonance and side-of-slope locking is also sensitive to amplitude noise from the probe laser. The PDH technique involves phase modulation of the probe beam as a means of differentiating between redshift and blueshift of the resonance, enabling high-bandwidth locking to the peak of the WGM resonance even under perturbative conditions.

In the configuration we've chosen, the tunable probe laser wavelength is actively locked to the toroid resonance in a feedback loop, and the error signal for the feedback loop serves as a direct measure of any changes to the toroid resonance wavelength (or anything that changes the relative shift between resonator and probe beam). Specifically, locking is achieved by phase-modulating the probe laser at high frequency (200 MHz), while monitoring the transmitted power with a high bandwidth detector. Phase-modulation of the probe produces the spectral sidebands (Figure 19a) necessary for PDH locking of the probe laser to the toroid resonance wavelength. The detected photocurrent has a component at the phase modulation frequency whose phase is a linear function of the detuning between the toroid resonance wavelength and the probe laser wavelength. This component can be isolated by electronically mixing in a local oscillator (Minicircuits ZX95-209+) and down-shifting to DC. This signal is low-pass filtered at 1.9 MHz to isolate the DC component and is termed the error signal. Transmission to the photodetector downstream from the resonator is affected by the phase-sensitive interference of the probe beam carrier and sidebands, and is a function of the coupling efficiency, coupled probe power, carrier/sideband ratio, and Q-factor.[162] Wavelength-scanning the phase-modulated beam across a toroid resonance produces a dispersive triplet peak (Figure 19 b,c), with a predicted shape that closely matches our experimental error signal. While locked the error signal is sensitive to resonance shift induced by photothermal dissipation by absorbing nanoparticles (Figure 19d).

The work of Eric Black[162] provides an excellent introduction to the underlying mathematics of the PDH technique as well as its practical application. I will briefly summarize the relevant theory here. Start with a monochromatic laser beam (the *carrier*) whose electric field is a simple sinusoid E_c:

$$E_c = \mathrm{E}_0 \mathrm{e}^{i\omega t} \qquad 2.5$$

where ω is the optical frequency (2π*192 THz in our experiments). Phase modulation at frequency Ω and amplitude β introduces a sinusoidal term into the exponent. Using the small angle approximation for this weak modulation and multiplying through we obtain for the incident probe beam (E_{inc}):

$$\begin{gathered} \mathrm{E_{inc}} = \mathrm{E_0 e^{i(\omega t+\beta \sin(\Omega t))}} \\ \mathrm{E_{inc}} \cong \mathrm{E_0 e^{i\omega t}\,[1 + i\beta sin(\Omega t)] = E_0 e^{i\omega t}}\left[1 + \frac{\beta}{2}\left(\mathrm{e}^{i\Omega t} - \mathrm{e}^{-i\Omega t}\right)\right] \\ E_{inc} = E_0 e^{i\omega t} + \frac{E_0\beta}{2} e^{i(\omega+\Omega)t} - \frac{E_0\beta}{2} e^{i(\omega-\Omega)t} \end{gathered} \qquad 2.6$$

This gives us three optical frequencies, the original carrier frequency (ω) and two sidebands offset by the phase modulation frequency Ω (Figure 19). We are interested in the power transmitted past the toroid when the probe beam is close to resonance. The transmitted field is given by:

$$E_{trans} = F(\omega)E_0 e^{i\omega t} + F(\omega+\Omega)\frac{E_0\beta}{2} e^{i(\omega+\Omega)t} - F(\omega-\Omega)\frac{E_0\beta}{2} e^{i(\omega-\Omega)t} \qquad 2.7$$

where F(ω) is the transmission coefficient as a function of optical frequency. The transmitted power is the squared magnitude of the transmitted electric field. Multiplying through gives nine terms which are either time-independent (DC) or oscillate at Ω or 2Ω. The detection path in the experiment, specifically the mixer and the low-pass filter, filters out all terms except for those oscillating at frequency Ω. Further, the mixing process is phase sensitive, so we can separate terms with sine(Ωt) and cosine(Ωt), discarding the latter. We then have an error signal with power given by:

$$P_{error} = 2\sqrt{P_c P_s}\, Imag[F(\omega)F^*(\omega+\Omega) - F^*(\omega)F(\omega-\Omega)] \qquad 2.8$$

where P_c is the power in the carrier and P_s the power in the sidebands. A plot of this equation for the reflected beam of a Fabry-Perot cavity is shown in Figure 19b. The experimentally obtained error curve is exactly the same shape (Figure 19c). This is referred to as the high modulation frequency or resolved-sideband regime.

I implemented the PDH technique in our experiment in the following way (Figure 20). After coupling the probe beam to a toroid and engaging phase modulation, the detected photocurrent is split into RF (> 50 MHz) and DC (< 10 MHz) components with a diplexer (Minicircuits ZDPLX-2150+). The magnitude of the DC component is determined by the coupling strength between the tapered fiber and the resonator, and is used to adjust the relative position of the fiber to optimize evanescent coupling by keeping the voltage on the DC tap constant. The RF component is amplified by an ultra-low noise AC amplifier (Minicircuits ZX60-P103LN+) and mixed (ZP-1MH+) with the 200 MHz local oscillator, generating a signal at DC (error signal) and at the second harmonic. Near resonance, the error signal is linearly proportional to the detuning of the toroid resonance from the probe wavelength. When exactly on resonance, the upper and lower sidebands cancel out and the carrier is coupled strongly to the microresonator, leading to very little light reaching the photodetector. Locking to this null point makes

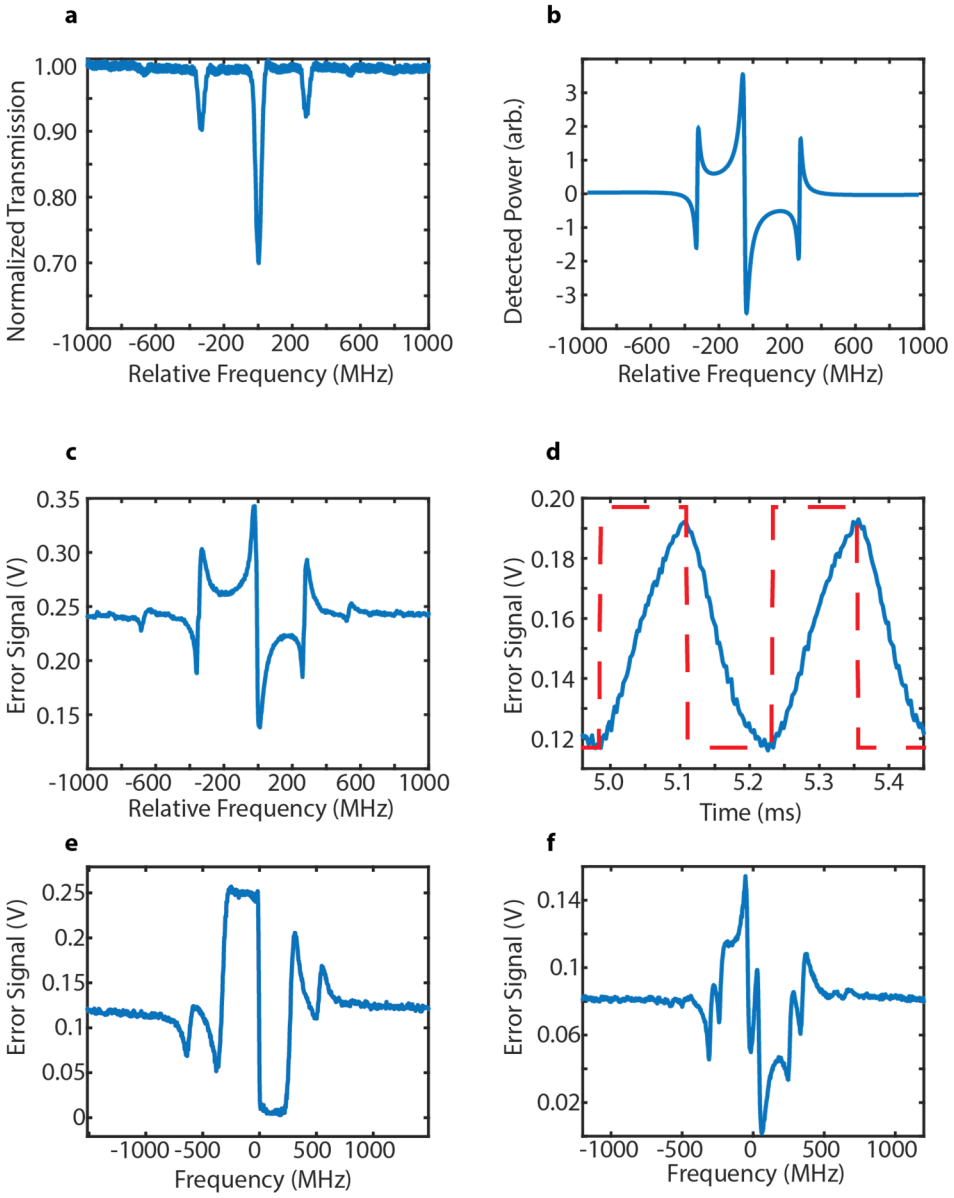

Figure 19: Pound-Drever Hall error signal.

*(*a) Transmission of the phase-modulated probe beam swept across a toroid resonance. (b) Theoretical error signal (output of mixer) as the probe wavelength is tuned across a cavity resonance. (c) Experimentally-measured error signal for the resonance shown in (a), displaying a lineshape very similar to the theoretical lineshape (b). The small peaks offset from the main triplet are second-order sidebands and are predicted by PDH theory. (d) Error signal (blue) when locked as the pump beam amplitude is modulated (red) while focused onto an absorbing nanoparticle. (e) Error signal when the mixer is saturated. It is relatively easy to saturate a mixer, depending on the choice of level compared to the RF power. Saturation (in this case visible as the flat-topped features near 0 V and 0.25 V) causes significant distortion, and complicates interpretation of the resonance. (f) Error signal of a WGM with resolvable doublet splitting. The splitting of the WGM causes a pair of local extrema near the optimal locking point, making it difficult to stably lock to this WGM.

the error signal largely independent of probe laser amplitude, nearly eliminating probe laser amplitude noise from the measurement.[162] Further, since the PDH error signal is essentially the derivative of the resonator transmission curve, the phase changes most rapidly at the center of the resonance, making this locking point a maximum in sensitivity to phase or frequency fluctuations. In essence, the center of the resonance offers maximum phase sensitivity to resonance frequency changes while simultaneously removing sensitivity to probe amplitude noise. In order to close the feedback loop and lock the probe laser wavelength to the toroid resonance, a PI controller (Newport LB1005) receives the error signal and applies a feedback voltage to the wavelength tuning input of the probe laser, correcting for drift in the toroid resonance wavelength or in the operating wavelength of the laser.

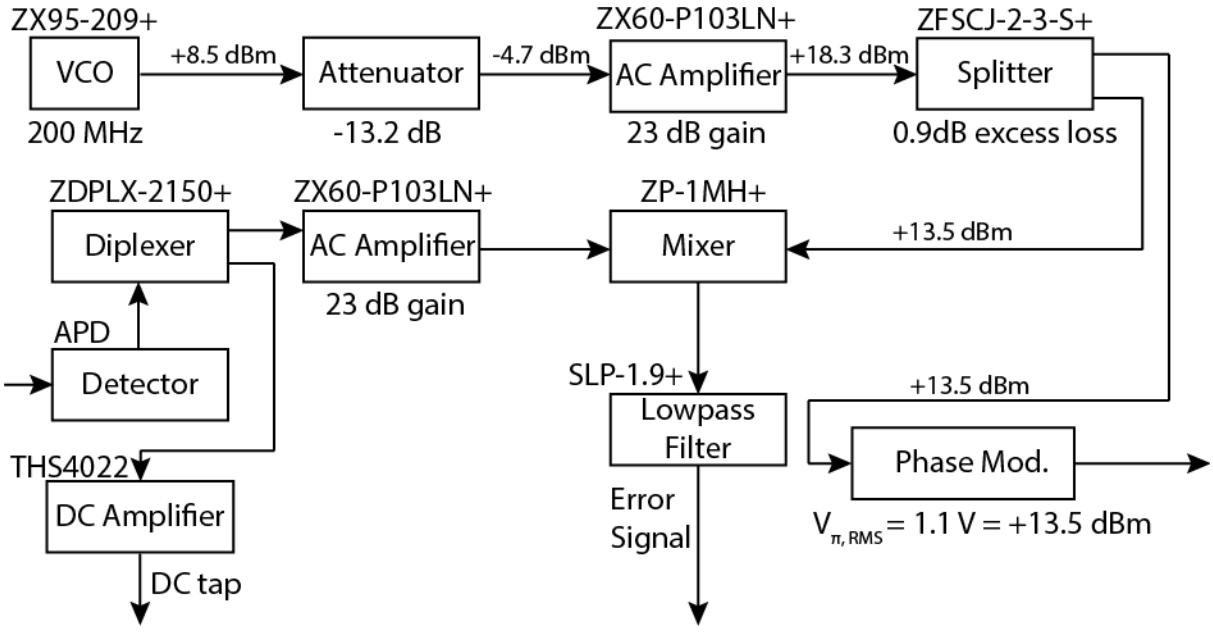

Figure 20: PDH Circuitry.

A block diagram of the circuitry involved in PDH detection in this experiment. Part numbers are listed on the top of blocks (Minicircuits in all cases except the THS4022EVM from Texas Instruments) and figures of merit below boxes. The RF power at each point is listed above the lines connecting boxes where relevant.

Some optimization of the RF equipment has been carried out. Phase modulation was originally employed with a function generator, but a reasonable-priced function generator can only reach 20 MHz. Since the phase modulator only needs a sine wave input, a simple VCO (voltage-controlled oscillator) can be used. VCOs are oscillators with a resonance frequency tunable via an input control voltage. The power output of the VCO is not typically tunable, which requires external attenuation or amplification to ensure that the correct power reaches the phase modulator and the mixer. I chose an ultra-low-phase-noise VCO from Minicircuits (ZX95-209-S+) that tunes from 200-215 MHz with a control voltage (0-10 V) output from a computer-controlled digital-to-analog (DAC) board (NI PCIe6351). Phase noise, which directly contributes to noise in the experiment (since PDH is a means of detecting the phase of the photocurrent), is quite low; this VCO is specified at -115 to -125 dBc/Hz phase noise with the 2-4 kHz offset from the carrier frequency typically used in our experiment. The 1st-generation and 2nd –generation resonator microscopes use somewhat different components in the rest of the PDH path. In generation 1, the VCO output is connected to a splitter (ZMSCJ-2-1 for 1-200 MHz) with 0.9 dB excess loss on each port (in addition to 3dB loss from splitting the power). The LO path is directed to the mixer (ZAD-1-1BR+) which is rated for a certain LO power, +7 dBm. Insufficient LO power in the double-balanced mixer will prevent the diodes from turning off and on completely during each cycle, increasing the conversion loss and hurting the S/N ratio. In practice (see the application notes on the Minicircuits website, especially “How to Select a Mixer”)[166] the LO power simply has to be greater than or equal to 3dB below the specified operating point. In the RF path, the other arm of the splitter first passes through a voltage-controlled attenuator (Minicircuits ZX73-2500+) operating at ~ 7dB of attenuation. This helps tune the depth of phase modulation. A fixed AC amplifier, Minicircuits ZX60-P103LN+, (23 dB gain, 1dB compression at 21 dBm, 0.6 dB noise figure) is used to boost the LO signal right before it reaches the phase modulator. At 1550 nm we use a Photline MPZ-LN-10 phase modulator with V_π = 6V (this is the voltage required for a π phase shift in the probe beam). To convert to dBm, first convert 6V peak to 2.12 V_{RMS}. At 50 Ω impedance, 2.12

V_{RMS} = 90 mW. In RF units, 90 mW is +19.5 dBm. The output of the APD first passes to a diplexer (Minicircuits ZDPLX-2150+). The RF output (>50 MHz) is immediately amplified with another ZX60-P103NLN+ AC amplifier and then connected to the RF port of the mixer. The DC side of the diplexer is amplified (THS4022EVM) and then monitored on the oscilloscope.

In the second-generation setup, the components are better optimized (Figure 20). The output of the VCO is first attenuated with a fixed 13 dB attenuation before being amplified by 23 dB (ZX60-P103NLN+). The resulting sine wave at +18 dBm is split with a higher-bandwidth splitter (ZFSCJ-2-3-S+, 5-300 MHz). The phase modulator arm is already at nearly the ideal power, since the second-generation resonator coupling setup uses a different phase modulator (EOSpace) with V_{π} = 3 V or +16.5 dBm. The mixer is Level 13 (ZP-1MH+) instead of Level 7, allowing for a much higher RF power before saturation. In both setups a 1.9 MHz cutoff lowpass filter is attached to the output of the mixer. A lower frequency cutoff would be ideal, but was not easy to find commercially available.

There are a few more tips and tricks worth noting. We tune the phase of the LO at the mixer by changing the VCO frequency,[167] which is more convenient than shifting the phase at a fixed frequency. It is easier to find a tunable VCO then a wideband phase shifter. The VCO frequency should be as high as possible (to increase the error signal) without reaching the bandwidth limit of the photodetector. Not all splitters have isolation; this is a specification that should be sought out to avoid noise problems associated with crosstalk. In addition to using a low-phase-noise VCO, the photodetector should be quiet at RF frequencies. I have had good results with an avalanche photodiode from Thorlabs. RF electronics usually specify power, not voltage, which are quadratically related and easy to interconvert since nearly all components are at 50 Ω impedance. Likewise, instead of peak-peak voltage, RMS powers are usually reported which must be divided by 2.83 to get peak-peak voltage. Finally, and this seems like an arbitrary distinction, a diplexer should be used to split the output from the photodetector into RF and DC paths. A bias tee operated in reverse is in theory the same device, but in practice causes more drift in the phase of

the error signal. Vertical drift of the taper will change the phase of the RF signal at the mixer, changing the error slope and eventually breaking the lock. Horizontal drift is less deleterious, as it decreases/increases the amplitude of the error slope depending on the direction of drift. However, horizontal (in-plane) drift does not change the shape of the error slope. Adjusting for horizontal drift is as easy as keeping the transmitted DC tap power constant. It should be noted that the position where the error slope is maximum is usually slightly undercoupled, since overcoupling lowers the Q-factor. The mixer must be robust enough to dissipate heat from the RF signal without saturation (Figure 19e). Saturation distorts the shape of the error signal and caps the achievable error slope. Another issue is the mode splitting often found in high-Q resonances. This negatively affects the error slope (Figure 19f), in some cases making it impossible to lock.[168]

2.9 Bandwidth narrowing via lock-in amplification

Although absorption spectroscopy is the goal of this experiment, rather than a technique designed to increase detection limits for microresonator sensing, it has the serendipitous side effect of enabling this improvement. This is because the photothermal signal is in some sense deterministic, since it is generated by the action of the pump beam on the analyte. Turning off the pump beam turns off the photothermal signal. Therefore amplitude modulation of the pump beam can be used to directly modulate the photothermal signal. The continuous readout of toroid resonance frequency enabled by PDH locking permits rapid amplitude modulation of the pump beam. The resulting periodic oscillation of the photothermal heating signal causes a synchronous oscillation of the toroid resonance wavelength visible through the PDH error signal. Macroscopic double-beam absorption spectrometers use this same technique for signal-to-noise improvement, albeit in a different geometry.

Amplitude modulation of the photothermal signal is enormously useful because of the large amount of low-frequency noise. Figure 21d shows the power spectrum of the error signal from 10 Hz to 10 kHz. 100% amplitude modulation of the beam at 4.01 kHz puts the entire content of the photothermal signal into a sub-Hz frequency band (Figure 21a) far away from the riffraff hanging out at DC. While all of the sources of technical noise are not known at this time, the linewidth of the probe laser is quoted as 200 kHz over 50 ms. Figure 21b shows that the error signal has Gaussian-distributed noise with a standard deviation of 217 kHz over 50 ms, strongly suggesting that probe laser frequency

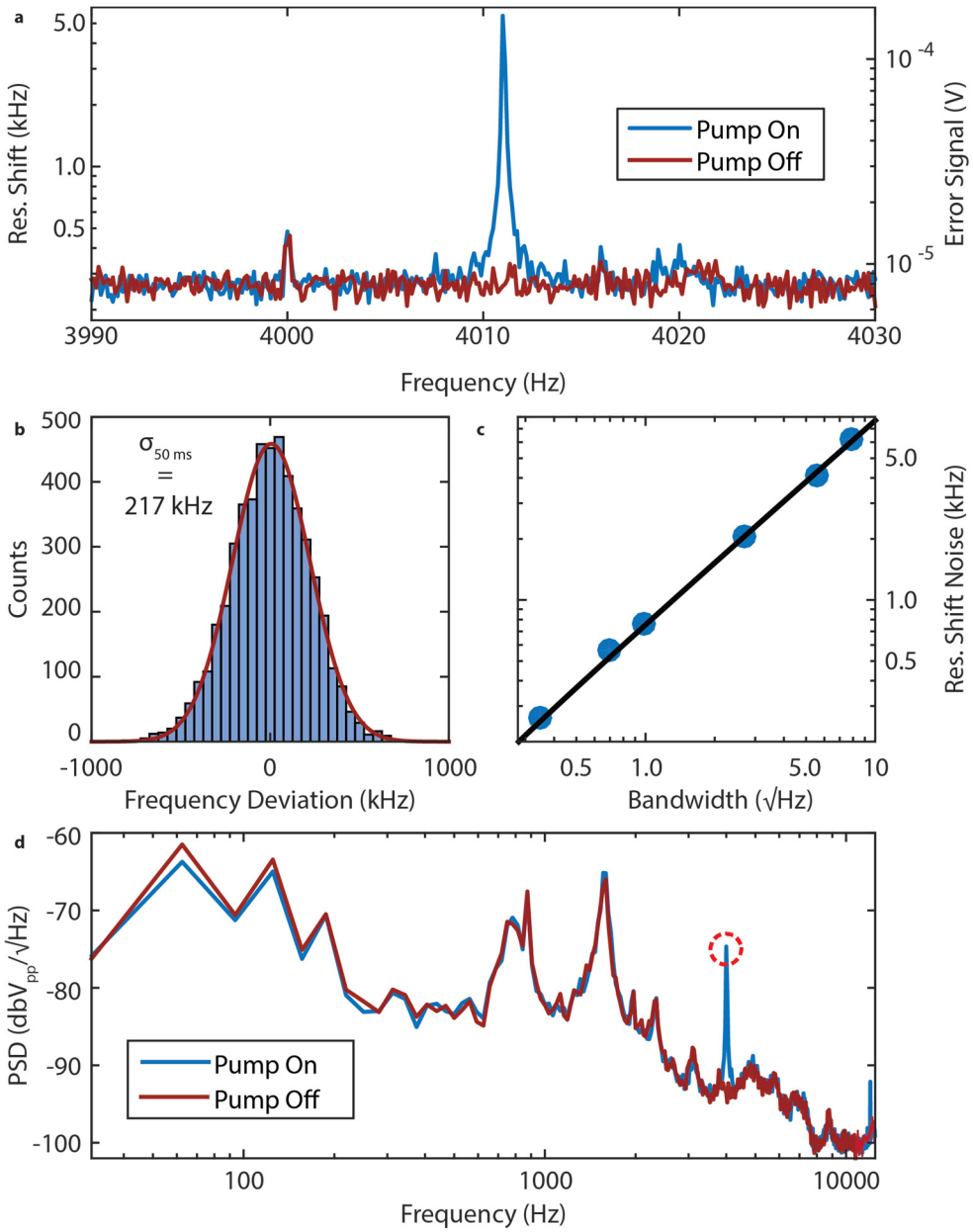

Figure 21: The Measurement bandwidth reduction advantage of double modulation.

(a) The error signal (V) and resonance shift (kHz) at 1550 nm is measured in the vicinity of the 4.011 kHz amplitude modulation frequency by a network analyzer with 0.122 Hz bandwidth. Measurements with the pump beam blocked (red) and unblocked (blue) differ only by the large peak at 4.011 kHz.(b) Histogram of frequency fluctuations as determined from the PDH error signal and error signal slope yielding an apparent 50 ms linewidth of 217 kHz. (c) Reduction in noise at 4 kHz with decreasing bandwidth. The linear trend (black line) results from the expected square root dependence of the noise upon the bandwidth. (d) Power spectral density (PSD) of the raw error signal. Blocking and unblocking the pump beam again results in a large peak (red circle) at the pump modulation frequency. All frequency-resolved data was acquired with a Stanford Research SR770 FT Network Analyzer. All of the data in this figure was obtained by Erik Horak.

drift is the largest source of noise in the experiment. Further, the noise spectral density is quite flat in the vicinity of the photothermal signal (Figure 21a), as evidenced by the expected square root improvement of signal/noise ratio with narrower detection bandwidth (Figure 21c).

How is it possible to only detect the 4.01 kHz component of the error signal? A lock-in amplifier (SR 7265) is design to only measure voltage with a frequency component matching a pre-determined reference frequency. The internal electronics of the lock-in amplifier are remarkably similar to those that generate the error signal. A VCO or similar oscillator is tuned to the reference frequency and input to a mixer along with the error signal. The output is low-pass filtered, and the resulting DC voltage is proportional only to the voltage of the error signal at the reference frequency (which is set equal to the amplitude modulation frequency of the pump beam). The phase of the reference oscillation must be adjusted to match the input phase, which does not tend to vary in our experiment. Implementing lock-in amplification increased our detection limit by approximately 10,000x, reaching sub-attometer resonance shift detection (Chapter 6). The equivalent noise bandwidth of the lock-in amplifier is 0.1375 Hz for a 1s time constant, and the experimental noise floor (Figure 21c) is on the order of 1.5 attometers (200 Hz) $/\sqrt{Hz}$.

The lock-in amplifier voltage is directly proportional to the absorbing nano-object's extinction coefficient, given by the following equation:

$$Resonance\ shift\ (fm) = 2.83 * \frac{V_{RMS}}{m_{error}} \qquad 2.9$$

where 2.83 converts RMS to peak-peak voltage, V_{RMS} is the RMS voltage of the error signal at the pump modulation frequency, and m_{error} is the error slope at the locking point in units of V/fm. The factor of 2.83 assumes that the photothermal signal is a pure sine wave, which was empirically determined to be a very good approximation.

2.10 Control software

All of the various parts of the experiment are ultimately controlled through Labview software (National Instruments). The Labview code (version 2013 SP1) has evolved through several generations as the needs of the experiment grew and my incompetence decreased. I will save the reader from close inspection of the codes I have written, but will mention the most important features—and lessons learned—in this section.

State machines are a much better method for organizing data flow than sequence structures. A state machine is a case structure inside of a while loop. Until a stop condition is met, the code runs and chooses a case to run based on its programming. State machines are useful when a single initialization routine feeds into several possible states, or when the result of a particular state determines which other states should be run. The state machine used in my code is shown in Figure 22. Initialization first connects to the wavelength tuning motor, steering mirror controls, analog read and write channels on the DAC, and pump power meter. Once initialized, the code stays in “Ready” mode, awaiting user input. The front panel allows for changing parameters on any of the connected equipment, allowing for example the user to optimize the beam position for maximum photothermal signal. Then, pressing a button begins running that state, for example “Take Photothermal Map”. After running the case, the code returns to the ready state. Based on the data just taken, the user may decide to realign, or to proceed with taking other kinds of data. In theory, all of the different states can pool data into a common file that is then saved when the code is stopped (I have left the implementation of this last feature to future generations). Tab control is used to automatically switch between front panel tabs so that the front panel is not unusably cluttered. A final important feature of state machines is that it makes it easy to add new functionality to the code without affecting existing code. Users that are intimidated by state machines will find that putting code into a case

structure will get you 90% of the benefits. I credit Alex Foote for inspiring me to use state machines through a well-presented group meeting.

MATLAB code can be run directly inside of Labview using a script node. I advise users to avoid MathScript, which is a limited version of MATLAB that is missing a number of commands. This is unfortunate, because scripts in script nodes are painful to debug. The most common bug is the different handling of arrays between MATLAB and Labview. Besides the fact that both programs define the first element of an array as variously 1 or 0, arrays will sometimes be transposed when passing from Labview into script nodes. Yet, the overwhelming utility of MATLAB makes script nodes worthwhile. One can process data and generate figures that are automatically saved when data is acquired. Better, complicated structures can be created and saved at the time of data acquisition. This structure can be drag-and-dropped into MATLAB, and can contain filenames, all of the raw data, scan parameters, etc. in a searchable structure which saves a lot of time on data processing. MATLAB is also quite good at curve fitting compared to Labview.

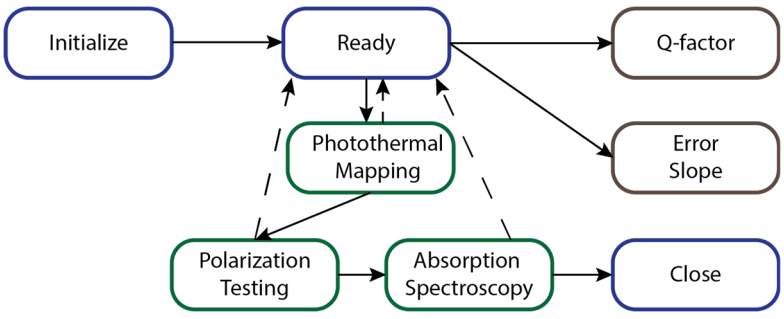

Figure 22. The state machine used for typical experiments with the toroid absorption spectrometer.

Utility cases (Initialize, Ready, Close) handle communication with instruments and data flow. Diagnostic cases (Q-factor, Error Slope) are used to query the WGM and error signal. Measurement cases (Photothermal Mapping, Polarization Testing, Absorption Spectroscopy) record and process data; based on the results of measurements, alignment of one of the three pump beam parameters (wavelength, position, polarization angle) may be adjusted and data retaken.

Usually it's better to use for loops for data acquisition rather than while loops. A for loop runs for a predetermined number of times, whereas a while loop will produce a dataset of random length. This becomes rather inconvenient when processing the data later on. Data should be stored inside arrays that are initialized with size and value 0 outside of the loop, passed through a shift register, and inserted into an array inside the loop. At the output shift register the data can be further processed and saved. Another issue with while loops is that if there are any errors during execution, especially involving COM/USB communication issues, the code may keep running forever.

Driver issues are the single largest source of frustration when coding Labview. Some of this happens because of quirkiness introduced by companies modifying drivers that were original meant for serial ports and using them in USB-controlled instruments. In this case all axes of an instrument might be called by the same COM address. A common rookie mistake is trying to open a second line of communication to an instrument. For example, if a standalone program is communicating with an instrument, Labview code that tries to call the same instrument will error out, requiring a restart. Other errors are somewhat inexplicable. Calling the control software for the Attocube from inside Labview will frequently cause the software for Thorlabs cameras to crash, even though the two standalone applications can coexist peacefully.

2.11 Procedure for taking data

Alignment of the taper, the chip, and the pump objective (which is fixed in place) is performed crudely by eye. The taper stage is moved by hand and by micrometer to a position with the narrowest part of the taper overtop the chip, and in the middle of the region illuminated by the lamp light coming through the pump objective. Then the taper stage is secured and the taper lowered as far as the user is comfortable, avoiding ramming into the substrate. A 10x objective in the top down view is used to align the fiber within

several microns of the toroid horizontally and ~ 30 μm vertically, to the point that under maximum magnification the Navitar camera displays both taper and toroid. Then the 60x objective is put into place, and the focus adjusted until the toroid and the taper are both on the field of view visible to the topdown camera. The 10x and 60x are reasonably parcentric, but sometimes after switching objectives the toroid is not visible in the top down view. In this case the Navitar can be used to move the toroid until it is in the center of the region lit by the light from the 60x objective (which is clearly visible in the side view). The 60x objective is deliberately misaligned from parfocality with the 10x objective, in such a way that it has to be manually lowered with the focus micrometers until it comes into focus. This helps protect the expensive objective from being accidentally rammed into the toroid.

Because the resonance frequencies of any toroid are determined by the stochastic CO_2 reflow process, they are not knowable in advance. Hunting for resonances begins with a 12 nm sweep of the probe laser frequency at 1 nm/s. The user watches the oscilloscope for evidence of peaks. PDH is helpful in this regard because a true resonance will show up in both the DC tap signal and the error signal, while a noise spike on the detector typically only shows up on the DC tap. In the past we have used noisier detectors (e.g. Menlo Parks FPD510) which made locating weak resonances more difficult. It can be difficult to find resonances sometimes, because multiple factors affect taper-toroid coupling. The probe polarization, taper height, taper normal distance, and probe laser wavelength all affect coupling to the toroid, and all must be somewhat well aligned to see resonances. In practice, this means that an inexperienced user may initially struggle and then quickly develop instincts for appropriate coupling conditions.

Once resonances are observed on the DC tap signal, the user chooses a strong resonance that appears to be extremely sharp with a 200 ms/division update rate on the oscilloscope. At this level Q-factors between 1×10^6 and 1×10^8 all look like a single pixel spiking away from baseline. Resonances are then investigated more closely by turning off the coarse wavelength tuning and sweeping the fine frequency tuning piezo inside the ECDL over a range of +/- 1 V (+/- 53 pm). At this scan range it is easy to characterize

whether a resonance (and the associated error signal) is good enough for measurement purposes. Once the laser is sweeping over a single resonance on this narrow wavelength range, it is easier to optimize the taper height and separation. Probe polarization is a more mysterious optimization process (since none of the 3 paddles are purely quarter-wave or half-wave plates) but qualitatively good results can be obtained with a minute of tweaking. The relative phase of the RF and LO signals at the mixer also needs to be optimized, which is taken care of by tuning the frequency output by the VCO. To be usable for PDH locking, the WGM resonance should have a reasonable Q-factor (low 10^5 Q at minimum but ideally > 5 x 10^6); extremely high Q-factors (Q > 2 x 10^7) are difficult to lock to and fortunately are rarely encountered.

A final complication is doublet splitting. Resonances with observable doublet splitting are typically not usable for PDH locking (Figure 19f). If the splitting is large enough, then the resonance is essentially two peaks, either of which could be locked to. In general, though, doublet splitting acts to substantially reduce the error slope near the locking point and also adds the possibility of an unstable lock that hops between the two peaks. Neither are good, so we avoid using doublet split resonances. O'Shea and coworkers offer a nice discussion of this problem.[168]

Once the coupling is optimized, the Q-factor and error slope can be measured with Labview. It is important to have an accurate measure of the error slope because this slope determines the conversion between the detected signal (volts on the lock-in amplifier input) and the desired signal (resonance shift of the toroid in wavelength). A Labview program developed by myself and Erik Horak acquires a scan of the error signal while sweeping across the resonance, and then plots the derivative of the measured signal. The value of the largest extrema is the slope of the error signal at the best locking point, exactly on resonance with the WGM. The derivative plot is more useful than the original error signal because there are some complications to avoid; specifically, the scans in the long and short wavelength directions may differ because of thermal effects and tuning hysteresis, and there will be multiple local maxima in the error signal depending on the sideband spacing and the presence of doublet splitting. If the phase of the

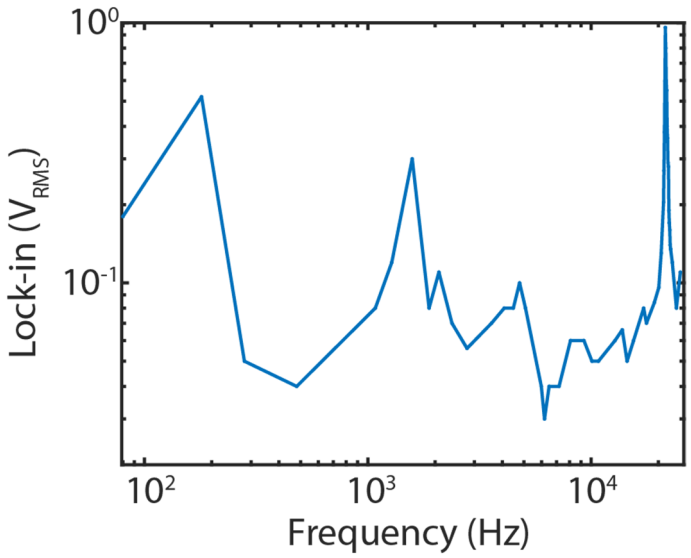

Figure 23 Bode plot of probe laser cavity noise.

Tuning the modulation frequency of the pump beam while measuring the error signal with the lock-in amplifier gives the noise spectrum of the probe laser. The peak at 180 Hz is a power line harmonic. Other resonances include ~1.2 kHz and ~21 kHz, likely mechanical vibrations.

LO is not correct at the mixer, the error signal will look less and less like the textbook PDH signal. In the derivative plot, the presence or absence of small doublet splitting can be ascertained as a pair of extrema. The absence of a strong central peak (or pair of peaks) provides further evidence that the phase of the LO is wrong.

After the error slope at the peak of the resonance is measured, the sweep span is turned to zero. The center frequency of the sweep is then tuned until the user observes the transmission fluctuating wildly. By watching the DC tap transmission and tuning the output offset until the transmission is minimized the locking point is found. It's important to note this level on the oscilloscope, with use of cursors, since any deviations from this level indicate locking problems and/or taper drift. With the span at zero and the center correctly adjusted, locking is turned on. If the resonance does not lock immediately, there are two knobs to adjust. The Gain knob and the input offset knob would ideally be independent from each other.

Gain controls the gain on the feedback applied to the probe laser tuning input, and input offset sets the locking point in voltage. In practice, however, changing the gain also changes the input offset. This frustrating effect is what makes locking an art rather than a science. Nonetheless, it is usually not too difficult to lock. Typical parameters in the current setup are ~ 5.5 input offset and 2.5 gain. The locking point is proportional to the residual DC voltage on the error signal (which is why it's not just set to 0 V) and the gain is a function of the error slope and the tuning curve of the probe laser, so it will vary between setups. After locking and engaging the pump beam, fine adjustment of the input offset is made until the resonance shift is maximized; this corresponds to optimizing the position of the locking point to the center of the resonance. Oscillation at 1.2 kHz frequently occurs; this is the first mechanical resonance in the frequency tuning piezo inside the probe ECDL cavity. Turning down the gain slightly will cease oscillations. The choice of amplitude modulation frequency must avoid probe cavity resonances (21 kHz is another strong resonance). Figure 23 gives the probe cavity noise resonance spectrum as a guide to which frequencies to avoid.

The general procedure for data taking starts by coarse mapping of the entire microresonator, after centering the pump beam spot on the center of the silicon pillar using the top-view camera. A typical map has 50 steps with 1.0 μm step size. Given the $1/e^2$ beam diameter of the focused pump beam of 2.35 μm micron, and the good dynamic range of photothermal mapping, these mapping parameters allows for the identification of all but the dimmest objects. For objects known to have strong polarization dependence (gold nanorods, some polymer nanoparticles, single molecules) we take two maps at orthogonal pump polarizations.

For each object identified by coarse mapping, we acquire a high-resolution photothermal map with 0.25 μm step size, allowing us to trace out the point-spread-function (PSF) defined by the nano-object. This is a useful confirmation that you are looking at a single object; if the PSF is clearly not circular, then we reject the image since it did not originate from a single object. One exception is near the rim of the

toroid, where oblongation in a direction normal to the toroid circumference can result from the beam being focused onto a highly-curved surface. Once each object is mapped at high resolution, we measure spectral dependence by tuning the pump beam wavelength from 1280 to 1365 nm and polarization dependence by tuning the waveplate through 180° mechanically (360° of rotation of the optical polarization). To correctly evaluate the nano-object in the presence of nonzero silica absorption, we take a background spectra/polarization curve on a spot that is several microns distant, with no nano-objects on it, and at the same radial distance from the center of the toroid. Photothermal shift is constant at a given radius, i.e. the photothermal map of the toroid itself is azimuthally symmetric.

Taper drift is a perennial issue. Drift is more of a problem in the equatorial direction, and less so normal to the substrate. However, the attocube/chip will tend to drift upwards for the first hour after the toroid chip is mounted. This is possibly caused by slow expansion of the double-sided tape used to stick the toroid chip to the stage. Sometimes the taper sticks to the toroid, and this is remedied by sharply backing away the piezostage holding the toroid by a few microns until the taper jumps free, and then carefully recoupling in. There are three other possible issues to avoid. The three-axis stage holding the taper holder must be very rigidly attached to the optical table, by tightening two tiedowns onto opposite legs of the stage as firmly as possible. Failing to do this increases taper vibration and/or drift. If any part of this 3-axis stage is touching the plexiglass enclosure around the setup the taper will be wiggling a lot, visible on the camera. Finally, a high-precision rotation stage must be attached between the taper holder and its 3-axis translation stage. This is because the taper (thickness 1 to 125 μm) has to be ~ 20 μm from the surface of the chip for the entire width of the chip, which is currently 3,500 μm wide. A very small imprecision in the angle of the taper will cause it to slam into the substrate. This angular tolerance is less than 0.5 degrees. An incorrect approach angle will cause the taper to stick to the substrate (noticeable as a sudden large decrease in transmission). Sticking to the substrate because of angular misalignment must

be distinguished from collision with a hair on the substrate, which sometimes happens when graduate students shed. The latter problem can usually be solved with a quick spray from an air can.

The biggest drawback with the instrument in its present form is the low throughput. A large part of this is the limited extent of automation. Some of the limitations are intrinsic to our choice of equipment. The lockbox from New Focus, for example, must be operated manually to tune and lock to each resonance. This requires the user to manually search for the locking point and tune the feedback settings on this somewhat unpredictable box. The toroids themselves are another major issue. Because the resonant wavelength of each microresonator is random, the user must "hunt for" high-Q resonances on each new toroid. This process takes some time, especially because doublet resonances (which range from occasional to universal, depending on the chip) cannot be used unless the doublet splitting is 2 FWHM or greater (which is rare). A less significant issue is that the beam scanning mirror actuators are not capable of repeatably moving to the same position, especially when approaching the same nominal position from different directions, and therefore the user must manually tweak the position back and forth until the photothermal signal is maximized. Further problems are the polarization control of the probe beam, requiring the user to adjust three different physical fiber loops to re-optimize the polarization for each new resonator and occasionally as the polarization of the fiber drifts; as well as drift in the position of the tapered fiber, which can occur either towards or away from the resonator and directly modify the error slope (vertical drift is also possible but less frequent). Sudden sticking by the taper to the toroid occurs randomly and would eliminate any feedback signal from position locking.

So in this sense, every nano-object that we characterize is measured by hand. This is unfortunate, but not remediable at the present time. None of the issues presented are insurmountable given a sufficiently large amount of time and money. For example, an FPGA could be used to replace the lockbox; an automated search program could be written to find resonances (using USB control to switch between coarse and fine scanning on the probe laser and joint programming with the FPGA); and a higher quality

beam steering motor (i.e. a galvo) would obviate that problem. Taper drift could be compensated for with an active feedback loop to lock the toroid's position relative to the taper,[169] and polarization drift could be potentially automated with an electronic state of polarization controller. A truly intimidating amount of Labview programming (months of grad student time) in addition to equipment cost made this prospect less attractive than taking data. The 2nd-generation resonator setup (Chapter 8) was designed to allow for a higher level of automation.

Chapter 3

3. Fabrication Protocols for Toroids and Tapers

3.1 Fabrication of toroid microresonators

Toroid fabrication was originally developed by Deniz Armani and coworkers in 2002.[106] The theses of Deniz Armani and Jean-Baptiste Jager were helpful as a guide to developing the process flow for fabricating toroids with the facilities available at UW-Madison.[170,171] Nonetheless, a sufficiently detailed protocol for fabricating toroids was not available at the beginning of my Ph.D. The fabrication in this thesis was performed by myself or Kassandra Knapper at WCAM (Wisconsin Center for Applied Microelectronics), with occasional early use of facilities at the University of Missouri and Argonne National Laboratories. It took several attempts to create a reliable process for making high-Q SiO_2-on-Si toroidal microresonators and I will outline the finished process flow below. Although the process flow is quite simple compared to an industrial fabrication process, there are several pitfalls for novice lithographers to avoid that I would like to highlight.

The process begins with wet thermal oxidation of prime grade <100> Si wafers, either 3" or 4" diameter. An MRL tube furnace at 1050 °C for 20 hours grows approximately 2 µm of thermal oxide, as verified by a Filmetrics F-20 optical reflectometer. It is also possible to buy wafers with the thermal oxide already grown. No serious difference has been reported in the literature in the obtainable Q-factor of finished resonators. Zhang et al. note that the silicon wafer should be intrinsic, because doping (especially boron doping) increases absorption losses and limits Q-factors.[172] After oxidation, the wafers are

degreased with a successive rinsing in acetone, IPA (isopropyl alcohol), and water followed by drying with nitrogen while spinning on a Headway spincoater. This step is designed to remove lingering organic residue, leaving behind a clean surface. The wafers are then treated with HMDS (hexamethyl disilazane) vapor to create a hydrophobic surface. HMDS treatment strongly enhances the adhesion of hydrophobic photoresists (including the Shipley S1800 series used by us in toroid fabrication). I have found that omitting the HMDS application causes peeling of the photoresist layer during the following wet etching step in BOE (buffered oxide etchant). When a wafer is reused after a poor attempt at applying photoresist or a low-quality photoresist (PR) exposure, it is vital to repeat this HMDS step. Immediately after applying HMDS, wafers are mounted on a spincoater and 1 large plastic pipette's worth of S1813 (Shipley, distributed by MicroChemicals) is dropped onto the wafer. This PR blob should cover most of the wafer. Visible air bubbles will cause incomplete coating of the wafer and should be avoided. PR is spread across the wafer by spinning; spread at 10s, 500 RPM, 500 Ramp; coat at 30s, 4000 RPM, 1000 Ramp; 500 ramp decelerate. This formulation and spinning speed leads to a PR coating approximately 1.4 μm thick. After a successful coating, softbaking is performed on a vacuum hotplate for 60 seconds at 115 °C to evaporate solvent from the film. UV exposure is performed with a dose of 72 mJ/cm^2 on a Karl Suss MJB-3 contact aligner in hard contact mode. Hard contact means that interference patterns are visible as the wafer is brought into contact with the photomask. The photomask should be chrome deposited on quartz. The current photomask is designed for 4" wafers and is subdivided into four sets of 25 toroids per column and approximately 20 rows, producing roughly 80 chips per wafer. The toroid to toroid spacing on each chip is 500 μm and each feature is a simple 60 μm chrome filled disk. On each chip a mm-sized text label is also patterned. Between every 3-4 exposures the photomask is cleaned by immersion in hot MicroPosit 1165 remover (a potent solvent mixture containing tetramethyl ammonium hydroxide and N-methyl pyrollidone). After exposure, development is with MicroPosit MF-319 (tetramethyl ammonium hydroxide at 0.24 N) for 30-40 seconds in a 136 mm crystallization dish, then quenching in water, followed by rinsing

for 30-60s with water, and drying with compressed N_2. Inspection is performed with a 20x brightfield optical microscope, and if defects or missing rows of disks are observed, lithography is repeated. If there are no lithographic issues visible, a hardbake for 120s at 125 °C on a vacuum hotplate is performed. This hardbake improves adhesion (which is important during BOE etching) and reflows the edge of the PR for a smoother disk. The reflow of PR is visible under optical inspection in the microscope as a rounding in the edge of the disks.

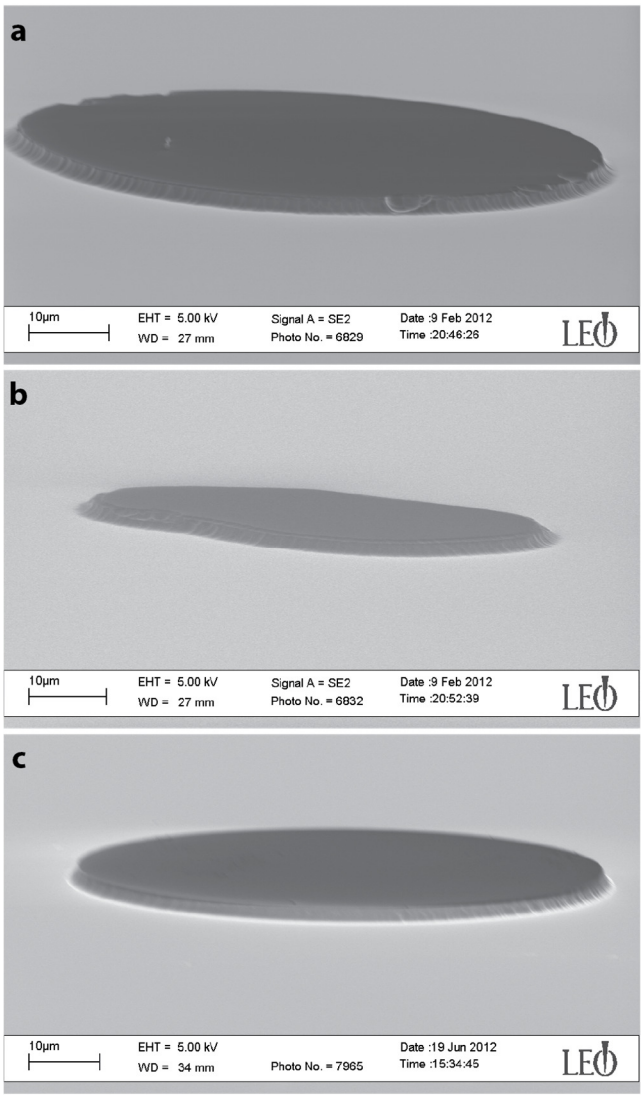

Figure 24 : Lithography and BOE etching.

(a) The dark region is silica, light grey is silicon. Defects from PR bubbles are visible in several locations. These wounds cannot be healed by the CO_2 laser reflow step. (b) Due to overexposure, overdevelopment, or other issues, this feature is lacks the circular symmetry required for making WGM resonators. (c) A correctly fabricated pad of 2 µm thick, 60 µm diameter oxide after BOE etching and successful lithography The regularly-spaced hatch marks are typical of BOE etching, and are smoothed out by later reflow.

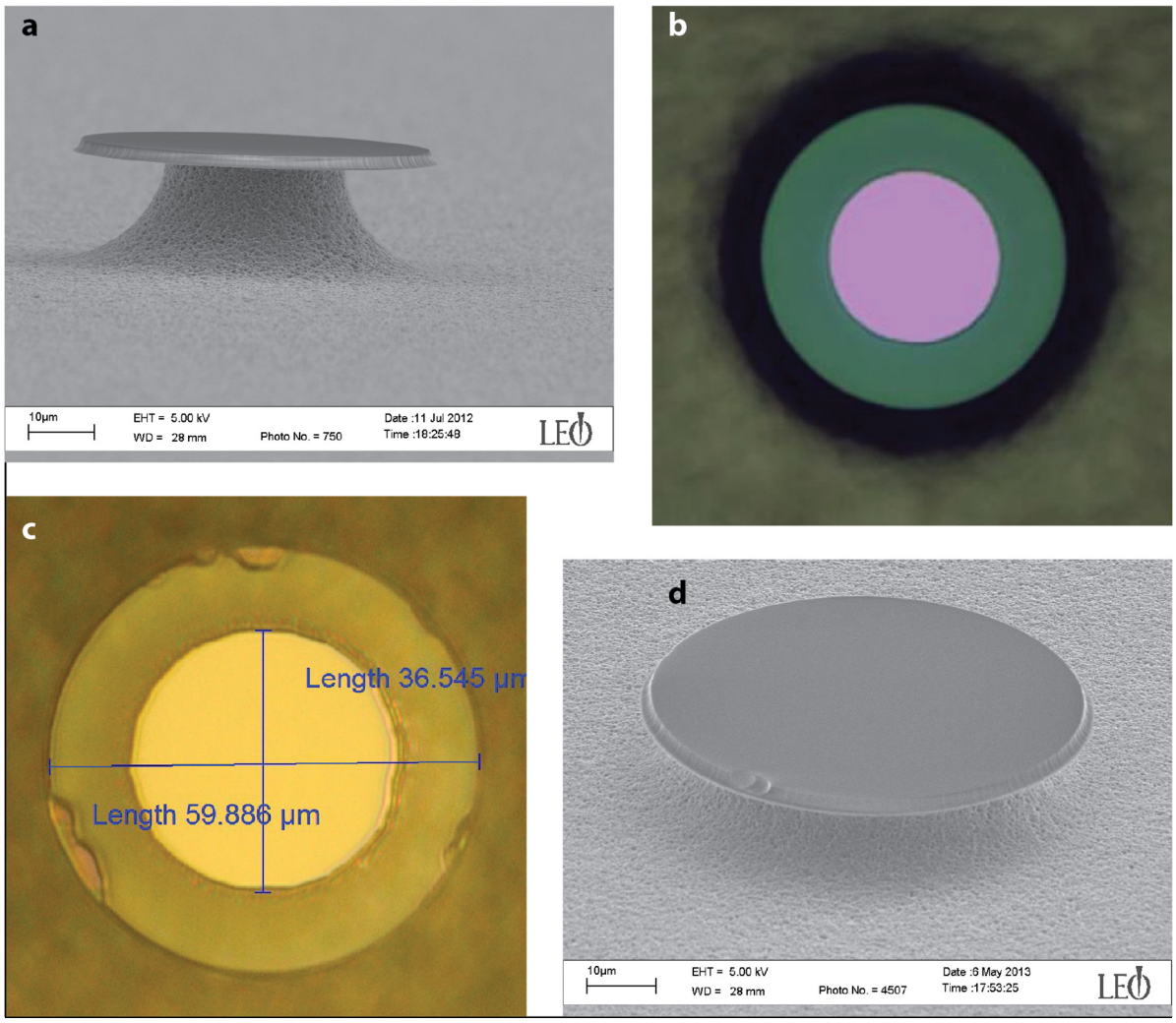

Figure 25: Microdisk fabrication.

(a) SEM image and (b) optical micrograph of successfully fabricated microdisk resonator. Regular striations on the rim of the disk are from the BOE etch and are always observed. The high symmetry and lack of visible defects is a requirement for proceeding to the reflow step. (c) Optical micrograph and (d) SEM image of flawed microdisks. Substantial divots are present, originating from the lithography. These microdisk will not reflow into symmetric toroids and are unusable for most applications.

The next step is to transfer the PR pattern into the silica layer. A buffered hydrofluoric acid (BOE) etch with a 6:1 ratio of HF solution (49% HF) to NH_4F (40% NH_4F). At WCAM a 33 minute etch was appropriate to break completely through the oxide layer. After quenching in a cascade rinser for 5 minutes, the wafers

were visually inspected to determine if the silicon surface was hydrophobic. If the oxide layer was completely removed, then the water will come off as a single continuous sheet. If not, it will bead up on the wafer surface like raindrops on a window. PR is removed by immersion in hot (80 °C) 1165 Microposit remover. A good etch leaves a silica pad on a silicon surface that is perfectly symmetric (Figure 24c). Bubbles in the photoresist film, usually introduced during the dropcasting of PR onto the wafer, will cause local voids in the PR film that are transferred into the oxide layer (Figure 24a). Erosion of the photoresist feature, likely during development, will lead to kidney-bean-shaped structures (Figure 24b). MicroChemicals published a Lithography troubleshooting guide that explores the cause and solution to issues like these in more detail.[173]

After BOE etching and cleaning, an isotropic etch is performed on the silicon layer. We initially tested this with SF_6/Cl_2 plasma etching and also SF_6/O_2. Both plasma etches did not exhibit any real selectivity to Si vs. SiO_2 and were therefore not useful. Amine gallate has also been used as an isotropic, selective silicon etchant,[174] although the paucity of established procedures and safety considerations steered us in other directions. We then worked with Suzanne Miller at Argonne National Laboratories using a Xactix XeF_2 etcher. While this produced the first generation of microresonators, the necessity to travel to a different city and to use the highly loading-dependent and humidity-sensitive XeF_2 etcher was inconvenient. Investigating alternatives, I found the process flow developed by Jean-Baptiste Jager at the University of Grenoble[171] (note that this thesis is written in French). Using the same model of ICP (inductively-coupled plasma) etcher manufactured by STS, I implemented the following recipe that Jager developed: 100 sccm of SF_6 and 50 sccm Ar with chamber pressure of 15 mT, with 450 W coil power and 8 W platen power. An etching time of approximately 20 minutes is appropriate for the 56 µm diameter microdisks I have used in this thesis, giving an isotropic undercut of 15 µm. For the experiments discussing in Chapter 4, a second etching step was sometimes performed to further decrease the diameter of the silicon support pillar after the CO_2 reflow step. This did not work with toroids where the first etching step had been performed via

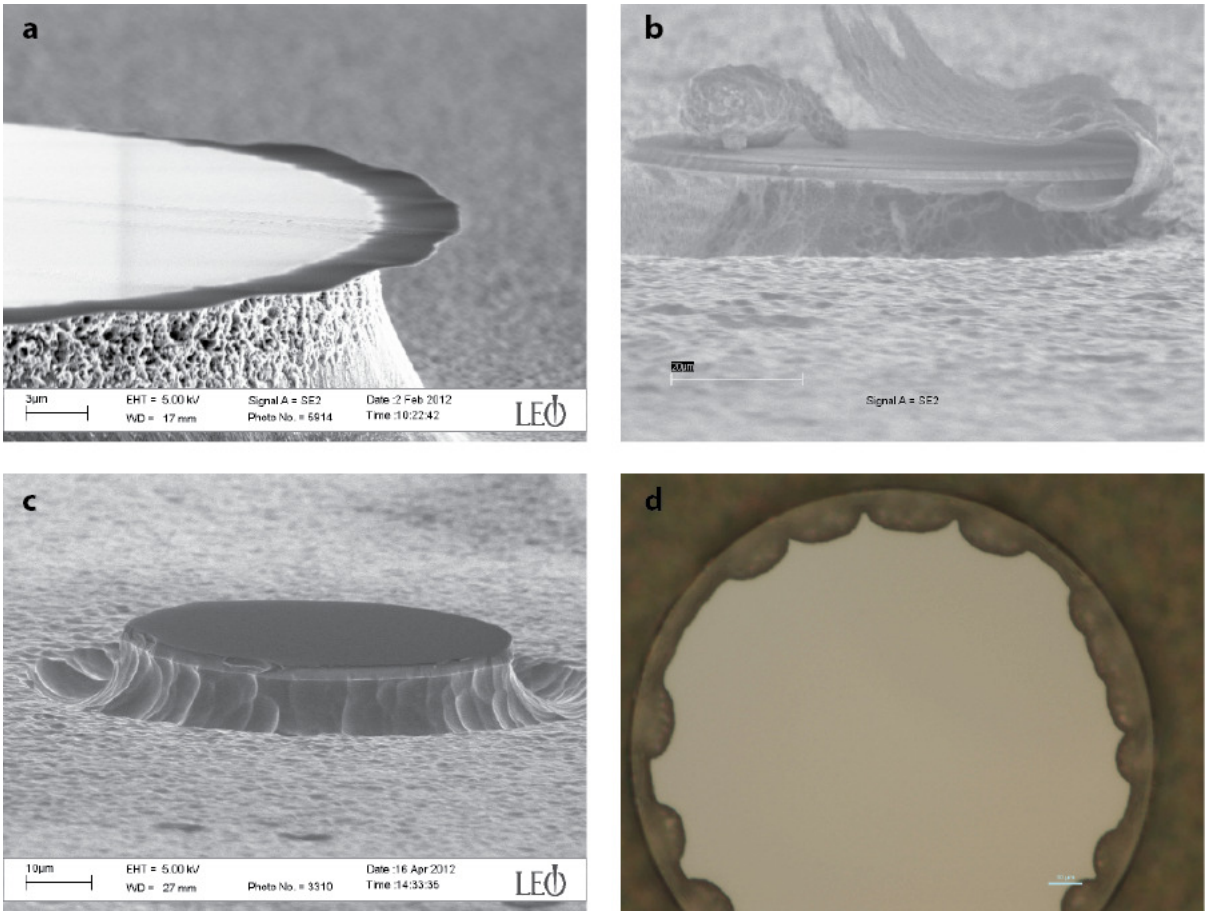

Figure 26 Problems during isotropic etching.

(a) SF_6/O_2 ICP etching will isotropically erode silicon, but at the cost of low selectivity towards silica, leading to a severely eroded microdisk that cannot support an optical mode. (b) Insufficient drying and/or cleaning before XeF_2 etching causes formation of a white, flaky film which we came to call "micro-bacon". (c) Attempting to clean off residue with sonication universally results in shattered toroids, even with acoustic insulation. (d) Insufficient drying or improper arrangement of wafer pieces inside the XeF_2 etcher leads to "mouse-bite" defects and consequently poor-quality toroids.

ICP etching. It worked much better when the re-etching step used a XeF_2 etcher. The cause of this difference is not exactly known but must involve differences in surface chemistry given the high chemical selectivity of both etches. Examples of isotropic etching problems with microdisk resonators are shown in Figure 26. Insufficient chemical selectivity gives near-complete erosion of the silica layer (Figure 26a).

Water vapor or other contamination during XeF2 etching gives a white flaky film all over the chip (Figure 26b). Attempts to remove etching contaminants by sonication only result in shattered microresonators (Figure 26c). Another issue that occurs sometimes with XeF2 etching is “mousebite” etching of the silicon pillar (Figure 26d), which is likely caused by the arrangement of chips inside the etcher or insufficient dehydration.

The final processing step is dicing. The wafer (now patterned with microdisk resonators) is coated with Shipley S1813 resist using the same spinning recipe as before, giving a resist thickness of approximately 1.4 μm. A semi-hardbake is performed for 60 s at 110 °C; the goal of this layer is to keep dicing debris from polluting the finished wafer, so a hardbake is not necessary. Diced chips are 3.5 mm wide and 17.3 mm in length (although the length may exceed this value as it follows the curvature of the outer edge of the wafer). Chips are typically kept with this dirty PR coating until needed and then cleaned off by rinsing in HPLC-grade acetone, IPA, and Millipore-filtered water before spinning dry on a spincoater. We have also explored cleaning off PR by rinsing with DMSO (dimethyl sulfoxide) followed by water and, upon drying, 1 hour of UV/ozone cleaning to remove lingering contamination. Recent work by Kassandra Knapper and Erik Horak in our group indicates that particulates are sometimes left behind after this cleaning, and a prefurnace-style RCA cleaning greatly helps. The prefurnace clean is a sequence of sulfuric acid piranha, ammonium hydroxide piranha, and hydrochloric acid piranha performed so that wafers are flawlessly clean before going into high temperature furnaces.

At this point the resulting structure is called a microdisk resonator, and under certain conditions can possess ultrahigh Q-factors.[175] Typically, however, a final stochastic laser-induced reflow step is required to achieve ultrahigh Q-factors.[106]

3.2 CO_2 laser reflowing of toroid microresonators

The final step in production of toroidal microresonators is the surface-tension-induced reflowing of the rim of the toroid. A high power laser is used to selectively melt the overhanging silica to produce the desired structure. A CO_2 laser at 10.6 μm is strongly absorbed by SiO_2 (and to a lesser extent by Si). After approximately 1 ms the rim of the toroid has absorbed enough light to heat up to the melting point of ~ 1600 °C. The extremely high surface tension of molten silica draws the melted edge of the resonator into a spherical shape that is pinned on one side by the un-melted part of the resonator. The inner region of the resonator will not melt, because the silicon pillar and silicon substrate effectively wick away heat. The extent of reflow can be loosely controlled by the CO_2 laser power; increasing the power beyond that needed to melt the outer edges will cause the melted region to move progressively inwards towards the silicon region. With a large enough undercut, a spherical WGM resonator can be formed upon reflow.[176] It is also important that the CO_2 laser be focused onto the sample with a circular beam spot, as an elliptical/stigmated spot will cause unwanted asymmetry in the production of toroids.

Safety: The CO_2 laser is invisible and very powerful (10-20 W, continuous-wave). Most importantly, it can ignite organic material instantly and will burn skin on contact. Eye protection must be worn at all times by all users in the same room—plastic safety glasses suffice. Attempts are made to confine as much of the beam path as possible with polycarbonate panels or tubes. Polycarbonate, unlike most plastics, does not release toxic gases during combustion. Whenever the user is not ready to fire, the shutter on the laser (Synrad V40) is closed. This provides a physical barrier; closure of the shutter also acts as an electronic interlock on the laser. Where beam dumps are necessary (most notably on the incident reflection of the beamsplitter), firebricks are used.

Alignment: The CO_2 beam is first coaligned with a red diode laser mounted onto the output coupler of the CO_2 laser. Co-alignment involves an index card taped to a firebrick. First, the red beam spot is marked on the card. Next the CO_2 laser is fired at low power in a short burst. A small (< 1 cm) hole is burned right through the card. The alignment screws on the guide laser mount are then adjusted to line up the red beam and the burned hole. Then the firebrick is pushed further down the optical table and the process is repeated until the beams are coaligned across the whole table (~ 2m). The two beams can then be easily aligned conventionally. The beam must propagate for approximately 1m to reach a Gaussian cross-section according to the manufacturer. After propagating, the beam is focused by a lens onto the sample. A stereoscopic microscope and a beamsplitter is used to image the toroid chip to be reflowed. The first step in alignment is to make a small hole on a microscope coverslip. Reasonable parameters are 3.5 W for 100 ms with a spot size of ~ 400 μm. The hole melted partway through the coverslip can then be focused on with the microscope. The spot on the camera is marked on the monitor displaying the camera feed, and then the sample stage is translated until the microresonator to be reflowed is on the same spot on the camera. This alignment step with the cover slip should be performed every time the setup is used to account for day-to-day drift. I found that the position of the focusing lens is fairly sensitive, and a 1 cm translation along the optical axis can cause a large change in the reliability of reflow. A spot size that is too small will make the alignment very sensitive, and the user will end up producing a fair number of toroids that are only partially reflowed.

Optics: Because silica absorbs CO_2 laser light very strongly all transmissive optics must be made from an alternate material. The only widely-used alternative is ZnSe. Two optics are necessary; a focusing lens to focus the beam onto a toroid, and a beamsplitter to enable imaging with a conventional telescopic microscope. In the original setup a mixture of Ag-coated silica mirrors and Ag-coated silicon were used. Eventually the first turning mirror failed when the beam ablated all the way through the silver coating. As

soon as it hit the silica substrate the mirror lit up and then cracked from the thermal stress. Therefore, at the powers used here, the correct choice is Ag-coated silicon, although Au-coated copper is another good choice.

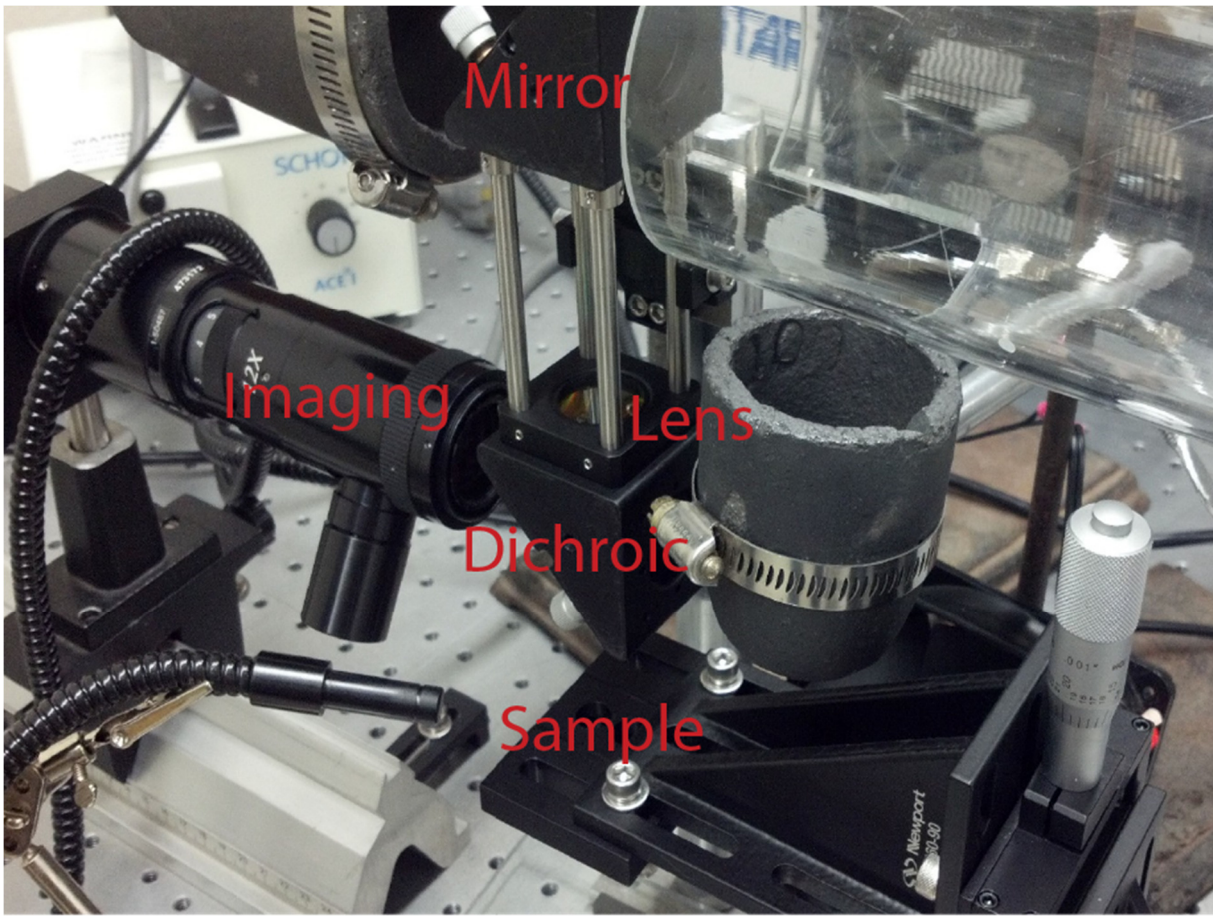

Figure 27: 1st-Generation CO_2 reflow setup.

The beam propagates horizontally about 1' above the table, enclosed in a safely-combustible polycarbonate pipe before being directed downwards by a mirror and focused onto the sample. Annotations (red text) mark the position of the turning mirror, focusing lens, dichroic beamsplitter, sample holder, and imaging microscope.

Imaging: The imaging microscope is a Navitar 1-50487 12x Zoom with a 2x lens. An early version of the setup (Figure 27) used a 0.5x lens with a much longer working distance. Although convenient to build, this setup made the toroids appear as small black dots, with no obvious change to mark whether reflow had been successful. This compounded the difficulties of initial testing to determine proper reflow conditions, which were made with insufficiently-undercut microdisks and a low power CO_2 laser. A later generation (Figure 28) used a Navitar 1-60350 6.5x Ultrazoom which provided much higher magnification. However, the high incidence angle of the microscope made the translation stage axes non-orthogonal to the image, a serious inconvenience. More importantly, the expensive apochromatic objective was placed extremely close to the beam path because of the short working distance. Since a single burst of the laser could easily damage the objective, the latest generation reverted to the 12x zoom. A change in sample mounting geometry enabled the use of a 2x lens adapter, increasing the magnification enough to clearly tell the extent and quality of reflow without endangering any optics (Figure 29). Wafer chips are mounted horizontally on a 3-axis translation stage with small pieces of double-sided tape. A fiber-coupled lamp is used for illumination, which works much better than flood illumination.

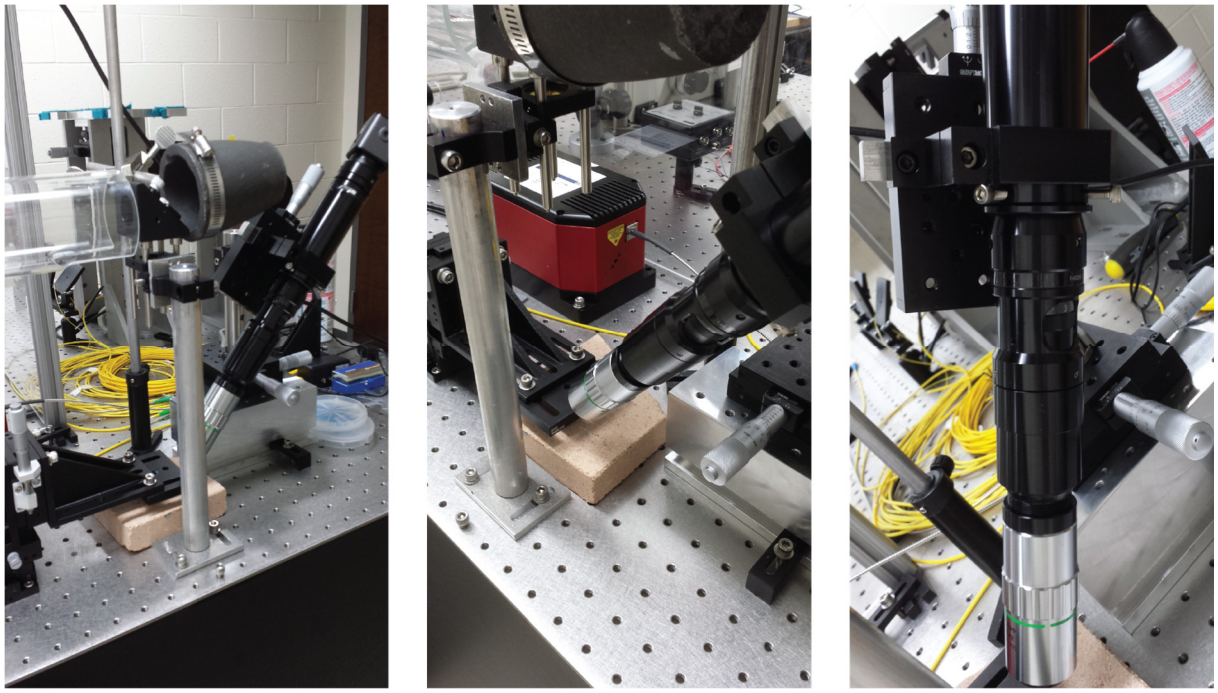

Figure 28 : 2nd-Generation CO_2 reflow setup

A high-magnification Navitar Ultrazoom microscope is mounted at a 60° angle to the table to bring it within imaging distance of the toroid chip. This angled mounting was inspired by the reflow setup of Jean-Baptiste Jager at the University of Grenoble. In this version the CO_2 beam propagates horizontally approximately 1’ off the table, before being reflected downwards.

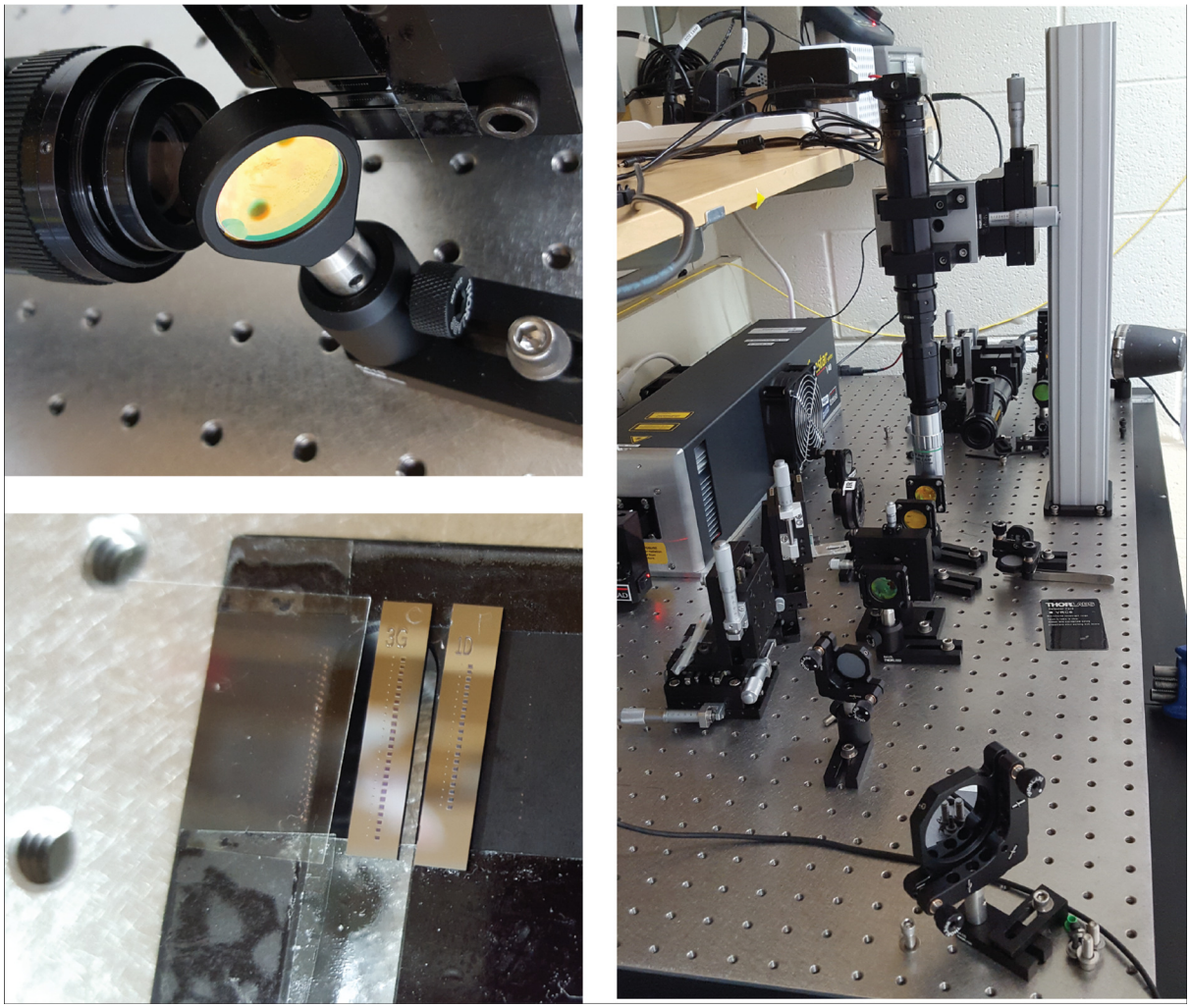

Figure 29: 3rd-Generation CO_2-laser-reflow setup.

A Navitar 12x zoom with a 2x adapter lens and a ZnSe dichroic are used for imaging. The CO_2 beam propagates horizontally approximately 4" above the table. Toroid chips are mounted with double-sided tape at the edges, next to a coverslip used for alignment of the beam. This setup provides plenty of magnification for determining reflow quality without requiring an expensive long-working-distance stereoscope/objective pair.

Troubleshooting: Partial reflow (where only part of the toroid rim is visibly reflowed) is an aiming problem (Figure 30e). The alignment of the CO_2 beam on the camera needs to be rechecked with a coverslip. If this is a recurring problem, it's possible that changing the focus between the cover slip and the toroid chip (which are different thicknesses) may cause the camera image to move laterally. This will occur if the

microscope is not mounted perfectly orthogonally to the optical path. Another solution is to increase the power by a few % of fullscale. This will increase the tolerance towards misalignment. However, increasing the power too far will cause sputtering of the silica as it overmelts (Figure 30d). Even higher powers will cause the toroid to shatter or melt into ruins (Figure 30a-c). The reflow duration does not seem to be important, although sub-ms exposure time leads to messy, incomplete reflow (Figure 30f). If the power needed to reflow has increased from day to day, this suggests that someone bumped the focusing lens or that the undercut of the microdisk resonators is less than is typical.

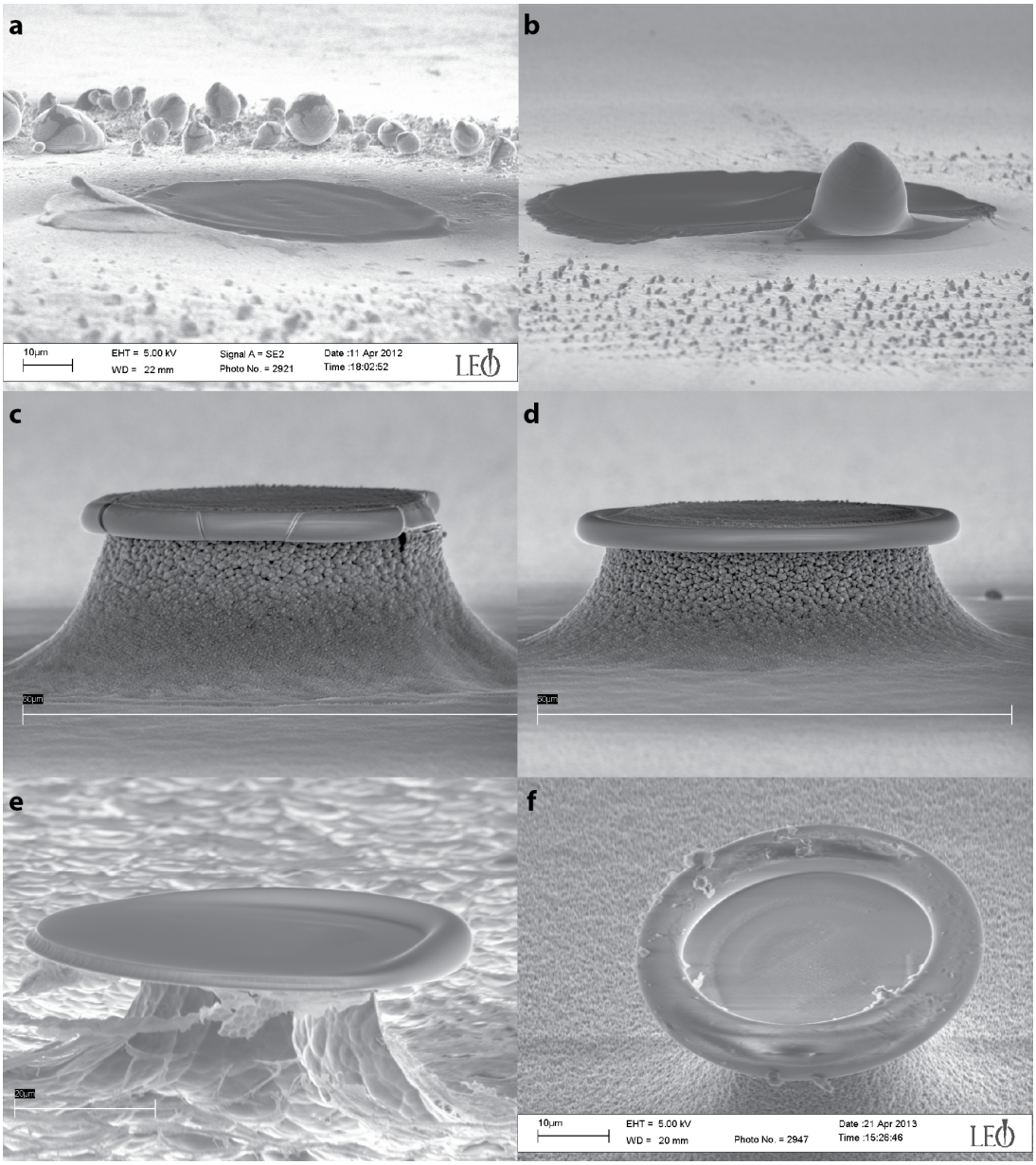

Figure 30: Gallery of reflow woe.

(a,b) SEM images of toroids reflowed with a 120 W CO_2 laser. At high enough fluence, the microdisk into a puddle of molten silica instead of a toroid. (c) At more moderate but still excessive power, the rim will successfully reflow but then fracture repeatedly (presumably during the cooling process). (d) At powers slightly elevated from the power needed to initiate reflow, the silicon regions will be clearly marked and experience their own form of thermal reflowing. Toroids with this morphology did not tend to have optimal Q-factors. (e) If the CO_2 laser power is too low, then aiming becomes difficult and toroids are frequently reflowed only on one side. Note the very short (~ µm) region over which reflow is arrested. (f) While toroids can be successfully reflowed over a wide range of timescales, 0.5 ms is too short. The seemingly "dirty" morphology of this toroid is entirely due to insufficient reflow.

3.3 Fabrication of tapers

Tapers are manufactured by heating a short section of optical fiber and pulling it to the desired final diameter.[153] This basic principle can be implemented in several different ways. Although a torch is most common,[177] ceramic heaters,[178] hydrofluoric acid etching,[179] and CO_2 lasers[180] as well as a recently-developed commercial system by 3SAE that employs a 3-electrode plasma source. We elected to use a hydrogen torch for its low cost and simplicity. Hydrogen is chosen because there is no possibility of depositing unburned hydrocarbons on the fiber during the tapering process.[157] A clean taper will have lower optical losses. Because of the optothermal effect in toroids coupled power must be kept low; efficient collection of light from the tapered region is critical to maintaining high signal to noise. Therefore a low-loss taper is desirable. In this context, a taper is referred to as adiabatic if light propagating through the fiber experiences no additional losses as it passes through the tapered region. Losses below 0.05% have been reported;[157] for our needs, losses of 30% or below are reasonable given the larger losses from bare fiber splices. Aside from fabrication problems, the main determining factor for transmission loss is that longer tapers are more adiabatic.[181]

Although a torch-based fiber pulling setup possess certain virtues, it does not tend to produce reproducible tapers. The flame tends to be a different size every time the hydrogen gas cylinder is opened. In practice, this means that a user might spend either 20 minutes or 2 days trying to pull a good taper. Recently Hoffman et al.[157] engineered a process for reliably producing ultrahigh transmission (99.95%), ultrathin optical fiber tapers using a hydrogen torch. This however requires a significant investment of resources, including a pair of imaging microscopes, several translation stages, and multiple mass flow controllers, and above all the time to carefully optimize the many parameters that can affect the taper pulling process. In the absence of this optimization, we focus on producing tapered fibers with relatively high adiabaticity (>75% transmission after tapering) and confirmed single-mode nature. The mode

structure of the tapered region can be monitored by launching a fixed-wavelength, single-mode laser through the tapered region and detected the transmitted light with a photodiode. Figure 31a shows a typical spectrum of the transmission through a fiber during the tapering process. Initially transmission is constant. At this point dopant has diffused and the entire tapered region is the core of a multimode fiber with air acting as cladding. After some time the transmission begins to oscillate with higher and higher frequency. This occurs as successive higher-order modes are stripped out by continued narrowing of the tapered region. This is equivalent to the V-number (Equation 2.4) of the waveguide decreasing. The oscillation results from changing interference between these higher order modes. Eventually interference stops when only a single mode, the LP_{00} mode, can propagate through the tapered region. This is the desired modal structure; it makes the taper act as a mode filter so that the WGM mode coupled into is the same mode that can couple back into the taper from the toroid, an advantage not found with prism coupling.[155] The removal of higher order modes from the taper during pulling is visible as chirp-like features in the short-time Fourier transform (Figure 31b).[157]

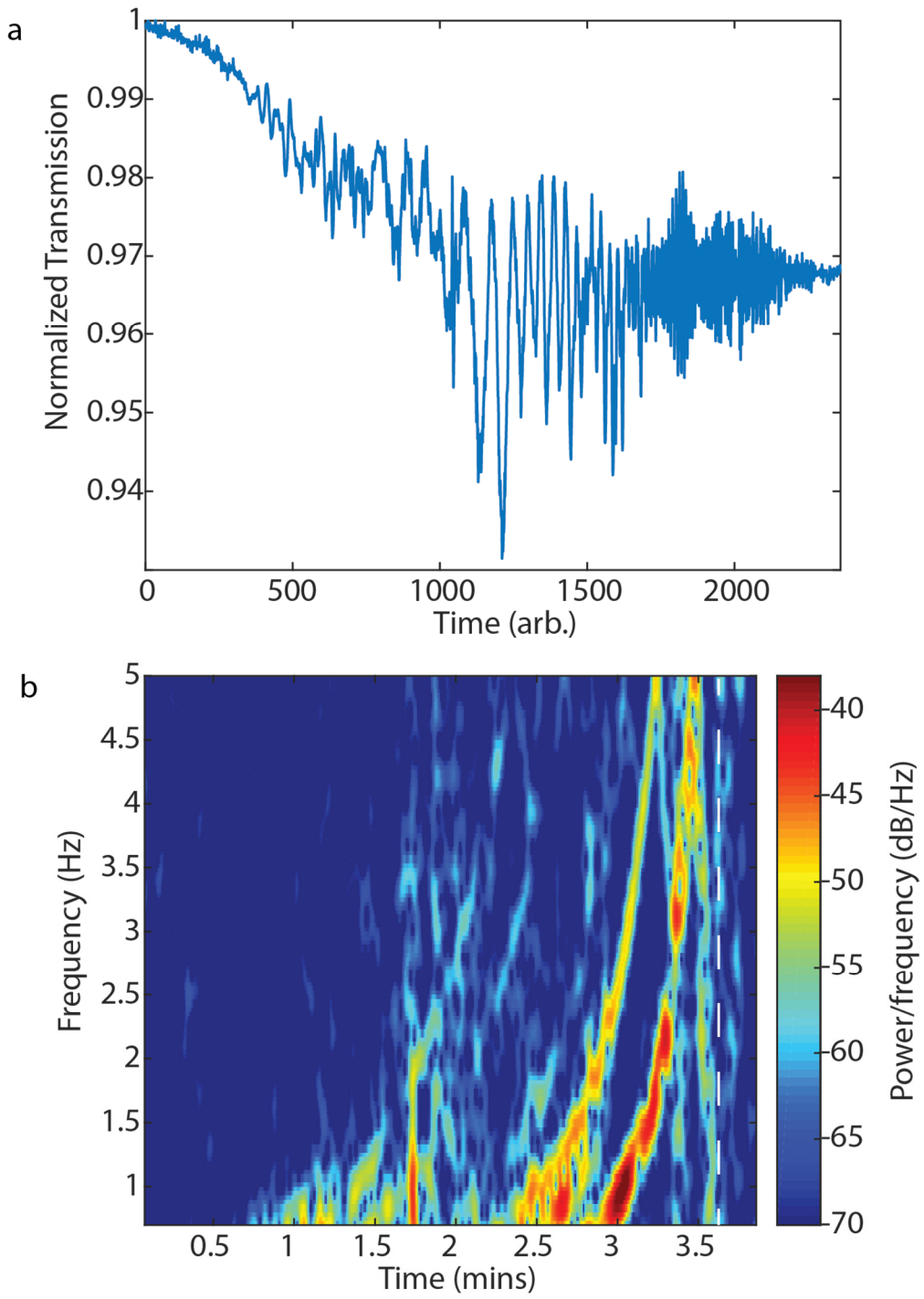

Figure 31: Transmission of light through the fiber during the tapering process.

(a) Light at constant wavelength (1.56 µm) is launched through the fiber and monitored with a power meter downstream of the tapered region. Oscillations are observed after pulling starts and until the fiber becomes singlemode and air-guided. (b) A short-time Fourier transform (Gabor transform) shows chirped oscillations as higher order modes are stripped out. When the fiber goes singlemode (vertical dashed line), there are no further oscillations.

The actual tapering process is straightforward. A picture of the rig in its original incarnation is shown in Figure 32. The torch heats a small (~ 1 cm) section of SMF-28e+ fiber (distributed by FIS, manufactured by Corning) from which the protective buffer layer has been stripped. The fiber is suspended between two holders that secure the fiber with rubber-tipped magnets (Thorlabs HFV001). Quick-release magnetic clamping (Thorlabs HFF003) was found to provide insufficient holding force, causing the fiber to slide along the holder rather than tapering. The two fiber holders are attached via a peg-and-socket joint to motorized translation stages (PT1-Z8) with 1" of travel and a minimum step size of 0.05 µm. After the torch is lit (using a lighter rather than a striker to avoid causing debris to rain onto the fiber), the two stages start moving simultaneously at a velocity of 40 µm/s. Although feedback for the taper's mode structure comes from launching a constant-wavelength 1550 nm laser and detecting with a fiber-coupled photodiode, the original version of the setup used a Navitar stereoscopic microscope with a 20x Mitutoyo long-working-distance objective. Visual inspection was useful for coarse alignment of the position of the torch relative to the fiber, and provides diagnostics about the potential problems with tapering. The thesis of E. W. Connolly provides more details[181] about diagnosing issues with torch-tapering of optical fibers. In our setup, the Navitar objective lens is shielded from the flame with a homemade blast shield, consisting of a holed microscope cover slide and custom barrel adapter bearing (Figure 32).

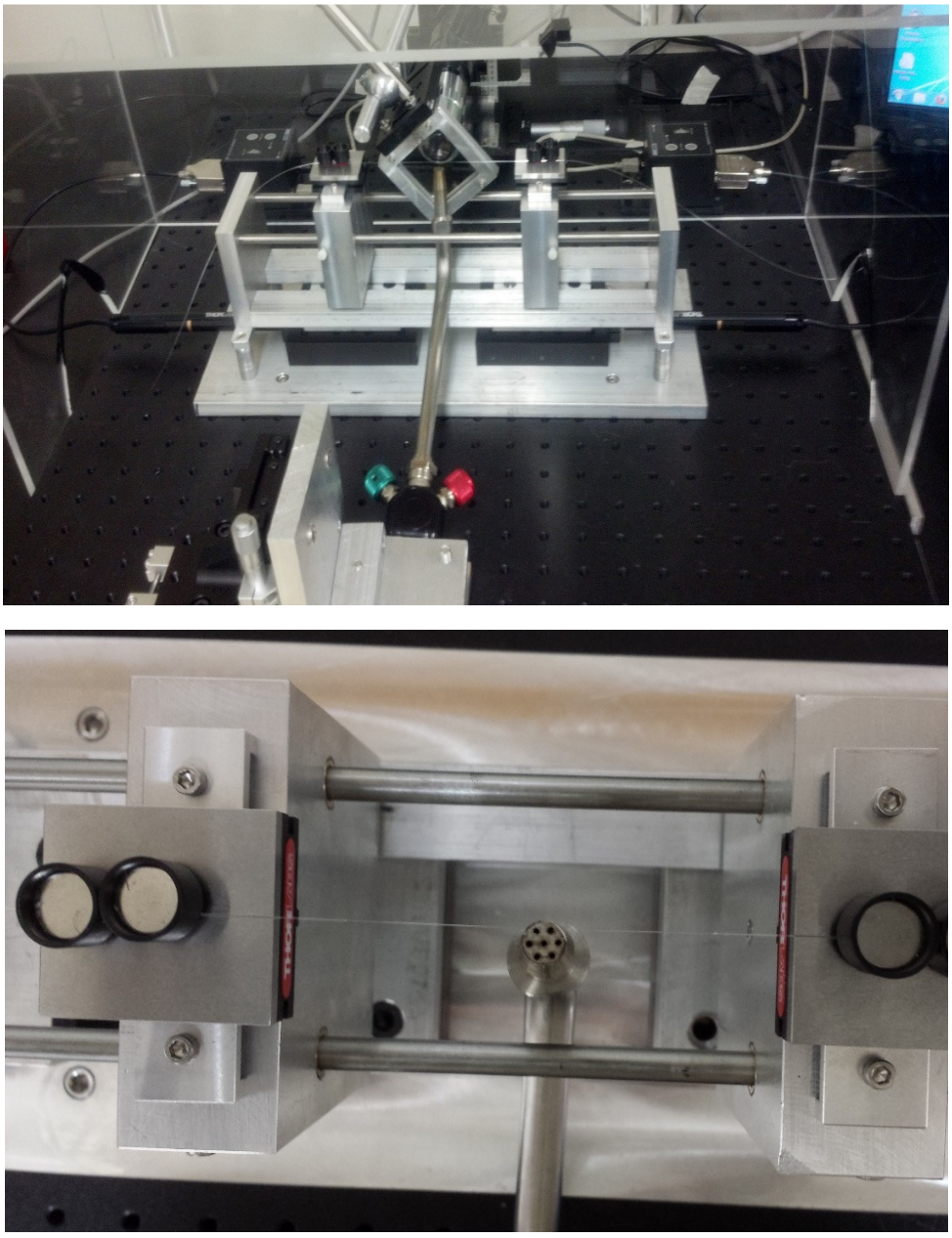

Figure 32: First-generation taper-pulling setup.

The imaging microscope is visible in the center with its blast shield attached. The position of the torch is controlled with a 3-axis translation stage. Two motorized stages (black) pull the shuttles (aluminum) apart through peg-and-socket joints (Figure 34). A pair of Nylon screws are used to gently lock the position of the shuttles after pulling and post-tensioning. The entire apparatus is partially shielded from dust with a PMMA box. The torch tip can be seen with the fiber near the edge of the torch. This is generally held to be the optimal position for the fiber.

Fibers are prepared for tapering by taking a length about 1m long from the fiber spool. The other end of the spool is connected to a 1550 nm laser, either through a bare fiber adapter or a permanently-connectorized terminal. A section of plastic buffer is stripped from a length of fiber using calibrated fiber strippers (Miller CFS-2 purchased from FIS) approximately 1-2 cm long. The stripped length should be as short as practical, since the buffer adds structural support, but long enough to avoid ignition of the buffer. Fire in the buffer is automatically quenched when it reaches the magnetic fiber clamps, fortunately. Remaining particles of buffer are removed from the fiber by taking several drops of HPLC-grade IPA or acetone and wetting a kimwipe, and then repeatedly wiping the wet kimwipe across the stripped region. Care is taken to avoid cleaning the fiber with the same part of the kimwipe each time. Recent work in producing ultrahigh transmission tapers[157] indicates that a more careful cleaning process helps increase the quality of tapers. The end of the fiber is also stripped and cleaned in a similar manner before being cleaved with a handheld fiber cleaver (FIS F16000). The leads on either end of the region to be tapered should be at least ~1m long in order to have enough to work with after the taper is manufactured. The tapered region is then clamped by the two bare fiber clamps, and positioned close to the torch. The optimal position tends to have the fiber not quite at the edge of the flame. Following the advice of Connolly,[181] we relax tension in the fiber by passing a heat gun over the stripped region for 10 seconds after placing it straight in the fiber clamps. This serves to release curvature in the fiber that results from it being stored on a circular spool. The hydrogen cylinder is then opened. H_2 passes through a flow regulator (Dwyer VFA-1-BV) and the regulator pressure is set to 7 PSI. The flow controller was never adjusted after initial setup. After lighting the torch, the pulling motors are started and data recording begins. When the tapering process is finished (either successfully or in failure) the pulling motors are stopped, then the torch is shut off. Placing the fiber under enough tension is critical—a loose taper causes fluctuations in the error signal, directly manifesting as noise, as well as making any experiments a frustrating and inefficient process. However, an over-tensioned taper will simply snap (and may not do so

immediately). The first version of the setup (Figure 32) had no means for adjusting the tension after tapers were removed from the torch setup. This meant that more than 90% of tapers broke while being moved to the resonator coupling setup. By breaking down the process of moving tapers between setups into a series of discrete actions and assessing when tapers snapped (Figure 33), I noticed that taper breaking could occur at a variety of different points. I then implemented a mechanism for increasing the taper's tension while mounted in the resonator coupling setup, allowing for safe movement of untensioned tapers.

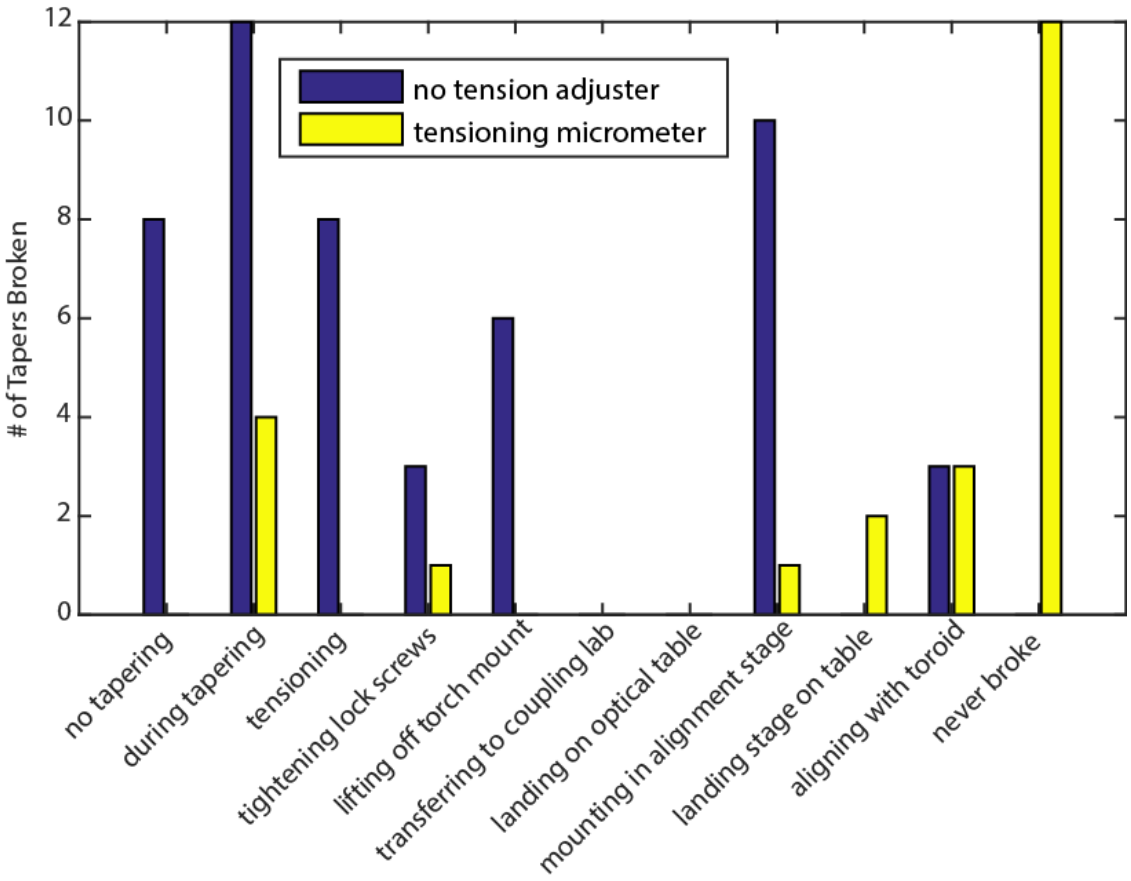

Figure 33 Taper breaking by action.

The process of making tapers and transferring them into the toroid coupling setup was broken down into 10 steps. The point at which each taper was broken was histogrammed before (blue) and after (yellow) adding a tensioning micrometer (visible at right in *Figure 34*) allowing for tapers to be transported under no tension.

In fact, while this tensioning mechanism worked, we have ultimately found that gluing tapers into place is more reliable. The jig that holds the fiber during the tapering process is too large and bulky to incorporate easily into the coupling setup. On the contrary, a much smaller U-shaped metal holder (Figure 34) is easier to handle. Once tensioning is finished, the U-shaped fiber holder is lowered on a 3-axis translation stage until it's in proximity to the taper. Glue (Quick Dry Tacky Glue, Aleene's) is applied to both sides of the U, and it is brought gently into contact with two ends of the taper. Care is taken to avoid getting glue on the tapered region of the fiber, as the transmission through the fiber will then swiftly drop towards zero. The glue takes up to 24 hours to fully dry, although it is fairly secure after 1 hour. This 1 hour wait is a reasonable time to wait before transferring to the coupling setup; the glue is firm enough to hold the fiber, but loose enough to leave it under-tensioned. After several hours, the fiber still drifts enough as the glue continues to dry that it cannot be used for experiments. Tapers made in this process can be used for several weeks, a lifetime limited by accumulation of particulates and by incidental breakage. In contrast to early analysis,[182] we find that non-cleanroom air can keep taper transmission from degrading even after a month if the taper is partially sheltered from dust.

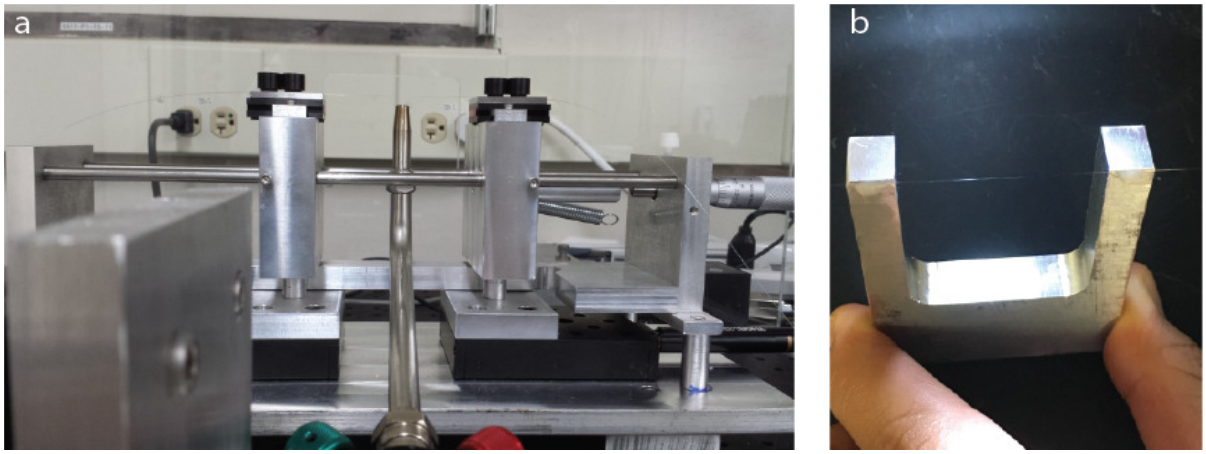

Figure 34: Modern taper-pulling setup.

(a) Two changes are prominent. One, the Navitar is not necessary once the setup is reasonably well aligned, feedback can be accomplished by pulling tapers and adjusting. Second, the tension of the pulled taper can be adjusted with the micrometer. (b) U-shaped metal holder with a taper glued into place. A normal size thumb and forefinger are shown for scale.

Chapter 4

4. Photothermal Background Mapping[1]

4.1 Abstract

We report a tuning method for ultrahigh-Quality factor toroidal optical microcavities capable of rapid modulation and resonance position control over multiple decades. A free-space laser is focused onto the resonator's silicon support pillar, rapidly heating the mode-containing silica. Microcavity photothermal response is spatially mapped. Resonance shift varies inversely with pillar diameter, reaching 1.5 x 10^5 fm/mW at 2 μm diameter, allowing switching with 1 μW control power. Larger pillar resonators can be modulated at high speeds (> 4 kHz). Heat flow simulations accurately model observed shifts. This versatile approach fulfills an outstanding need for fast, flexible control over toroid resonances.

4.2 Main text

Whispering-Gallery Mode (WGM) optical microcavities are rich experimental platforms for quantum optics,[69,120,183] photonics,[184-187] and sensing.[72,94,187-190] Ultrahigh-Quality factor (Q) toroidal optical microcavities[106] are particularly suited for nonlinear optics[61,70,191] and single particle detection,[90,192] due to their combination of extremely narrow linewidths and small mode volumes.[135] Sensing applications typically entail detection of analyte binding via small shifts in the resonance wavelength,[190,192] resonator

[1] The material in this chapter was originally published as: Heylman, K. D. & Goldsmith, R. H. Photothermal mapping and free-space laser tuning of toroidal optical microcavities. *Appl Phys Lett* **103** (2013).

Q-factor,[86,193] or mode splitting.[104] One advantage of the toroidal geometry is the simplified mode structure relative to other microresonator geometries, which leads to widely separated resonances. However, the high finesse (10^6) presents a significant experimental difficulty. The absolute resonant wavelengths are determined by minor variations in the fabrication conditions. In particular, laser-induced reflow, a crucial fabrication step, relies upon a runaway thermal process, although larger diameter toroids have been produced without this step.[175] Typically, tunable external-cavity diode lasers are used to couple light into the resonator, as they possess narrow linewidth and wavelength tunability greater than the resonator's free spectral range (FSR). However, the need for expensive tunable light sources impedes applications that require low-cost fabrication or integration into massively parallel device architecture. Exploration of emergent properties of multi-resonator architectures,[194-196] would benefit from the ability to rapidly and independently control multiple toroid resonance wavelengths. More broadly, a convenient method of tuning toroid resonances would enable these microcavities to be incorporated into a wider range of optoelectronic applications.

Much progress has been made in controlling absolute resonance position in WGM microcavities. These efforts include chemical etching[147] and UV irradiation,[197] though these processes are irreversible, and have not been demonstrated with microtoroids. The entire silicon chip can be heated,[139] although this approach cannot achieve independent control of multiple toroids and is limited by slow switching speeds. A photochromic thin film can be optically pumped to photothermally heat the resonator,[198] but is slowed by the recovery time of the molecule's ground state (~ 11 s). Similarly, a highly absorbing polymer film can be applied to a microsphere and optically pumped, but with limited tuning range (25 pm) and speed (165 ms).[199] Toroids can be individually functionalized with a heating element,[148] but this approach increases fabrication complexity. A second fiber-coupled light source can be used to photothermally tune the resonance,[149] but requires high powers due to the transparency of fused silica at the pump wavelength and is consequently limited to a narrow tuning range. The variety of innovative techniques that have been

developed for resonance tuning of optical microcavities demonstrates the importance of the problem as well as the difficulties inherent in solving it.

Here we demonstrate tuning of the resonance of a toroid microcavity by modulating the position and intensity of a free-space visible, CW pump laser whose output has been focused onto the resonator. By varying the power of the pump laser, a tuning ratio of 1.5 x 10^5 fm/mW is achieved on a toroid with a 2 μm diameter silicon pillar. A fraction of the heat generated from the silicon absorption is transferred to the silica, redshifting the resonant frequencies due to the positive thermo-optic coefficient of silica. For comparison, use of two fiber-coupled beams as described above attained a tuning ratio of 250 fm/mW.[149] Previously, a focused free-space pump has been used to continuously tune photonic crystal microcavities with Q near 10^4 and the spatial dependence was explored,[195] though the time dependence was not examined. Ultra-high Q toroidal microcavities possess an intricate geometry, and spatial mapping of the photothermal shifts is a primary focus of this current work.

Toroidal microcavities are fabricated via literature procedures[106,176] (see supplementary material to the manuscript for fabrication details). Two pillar diameters were constructed (termed “standard” and “re-etched”), distinguished by an optional post-reflow etch.[194] An external cavity diode laser (New Focus, 1560 nm) is coupled into toroids via tapered optical fiber.[106] Typical coupled powers range from 40-150 nW to avoid nonlinear thermal effects.[140,200] A fixed-wavelength CW diode laser (Blue Sky Research, 640 nm) is focused to a 2 μm diameter spot with a 40x 0.75 NA microscope objective. A gimbal-mounted mirror positioned at an optical plane conjugate to the back aperture of the objective is used to control the position of the laser spot in the toroid plane.

Resonance shift of the toroid is spatially mapped by scanning the pump beam over the resonator and surrounding area, Figure 35. The laser spot is small compared to the size of the resonator, Figure 37 inset, enabling a high-resolution map. The maximum shift is closely associated with illuminating the silicon

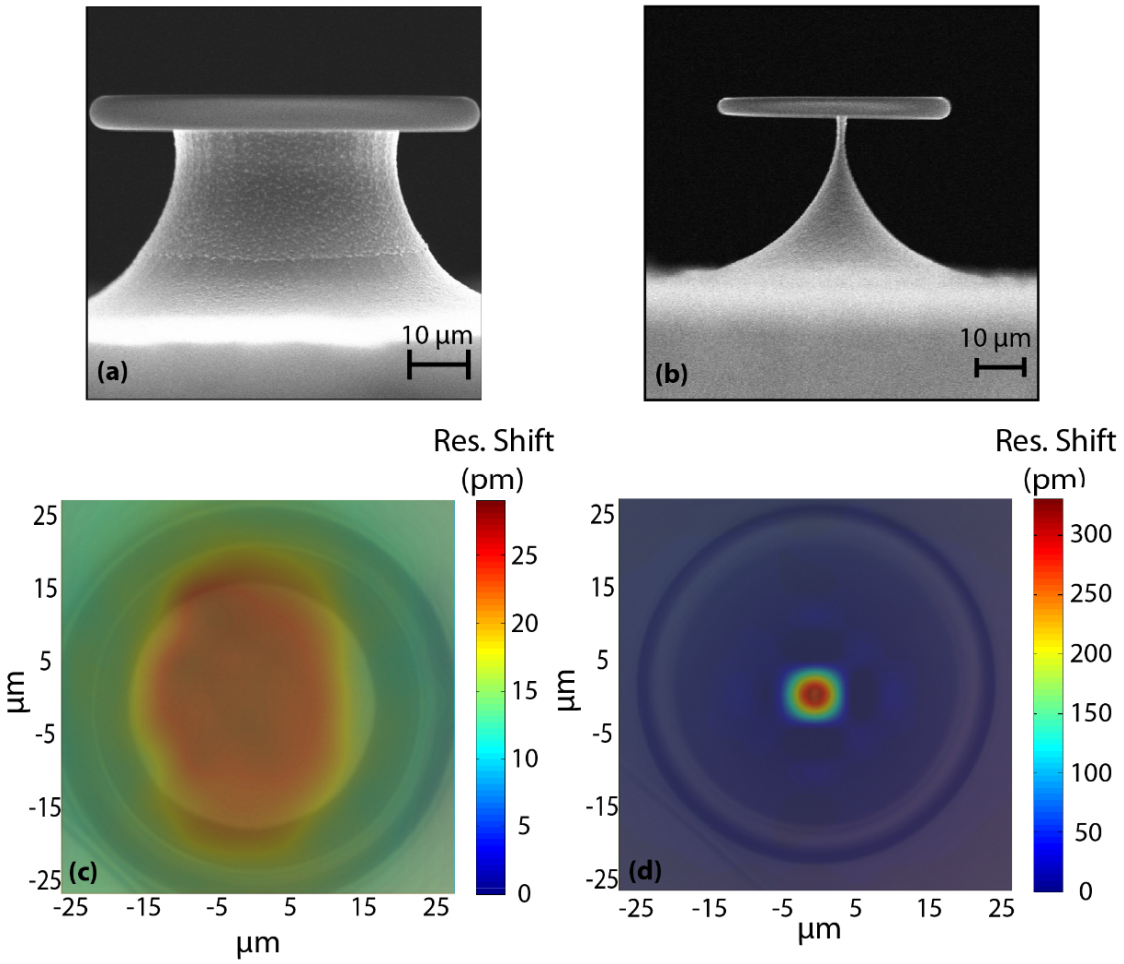

Figure 35: SEM images (a,b) and photothermal maps (c,d) of the spatial dependence of resonance shift for a standard (a,c) and re-etched (b,d) toroid.

Each map is constructed from 13x13 grid with 4 µm increment, where each shift at constant (4.2 mW absorbed) pump power is referenced to the shift with no external pump. An optical micrograph is superimposed on the map, showing the correlation between maximum shift and the silicon pillar.

pillar where the shift is essentially constant with position. The resonance shift, 3200 fm/mW pump power, is approximately five times larger on the silicon pillar than when the spot position is well-separated (80 µm) from the toroid. Decreasing the size of the toroid support pillar with an additional etching step (re-etched toroid) significantly amplifies the effect (Figure 35, Figure 36) and the slope rises to 1.5 x 10^5 fm/mW, Figure 37, without compromising the Q-factor. The high power density (10^8-10^9 W/cm^3) in the

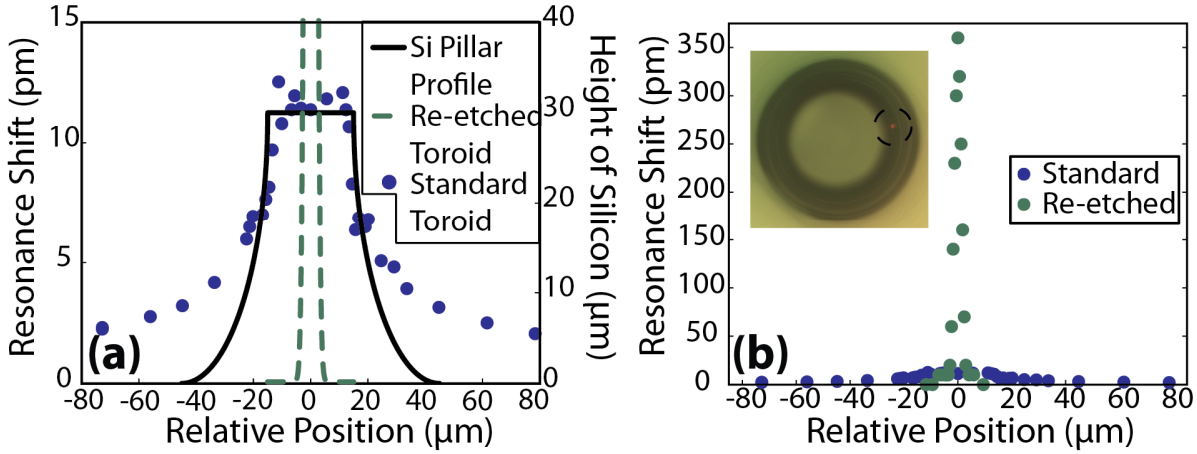

Figure 36: Photothermal linescans of a standard and re-etched toroid on two scales (a,b).

The laser spot is scanned laterally across the center of the toroid at constant power (4.2 mW absorbed) and the resonance shift measured as a function of laser position. The profile of the silicon pillar is shown for the standard toroid (a). The greater sensitivity of the re-etched toroid is conspicuous in (b). (Inset) Optical micrograph taken during a linescan, with the pump laser spot marked.

heated volume drives the high sensitivity of this tuning method. The increased sensitivity of the re-etched toroid is attributed to the reduced heat capacity of the smaller silicon pillar, leading to a greater temperature increase at the silicon-silica interface, and consequently greater equilibrium temperature at the mode-carrying silica.

To understand the relevant heat flows, numerical simulations were performed in COMSOL Multiphysics, Figure 38 (see supplementary material to the manuscript for discussion of the model parameters). The redshift in resonance wavelength ($\Delta\lambda$) as a function of the change in temperature is given by,

$$\lambda_T - \lambda_0 = \Delta\lambda = \frac{\lambda_0}{n_0} \times \frac{dn}{dT}(T) \times (T - T_0) \qquad 4.1$$

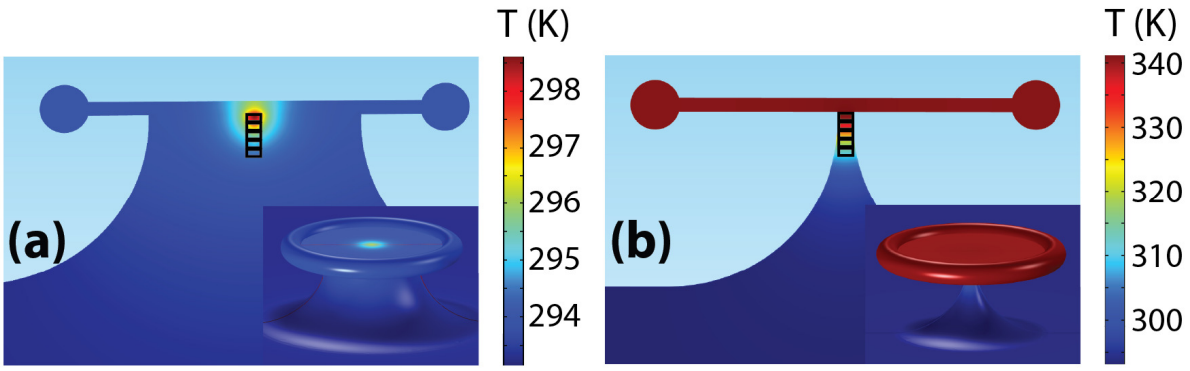

Figure 38: Simulations of the temperature profile of the toroid upon excitation at its center for a standard toroid (a) and re-etched toroid (b).

The heating source is shown in black wireframe (see Appendix 1 of the manuscript for details of the thermal modelling). Absorbed power is 4.2 mW in both simulations.

with $\lambda_0 = 1.566\,\mu m, n_0 = 1.444,$ and $\frac{dn}{dT}(T) = 2.6 \times 10^{-8}\,\mathrm{K}^{-2} \times \mathrm{T} + 7.5 \times 10^{-7}\,\mathrm{K}^{-1}$, an expression

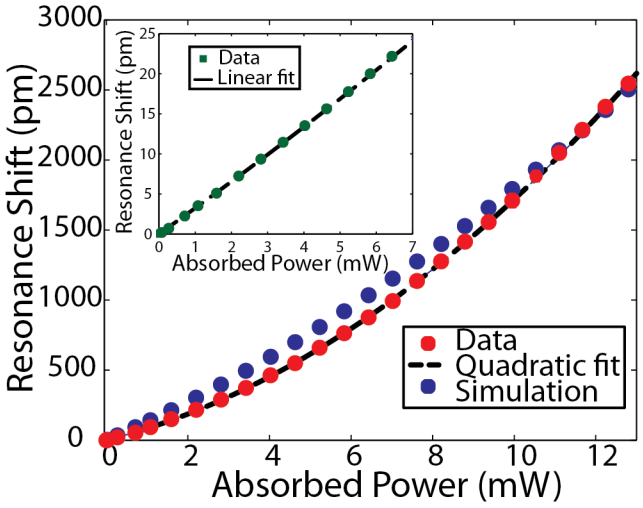

Figure 37: Power dependence of photothermal shift from silicon pillar.

The shift is seen to be quadratic for a re-etched toroid and to extend to over half the FSR of the resonator. Simulations capture the quadratic dependence and were performed by calculating equilibrium temperature at the silica rim from the measured pump power and extrapolating resonance shift with Equation 4.1. Error bars are present but too small to see on this scale. (Inset) A standard toroid shows a shallower slope and is linear over the range examined.

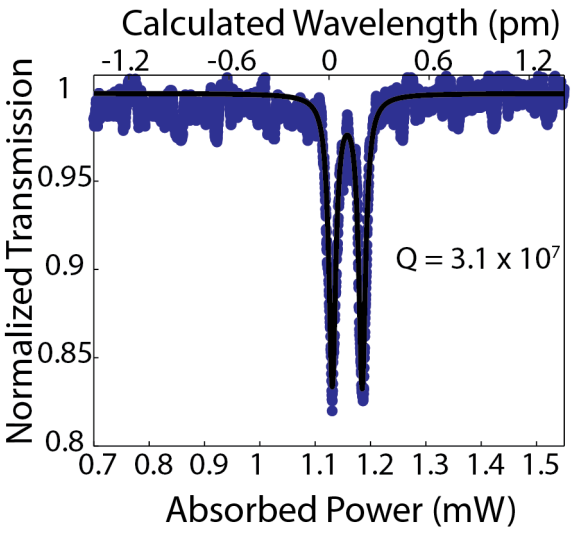

Figure 39: Scan of toroid resonance via photothermal heating and Lorentzian fit.

The probe wavelength is fixed at 1566.93 nm, while the pump laser power is scanned with a triangular waveform. The wavelength is calculated from the measured temperature dependence of the toroid resonance (3200 fm/mW).

derived from linear extrapolation of data from Leviton. [112] The model accurately matches the experimental power dependence, Figure 37. Over a tuning range of 0-25 pm for a standard toroid the tuning curve is linear, Figure 37 inset, in agreement with Armani et al.[148], with a slope of 9.2 pm/K. At the much greater shifts possible with a re-etched toroid, the shift appears quadratic in both simulations and experiments (consistent with observations in Ma et al.[57]) due to the temperature dependence of the thermo-optic coefficient ($\frac{dn}{dT}$). At 12.7 mW of pump laser power, the silica heats up to 443 K. At larger pump powers (> 2 mW absorbed), the re-etched toroid resonances exhibited minor fluctuations consistent with small intensity shifts in the pump laser (see supplementary material to the manuscript for more details).

The strengths of this approach are versatility of control and sensitivity. We demonstrate continuous and convenient tuning of resonance position over more than one half of the resonator's FSR (Figure 37), limited by the power of the pump laser. Alternatively, as little as 1 µW shifts the resonance by one full width at half maximum (FWHM), a low-power switch. As a demonstration of the elimination

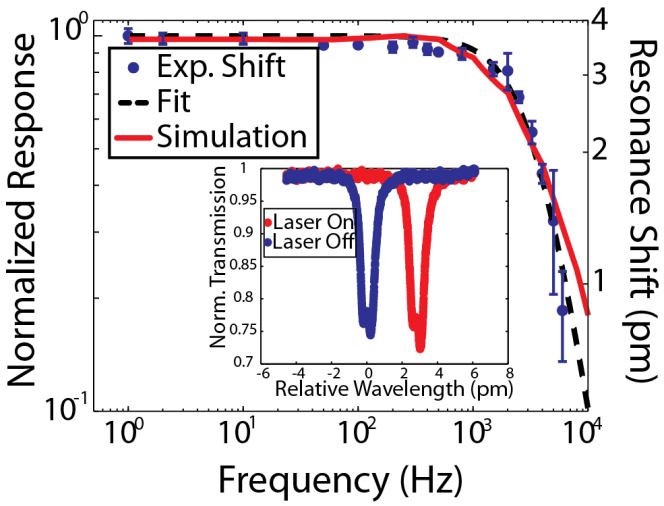

Figure 40: Frequency response of a standard toroid during pump beam modulation (circles). The toroid has a cutoff frequency of 4200 Hz, and is fit with exponential time dependence (dashed line, $1\text{-}e^{(-t/\tau)}$). Simulation (solid line) predicts a cutoff frequency of 5000 Hz. (Inset), scan of resonance with pump laser off (black) and on (grey).

of the need for a tunable probe, we show that ultrahigh-Q factors are observed by photothermally tuning the resonance and probing at a fixed wavelength, Figure 39. The splitting of the resonance is caused by backscatter-induced degeneracy lifting of the clockwise and counterclockwise WGM, and is routinely observed in toroidal microcavities.[135] Control over multiple orders of magnitude of spectral position is a highly useful experimental parameter.

The timescale of the resonance shift, a critical parameter for optical switching applications, was measured by modulating the pump beam with a square wave while recording the relative position of the modulated and un-modulated resonance. The maximum wavelength shift is set (by controlling the pump intensity) to 2.8 pm, ~30 linewidths for Q = 1.5 x 10^7. A shift of only several linewidths is sufficient for switching. When the time interval falls below the thermal equilibration time of the toroid the shift decreases. Figure 40shows a modified Bode magnitude plot of a standard toroid demonstrating a cutoff frequency of 4200 Hz, over an order of magnitude faster than previously reported thermal control

mechanisms.[148] Time-dependent simulations predict a comparable cutoff of 5000 Hz on a standard toroid. The re-etched toroid has a lower cutoff frequency of 400 Hz, likely due to the larger path length for heat to travel through the silica between the silicon pillar and the silica rim.

In summary, a highly versatile method of tuning the resonance position of toroidal microcavities is demonstrated. A visible, fixed-wavelength laser at modest power is used to reproducibly shift the resonance by a few to more than 10,000 times the FWHM. This technique places few requirements on the wavelength, linewidth, or tunability of the pump beam. Re-etching the silicon pillar greatly increases the sensitivity without compromising the ultrahigh-Q. The re-etched toroid can be continuously tuned over half the FSR, with fast modulation times. These toroids can also be switched over one FWHM with approximately 1 μW of pump beam power, an important consideration for optical processing. Critically, this method reduces the need for expensive tunable probe sources, as now a simple and inexpensive pump laser can be used to shift the resonance of a microcavity to be resonant with a fixed wavelength probe.

In future experiments, the linking of pump intensity modulation with an error signal from the fixed wavelength probe beam will allow locking the resonator to the probe beam, enabling prolonged stable coupling resistant to ambient temperature fluctuations.[169] Looking forward, this method is conducive for control of ultrahigh-Q wedge-resonators which do not require the highly stochastic reflow step.[175] This method is also capable of being used for simultaneous control of individual members of large arrays of resonators through use of inexpensive on-chip light sources or spatial light modulators.[201] Improved control strategies will enable exciting and novel applications of on-chip microresonators.

Chapter 5

5. Photothermal Mapping of MWCNTS[2]

5.1 Abstract

A powerful new paradigm for single-particle microscopy on non-luminescent targets is reported using ultra-high Quality factor optical microresonators as the critical detecting element. The approach is photothermal in nature, as the microresonators are used to detect heat dissipated from individual photoexcited nano-objects. The method potentially satisfies an outstanding need for single-particle microscopy on non-luminescent objects of increasingly smaller absorption cross-section. Simultaneously, our approach couples the sensitivity of label-free detection using optical microresonators with a means of deriving chemical information on the target species, a significant benefit. As a demonstration, individual non-photoluminescent multi-walled carbon nanotubes are spatially mapped and the per-atom absorption cross-section is determined. Finite-element simulations are employed to model the relevant thermal processes and elucidate the sensing mechanism. Finally, a direct pathway to the extension of this new technique to molecules is laid out, leading to a potent new method of performing measurements on individual molecules.

[2] The material in this chapter was originally published as: Heylman, K. D., Knapper, K. A. & Goldsmith, R. H. Photothermal Microscopy of Nonluminescent Single Particles Enabled by Optical Microresonators. *J Phys Chem Lett* **5**, 1917-1923 (2014).

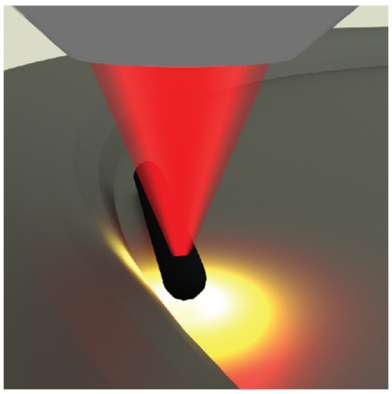

KEYWORDS. Optical Microresonators, Photothermal, Single Particle Spectroscopy, Carbon Nanotube, Single Particle Imaging

5.2 Main text

Measurements on individual particles and molecules are critical to the elucidation of nanoscale behavior. These types of measurements, whether optical, electrical, or scanning probe, are uniquely capable of exposing the tremendous heterogeneity and unsynchronized dynamics that exist at the nanoscale, behavior that directly governs emergent functional macroscopic properties. Optical measurements on individual particles are particularly adept at discerning electronic structure, correlating electronic structure with particle morphology and microenvironment, and doing so in a non-contact experimental geometry. For example, single-particle optical measurements have enabled significant progress in understanding the behavior of nanoparticles,[202-208] carbon nanotubes,[209,210] and conductive polymers.[211-214] The majority of optical single-particle measurements rely on photoluminescence from the target nano-object, an approach that allows high sensitivity and low background.[28] However, if the target system is non-luminescent, it is completely opaque to most single-particle optical probes. Consequently, there is an outstanding need to develop new single-particle probes that do not rely on photoluminescence, can operate at room temperature, and can allow single-molecule sensitivity.

This letter describes a new paradigm for single-particle and ultimately single-molecule microscopy that takes advantage of the tremendous sensitivity of ultra-high Quality factor (Q) optical microresonators. Ultra-high Q optical microresonators are extremely sensitive to small perturbations in their microenvironment. The propagating whispering gallery mode makes many repeated interactions with the microresonator surface, amplifying the effect of small changes in the local index of refraction. Consequently, optical microresonators have emerged as important diagnostic tools,[189,215-217] and enabled single-particle detection.[72,86,104] In the typical experimental sensing geometry, the binding of a single analyte molecule or particle results in a fractional spectral shift of the resonance of the microresonator. Detection of single proteins and viruses by microresonators has been achieved via the induced offset in resonance wavelength caused by the presence of a polarizable object interacting with the propagating optical mode.[72,86,218-220] However, this geometry offers little *chemical* information about the bound species. Some chemical information may be obtained by selective functionalization of the microresonator surface,[189,216] but there is a critical need for more detailed optical characterization of the adsorbed species. Such an advance would significantly amplify the power and utility of microresonator sensing.

In this work we leverage the high intrinsic sensitivity of ultra-high Q optical microresonators as the critical detection element for photothermal absorption microscopy. In such an experimental geometry, the goal is not the *detection* of non-chromophoric analytes as above,[72,90,94,220] but the *spectral measurement* of non-photoluminescent chromophoric target nano-objects via light absorption. This new approach has the potential to simultaneously provide spectral information for sensing applications, as well as offer a new tool for observing single-molecule dynamics without fluorescence. As a test system, individual multi-walled carbon nanotubes (MWCNTs) are pumped with a focused free-space laser. The local increase in temperature caused by heat dissipation from the absorbing nanotube redshifts the resonant wavelength of the microresonator due to the positive thermo-optic coefficient of silica.[113] A resonance shift of almost 40 linewidths is observed at modest pump power ($Q = 3.3 \times 10^6$, $I_{pump} = 9 \times 10^4$

W/cm^2). Photothermal shifts as a function of excitation beam position and input polarization are used to image the nanotubes and explore their electronic transitions.

A number of other approaches have been used to image or spectrally analyze individual absorbing nano-objects without photoemission, including detection of Rayleigh scattering,[209] spatial modulation,[221] balanced detection,[222] Coherent Anti-Stokes Raman scattering,[223] detection of conductance,[224] high-frequency signal modulation from ground state depletion,[38] and photothermal detection.[20,21,52,225] The first optical detection of individual molecules employed frequency modulation to enable detection via direct absorption, but required cryogenic temperatures.[3] In a particularly successful implementation of photothermal detection, scattering is used as a readout of the local temperature shift.[21,52] This approach enabled single-molecule detection[51] as well as insights into the electronic structure of nanotubes[226] and nanoparticles.[227] However, scattering is an inherently low cross-section process for small objects, limiting the ultimate sensitivity. A more responsive probe of local temperature could allow substantial increases to the sensitivity of non-luminescent single-particle and single-molecule measurements, ultimately enabling high-resolution spectroscopy of such objects and time-resolved fast dynamics.

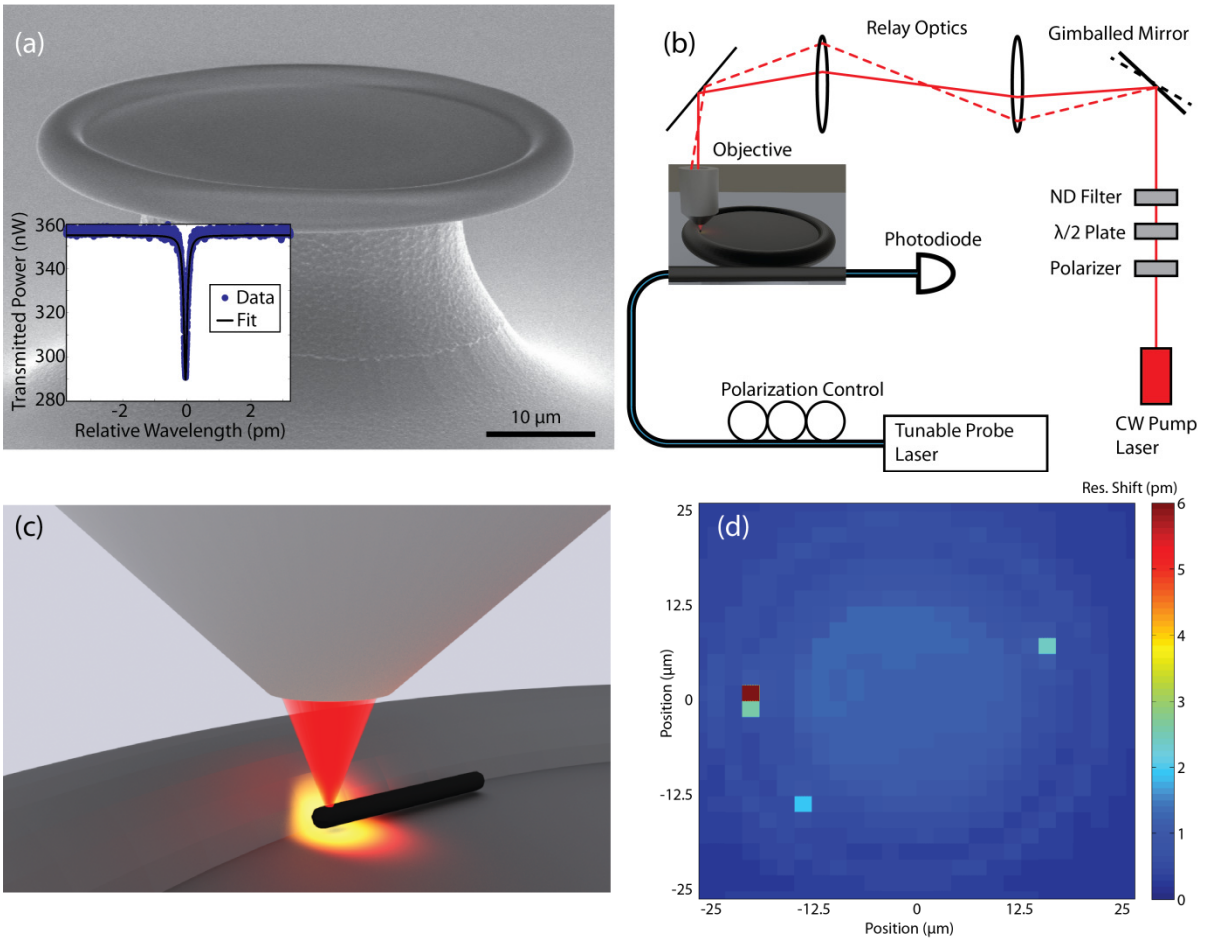

Figure 41: Photothermal detection of non-luminescent objects using optical microresonators.

(a) SEM of a toroidal microresonator. Inset: Resonance scan of a toroidal microresonator. Fitted Q-factor is 1.3 x 10^7 (pre-deposition). (b) Schematic of optical path of pump laser (red) and probe laser (blue/black). Abbreviations: ND = Neutral density; CW = Continuous-wave. (c) Rendering (Blender) of the photothermally-pumped nanotube on a microresonator. (d) Coarse photothermal map of an entire resonator, showing three distinct nanotube signals. The photothermal background from the silicon substrate is faintly visible.

Toroidal microresonators, Figure 41a, are fabricated by lithographically defining silica discs on a silicon substrate[106] and undercutting the silica with an isotropic SF_6/Ar etch.[176] This procedure is followed by a laser-induced reflow step.[106] The details of our fabrication process have been reported.[132] Toroidal optical microresonators are used due to their unique combination of ultra-narrow linewidths[106] and small

mode volumes.[135] Probe light is coupled into the microresonator via a tapered optical fiber controlled by a 3-axis piezopositioner (Attocube ECS 3030), Figure 41b. Two orthogonal microscopes are used for alignment (Navitar Ultrazoom) and excitation beam delivery (Nikon FN1). A fiber-coupled tunable diode laser (New Focus, Velocity, 1560 nm) is used to probe the resonant wavelengths. The fiber-coupled probe power was kept low (~250 nW) to avoid thermal broadening of the toroid resonance.[200] Nanotubes are photoexcited with a pump beam (Blue Sky Research, 640 nm) focused by a microscope objective (60x, 0.95 NA, Nikon) to a near-diffraction-limited spot (780 nm $1/e^2$ diameter). A gimbal-mounted mirror placed at a plane conjugate to the objective back aperture is used to control the beam position on the resonator,[132] Figure 41b. A polarizer and half-wave plate are used to adjust the linear polarization angle at the target nano-object. Additional experimental details are available in the Supporting Information of the manuscript.

Photothermal images at variable resolution are taken by scanning the pump beam across the top surface of the resonator, Figure 41c. Wide-area maps (50 μm x 50 μm) at low resolution (2 μm/pixel) are used to locate individual absorbers, Figure 41d. High-resolution maps (3 μm x 3 μm at 250 nm/pixel) are taken to define the shape of the nanotube, Figure 42. These maps highlight the utility of using a whispering gallery mode-coupled probe beam while performing excitation with a scanning free-space pump beam. At every pixel the resonance wavelength is measured with the pump beam off and on, allowing for background subtraction, and five successive scans are averaged at each pixel. Scanning Electron Micrographs (SEMs) taken before and after photothermal experiments confirmed that the nanotubes were not significantly altered by the measurement and allowed correlation between the observed photothermal map and the physical dimensions, Figure 43

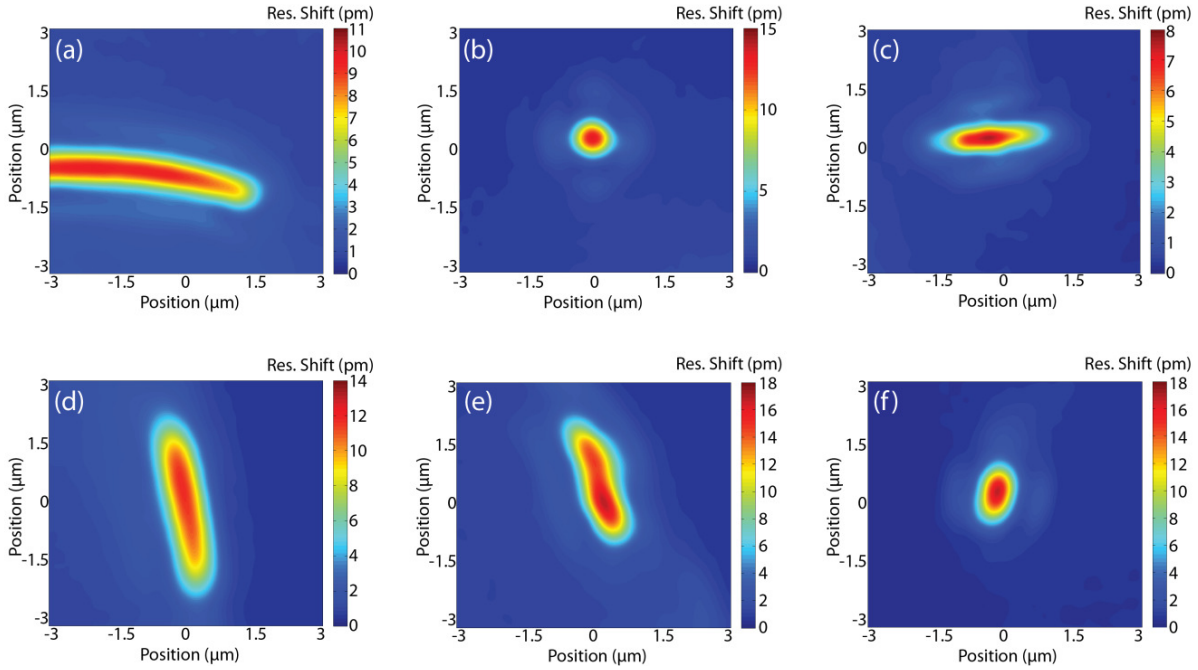

Figure 42: Gallery of photothermal maps of MWCNTs.

(a)-(f) are representative samples of photothermal maps taken on separate nanotubes under identical conditions. Incident power was 440 μW, resolution = 250 nm/pixel, each pixel is an average of five scans.

MWCNTs (Sigma, >90% carbon basis) were dissolved in N-methyl pyrrolidone (Sigma) with ultrasonication at a concentration of 60 μg/mL without further purification and deposited onto resonator wafer chips by spincoating. Microresonators were plasma activated immediately prior to spincoating (O_2 plasma, 250 W, 5 min) to enhance adhesion. High Q factors were largely maintained ($Q > 2 \times 10^6$) after nanotube deposition ($Q \sim 10^7$ pre-deposition). Nanotubes typically stick to the inside of the silica rim during deposition, Figure 43b, and are able to substantially thermally influence the propagating mode after photoexcitation, Figure 44. On the other hand, the nanotubes do not strongly influence the mode via direct absorption, as confirmed by the small reduction in Q and shown in Figure 44c. Both coarse and high-resolution photothermal maps are acquired in 7 minutes, although the thermal equilibration time of

the microresonator (~250 μs)[132] could allow for much faster acquisition. Multiple molecules or particles on a single resonator can be individually spatially selected and probed, allowing for faster throughput, though more dense surface coverage will ultimately compromise the resonator quality factor. Other techniques used to enhance sensitivity in nanoparticle-resonator binding studies, such as Pound-Drever-Hall locking,[161,169,228] backscattered light detection,[95] and all-fiber interferometry[90] could be used to improve the sensitivity.

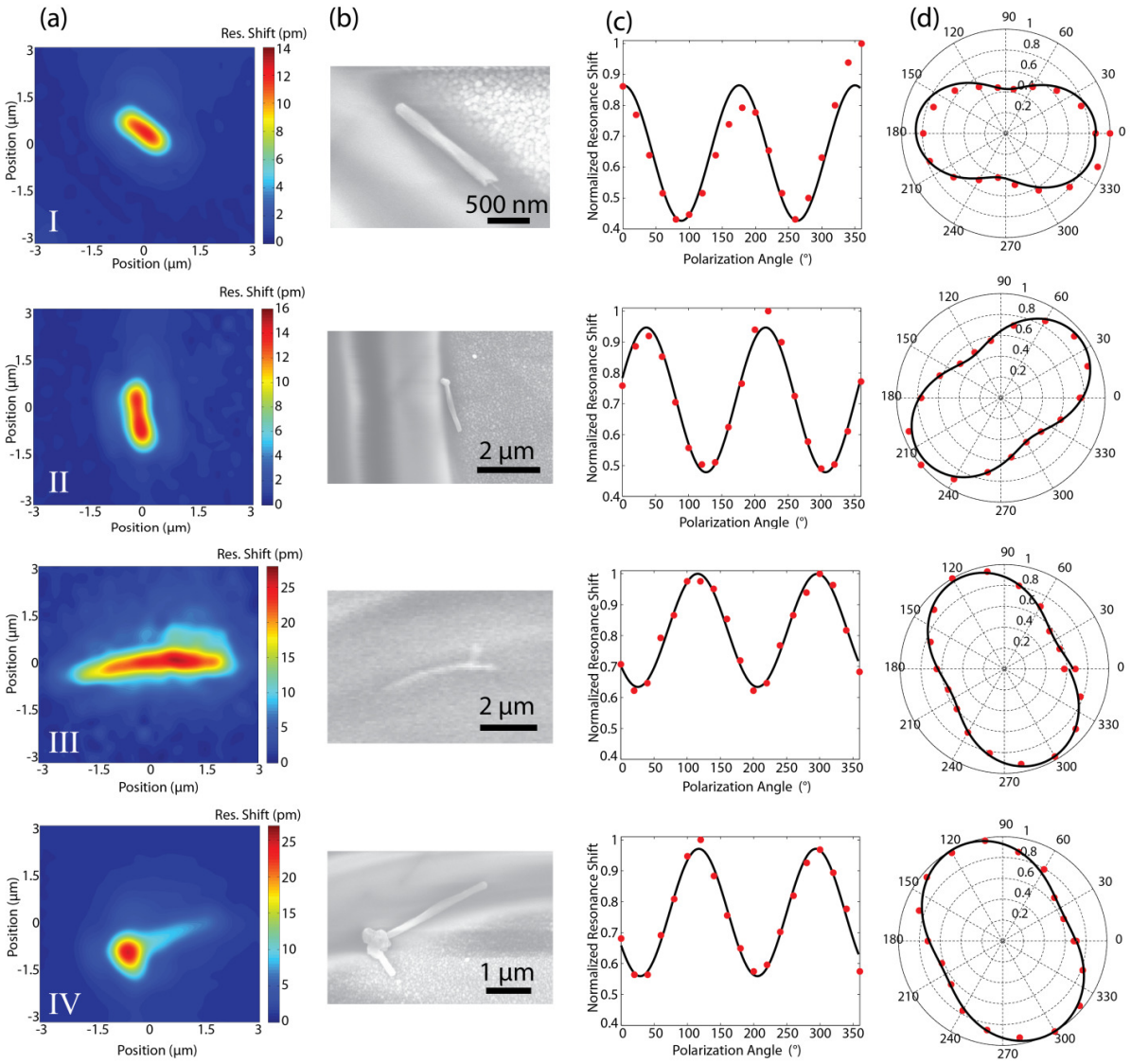

Figure 43: Photothermal characterization of four different nanotubes.

Nanotubes are labelled I-IV from top to bottom. (a) Photothermal map of MWCNTs. The pump beam is scanned at 250 nm/pixel with 440 μW incident power at 640 nm. (b) Scanning electron micrographs. (c) Polarization dependence of photothermally-induced resonance shift. (d) Polarization dependence plotted in polar coordinates for clarity.

Table 1. ***Parameters for Photothermal Measurement of MWCNTs***[a]

	Resonance Shift (pm)	Diameter (μm)	Length (μm)	Dissipated thermal power (μW)	Carbon fraction absorbing, β (%)	Per-atom absorption cross-section (1×10^{-18} cm^2/ atom)	Polarization extinction ratio
I	13.5	0.104	1.41	88	33.0	2.7	2.0 : 1
II	14.1	0.111	1.71	92	27.2	2.5	2.3 : 1
III	24.0	0.157	4.04	163	11.5	2.3	1.8 : 1
IV	16.6	0.154	2.99	111	15.4	1.6	1.6 : 1

[a]This table lists the relevant parameters for the four MWCNTs presented in Figure 43. The measured resonance shift, physical dimensions, and polarization extinction ratio are directly measured via photothermal absorption or SEM. The dissipated thermal power is calculated using finite-element simulations. The carbon fraction absorbing (β) and the per-atom absorption cross-section are calculated by analyzing the combined results of measurements and simulation.

A representative family of photothermal images is shown in Figure 42. MWCNTs are observed to be up to several microns in length but appear with a diffraction-limited thickness, consistent with their high aspect ratio. Very high contrast is observed against the background. For example, the nanotube in Figure 42f exhibits a Signal-to-Noise = 425 and Signal-to-Background = 36. A case study of four MWCNTs is presented in Figure 43, with photothermal maps (a), SEM images (b), and polarization dependence (c, d) presented side by side. The photothermal image matches the SEM image, including photothermal hotspots corresponding to the carbon-rich globules surrounding residual catalyst evident in nanotubes in Figure 43b-d.

To calibrate our photothermal technique, the absorption cross-section was determined on a per-atom basis to account for the variation in size between nanotubes, Table 1. The absorption cross-section of nanotubes is a critical parameter for understanding their optical and device parameters and has been the subject of several recent single-particle studies. All cross-section measurements were performed on regions of MWCNTs that were distant from any residual catalyst particles to avoid their influence on the calculation. Calculation of the absorption cross-section requires knowledge of the amount of light

absorbed by the target, which can be determined from the magnitude of heat released. The heat dissipated can be calculated from the measured resonance wavelength shift of the microresonator. However, the relationship between the heat dissipated and the photothermal shift is a function of the position of the nanotube along the microresonator, which was determined from the SEM images. Then, finite element simulations were performed using the COMSOL Multiphysics package to calculate the temperature elevation at every point in the mode volume as a result of a nanoscopic heat source, Figure 44a,b. The same approach was shown to correctly model the resonance shift of the microresonator in the absence of absorbing nano-objects as a result of the absorption from the silicon substrate.[132] The temperature along the rim of the microresonator is measured in a series of 2D slices at regular azimuthal spacing (5°). Using the literature value for the thermo-optic coefficient,[113] the shifted refractive index is calculated at each point. The shift in the refractive index is then weighted by the relative intensity ($|E|^2$) of the propagating mode,[117] Figure 44c. The total resonance shift of the toroid is calculated by averaging the resonance shift contribution from each slice.

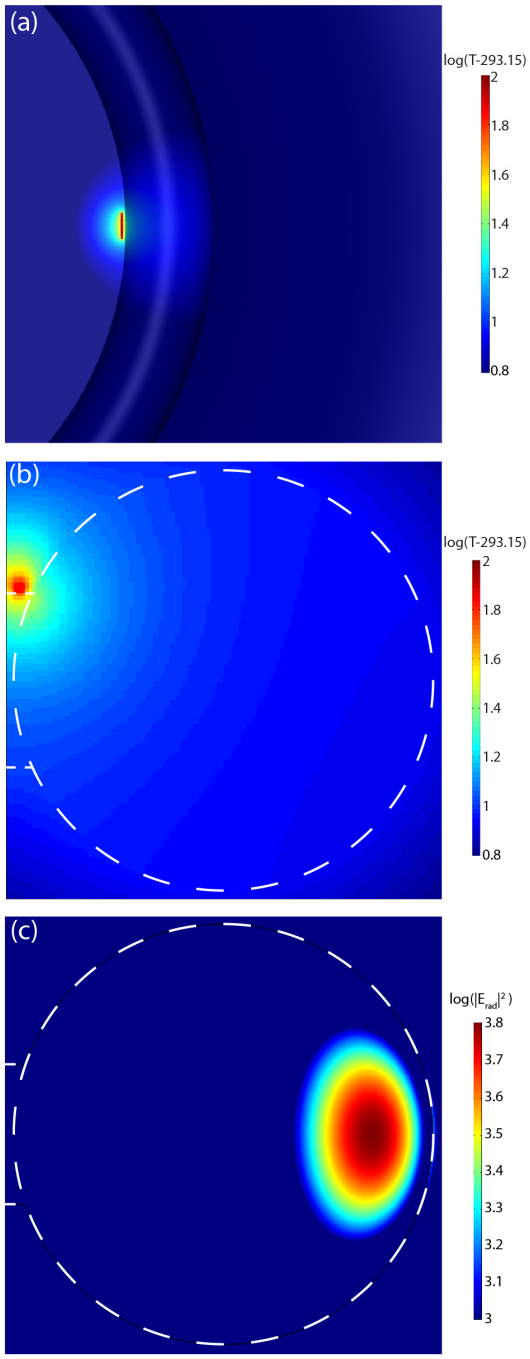

Figure 44: Simulations of photothermal absorption and propagating modes.

(a) 3-dimensional temperature distribution resulting from an absorbing nano-object on the surface of a microresonator. The physical parameters are equal to those used to model Nanotube I. Log(T-293.15) is plotted where T is the temperature in Kelvin. Room temperature is defined as 293.15 K. (b) 2-dimensional slice of (a) at an azimuthal plane crossing the nanotube. (c) Propagating mode in toroidal microresonator (log[E x E*]). The physical dimensions of the resonator are marked with dashed lines. The log scales are shifted by a constant for clarity.

The dissipated thermal power is then determined by matching the observed resonance shift. The pump intensity can be easily determined from the optical pump power and the spot size. Finally, the known atom density and physical dimensions of the tube can be used to extract the absorption cross-section per carbon atom, as summarized in Equation 5.1,

$$\sigma_{abs} = \frac{P_{thermal}}{P_{optical}} * \frac{1}{(1-\varphi_{lumin})} * \left[\pi * \left(\frac{w_0}{2}\right)^2\right] * \frac{M}{\pi * \left(\frac{d}{2}\right)^2 * L * \rho * N_a} * \beta \qquad 5.1$$

where σ_{abs} is the absorption cross-section per carbon atom, $P_{thermal}$ the heat dissipated, $P_{optical}$ the pump beam power (440 µW), φ_{lumin} is the quantum yield for luminescence (0 for MWCNT), w_0 the $1/e^2$ beam diameter (780 nm), d and L are nanotube diameter and length respectively, ρ is the density (1.75 g/cm^3),[229] N_a is Avogadro's number, M the molar mass (12.01 g/mole carbon), and β the fraction of atoms in the nanotube excited by the pump beam. β is calculated by taking an overlap integral between the measured spot size of the pump laser and the physical dimensions of the nanotube as measured by SEM (see Supporting Information for the manuscript). This correction is necessary because the spot size is the same order of magnitude as the diameter (100-170 nm) and length (1000-4000 nm) of the nanotubes. This procedure ultimately yields a value of 2.3 +/- 0.5 x 10^{-18} cm^2 /C.

MWCNTs of this size (>100 nm diameter) should have a per-atom optical absorption cross-section approaching that of bulk graphite due to the MWCNTs' relatively gentle curvature. Reported per-atom cross-sections of graphite range from 2.5 - 2.8 x 10^{-18} cm^2/C,[230-233] in excellent agreement with our results. The absorption cross-section of MWCNTs has been roughly estimated[234] by dividing the bulk absorption of a MWCNT sample by the carbon atom density at 3.4 x 10^{-18} cm^2/C. To our knowledge, our work reports the first per-atom absorption cross-section of MWCNTs made on individual nanotubes. Single-walled carbon nanotubes are less directly analogous, but serve as a useful comparison. Literature reports for the per-carbon cross-section of single-walled carbon nanotubes vary from 1-3 x 10^{-17} cm^2/C.[221,225,235,236]

Polarization dependence of the photothermal signal was investigated Figure 43c, d. Angular dependence clearly follows a $\sin^2\theta$ dependence, with the maximum photothermal shift observed with the pump beam polarized parallel to the long axis of the nanotube, as expected.[210,221,224] The contrast ratio between parallel and perpendicular polarization was approximately 2:1. The lack of complete extinction is consistent with previous measurements of single-walled nanotubes on silicon and on silicon dioxide,[221,224,237] where a 2:1 contrast ratio was also observed, and largely resulted from the symmetry-breaking influence of the substrate,[237] though the weaker curvature of a MWCNT can also play a role.

Looking forward, the tremendous sensitivity of ultra-high Q optical microresonators can also enable single-molecule photothermal microscopy and spectroscopy. Extrapolation to the absorption cross-section of a single chromophore (~ 1×10^{-16} cm^2) [28] from a nanotube suggests a molecular shift of 2.1 fm, a value significantly greater than the smallest detectable resonance shifts in toroidal microresonators achieved thus far.[90,95,104] The most significant technical barrier to realizing single-molecule resolution is pump absorption by silicon, a factor that allows convenient tuning of resonance spectral positions[132] but ultimately contributes a prohibitively high background photothermal shift. Future efforts are focused on minimizing the effect of this background absorption via chemical modification and signal processing.

To summarize, we have presented a new method for measuring optical absorption at the single particle level by combining the sensitivity of ultra-high Q optical microresonators with the spectral specificity of photothermal absorption. We successfully measured the polarization-dependent per-atom absorption cross-section of individual MWCNTs by mapping out the spatially-resolved optical absorption and heat dissipation. The ultimate limit of sensitivity is calculated to be several orders of magnitude smaller, allowing for detection of absorption by non-luminescent single molecules under ambient conditions. This technique places few requirements on the target system's properties and does not require multiple objectives or a transparent substrate. Photothermal approaches are also immune to

contributions from scattered light and, when combined with direct absorption approaches, provide complementary information in regard to characterizing the flow of energy in nano-objects. Further, toroidal microresonators are compatible with water[110] and could be used to study chemical or biological reactions in real time. Looking forward, the simple fixed-wavelength pump laser used in this experiment could be replaced with a tunable source to perform broadband visible absorption spectroscopy using toroidal microresonators. Extending spectroscopy of non-luminescent targets towards single molecules and smaller nano-objects would provide a powerful new tool for investigating structure and dynamics at the nanoscale while also offering needed additional chemical information for label-free sensing.

Chapter 6

6. Optical Microresonators as Single-Particle Absorption Spectrometers[3]

6.1 Abstract

Optical measurements on nanoscale objects offer significant insight into fundamental biological, material, and photonic properties. In absorption spectroscopy, sensitivity limits applications at the nanoscale. Here we present a new single-particle double-modulation photothermal absorption spectroscopy method that employs on-chip optical whispering-gallery-mode (WGM) microresonators as ultrasensitive thermometers. Optical excitation of a nanoscale object on the microresonator produces increased local temperatures proportional to the absorption cross-section of the object. We resolve photothermal shifts in the resonance frequency of the microresonator smaller than 100 Hz, orders of magnitude smaller than previous WGM sensing schemes. Application of our new technique to single gold nanorods (AuNRs) reveals a dense array of sharp Fano resonances arising from the coupling between the localized surface plasmon (LSP) of the AuNR and the WGMs of the resonator, allowing for the exploration of plasmonic-photonic hybridization. At a broader level, our approach adds label-free spectroscopic identification to microresonator-based detection schemes.

[3] The material in this chapter was originally published as Heylman, K.D., Thakkar, N., Horak, E.H., Quillin, S.C., Cherqui, C., Knapper, K.A., Masiello, D.J., Goldsmith, R.H. Optical microresonators as single-particle absorption spectrometers. *Nature Photonics* (2016)

6.2 Introduction

Single-molecule and single-particle measurements have revolutionized our perception of the nanoscale. Most approaches require luminescent targets, demanding burdensome labeling strategies and limiting applications. Although label-free observation of single-molecule[72,73,84,238] or single nanoparticle[74-76,90,94] binding events can be resolved using microscale optical and nanoplasmonic resonators, only *detection* is achieved, with limited information available about target properties or identity. Adding *spectroscopic* measurement, as demonstrated on individual nanoparticles,[21-24] to microresonator-based label-free detection schemes[239] would add a powerful new dimension of analytical capability. Although several recent methods have demonstrated *imaging* of single molecules without luminescence,[29,38,42,51] direct absorption *spectroscopy* has only been demonstrated at low temperatures.[3,240-242]In one implementation,[51] non-radiative relaxation of an optically excited molecule causes a local rise in temperature which correlates with the molecule's absorption cross-section (σ_{abs}) and enables imaging through photothermal contrast. This scheme employs two beams: a pump laser for excitation and a non-resonant probe laser which samples the photothermally-induced change in local refractive index. For weak absorbers such as single molecules, this change is very small, and immersion in media with high thermo-optic coefficient is required for single-molecule resolution. Thus, a more acute microresonator-based local probe with higher sensitivity would augment single-molecule label-free detection with spectroscopy.

To that end, we employ ultrahigh-quality-factor (Q-factor) WGM optical microresonators as near-field thermometers. In particular, we use on-chip toroidal microresonators (Figure 45) with optical *Q*-factors up to 10^7 and mode volumes of ~ 300 μm^3.[106] This combination of narrow linewidths and small mode volumes provides a versatile platform for quantum optics[183,243] and label-free sensing.[74,75,90,94] In this article, we show that photothermal spectroscopy with optical microresonators yields sensitivity

exceeding the current state of the art in WGM sensing by multiple orders of magnitude while achieving sensitivity comparable to the best room-temperature absorption techniques. To demonstrate our approach, we perform absorption spectroscopy on single LSP-supporting gold nanorods (AuNRs) with negligible luminescence[244] and observe dense sets of Fano interferences, spectroscopic signatures of coherent LSP-WGM interaction. These spectral features allow estimation of the interaction energies of the resulting plasmon-dressed microresonator modes and offer a unique perspective on the evolution of the interference between the LSP and the WGMs as they are brought in and out of resonance.

6.3 Photothermal absorption spectroscopy with sub-100-Hz detection limit

Typically, WGM microresonator sensors employ the reactive mechanism[219] to detect the binding of a single unlabeled biomolecule at the resonator surface.[72,73,84] Molecular signals are observed as discrete jumps of WGM resonances at random times, and must be distinguished from other processes, including resonance energy thermal drift and probe laser jitter. This process is made more difficult by the inability to signal average over multiple iterations. Further complications arise from the strong dependence of the measured signal on the target's binding location. Though some degree of chemical specificity for target binding can be achieved by surface functionalization,[73,239] a means of spectroscopic interrogation could provide unambiguous molecular identification, augmenting label-free single-molecule detection capability with label-free single-molecule identification. Here we show that a two-beam geometry incorporates label-free absorption spectroscopy into the apparatus, significantly enhancing sensitivity, and providing a powerful tool for nanoscale characterization.

Our microresonator-based spectrometer measures the shift in WGM energy upon optical excitation of a single absorbing particle or molecule (Figure 45a). Optical absorption by the target results in heat dissipation into the microresonator proportional to the target's absorption cross-section. The shift in WGM resonance frequency,

$$\Delta\omega_m = \left(\frac{\omega_m}{n} \frac{dn}{dT} \right) \Delta T, \qquad 6.1$$

is linearly proportional to the increase in microresonator temperature.[132] Here $\omega_m = mc/nR$ is the mth WGM resonance frequency, m is the azimuthal mode number, n is the index of refraction (1.44 for fused silica), ΔT is the temperature change, dn/dT is the thermo-optic coefficient (8.6×10^{-6} K^{-1}, see Methods), R is the toroid major radius (~23 μm), and c is the speed of light. Resonance shift is monitored with a probe laser evanescently coupled to the resonator via a tapered optical fiber.[106] To maximize sensitivity and measurement bandwidth, the resonance frequency of the toroid is continually tracked with the phase-sensitive Pound-Drever-Hall (PDH) locking technique,[92,100,162,163] where the probe laser is actively locked to the toroid resonance (Supplementary Section 1 in the manuscript). The combination of phase-sensitive detection and extremely narrow molecular absorption resonances was critical in acquiring the first single-molecule absorption spectra at low temperatures,[3] and we benefit from a similar combination at room temperature using ultranarrow (ultrahigh Q) WGM resonances. Because the photothermal signal occurs at a pre-determined frequency and is continuously monitored through the PDH error signal, the large noise amplitude at low frequencies that plagues WGM sensing schemes can be minimized. Specifically, amplitude modulation of the excitation beam at a known frequency moves the desired signal into a sub-Hz (down to 0.1375 Hz) band at several kHz and allows use of lock-in amplification. This double-modulation scheme, and the narrow measurement bandwidths it allows, is critical to the unprecedented resonance-shift sensitivities we present below and is not possible with earlier sensing methodologies (Supplemental Section 1 in the manuscript).

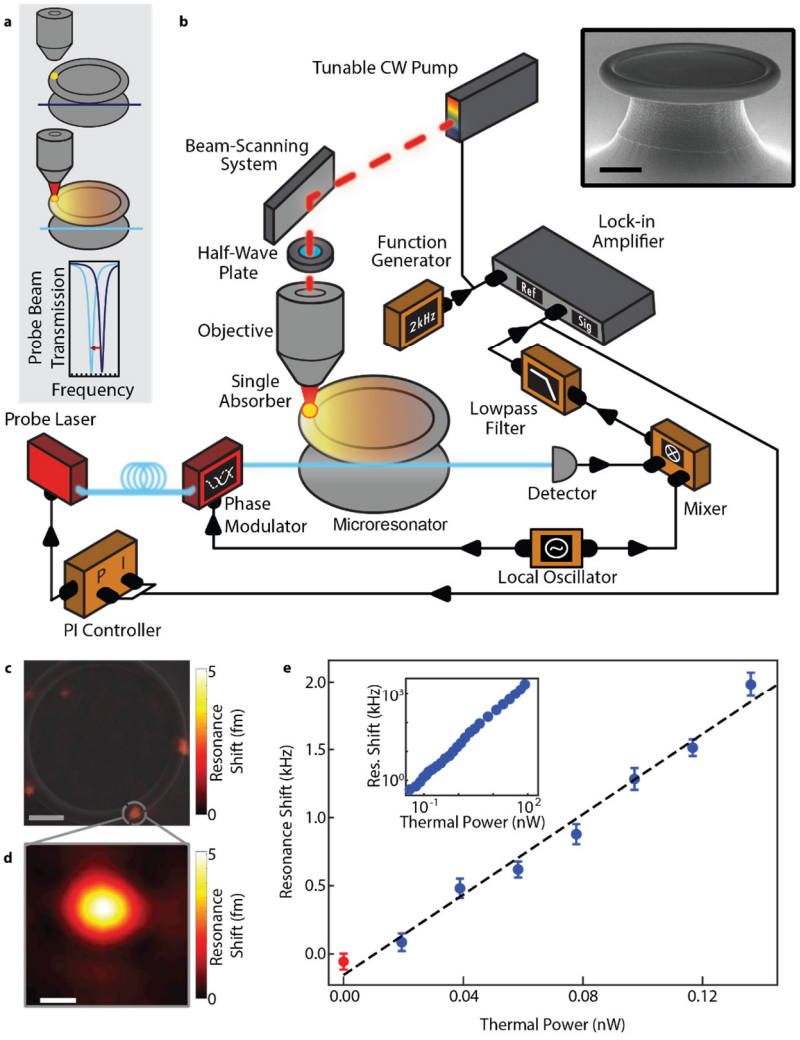

Figure 45: Microresonator-based absorption spectroscopy.

a, The resonant frequency of a toroidal microresonator is probed with a fiber-coupled tunable frequency laser. Excitation of a single nanoparticle (gold) with a focused pump beam (red) generates a photothermal absorption signal, shifting the toroid resonance frequency (as displayed, from blue to cyan). **b**, Schematics of spectrometer. The photothermally-induced signal is amplified with a phase-sensitive feedback loop (see Text and Methods for details of the experimental setup). Inset: Scanning electron micrograph (SEM) of a typical toroidal microresonator (10 µm scalebar). **c**, Wide-area photothermal map of the entire microresonator (10 µm scalebar), acquired at 0.94 eV pump energy, superimposed onto an SEM image of the same microresonator. **d**, High-resolution (1 µm scalebar) photothermal map of the AuNR marked in panel **c**. **e**, The detection limit was measured by systematically decreasing excitation power while detecting the resonance shift from an absorbing AuNR (blue dots). Error bars are generated by taking the standard deviation of the mean of 30 samples of 1-second measurements of the resonance shift. The red dot represents measurements taken with the pump beam blocked, and is used to determine background. The Q-factor for WGM used to acquire this data was 2 x 10^7 Inset: the resonance shift is linear (black dashed line: linear fit) over more than four orders of magnitude.

We spatially map individual absorbers,[133,245] (Figure 45c,d) by scanning the tightly focused (full-width at half maximum of 1.38 μm) free-space pump laser across the microresonator surface (Figure 45b). Quantification of absolute absorption cross-section is achieved by relating the heat dissipated by the absorber to the observed resonance shift via finite-element thermal simulations previously validated with background silicon absorption and absorption by single carbon nanotubes,[132,133] (Supplementary Section 2 in the manuscript). Critically, though sensitivity is a function of particle location, an issue adding significant ambiguity in existing WGM sensing methods,[246] photothermal imaging[133,245] allows us to discern the target's position and measure an accurate absorption cross-section anywhere on the resonator.

Decoupling the pump and probe in our two-beam geometry facilitates easy scanning of the pump energy, position, and polarization without affecting the probe beam coupling. When applied to high aspect-ratio AuNRs as targets (Figure 46), tuning of polarization universally results in AuNR absorption varying from a maximum value to zero absorption with a cosine-squared dependence on the angle of excitation polarization, as expected for a single dipolar absorber. We tune the pump energy from 0.905−0.969 eV (1280−1370 nm) to acquire absorption spectra. The AuNR's geometry determines the LSP resonance, $\hbar\omega_0$, and the polydispersity of the AuNRs is evident in their absorption spectra with distributed resonance energies. While we sometimes observe (Supplementary Section 4 in the manuscript) the peak of a Lorentzian feature (Figure 46a), we often observe the side of a Lorentzian (Figure 46b,c), since the distribution of LSP resonance energies ($\hbar\omega_0$) of our AuNRs is broader than the observation window set by our pump laser. While the absorption cross-section drops significantly at energies far from $\hbar\omega_0$, we can still infer the LSP linewidth and $\hbar\omega_0$. We find a median linewidth (68 meV) in close agreement with earlier measurements (69 meV)[24] and a median absorption cross-section (1×10^{-10} cm^2) and LSP resonance energy (0.93 eV) in agreement with the manufacturer-reported ensemble values (0.9×10^{-10} cm^2) and 0.91 eV respectively, see Supplementary Section 4 in the manuscript).

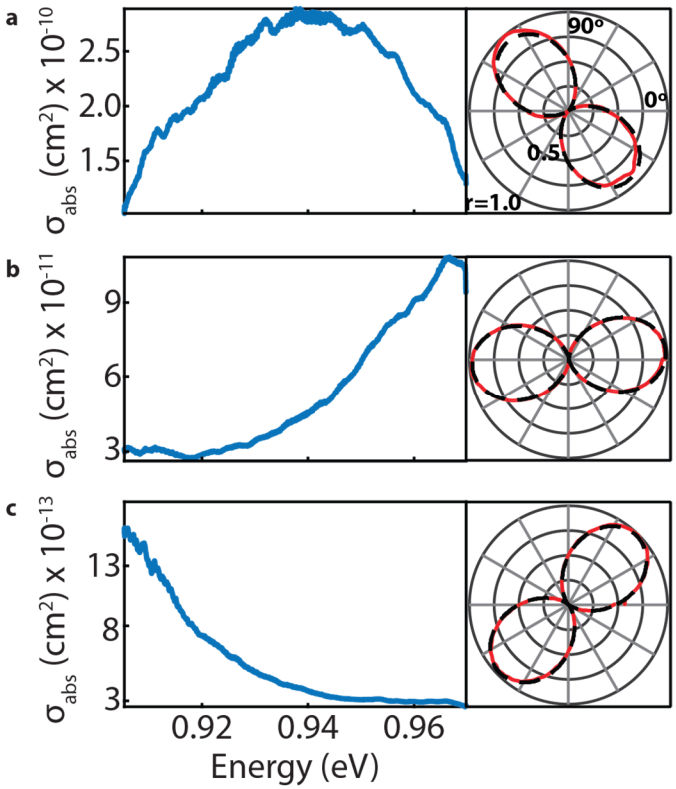

Figure 46: Representative spectroscopic measurements on single AuNRs.

a-c, Absorption spectra (left) and corresponding polarization dependence (right) of single AuNRs acquired with coarse spectral resolution (1.4 meV). The distribution of LSP ω_0 resonance energies is larger than the spectral window being probed (Supplementary Section 4 in the manuscript), resulting in the observation of a mixture of Lorentzian peaks **a** and sides of a Lorentzian **b-c**. The polarization dependence of absorption (red) for each AuNR is displayed, acquired with the pump energy fixed at 0.94 eV. The black dashed line is a fit to $\cos^2(\theta)$. Radial contours (r) indicate normalized absorption.

To evaluate our microresonator absorption spectrometer's limit of detection, we systematically decreased the excitation intensity on a single AuNR (Figure 45e) (Supplementary Section 5 in the manuscript). With excitation intensities ranging over more than 4 orders of magnitude, the photothermal signal is linear, as expected from Equation 6.1. The lowest recorded signal of 20 pW was detected by a shift in the WGM frequency of approximately 84 Hz, corresponding to an average change in microresonator temperature of $\Delta T \sim 100$ nK ($\Delta n/n \sim 1 \times 10^{-12}$) and a WGM resonant wavelength shift of 1

attometer. This detection limit, ~ 0.1 kHz of resonance shift, represents an improvement in WGM resonance shift detection in a sensing experiment by approximately two orders of magnitude over state-of-the-art optomechanical and Raman lasing WGM approaches to nanoparticle and molecular detection, which both reported sensitivity limits near 12 kHz. Alternatively, extremely low noise levels in determining resonance shifts have been achieved with balanced homodyne detection and Hänsch-Couillaud polarization spectroscopy and used to probe microresonator mechanical resonances in the 10's of MHz range.[89] Our increased sensitivity is a direct consequence of our double modulation scheme where the desired signal is forced to be at a pre-determined frequency with an extremely narrow bandwidth (0.1375 Hz), a benefit only available when detection is simultaneously coupled with interrogation of spectral features. Moreover, these other approaches could potentially be used to further enhance the limit reported here by providing additional means of signal amplification and noise suppression. Coupling lower noise detection geometries with lower measurement bandwidths suggests even lower limits of detection will be readily achievable. Though we demonstrate this advantage with plasmonic absorption, this approach could be applied to molecular electronic or vibrational transitions as well. Our resonance shift limit of detection translates into a thermal power detection limit approaching 10^{-11} W, multiple orders of magnitude lower than the demonstrated photothermal signal of 10^{-8} W from a single dye molecule.[51] This comparison indicates that robust detection of photothermal signals from single molecules is achievable.

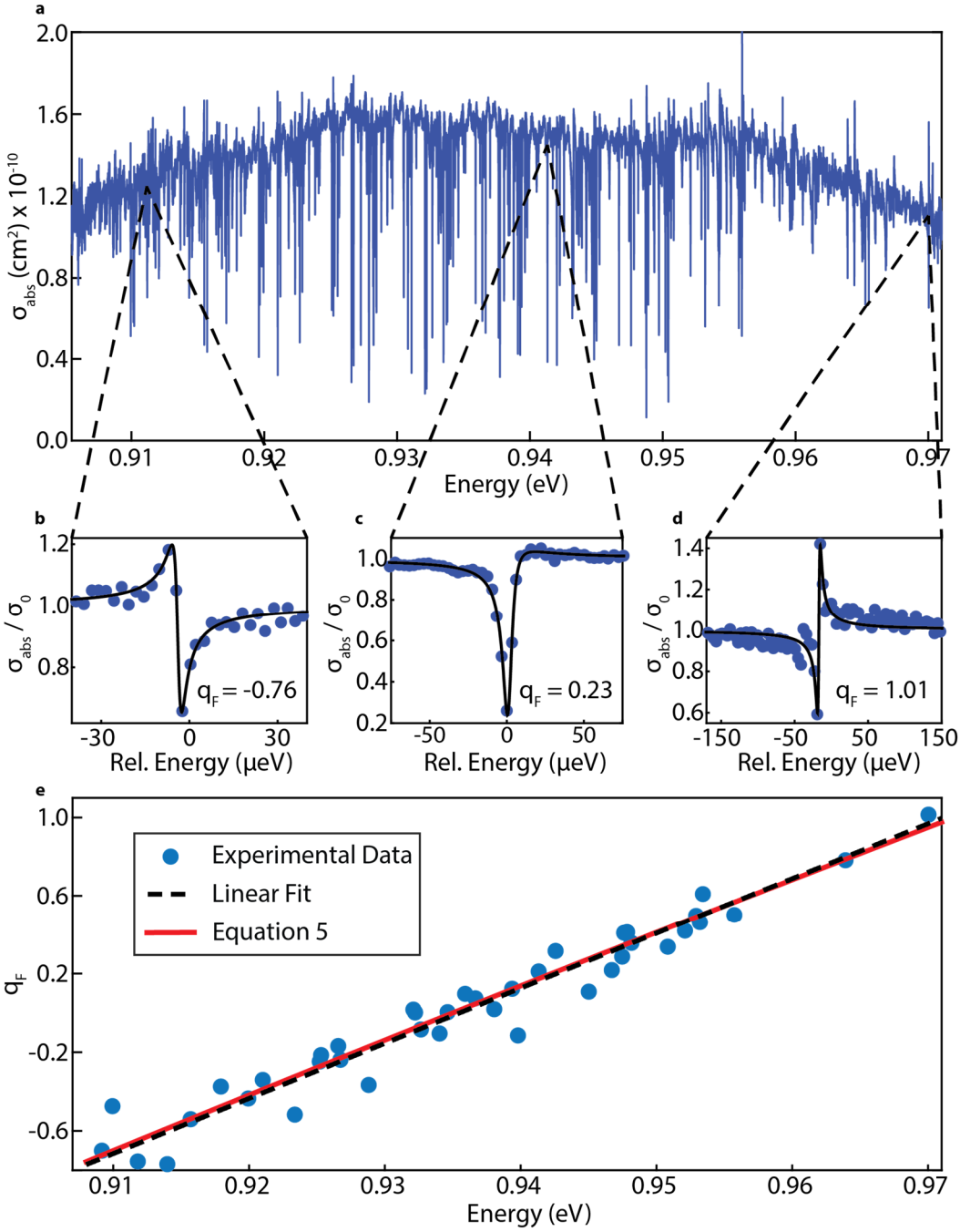

Figure 47: Progression of Fano lineshapes within the absorption spectrum of a AuNR coupled to a set of WGMs.

a, Fine resolution (3 μeV) spectrum (blue). **b-d**, Individual Fano resonances, with the experimental spectrum (blue dots), and fits to Equation 4 (black line). The absorption cross-section of the LSP envelope (σ_0) is divided out for clarity. **e** The Fano lineshape parameter q_F plotted as a function of energy. Fits to individual Fano features (blue dots) using Equation 6.5 show a linear (black dashed line) dependence on pump energy, in quantitative agreement with the theoretical predictions of Equation 6.6 (solid red line).

6.4 Signatures of WGM-plasmon interaction

Closer investigation of the AuNR spectra reveals a striking departure from previous single-particle absorption spectroscopies.[21-24] While spectra of AuNRs located far from the microresonator's rim have unmodified Lorentzian lineshapes, AuNRs near the rim show a more complex set of narrow, asymmetric spectral features overlaid on the LSP's Lorentzian envelope (Figure 47), only visible by increasing spectral resolution from 1.4 meV (coarse resolution) to 3 μeV (fine resolution). These sharp spikes and dips only appear when the AuNR is located on the toroid's rim where the WGM fields are largest, indicating that their presence is a signature of coherent interaction between the WGMs and AuNR's LSP.

To understand these narrow spectral features we use a coupled oscillator model described schematically in Figure 48 (Supplementary Section 3 in the manuscript). The LSP is modeled as a lossy cavity, with generalized momentum $p_0(t)$ and resonance frequency ω_0. The LSP interacts with a set of WGMs modeled as cavity modes with generalized momenta $p_m(t)$ and resonant frequencies ω_m. The LSP-WGM couplings, characterized by g_m , are proportional to the overlap between the LSP and WGM electric fields and are therefore dependent on the AuNR's location and orientation on the toroid. These g_m model WGM excitation by the LSP and back-action on the LSP. The equations of motion are

$$\ddot{p}_0 + \gamma_0 \dot{p}_0 + \omega_0^2 p_0 + \sum_m g_m^2 \omega_0^2 p_m = \omega_0^2 \sqrt{V_0} E_0 e^{-i\omega t} \qquad 6.2$$

$$\ddot{p}_m + \omega_m^2 p_m + g_m^2 \omega_m^2 p_0 = 0 \qquad 6.3$$

where $E_0e^{-i\omega t}$ is a harmonic forcing term modeling the pump laser's field along the AuNR's long axis and V_0 is the LSP mode volume. Equations 6.2-6.3 includes damping characterized by the frequency γ_0, which models plasmon decay on the order of 10 fs due to coupling with dissipation pathways such as heat.[244] By

contrast, we assume an infinite lifetime for the WGM modes in the absence of coupling to the LSP since the WGMs have Q-factors ranging from 6 x 10^5 - 10^7.

Although the model can be solved exactly for an arbitrary number of WGMs, it is instructive to initially consider the LSP's interaction with a single WGM with energy ω_1. We then have two interacting

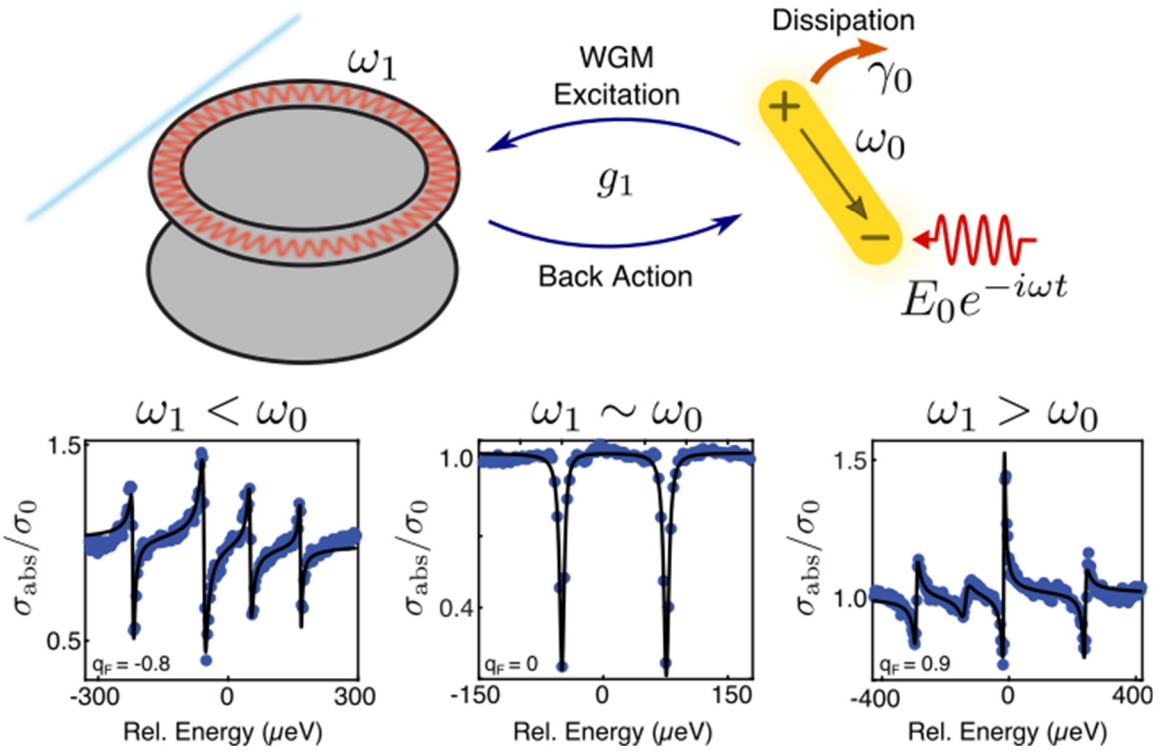

Figure 48: Schematic demonstrating the coupled oscillator model of coherent WGM-LSP interaction.

a, For the simplified case of a single WGM, we define the WGM resonance frequency ω_1, and we define the LSP resonance frequency ω_0. The LSP is pumped by an external electric field, $E_0e^{-i\omega t}$, and dissipates energy at rate γ_0. The overlap of the WGM and LSP electric fields, determining the amount of energy transfer between the LSP and WGM, is characterized by g_1. Fine-resolution experimental spectra (blue dots) fit to Fano profiles (black lines) show three parameter regimes: **b**, when $\omega_1 < \omega_0$, the Fano interference is constructive at lower energy but destructive at higher energy, **c**, when $\omega_1 \sim \omega_0$, the Fano interference is always destructive, and **d**, when $\omega_1 > \omega_0$ the lineshape is reversed and the interference is constructive at higher energy but destructive at lower energy. The model predicts that Fano's asymmetry parameter, q_F, is a function of $\omega_1 - \omega_0$, capturing the evolution of the Fano lineshape across these regimes

oscillators, one broad and one discrete, and from the WGM's perspective, the LSP provides a means to couple to the excitation field and a near-continuum of dissipation channels. This general problem, a discrete state coupled to a continuum, was studied in detail by Fano[247] and Anderson,[248] and has been observed in many contexts,[249-252] such as plasmonic systems.[249,253] As a result, there are a variety of approaches to modeling Fano systems,[249,254] including systems with WGM microresonators coupled to plasmonic nanoparticles.[82,255-257] The spectral profiles are often described in terms of Fano's asymmetry parameter, q_F. In most contexts, it is valid to treat q_F as a constant over the frequency interval of interest. In contrast, by measuring a q_F for each individual WGM distributed across the LSP spectrum, we have the unique opportunity to measure q_F as it changes across a single spectrum.

The absorption cross-section of the coupled LSP-WGM system can be calculated from the equations of motion (Equations 6.2, 6.3), giving

$$\sigma_{abs}(\omega) = \frac{4\pi V_0 \omega}{c} Im\left\{ \frac{\omega_0^2(\omega_1^2-\omega^2)}{(\omega_1^2-\omega^2)(\omega_0^2-\omega^2-i\omega\gamma_0)-g_1^4\omega_1^2\omega_0^2} \right\} \qquad 6.4$$

$$\sigma_{abs}(\omega) \approx \sigma_0(\omega) \left| \frac{\omega\Gamma q_F+\omega^2-\Omega^2}{\omega^2-\Omega^2+i\omega\Gamma} \right|^2, \qquad 6.5$$

Where $\omega\Gamma = -g_1^4\omega_1^2\omega_0^2 Im[Z_0]$ and $\Omega^2 = \omega_1^2 - g_1^4\omega_1^2\omega_0^2 Re[Z_0]$ for $Z_0^{-1} = \omega_0^2 - \omega^2 - i\omega\gamma_0$. The cross-section can be approximated as the product of two terms, $\sigma_0(\omega)$ describing the isolated LSP absorption lineshape, and the well-known Fano profile[247,249] (Supplementary Section 3 in the manuscript). Here, Ω and Γ characterize the spectral location and width of the Fano resonance. In the weak-coupling limit applicable here, Γ is small and approximately constant, $\sim g_1^4\gamma_0$, and the Fano resonance is spectrally narrow and located near the WGM resonance frequency, $\Omega \sim \omega_1$. The absorption cross-section can approach zero at higher (lower) energies than ω_1 but rise rapidly at lower (higher) energies, an asymmetric behavior due to the WGM rapidly changing phase, moving from destructively to constructively interfering with the LSP. Changes of over an order of magnitude in the absorption cross-section are observable (Figure 47a). The degree of asymmetry in the Fano lineshape due to the rapid phase change is quantified by

$$q_F(\omega_1) = \frac{\omega_1}{\gamma_0} - \frac{\omega_0^2}{\omega_1\gamma_0} \approx \frac{2}{\gamma_0}(\omega_1 - \omega_0), \qquad 6.6$$

where the linearization carried out in the vicinity of ω_0 shows the connection between this classical model and others in the literature[258] including those[254] that follow Fano's quantum mechanical approach[247] more closely. Thus, the asymmetry in the lineshape is independent of the LSP-WGM coupling and is an approximately linear function of the detuning between ω_0 (LSP) and ω_1 (WGM). As ω_1 is varied across the LSP profile, q_F changes sign and the Fano resonance flips (Figure 48b-d).

Our experiment examines LSP interaction with a dense set of WGMs spanning the LSP profile, offering a novel means to explore the frequency dependence of q_F. In Figure 47, we fit Equation 6.5 to individual Fano resonances (Methods), and determine the corresponding q_F values. Comparison to the behavior predicted in Equation 6.6, where the slope is taken from fitting the spectral envelope to $\sigma_0(\omega)$, demonstrates nearly perfect agreement between experiment and theory (Figure 47e). To our knowledge,

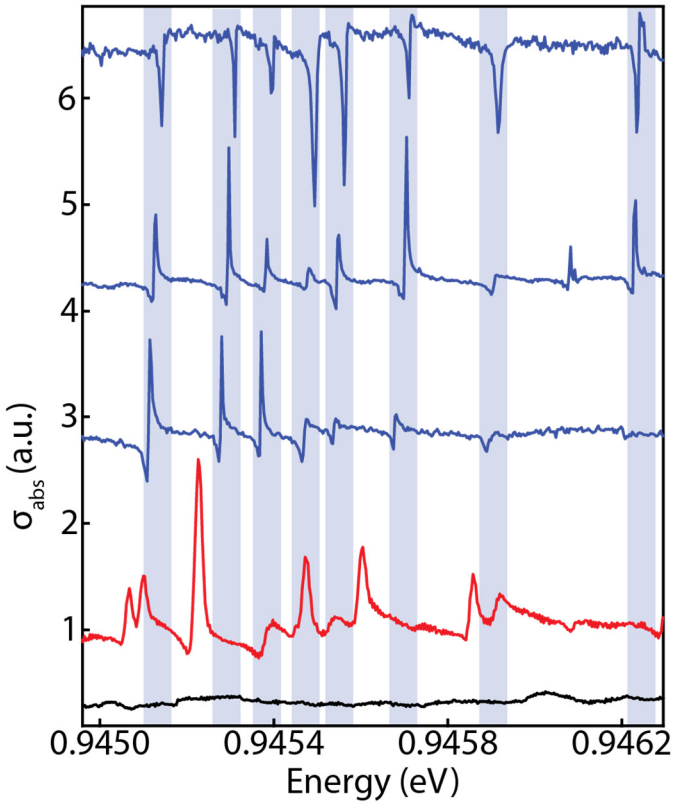

Figure 49: Correlation of fine-resolution AuNR absorption spectra.

Different AuNRs deposited on the rim of the same microresonator (blue curves) exhibit Fano resonances at highly correlated spectral positions (blue stripes). By contrast, AuNRs on the rim of different microresonators (red curve) exhibit Fano resonances with different spectral positions. Spectra of AuNRs located far from the rim of any microresonator do not show Fano resonances (black curve).

this is the first experimental demonstration of the systematic variation of q_F as a function of frequency within a single spectrum, and this is a unique verification of the classical coupled oscillator model of optical resonators.

From Ω and Γ we can also estimate the interaction energy, $\hbar g_1 \sqrt{\omega_1 \omega_0}$, between the WGM and LSP. We find that $\hbar g_1 \sqrt{\omega_1 \omega_0}$ ~ 20 meV, a value comparable to calculations on other plasmonic systems.[259] Our estimate of g_1 indicates that shift in ω_1 due to coupling with the LSP will be negligibly small (~ 1 meV) compared to the LSP linewidth, and we therefore expect that the Fano resonances' energies

will be independent of AuNR location and orientation. Thus, multiple AuNRs coupled to the same toroid should have Fano resonances at the same energies, while the resonance lineshapes should be AuNR-dependent. This prediction is experimentally verified in Figure 49: multiple AuNRs on the rim of one resonator exhibit interference features at the same energies, consistent with their interaction with the same WGMs. Fano resonance positions are not correlated between AuNRs on different microresonators, indicating the spectral locations are a property of the microresonator itself, independent of the coupling g_m. AuNRs far from the rim exhibit no interference features, consistent with the model at zero interaction energy.

Since AuNRs are randomly cast on a given resonator, multiple AuNRs on the rim can be efficiently coupled to the same WGMs. In these cases, AuNR absorption spectra may exhibit an additional WGM-induced modulation to the Lorentzian envelope. Fine-resolution spectra (Figure 50a) show sharp Fano resonances as well as a shallow, periodic modulation to the LSP envelope more clearly seen with coarse resolution (Figure 50b). The energy spacing of the absorption dips (5.34 meV) is near the microresonator's free spectral range (5.46 meV), indicating this periodic modulation is also due to LSP-WGM interaction. To understand this modulation, we extend the model to include a second AuNR on the rim as another oscillator, with frequency $\widetilde{\omega_0}$ and linewidth $\widetilde{\gamma_0}$. In contrast to the original LSP oscillator, the second, distant LSP is uncoupled from the pump laser but is still coupled to the WGMs. This coupling can be recast (Supplementary Section 3 in the manuscript) as an additional dissipation term in the equations of motion, with rate proportional to interaction energy and $\widetilde{\gamma_0}$. Thus, the second AuNR can be viewed as a defect to these WGMs. Fine and coarse resolution calculations (Figure 50) demonstrate both narrow and broad interference features that are comparable in size and shape to those observed experimentally. Significant coupling to the second AuNR decreases the *Q*-factor of the WGMs, making interference features between the pumped LSP and the defective WGMs broaden. That this effect only occurs under specific coupling conditions (Supplementary Section 3 in the manuscript) indicates that it should be relatively uncommon,

a claim which is supported by the data. This intriguing interpretation implicates a long-range coupling between distant AuNRs mediated by a common network of essentially lossless WGMs (distinct from that predicted by the simulations of Wiersig[260]), and we are continuing to investigate this phenomenon.

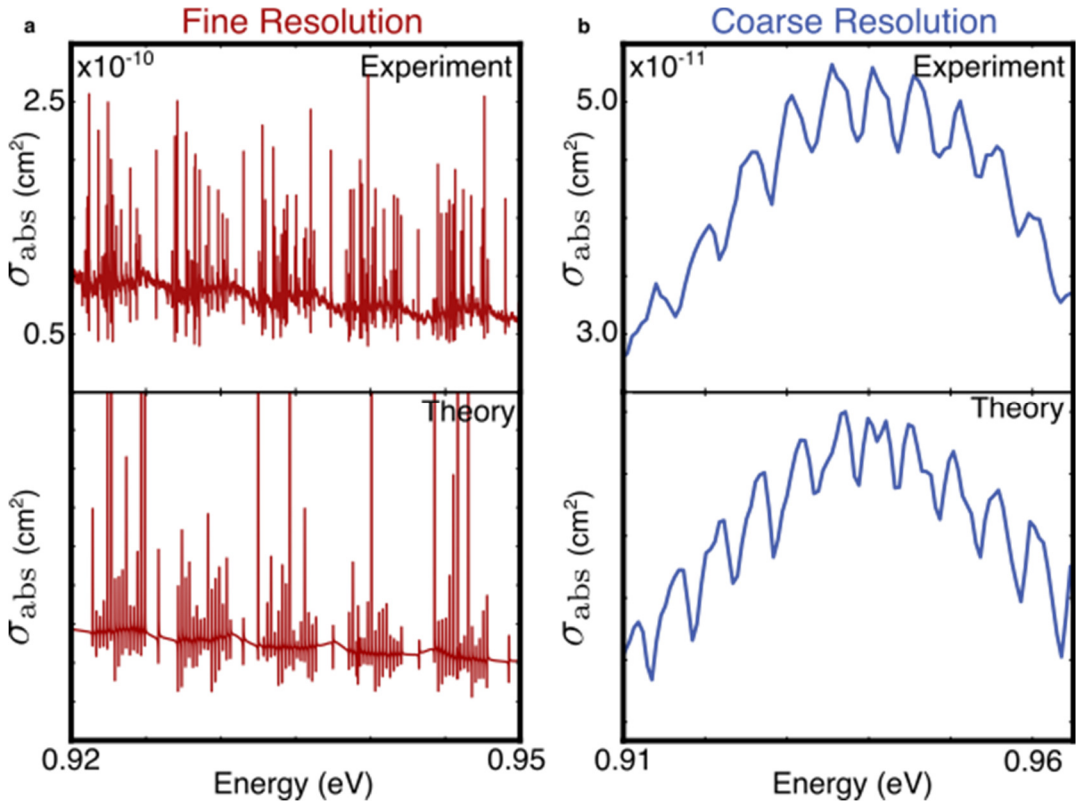

*Figure 50: Fine (**a**) and coarse (**b**) spectra and comparison with theory.*

Occasionally (14 of 61 spectra), the coarse resolution spectrum retains relatively broad and periodic dips. Extending the model to include other AuNRs and many WGMs with normally distributed coupling constants, g_m, on the order estimated in Figure 47, gives theoretical spectra which agree qualitatively with the data at both fine and coarse resolution. This indicates that the broad modulation to the LSP envelope is due to the presence of other AuNRs elsewhere on the resonator reducing the Q-factors of a subset of the WGMs and broadening the resulting Fano interferences.

6.5 Conclusions

In this work we have demonstrated a microresonator-based absorption spectrometer with unparalleled, sub-100-Hz resonance shift sensitivity, translating into photothermal sensitivity of tens of pW, far beyond the limit needed to detect light absorption by single non-luminescent molecules. This approach derives spectroscopic information from the detected nanoscale object, significantly enhancing the information content of label-free detection schemes. Though our demonstrated spectra are in the near infrared, broadband spectroscopy can be accomplished using more widely tunable excitation sources with microspheres or all-glass microtoroids[245] that are devoid of background-causing silicon substrates.

Application of our spectroscopy on single AuNRs reveals arrays of Fano features of narrow linewidth comparable to the narrowest Fano resonances seen in plasmonic systems.[253] Since the AuNR interacts with multiple WGMs across the experimental spectral range, we are able to track the change in the Fano profile and, for the first time, experimentally probe the spectral dependence of Fano's asymmetry parameter, q_F. Fits to the Fano resonance based on a coupled oscillator model are used to estimate the LSP-WGM interaction energy. A key enabling factor for the characterization of narrow Fano resonances is the ability to tune the colour of excitation light over a wide range (10^{-1} eV) with high energy resolution (10^{-6} eV).

Facile creation of broadband Fano resonance networks will have multiple applications. Nanoparticles engineered with narrow Fano resonances offer increased sensitivity to small frequency shifts from molecular binding events.[261] Independently, single-molecule detection of binding events, without spectroscopy, on WGM microresonators has been enabled through plasmon-enhanced interactions.[72,73] In this context, our work represents a convergence of these two approaches, with hybrid WGM-plasmonic Fano resonances reaching the narrow linewidth of WGMs. Our arrays of Fano resonances

can potentially allow multiplexed self-referenced sensing schemes,[75] all-optical switching,[253] enhanced four-wave mixing processes,[257]and access to single-molecule CARS (Coherent Anti-Stokes Raman spectroscopy),[256] all in a convenient condensed-phase, on-chip geometry with a wavelength range limited only by the transparency window of silica (~ 0.4-2.0 μm).

6.6 Methods

Sample preparation: Toroidal microresonators are fabricated according to literature procedures[106] with one modification.[176] Briefly, 2 μm of thermal oxide is grown on a ⟨100⟩ silicon wafer. Disks in the oxide layer (60 μm) are patterned via photolithography and a wet chemical etch with 6:1 BOE (buffered oxide etch). Microdisk resonators are formed by isotropically etching the oxide disks with an SF_6/Ar plasma etch. A final laser induced reflow step is used to produce the surface-tension-induced smooth rim necessary for high *Q* factors. High-aspect-ratio (~10) AuNRs are purchased from Nanopartz (250 nm length × 25 nm diameter), diluted into Millipore 18 MΩ water by 10x, and dropcast onto the toroid chip for 30 seconds. This method deposits isolated single AuNRs at a concentration of 0-6 per toroid. A further 5x dilution (50x total) results in higher *Q*-factors and fewer AuNR per toroid. Aggregates of AuNRs are avoided by not characterizing any photothermally-mapped nanoscale object with nonzero absorption at orthogonal pump polarization. Although the complex geometry of toroidal microresonators makes it impossible to image every AuNR in the SEM, approximately 50% of the entire data set (*N* = 61) was directly correlated to SEM images, with only one object incorrectly assigned as a single AuNR. To avoid thermal annealing of AuNRs during excitation,[262] the pump beam power is kept below ~0.01 mW. The change in average resonator temperature is also small, typically less than 50 mK, justifying the treatment of dn/dT as a constant.[113,132] We also omit the effects of thermal expansion of the microresonator, as is common

practice when working with toroid microresonators.[89,112] Thermal expansion[114] accounts for only 8% of the total observed resonance shift, and was discounted in the above analysis.

Experimental setup of the microresonator absorption spectrometer: After deposition of AuNRs, the tunable (1520-1570 nm) probe laser (Newport TLB-6728) is coupled into a toroid and locked to a high-*Q* WGM resonance with the PDH technique. To implement PDH locking the probe laser is actively locked to the toroid resonance in a feedback loop, and the error signal for the feedback loop serves as a direct measure of any changes to the toroid resonance frequency. Locking is achieved by phase-modulating the probe laser at high frequency (200 MHz) and measuring the transmitted photocurrent. This photocurrent has a component at the modulation frequency whose phase is a linear function of the detuning between the toroid resonance frequency and the probe laser frequency. Thus, phase-sensitive detection of the high-frequency photocurrent provides a sensitive readout of the toroid resonance frequency. Individual absorbers are mapped (Figure 45c-d) by steering the position of the focused pump laser spot with a gimbal-mounted mirror located at a plane conjugate to the objective's back aperture, and linear polarization at the sample is adjusted (Figure 46) with a motorized half-wave plate immediately prior to the objective. Amplitude modulation of the tunable (0.91−0.97 eV) pump beam (Thorlabs TLK-L1300R) and the resulting periodic oscillation of the photothermal heating signal causes a synchronous oscillation of the toroid resonance frequency. This oscillation is observed in the PDH locking loop error signal, and readily measured with a lock-in amplifier operating at the amplitude modulation frequency (2.010 kHz or 4.010 kHz). Further details are available in Supplementary Section 1 in the manuscript.

Fitting: Particular spikes and dips are fit using Equation 6.5 in a two step process: first, we fit the LSP profile $\sigma_0(\omega)$ on the full spectral range to extract estimates of ω_0 and γ_0, and then, dividing out the LSP envelope, we fit particular interference features to the Fano profile and estimate Ω, Γ, and q_F. The least-squares curve fit for each Fano resonance accounts for finite spectral resolution and nonzero background in experimental data by including free parameters for amplitude scaling (typically ~0.7) and baseline

offset (typically ~0.005) in the fitting equation (Equation 6.5). These parameters do not have a significant effect on the resulting q_F. Three interference features are shown for reference in Figure 48b-d, and we see asymmetric line shapes which change as a function of spectral location. We then collect estimates of q_F for 40 different Fano features spread across the spectrum, and compare to Equation 6.6, where the slope is taken from fitting to $\sigma_0(\omega)$. This comparison is shown in Figure 47e, and we see that the data confirms the linear dependence on detuning.

Chapter 7

7. Tunable Photonic-Plasmonic Resonator and Fisher Information Theory of Fano Resonances[4]

7.1 Introduction

Surface plasmon resonance, the coherent excitation of conduction electrons at the surface of a material, has found a wide range[263] applications in fundamental science and in commercial sensing devices. Gold nanoparticles are one of the most commonly used plasmonic materials. Rod-shaped gold nanoparticles in particular exhibit a strong, size-tunable plasmon resonance.[244] Besides tuning the aspect ratio during initial synthesis,[264] thermal modification of gold nanorods[262] is widely explored as a means of trimming the plasmon resonance to a specific wavelength. Both ensemble measurements[265-267] and single-particle measurements[268-270] have been performed. In particular, at the single-particle level the mechanism of melting has been a focus of investigations.[268,271-274] The melting process in rare cases can be driven in the reverse direction by radiation pressure[275] with sufficiently high laser intensity. In nearly all cases, however, the plasmon frequency of the longitudinal surface plasmon (LSP) resonance increases monotonically and irreversibly with thermal dose.

A plasmonic nanomaterial is useful because of the large enhancement in local field intensity owing to the nanoscale mode volume (V).[276] However, the quality factor (Q-factor) for an AuNR is only 10^1 because of high absorption losses. Many applications, especially sensing, benefit from the ratio of Q/V.[81,135,238,276] In essence, the Q-factor determines measurement resolution and the mode volume

[4] The material in this chapter is a manuscript in preparation.

determines the size of the signal. Hybridizing low-V plasmon resonances with high-Q dielectric microresonator modes is one means of resolving this dilemma. Plasmonic interaction with an on-chip ultrahigh-Q optical whispering gallery mode (WGM) in a dielectric toroidal microresonator[27,243,277] creates a hybrid mode with some of the properties of each type of resonance. Toroidal microresonators, possessing ultrahigh Q-factors (10^8) and small mode volumes[135] (~ 300 μm^3), are widely used in cavity optomechanics[70,278,279] and single-particle or single-molecule sensing.[74,75,90] One example of plasmonic-photonic hybridization in toroids was previously demonstrated by coating the toroid with a thin silver film,[277] although this depressed the Q-factor to low 10^3. Single plasmonic nanoparticles, on the other hand, provide local field enhancement while allowing for the superlative Q-factors of the host WGM microresonator to be retained.[27,72,73] Hybrid modes formed between microresonator WGMs and gold nanoparticles has been exploited for label-free, single-molecule detection[72,73] and even single aqueous ions.[280] Previously we have shown that plasmonic-photonic hybridization with AuNRs on toroids produces sharp Fano resonances[247,248] between the high-Q WGM modes and the broad LSP mode.[27] Silica WGM microresonators are attractive for applications like nonlinear frequency conversion and biosensing because they exhibit high-Q WGMs over a wide wavelength range spanning 400-2000 nm, a range over which the LSPs of AuNRs with different aspect ratios can be excited. Here we show that high-resolution single-particle absorption spectroscopy of AuNRs on toroids combined with a simple hotplate[281] treatment gives heat-tunable, high-Q hybrid plasmonic-photonic resonators.

Fano resonances are often deliberately engineered in plasmonic nanoresonantors[256,257,261] because the resulting dispersive-shaped feature in the absorption spectrum can be tracked with greater precision than the unmodified Lorentzian absorption peak. Sensing experiments with plasmonic resonators typically track changes in the plasmon resonance frequency as a result of an analyte binding to the resonator. In this work we will use the theory of Fisher information[282] content to analyze the measurement of subtle shifts in the LSP frequency using WGM-LSP Fano resonances compared to

measuring the Lorentzian resonance of an unperturbed LSP. The Fisher information is closely related to the theoretically optimal measurement precision. We will quantitatively determine the expected Fisher information for the Fano resonance as well as the underlying LSP resonance frequency and compare the two. We hope to provide an example to other spectroscopists to employ expected Fisher information when discussing measurement precision.

7.2 Experimental methods and results

The toroid microresonator single-particle absorption spectrometer has been reported previously.[27] Briefly, a tapered optical fiber[153] is used to evanescently excite WGM resonances (Figure 51). A single WGM resonance is monitored by locking the wavelength of this probe laser to the resonance using the Pound-Drever-Hall (PDH) technique.[94,161,162] The probe laser is tunable near 1550 nm, substantially off resonance with the LSPR. Measuring WGMs at more detuned wavelengths (e.g. 780 nm) would allow for higher WGM Q-factors, which is however not necessary here. Simultaneously, a tunable-wavelength (1280-1365 nm) pump laser is focused onto single AuNR on the surface of the toroid. The AuNR absorbs light in proportion to its wavelength-dependent absorption spectrum. Sweeping the pump wavelength and measuring the dissipated heat produces the absorption spectrum. Amplitude modulation at 2 kHz of the pump beam is coupled to lock-in amplification to narrow the detection bandwidth to Hz levels and greatly improve the signal/noise ratio.

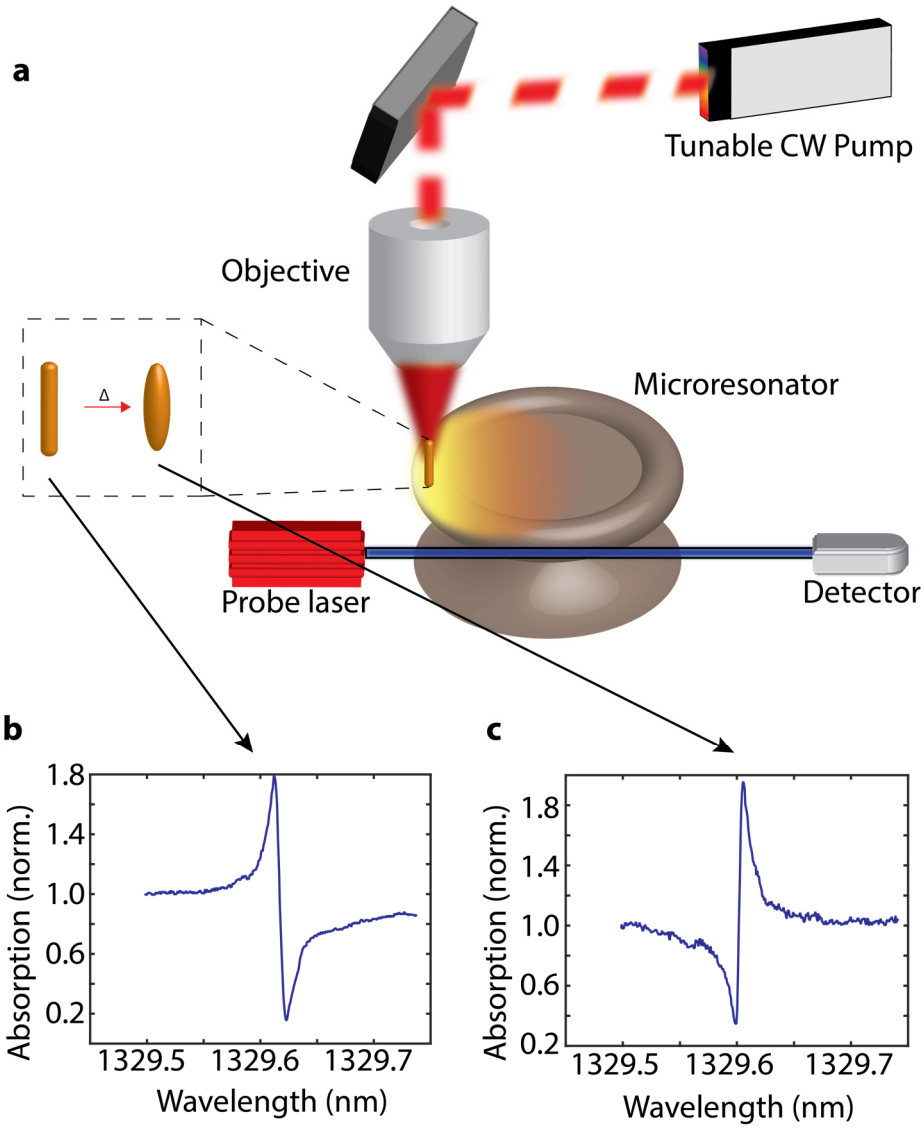

Figure 51: Tunable photonic-plasmonic microresonator.

(a) WGM resonances of toroid microresonators are probed with a fiber-coupled laser (blue). A second free-space laser (red) is used to optically excite AuNRs at the microresonator rim. (b),(c) High-resolution photothermal absorption spectroscopy of single AuNRs allows characterization of LSP-WGM Fano resonance. Annealing of AuNRs decreases the aspect ratio and shifts the LSP_{max}, producing a concomitant shift in the Fano resonance [(b) shifts to (c)).

We use commercially available high-aspect ratio AuNRs (Nanopartz) with a nominal LSP_{max} at 1400 nm. In contrast to early single-particle laser or electron-beam melting experiments on single gold nanorods, we choose to anneal an entire resonator chip on a hotplate and then individually probe AuNRs.

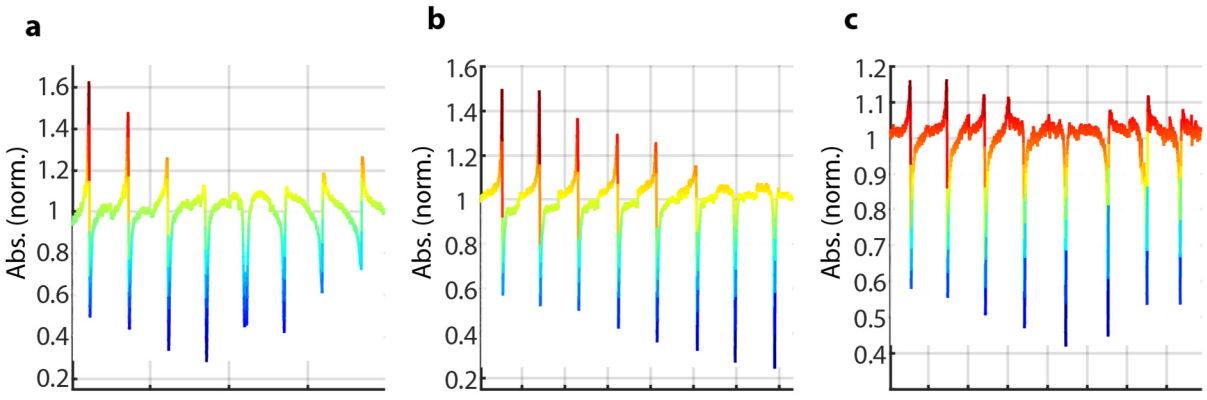

Figure 52: Evolution of Fano resonances.

A collection of AuNRs on the same toroid chip at various annealing temperatures. For each AuNR a representative Fano resonance is displayed here. The Fano resonance at each temperature is concatenated. The x-axis is therefore not meaningful. Spectra are divided by the mean value at the beginning and end of each trace to normalize the baseline. Annealing temperatures are (140, 145, 150, 153, 156, 159, 162, 165) in °C.

Using a fixed heat source instead of one that depends on the AuNR's absorption cross-section avoids complications from the feedback process where melting the nanorod causes the LSPR to redshift closer to resonance with the excitation laser, consequently increasing the nanorod temperature in a runaway process. After each annealing step, AuNRs are characterized individually via photothermal spectroscopy. Repeatedly probing the same ensemble of WGMs as a function of annealing shows the tuning of Fano resonances on several different AuNRs (Figure 52). A steady progression from the initial lineshape is observed. The lineshape of the Fano resonance[27,247,248] is characterized by a 5-parameter fit

$$y_{true}(\omega) = offset + \sigma_{scale} * |\frac{\omega\Gamma q_F + \omega^2 - \Omega^2}{\omega^2 - \Omega^2 + i\omega\Gamma}|^2 \qquad 7.1$$

where ω is pump energy (eV), Γ is the linewidth of the Fano resonance, Ω is the resonance wavelength in eV (almost exactly equal to the original WGM wavelength), σ_{scale} and offset are respectively scaling and offset terms. These final two parameters, not found in the original derivation[247] but used sometimes since then to account for incomplete coupling of the continuum and discrete resonance, is necessary here to

fit most of the observed Fano resonances. Fano resonances can also be fit very well by letting q_F be complex, which is more general than Fano's original derivation and is related to dephasing or to combination of coherent and incoherent pathways.[283,284] Occasionally doublet splitting is observed in Fano resonances, an observation consistent with the splitting of the underlying WGM being stochastic. q_F is a shape parameter that is a function of the energy and width of the LSP and detuning from ω_0:[27]

$$q_F(\Omega) = \frac{(\Omega^2 - \omega_0^2)}{\Omega\gamma_0} \cong (\frac{2}{\gamma_0})(\Omega - \omega_0) \qquad 7.2$$

Thus, q_F can be used to determine ω_0. A plot of q_F against ω_1 (or Ω) should be linear with a slope of $\gamma_0/2$ and intercept of $-\gamma_0\omega_0/2$. This is in fact observed. Further, plotting the calculated value of ω_0 against annealing temperature reveals a linear trend in blueshift (Figure 53). Measuring the LSP spectrum at lower spectral resolution over the full tuning range of the pump laser (1280-1365 nm) provides the LSP absorption more directly (Figure 55), largely unmodified by the weak coupling with the WGMs aside from the Fano resonances. Further, the theoretical line (Equation 7.2) obtained from fitting a Lorentzian to the LSP absorption (Figure 55) closely agrees with the trend assigned from q_F (blue and red data points). The somewhat limited spectral range of the pump laser introduces uncertainty into assignment of γ_0, and in ω_0 when it is outside the pump laser range. However, a clear correlation is seen between annealing temperature, change in ω_0 from directly fitting the LSP, and change in q_F and thus ω_0 obtained from measuring Fano resonances. The LSP resonance can thus be tuned to the desired wavelength band by varying the thermal dose and characterizing with single-particle photothermal spectroscopy. Further, the plasmon frequency shift is linear with annealing temperature in agreement with previous results.[281]

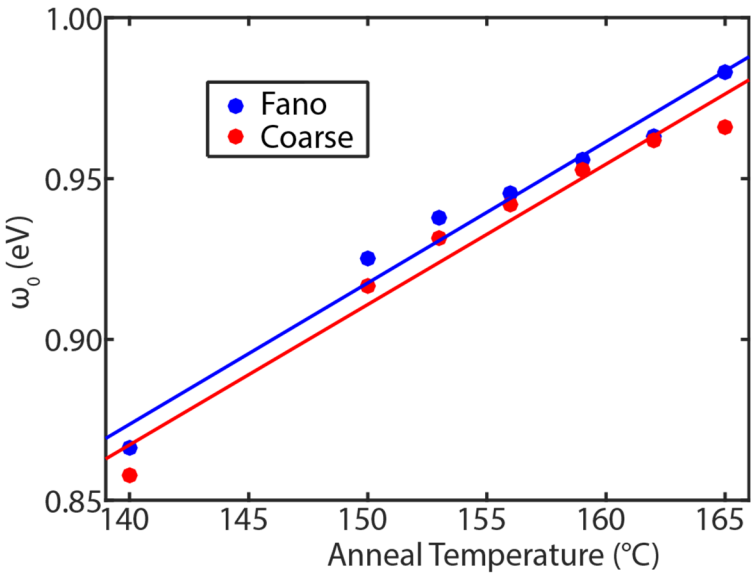

Figure 53 Determination of ω_0 tracked through evolution of Fano resonances.

The ω_0 calculated from Equation 7.2 for a collection of 22 Fano resonances on a single AuNR (Figure 52) is plotted for several annealing temperatures (blue dots) with a linear fit (blue line) for clarity. Each Fano resonance is fit with Equation 7.1. Fitting the coarse resolution spectrum (Figure 55) directly is an alternate source of ω_0 and is shown in red (dots) with a linear fit for clarity (red line). Over a wavelength range larger than the spectral window of the pump laser, both methods agree closely. Further, the blueshift in ω_0 is linear as a function of annealing temperature.

7.3 Fano resonance potential for sensing:

When fitting experimental data to a model, we are starting with a set of observations and trying to infer the underlying model parameters that generated this set of data points. In this specific case, the measured data is a set of known pump wavelengths x_i and corresponding photothermal absorption values y_i. The set of y_i are equal to the true value of the Fano-resonant absorption spectrum plus experimental noise. Because noise is present in all measurements, it is important to consider its impact on the maximum precision with which the model parameters can be known. To progress further in our analysis we need a statistical model of the noise. The Gaussian distribution is widely used in noise modeling. Here, analyzing the photothermal absorption data away from a Fano resonance reveals that the noise intensity is very well fit to a Gaussian distribution (Figure 56). We can further postulate that the experimental noise is i.i.d.,

independent and identically distributed. The measured values y_i are normally distributed about the value at x_i of the curve generated by the true parameter values. Every time we measure the same Fano resonance, we are sampling this normal distribution and should expect to see a slightly different set of y_i for the same x_i. However, because the experimental noise is uncorrelated between data points (white noise dominates over drift), a single spectrum can still yield high precision about the model parameters. Each additional data point [x_i,y_i] gives more information about the true parameter values. The likelihood that a given set of model parameters determined from fitting the data is equal to the set of true value is given by:

$$L(\theta|y) = P(Y = y;\ \theta) \tag{7.3}$$

where L is the likelihood function, θ is a vector where each element is a model parameter, y is the vector of y_i values and Y is the vector of true values (y_{true}) of the model. Specifically, for the five-parameter Fano resonance we use here the likelihood function is:

$$L(q_F, \Omega, \Gamma, \sigma_{scale}, offset) = \prod_{i=1}^{n} e^{\frac{-(y_{true}-y_i)^2}{(2*\sigma_{noise}^2)}} \tag{7.4}$$

where y_{true} is Equation 7.1 with the true parameter values, n is the number of data points, and σ_{noise} is the standard deviation of the noise level in the experiment, which is easily. Here we have decided to normalize the underlying LSP Lorentzian to amplitude 1. Taking the negative log for convenience gives:

$$-\log(L) = \left(-\frac{1}{2\sigma_{noise}^{2}}\right)\sum_{i=1}^{n}(y_{true} - y_i)^2 \tag{7.5}$$

We use the log likelihood function to calculate the Fisher information matrix,[282] whose elements are:

$$LL(\theta)_{ij} = E[(\frac{\partial}{\partial\theta_i}\log(L))(\frac{\partial}{\partial\theta_j}\log(L))|\theta] \quad 7.6$$

Each of these matrix elements are functions of the true value of each measurement parameter as well as the noise level and the number of data points in the spectrum. Intuitively, larger n (more data points) gives more Fisher information. More noise (σ_{noise}) corresponds to less certainty about the curve fit, and is manifested in lower expected Fisher information. For a given set of parameters, the expected fisher information can be found by substituting in to the Fisher information matrix and summing over x_i. Further, at each point x_i we sample from a normal distribution with standard deviation σ_{noise} centered at $y_{true,i}$ to account for the effect of noise.

The resulting 5x5 Fisher matrix can be inverted to get a matrix whose diagonal elements are the squared measurement uncertainties for each parameter value. In our experiment, this inversion must be performed symbolically before substituting in numerical values because the uncertainty about Ω is many orders of magnitude smaller than uncertainties in other parameters, leading to machine precision errors during inversion. Nonetheless, symbolic inversion followed by substitution gives uncertainties shown in Figure 54a,b. The uncertainty in Ω for a typical single Fano resonance (for example Figure 56a) is less than 1 neV. Measurement uncertainty is minimized at q_F = +/- 0.5 and increases at larger q_F. This is attributed to the rapid change of curvature in the lineshape of the Fano resonance at these intermediate q_F values, and is in marked contrast to a simple Lorentzian. At still larger q_F it begins to decrease again, possibly because the amplitude of the Fano resonance theoretically increases as detuning is increased. On the other hand, uncertainty in q_F (and consequently ω_0) is relatively constant for $-1 < q_F < 1$, and increases with further detuning of ω_1 from ω_0 (larger amplitude q_F values). This is consistent with the information derived from measuring the Lorentzian itself. As a function of noise level, the uncertainty in both Ω and q_F increases quadratically with increasing noise (Figure 54c,d). The Fisher information for a simple Gaussian

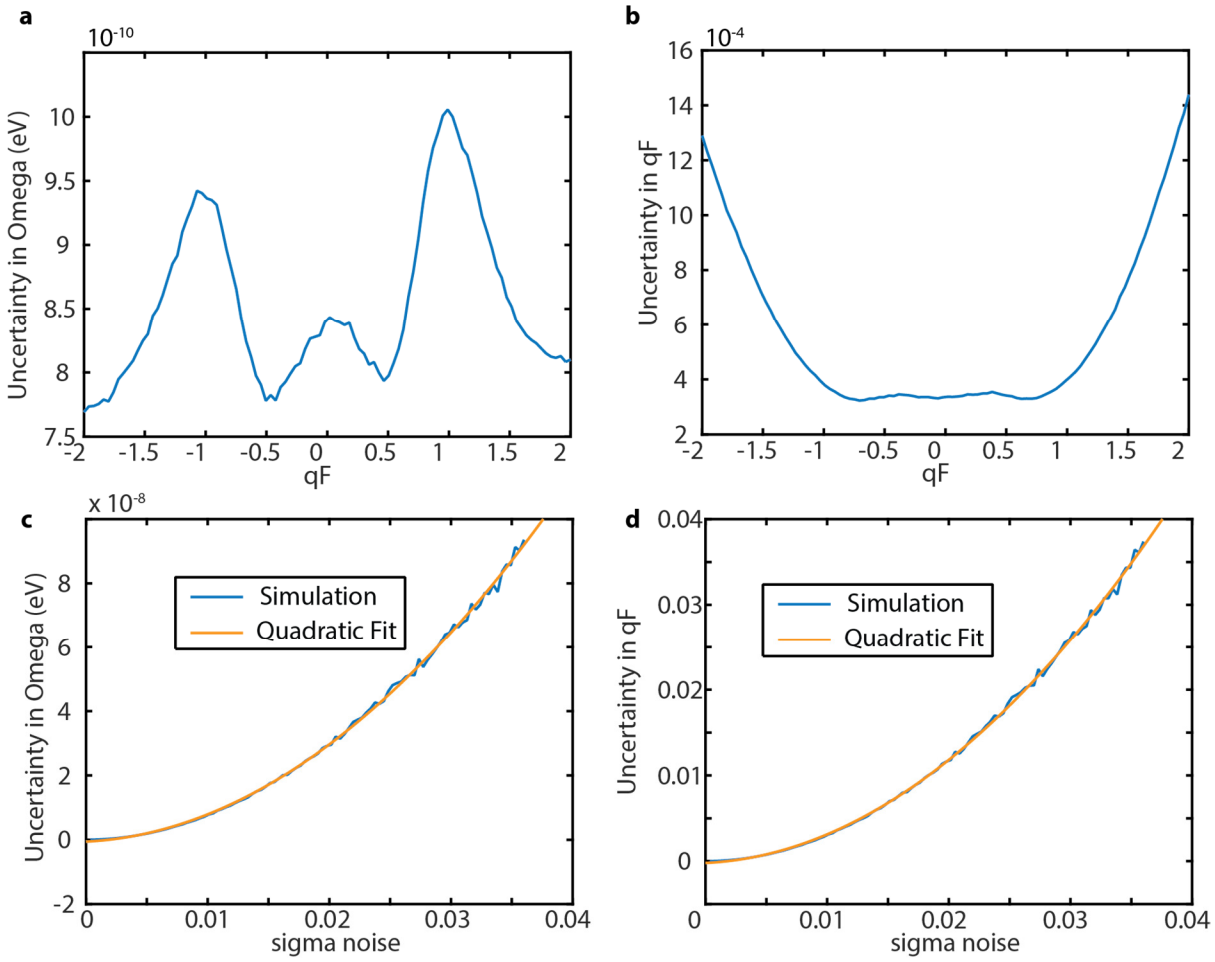

Figure 54: Measurement uncertainty in Fano resonance.

(a) Measurement uncertainty in Ω as a function of q_F (at constant ω_0). (b) Measurement uncertainty in q_F as a function of q_F. (c) Measurement uncertainty in Ω (blue) as a function of the noise level in the experiment. The Fano resonance is set to q_F = 1, with the noise level being proportional to the normalized Lorentzian amplitude of 1. A quadratic fit (orange) is shown. (d) Measurement uncertainty in q_F as a function of the experimental noise level.

distribution is proportional to $1/\sigma^2$, so this is what we would expect and serves as an important sense check for the calculations.

We can compare the calculation of the LSP resonance wavelength as determined by fitting the LSP spectrum directly to measuring several Fano resonances and calculating ω_0 from q_F with Equation 7.2. The Fisher information from each Fano resonance is additive and so each additional measured Fano

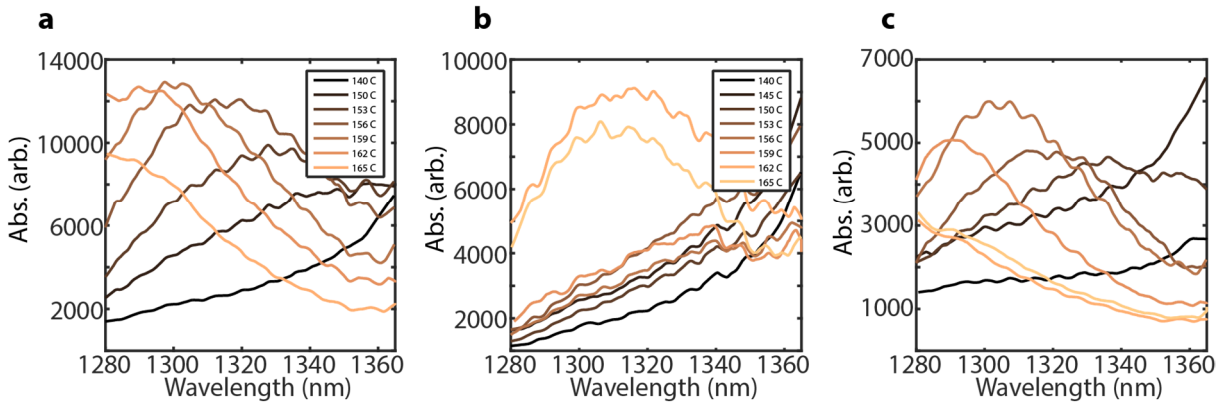

Figure 55: Coarse spectra of tunable Fano resonant AuNRs.

The coarse spectral resolution of six AuNRs as a function of annealing temperature reveals a gradual and particle-dependent redshift in the LSPR. To acquire spectra, the pump wavelength is tuned from 1280-1365 nm and the absolute absorption cross-section is determined by photothermal spectroscopy. A 5nm loess smoothing is applied for clarity. The y-axis is photothermal absorption signal in arbitrary units (femtometers of resonance shift per milliwatt of pump power).

resonance improves the precision in determination of ω_0. Because γ_0 is only a weak function of ω_0 for the long-wavelength LSPR we are measuring,[24] and geometrical reshaping is minor for the small changes in LSPR, it will not change during a typical sensing experiment. By contrast LSP_{max} will shift whenever the local refractive index changes. In a sensing experiment, this occurs when a single analyte binds to the AuNR. We can then take a typical[24,27] value of the AuNR γ_0 of 70 meV and further note that since Ω is very nearly equal to the WGM frequency, it will shift much less than ω_0. This assumption is justified as Ω remains constant despite substantial changes in ω_0 (Figure 52). A further justification is provided by the minuscule measurement uncertainty in Ω compared to ω_0. A shift in q_F is related to ω_0 by $\Delta[\omega_0] = (-\gamma_0/2)*\Delta[q_F]$. The smallest detectable $\Delta[\omega_0]$ is limited by the measurement uncertainty in ω_0 which is equal to $(-\gamma_0/2)$ times the uncertainty in q_F. For a typical trace, the uncertainty in ω_0 is 2-4 x 10^{-4} eV for $-1 < q_F < 1$ (Figure 54).

As for the Lorentzian peak, we repeat the derivation of the Fisher information matrix using a function of the form $\frac{C}{((x_i-b)^2+(0.5*a)^2)}$ where a is the FWHM (full width at half maximum), and b is the

center frequency, with *C* the normalization constant (not parametrized). Using the same noise level found for a single Fano resonance and used in Figure 54 (σ_{noise} = 0.0036), and with γ_0 = 70 meV, ω_0 = 0.94 eV, probing a measurement range of twice the FWHM, we find an uncertainty of 0.3 x 10^{-6} eV in determining ω_0. The improved performance resulting from measuring the LSP directly compared to measuring a single Fano resonance is not practically achievable in the experiment we report here. The noise level is much larger when the spectral range covers tens of meV (for the LSP) instead of tens of μeV (for a single Fano resonance). Over a wide spectral range, fluctuations in pump power and optical system transmission or polarization are more significant, which may be the source of this increased noise. The experimentally measured noise for a typical spectrum with ω_0 = 0.94 eV can be approximated by taking an experimental trace (Figure 55), fitting to a Lorentzian, dividing out the Lorentzian, removing smoothing, and taking a standard deviation. Doing this for a representative spectrum gives σ_{noise} = 0.052. This number is more than 10x higher than the noise over the ultranarrow spectral range of a single Fano resonance. Plugging this number back into the Fisher information calculations gives a measurement uncertainty for ω_0 of 0.058 meV. Thus measuring a half dozen Fano resonances gives as much Fisher information as measuring the whole LSP with a range of twice the FWHM, which would requires 140 meV of spectral range (about twice the tuning range of the pump laser we currently use). By contrast, the high density of WGM modes means that Fano resonances are easy to find. There are two other well-resolved Fano resonances within 0.3 meV of the resonance shown in Figure 52c. This calculation of the Fisher information for the LSP Lorentzian further assumes that ω_0 is located exactly in the center of the measurement window, which in general is not accurate. Detuning of ω_0 from the center of the measurement window will decrease the Fisher information.

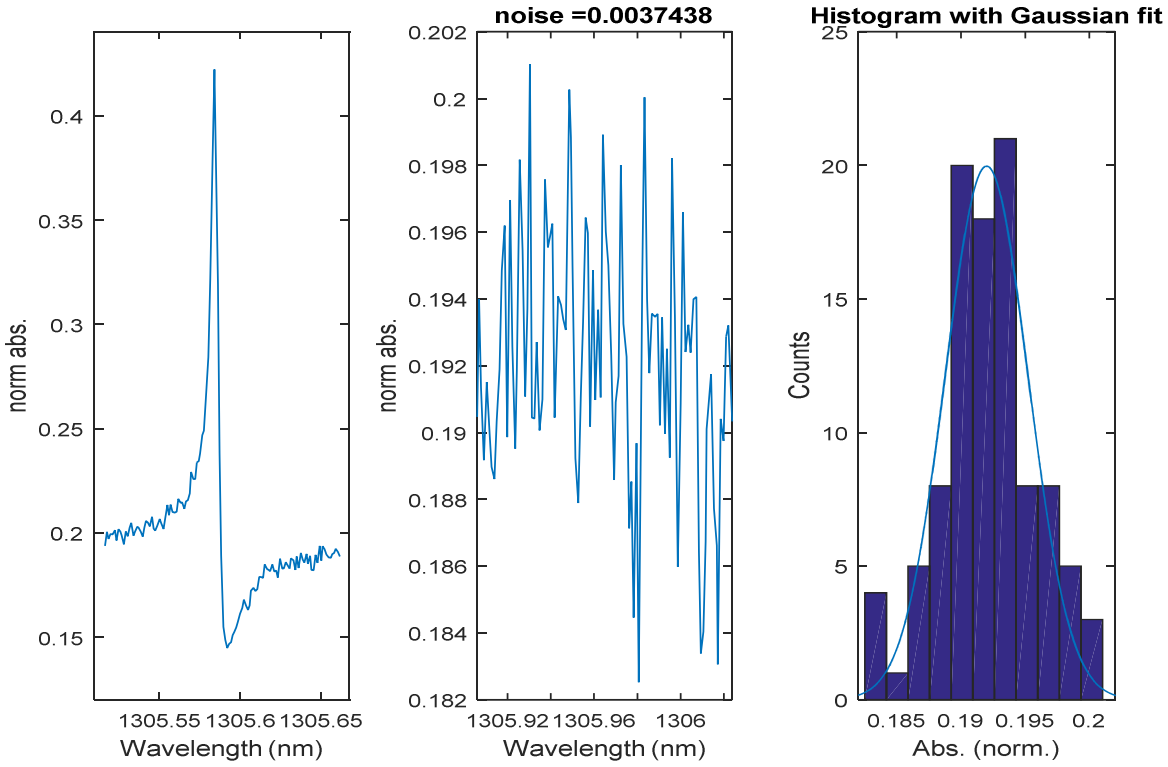

Figure 56: Representative Fano resonance and noise

(a) Sample Fano resonance used in calculations. This is a representative Fano resonance obtained in this experiment. (b) Photothermal signal (normalized to LSP maximum) away from the Fano resonance in (a). (c) Histogram of the 100 points shown in (b). A Gaussian fit (blue line) is shown.

And still the uncertainty in the Fano resonance assignment from q_F is much larger than it could theoretically reach. Uncertainty in ω_0 largely comes from the coupling between the scaling term σ_{scale} and q_F, which lessens the information available from q_F (which in a simpler system would control the amplitude of the resonance as well as the lineshape). A simpler 3-parameter Fano fit (q_F, Ω, Γ), again with σ_{noise} = 0.0036 and q_F = -1, has uncertainty of $q_F = 1.2 \times 10^{-5}$ which gives uncertainty in ω_0 of 4×10^{-7} eV, which is far more accurate than in the 5-parameter Fano resonance fit. More controllable coupling of the LSP and WGM, as is achieved through WGM optical trapping by Arnold et al.,[285] would be desirable because

making the orientation and position of each nanorod consistent may standardize the amplitude of the Fano resonances.

7.4 Conclusion

One advantage of measuring Fano resonances is that the spectral range of the Fano resonance is several orders of magnitude narrower than the full Lorentzian owing to the relatively dense mode structure of the microresonator. A single Fano resonance can be characterized with a scan range of 0.1 meV, far narrower than the > 100 meV required to record the full LSP spectrum. Chromatic aberration correction over a spectral range this wide is usually a nontrivial problem in single-particle absorption microscopy.[22] Moreover, Fano resonances in hybrid plasmonic-photonic resonators are a promising tool for photonic and sensing applications. Controllably tuning the LSP resonance in the presence of a forest of high Q-factor WGM modes provides utility. We have shown that these narrow Fano resonances, are a quantitatively useful proxy for the LSP_{max} wavelength. Exploiting the additive property of Fisher information indicates that measuring a collection of Fano resonances will lead to more accurate determination of the LSP shift from a sensing event than merely measuring the LSP spectrum. This analysis with Fisher information might be used by spectroscopists in other circumstances to get uncertainties in model parameters. Although heretofore largely confined to superlocalization microscopy,[286] determination of uncertainty through Fisher information is a tool with broad usefulness in spectroscopic fitting.

Chapter 8

8. Outlook and Future Directions

8.1 Improving detection limits

As discussed in Section 2.9 the largest source of noise currently appears to be jitter in the probe laser frequency. The pioneering work of Lu et al.[90] achieved then-record detection limits of single-particle binding on toroids using a common-path interferometer. The probe beam is split before the taper, with the signal path coupled into the toroid and the reference path split further and recombined. This forms a Mach-Zehnder interferometer, providing a real-time readout of the probe laser frequency. In this experiment, drift on the timescale of seconds was crucial to suppress, and so it was necessary to immerse the interferometer arms into an icewater bath to avoid room-temperature-induced fluctuations in the temperature of the fiber. In our experiment, noise is most important at 2-4 kHz, a frequency band where the room temperature is hardly fluctuating. This would potentially render the primary drawback of this technique—the long time required for stabilization of the icebath temperature—irrelevant.

The importance of minimizing the excitation volume has been extensively discussed elsewhere in this thesis, but it should be mentioned again since it is a primary path towards single-molecule resolution. We are currently pursuing this approach by exploring different microscope objectives with higher numerical aperture, particularly those that are not designed for a coverslip. Another approach would be to fabricate all-glass toroids[245] on a coverslip-thickness wafer and deliver excitation light through the back of a wafer with high-NA oil immersion objectives.

Aside from probe laser frequency jitter and toroid background absorption, what contribution do other fundamental noise sources put on the ultimate limit of detection? Shot noise and thermorefractive noise are the two largest non-technical noise sources. Other sources such as radiation pressure noise, ponderomotive noise, and photothermal noise can reasonably be neglected.[85] First we will consider shot noise. The power in the probe beam is limited to approximately 1 μW to avoid thermal bistability with toroids. The shot noise in the detected PDH signal is worked out in the supplementary information to the Nature Photonics manuscript, and is a function of toroid finesse (Q-factor), refractive index, major radius, and probe wavelength.[162] For typical parameters of $F = 1.2 \times 10^5$, $n = 1.44$, $\lambda = 1550$ nm, and $R = 24$ μm, the shot noise is 0.008 attometers of resonance shift. This value is incredibly small, corresponding to a photothermal heat source of 0.04 pW, compared to a peak single-molecule signal of 10,000 pW. In more conventional single-molecule experiments reaching the shot-noise limit is a desirable goal; here, it can be safely ignored. The actual fundamental detection limit comes from thermorefractive noise. This can be understood as fluctuations in the refractive index of the microresonator driven by statistical temperature fluctuations. This is not the same thing as ambient temperature drift, which is both much larger and much easier to filter out. Thermorefractive noise occurs at all frequencies and, within the bandwidth of the lock-in amplifier, is indistinguishable from a single-molecule photothermal signal. Calculating thermorefractive noise requires a detailed model of heat equilibration within the resonator and its surroundings. Building upon the work of Matsko[287] and Dobrindt,[288] I calculated the thermorefractive noise for a 2 kHz modulation frequency and 1s time constant in the Supplementary Information to the Nature Photonics manuscript. The value of 0.2 attometers resonance shift corresponds to a single-molecule photothermal signal of 1 pW, still several orders of magnitude below the threshold needed for single-molecule spectroscopy and a bit below current detection limits (Figure 5).

8.2 Underwater experiments: 2nd-generation resonator microscope (POSEIDON)

Single-molecule absorption spectroscopy would be a potent analytical tool for biochemistry. Single-molecule fluorescence for biological investigation is both the subject of a Gordon research conference and the 2014 Nobel Prize. The major challenge that has to be overcome is the operation of our toroid-based absorption spectrometer in an aqueous environment. Because the surrounding medium for any WGM must have a lower refractive index than that of the resonator, there are only a few possible surrounding media for a silica (n = 1.44) resonator like the toroid. Air (n = 1.00) and water (n = 1.33) are the only examples demonstrated in the literature. Toroids have been operated in water[110] before, sensing single viruses[220] and plasmonic nanoparticles.[94] Moving underwater presents some engineering challenges specific to our experiment, however. The photothermal signal will be reduced by immersion into water, biofouling will be an issue, and both pump and probe excitation must be moved to visible wavelengths.

The reduction of the photothermal signal results from the large thermo-optic coefficient of water partially offsetting that of the silica. Although COMSOL simulations show that only ~4% of the mode propagates in water for an 80 μm diameter toroid, the thermo-optic coefficient of water is ten times larger and of different sign than silica. Larger diameter toroids are necessary because the lower refractive index contrast between silica and water increases radiation losses at smaller diameters, making the Q-factor of smaller toroids unusably low. Larger toroids will have a smaller evanescent field, which ameliorates this affect somewhat, but the change in temperature for a given molecular heat flow scales inversely with toroid diameter, and so the toroid should be as small as possible to minimize the mode volume. Replacing water with D_2O, which has a much smaller thermo-optic coefficient, is one option. Another option is to mix water with glycerol, which has a much higher thermo-optic coefficient. Glycerol, used in the previous

single-molecule photothermal experiment,[51] has a thermo-optic coefficient so large it will drown out the silica contribution to the toroid resonance wavelength. However a delicate balance is in play here, because higher concentrations of glycerol in water will cause the refractive index of the solvent to exceed that of silica, at which point the toroid is no longer a waveguide. A more promising approach might be to coat the resonator with a thin layer of PDMS or PMMA. This is often used to suppress or ultimately enhance the thermal sensitivity of toroids because the large, negative thermo-optic coefficient of the polymers can overwhelm the thermo-optic coefficient of the silica.[289] In any event, mere suppression of the photothermal signal caused by water is unfortunate but not crippling.

Biofouling of tapered optical fibers is a side effect of the exposure of the optical mode to the surrounding medium.[73] The evanescent field of the probe beam in the air-guided region of the taper acts as an optical trap, attracting molecules from the solution to deposit onto the taper. Not only does this degrade probe beam transmission, it will cause buildup of an absorption background on the taper. The simple solution is to make fresh tapers for each experiment, although this would be tremendously inconvenient. A better solution might involve alternate means of coupling into the resonator, whether from a monolithic waveguide on a different chip or via the Fano-resonance-assisted free-space-coupling method discussed later in this chapter. The design of the underwater microscope (CODENAME: POSEIDON) takes these possibilities into account, allowing for either taper coupling for this other, more speculative means of coupling.

Switching excitation to visible wavelengths mostly provides a fabrication challenge. We have recently demonstrated fabrication of all-glass toroids with a transparent substrate.[245] The use of a polished, transparent wafer motivates a further development, all-glass toroids on a cover slip. Unlike a normal Ø 4” wafer with 525 µm thickness, these substrates are 170 µm thick. This would allow the use of a high-NA oil immersion (NA = 1.4) objective which have a working distance of ~ 170 µm. As noted in Chapter 1, increasing the NA provides a quadratic increase in signal/background ratio. An alternative is to

use a water-dipping objective, typically 1.0 NA with a 1-2 mm working distance. In the 2nd-generation resonator setup, excitation may end up being through the chip or from the front of the chip, in either air, oil, or water. The microscope design must be flexible enough to allow for this.

The design is shown in Figure 57. Initial testing used a tunable 780 nm laser, coaligned to an easily visible 488 nm guide laser. The guide laser is capable of 20 mW of power at the laser head and may also be used for absorption testing experiments. The 780 nm laser is a New Focus ECDL, and its lower noise and wavelength tunability make it substantially more versatile. Pump light propagates 4" off of the table surface until the final Ø 2" 45° mirror that reflects it upwards through a motorized half-wave plate and a high-NA focusing objective onto the toroid chip. In the 1st-generation setup, the use of an upright microscope necessitated using a gigantic periscope to bring the laser light up off the table. This was difficult to align and is removed from the 2nd-generation setup. The excitation objective may be oil, air, or water immersion, depending on the type of sample. The excitation objective is connected by a metal bracket to a hybrid drive differential micrometer / closed-loop piezo actuator with a nominal 10 nm resolution. This is important because the photothermal signal varies strongly with the pump objective focusing. A 3-axis, 20mm travel piezostage (Attocube) mounted on a 3-axis translation stage (Thorlabs) holds the sample and allows for relative positioning of the sample between the three objectives. Figure 57c shows a close-up view of the sample holder, which grips the sample on one end. This design is necessary to allow close approach by the short working distance objectives on the other three sides of the chip. A Navitar stereoscopic microscope with a Mitutoyo 20x ELWD apo objective provides height adjustment for the toroid and the taper (which is held from the same side as the toroid using a 3-axis translation stage). The Navitar and taper holder are both mounted on 66mm optical rails (Thorlabs) allowing for quick coarse alignment and disengagement, similar to an artillery carriage.

Transmitted light is collected by a second objective placed above the toroid chip. In this setup, excitation light will be visible, requiring exclusive use of all-glass toroids.[245] Imaging is provided by

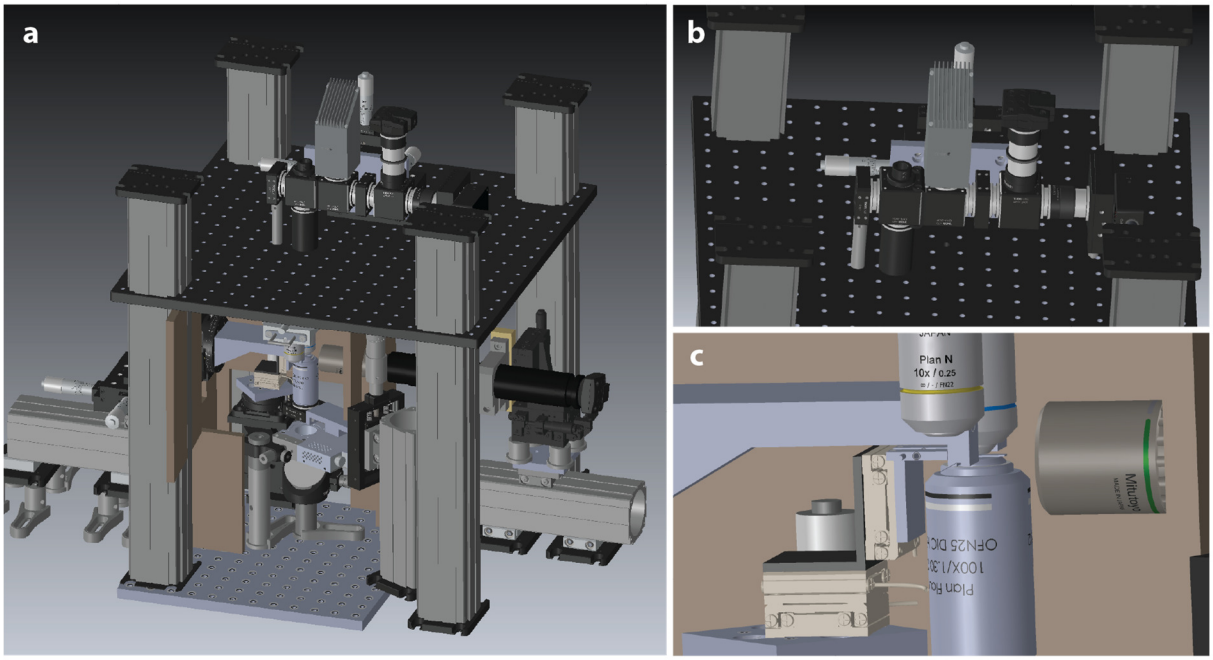

Figure 57: 2nd generation toroid spectrometer setup (POSEIDON).

(a) View of the entire microresonator coupling and excitation setup. (b) Imaging for alignment purposes and detection of transmitted light. (c) Zoomed-in view of coupling area. Both low-magnification (10x, yellow ring) and high-magnification (40x, blue ring) collection objectives are shown. This design was produced in Solidworks, a CAD (computer-aided design) program.

reflection from the toroid of lamp light inserted from the top. The detection path (Figure 57b) is designed to allow both white light imaging (for alignment) and collection of transmitted light from a tunable 780 nm beam (potentially used for interrogation of Fano-resonant AuNRs). Because visible excitation power may exceed 50 mW, the setup includes a 650 nm longpass dichroic filter directed into a beam dump. A second absorptive longpass filter provides OD 5 in the stopband (visible light) while transmitting near-IR light. This will cut down on the available light for imaging, regrettably, but the white light lamp could be replaced with a NIR LED for more illumination intensity. A 50:50 beamsplitter after the filters is used to direct light simultaneously to a camera (Thorlabs DCC1545M) and APD (Thorlabs APD430A). The APD collects transmitted probe light, potentially allowing for the free-space coupling experiments discussed later in this chapter. The entire imaging path is built on a breadboard mounted on four vertical 66mm

optical rails. Micrographs in Figure 58 show POSEIDON as it actually stands today. The size of the focused beam cannot be accurately imaged through transmission mode because the lower NA of the collection objective will overestimate the spot size.

The entire optical table is shielded with acoustic panels (AcousticsFirst AFBF1M) designed to damp out air currents, temperature fluctuations, and humidity fluctuations. They also serve to block visible pump light from escaping (useful from a safety perspective) and thermal light from entering (good from a thermal stability perspective). Each panel is a mixture of acoustic foam for absorbing vibrations, a hard polyurethane barrier for reflection, and a thin aluminum film for reflecting IR radiation. The side panels are held on by magnets that are drilled into the panels and attached to carriers on the 10S 1” rail (80/20 Corporation) that provides a superstructure for panel mounting. This allows easy removal and secure mounting of the acoustic panels. I also mounted 3/32” polycarbonate panels to the inside surface of the acoustic panels to give a rigid material for bolts to be tightened against, and handles to enable the panels to be picked up and manipulated. These 4’ x 2’ acoustic panels tend to curl up along the long axis, a problem solved by mounting a 3’ length of angle stock aluminum along the long axis. Holes were drilled into the box at strategic locations to allow feedthrough of power cables and signal cables.

Figure 58: 2nd-generation resonator setup (POSEIDON).

(a) Fully enclosed resonator setup alongside instrument racks. (b) Setup with no Navitar or taper, and both objectives coupled to an all-glass toroid chip. (c) Alternate view of coupling area including imaging/detection stack. (d) Rear view of coupling setup showing freespace optics with 488 nm and 780 nm ECDL lasers.

8.3 Simultaneous absorption, luminescence, and polarization

Combined measurements of absorption and polarization have not been performed at the room-temperature, single-molecule level before. Adding fluorescence spectroscopy to our existing setup would require nothing more complicated than adding an emission filter in front of the transmitted light detector (on POSEIDON) or adding a filter and detector (on SCORPIO). As an example of where this measurement capability would be fascinating, consider the problem of charge trapping in organic photovoltaics and organic light-emitting diodes.[213] Charge traps are thought to come from a variety of different causes including impurities, grain boundaries, and chemical changes (e.g. oxidation). A heterogeneous system with lots of low-concentration but high-importance electronic and conformational perturbations sounds like a perfect system for our single-object absorption spectrometer. Adding luminescence allows for correlation of emissive properties with physical structure and electronic structure, giving a deep understanding of what kinds of defects and other irregularities are important for affecting emission and charge transport.

8.4 Free-space coupling with gold nanorods and Fano resonance

Single-particle absorption spectroscopy, first demonstrated by Orrit et al.[20] in 2002, is an increasingly popular technique for characterizing nanoscale materials. A number of different approaches exist for reaching sufficiently high signal/noise ratio (S/N). One particularly successful approach is Spatial Modulation Spectroscopy (SMS), which involves periodic modulation of the position of the sample or the excitation spot by hundreds of nm.[23,24,290-292] Lock-in amplification at the modulation frequency (typically 1-2 kHz, limited by scanning equipment) provides a sensitive measure of the spatial dependence of

absorption. The signal is proportional to the spatial variation of the absorption signal, which is a combination of the spot size (invariant) and the size of the absorber. This method efficiently discriminates against background. Wideband absorption have been obtained through SMS with a simple white light source.[292] Another interesting technique is polarization modulation microscopy.[126] However, a single-molecule signal would give contrast of only 10^{-8} to 10^{-9}, which is simply not detectable with modern polarization equipment.

The tiny magnitude of a single molecule's extinction was our motivation for using the toroid; the extinction of a single-molecule is nearly impossible to detect without transduction. However, this introduced another set of problems. Coupling to toroidal microresonators generally requires a tapered optical fiber.[106,153] Tapers are fragile, easily contaminated (at least at the single-particle level), and most importantly, small fluctuations in their position alter the slope of the PDH error signal and thus contribute noise to our experiment. Further, their instability and propensity to drift in multiple directions, in addition to their tendency to jump and stick to toroids, makes it hard to signal average, an approach that would otherwise be a powerful addition to our toolkit. Integrating waveguides with toroids would solve this issue, but the only known report requires difficult fabrication with an impractically thick layer of thermal oxide.[156] Recently developed inverted toroids[293] with integrated waveguides are an intriguing prospect, but ultrahigh Q-factors have yet to be demonstrated. Free-space coupling into WGM microresonators is another area of active research. Slightly deformed on-chip toroidal-like resonators can possess high Q-factors and couple to end-fired light.[86,151,152,294] The mechanism involves resonant tunneling between high-Q WGMs and low-Q, free-space-coupled chaotic modes. The resulting tunneling involves a Fano resonance as excitation of the two modes by free space light interferes. However, critical coupling has not yet been demonstrated through this coupling mechanism. Therefore, a method of stable, long-term critical coupling to toroidal microresonators remains an ongoing challenge.

Recently we demonstrated that plasmonic nanoparticles deposited on the rim of a toroid will couple to the whispering gallery modes and produce Fano resonances visible in the particle's absorption spectrum.[27] Further, these Fano resonances are essentially equal to the unperturbed WGM frequencies because of the weak coupling between WGMs and the AuNR LSP. Now we aim to demonstrate that these absorption features can be used to sense the resonant wavelengths of toroid WGMs without actually coupling into the resonator. Free-space coupling offers the benefits of toroids for sensing (ultrahigh Q-factor, low mode volume) without the biggest drawback (coupling with finicky, fragile tapered optical fiber). It offers an alternative path towards a miniaturized optical device or one that could be integrated into a standard confocal microscope, because excitation is only provided tangent to the chip.

Removing the tapered fiber from the equation requires detecting the pump/probe beam via transmission. A gold nanorod has an absorption cross-section of approximately 1×10^{-10} cm^2 at the peak of its longitudinal surface plasmon resonance (LSPR).[27] A focused laser beam at $\lambda = 780$ nm and NA = 0.95 of Ø820 nm. This gives an area for the focused beam of 2×10^{-8} cm^2. Therefore, under ideal conditions the nanorod can absorb about 0.5% of the beam. The significant scattering contribution provides additional extinction. On a coverslip, AuNRs are easy to detect (Figure 59b) without SMS. A further enhancement in signal/noise ratio comes from implementing SMS. SMS has previously been used to take absorption spectra on gold nanorods and other nanoparticles.[16,295] By sinusoidally dithering the position of the beam by approximately the width of the PSF, a signal proportional to the spatial derivative of extinction is measurable. The sharp spatial dependence associated with a nanoscale absorber produces strong contrast with the much more slowly varying background from substrate scattering and instrument response. SMS imaging of single AuNRs on a cover slip is shown in Figure 59a.

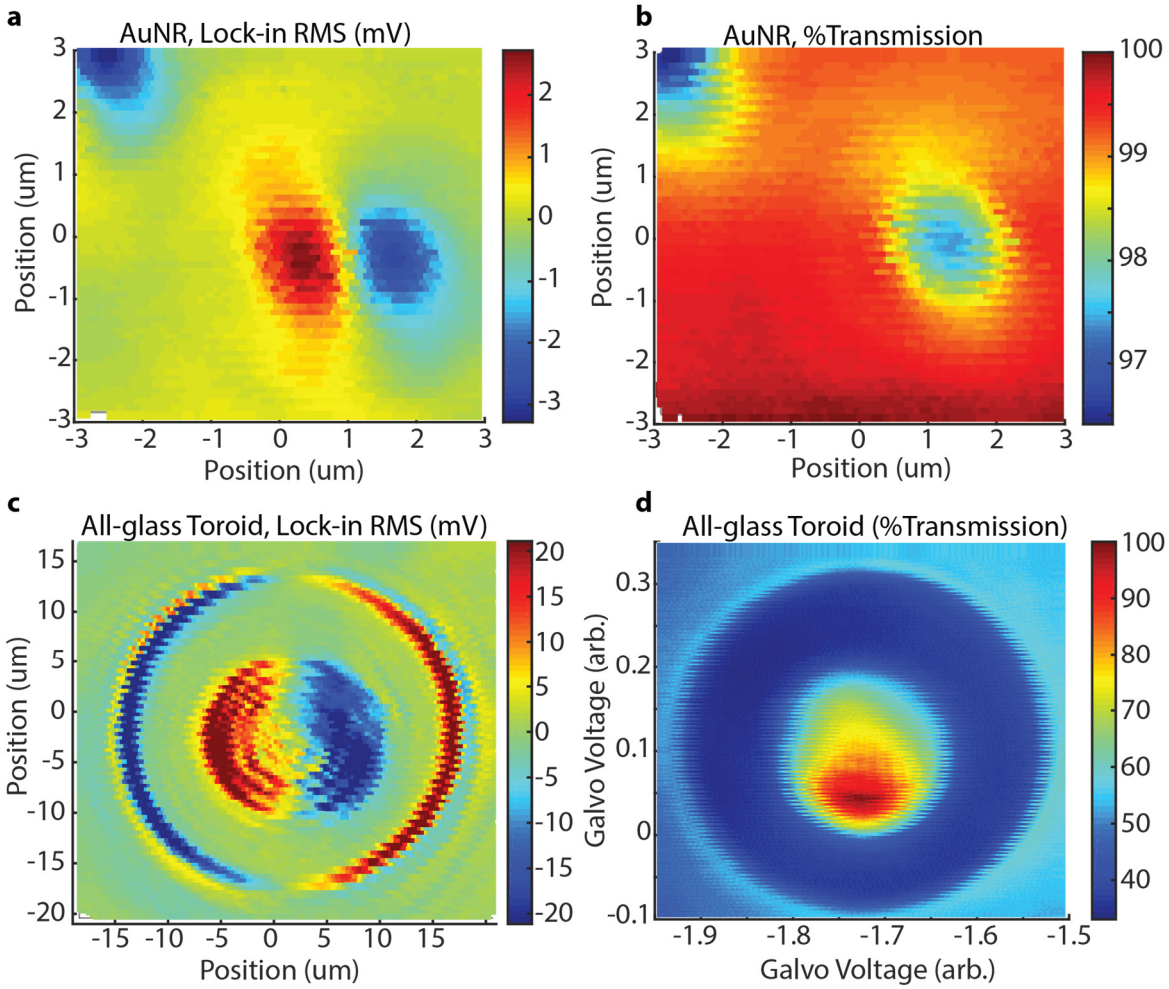

Figure 59: Transmission and SMS maps of AuNRs and Toroids at 780 nm.

(a) SMS for gold nanorods on a coverslip. The amplitude is the RMS voltage on the lock-in amplifier for the SMS signal in mV. (b) Corresponding transmission map of the same AuNRs. Transmission is normalized to the through-substrate transmission. (c) SMS map of an all-glass toroid. The pillar and rim are visible. The axis of SMS motion is horizontal. The lock-in scale was inadvertently saturated, causing this map to understate the magnitude of the background SMS signal. (d) Corresponding transmission map of the same toroid. Transmission is normalized to the maximum signal, which is substantially greater than the background transmission. This final affect is attributed to refraction by the curvature of the support pillar.

However, unlike all previous reports of SMS on single particles, we are not employing a flat, featureless substrate. In the 2-objective confocal geometry we employ here, transmitted power is a

function of both absorption, scattering, and refraction. The highly curved rim of the toroid presents a massive background to extinction measurements because it scatters incident light (Figure 59d). This motivates the switch to a new kind of spatial modulation spectroscopy. The SMS signal normal to the rim of the toroid is actually very large as the beam either scatters off the silica or transmits through free space. At 90° azimuthal from the maximum signal, however, the SMS of the toroid background drops to zero since the beam is sampling tangent to the rim (Figure 59c). As a result, we decided to try modifying SMS such that it constantly tracks the curvature of the toroid and is at all times tangent to the shape of the toroid. We refer to this new technique as circular SMS. At the time of writing, issues with relative phase drift of the two galvo channels prevents complete cancellation of the toroid background. Future work will be aimed at completely eliminating the toroid SMS background, detecting single nanorods, measuring their absorption spectrum in transmission, and using PDH locking to lock to Fano resonances.

Appendix 1

9. Finite-Element Simulations with COMSOL Multiphysics[5]

9.1 Overview of finite-element simulations of toroids

Because Maxwell's equations cannot be solved analytically for toroidal microresonators, optical whispering-gallery modes must be determined numerically. We employ the finite-element simulation of WGMs in toroids developed by Oxborrow.[117] This model takes advantage of the toroid's axial symmetry to greatly reduce the computational cost, modeling the toroid as an axially-symmetric 2-dimensional slice. The simulated optical mode intensity profile (Figure 60a) is converted into a three-dimensional intensity distribution by revolving about the axis of the toroid in post-processing. The optical intensity in the WGM is related to the electric displacement field (D) by:[117]

$$I=Re\{D_{azimuthal}\}^2+Im\{D_{axial}\}^2+Im\{D_{radial}\}^2 \qquad 9.1$$

One of the uses of this simulation is calculation of the fraction of light propagating through the surrounding medium, which is a function of toroid major diameter and the refractive index of the medium. Integrating the optical intensity allows for determination of this partitioning. For a typical major diameter of 45 μm, probe wavelength of 1.55 μm, and index of 1.00 (air), the fraction is slightly less than 1%. A larger fraction can be achieved by shrinking the toroid or increasing the surrounding medium's refractive index, although the radiative-limited Q-factor is dramatically suppressed as a consequence.

[5] Certain figures and sections of text in this chapter come from the Supplemental information to the manuscripts published in Nature Photonics, Journal of Physical Chemistry Letters, and Applied Physics Letters.

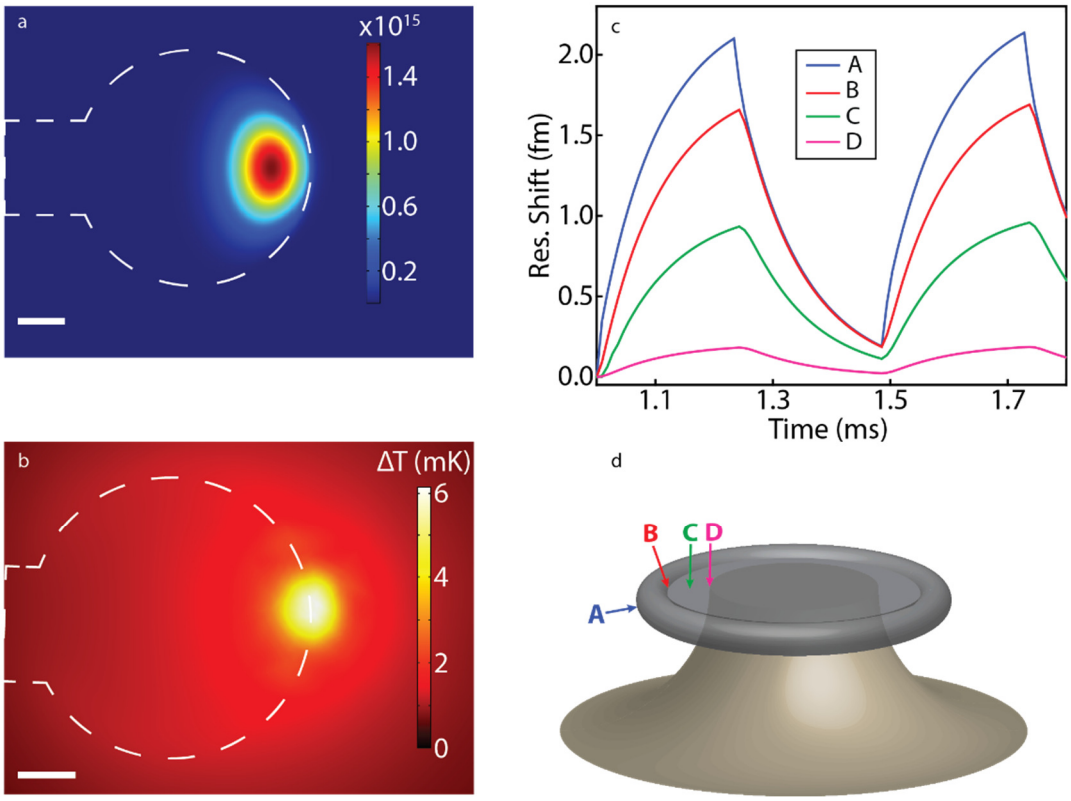

Figure 60: Finite-element simulations are used to determine absorption cross-sections.

a, Optical simulations of WGM modes are carried out with an axisymmetric 2-dimensional model. Color indicates the optical intensity as given by Equation 9.1. **b**, A 2-dimensional cutaway of the full 3-dimension photothermal simulation with a 10 nW heat source at the outer rim of the microresonator. Color indicates the temperature rise from ambient (mK) with a 2 kHz amplitude modulation frequency. **c**, The position of the same 10 nW heat source affects the resulting resonance shift. At the rim of the toroid, the measured shift is larger than in the interstitial region (between the rim and where the silicon pillar meets the oxide disk) or closer to the center of the toroid (at the edge where the pillar meets the oxide layer). The calculated absorption cross-section is scaled by the location of the nano-object using this simulated dependence. **d**, Schematic of the heating source positions on the resonator corresponding to the time-dependent resonance shifts measured in **c**.

I developed a series of thermal simulations to model the effect on the microresonator temperature from various heat sources. In Chapter 4, this simulation was used to model the effect of absorption of the pump beam on the silicon pillar for both conventional and re-etched toroid geometries. In Chapter 5 individual multi-walled carbon nanotubes were included in the model, with dimensions

extracted from SEM images, and treated as boundary heat sources. In Chapter 6 the pump beam modulation required a time-dependent solution, which was implemented in COMSOL. In this case the nanoscale gold nanorods were small enough to approximate as point sources. The position of the heat source on the top surface of the toroid was investigated as well, since in the experiment nanorods can be found on any part of the silica surface of the toroid.

9.2 Building the model

Photothermal effects on the toroid were modeled with the Heat Transfer Module of COMSOL Multiphysics. The physical dimensions of the toroid were extracted from side-view SEM images (Figure 35). The substrate (silicon wafer) and surroundings (air) were included in all simulations. Convection was found to have a negligible effect on the observed temperature increase (< 1%) and was not included in any simulations. In all simulations except for the measurements on re-etched toroids in Chapter 4 the change in temperature of any part of the toroid was a few Kelvin or less, so disregarding convection is reasonable. Material properties, except for the thermo-optic coefficient (discussed below) were taken from the COMSOL library. Equilibrium temperature is calculated by solving for the stationary solution with conductive heat transfer physics. Time-dependent simulations were conducted with all the parameters identical to the stationary simulations. Resonance shift calculations vary depending on the experiment and will be discussed individually.

As introduced in Equation 1.4, quantitative determination of the absorption cross-section requires a conversion between the measured resonance shift and the amount of heat dissipated by the absorbing nanoparticle. I is easily measured with a power meter and independent assessment of the excitation spot size, while q_{heat} must be determined from the measured resonance shift. This is facilitated by finite-element simulation where time-dependent heat transfer from a point source to the

microresonator is calculated. A three-dimensional model of the toroid with a point heat source at a particular location on the surface of the toroid (Figure 60b) is used to model the resulting temperature distribution with a 2 kHz modulation of the pump beam (Figure 60c). The change in resonance frequency is calculated by taking an overlap integral between the optical intensity of the fundamental mode and the temperature profile of the toroid, after scaling by the thermo-optic coefficient (dn/dT) of silica.[113] We have previously shown this approach agrees closely with experiment.[132,133] The resulting resonance shift can be plotted as a function of time and nano-object location Figure 60c). In this manner, the magnitude of the photothermal heat source can be determined by combining the scaling factors generated by the finite-element simulation with the experimentally determined resonance shift and position. If we assume negligible quantum yield of emission, then the heat dissipated by the single absorber is exactly equal to the energy of the light absorbed from the pump beam. The wavelength-dependent absorption cross-section is the ratio of energy absorbed to excitation intensity, given by Equation 1.4. Experimental absorption cross-sections are corrected for spatial dependence (Figure 60c) using the location determined by photothermal mapping (Figure 45).

9.3 Photothermal mapping of toroid background

Heating by the 640 nm pump laser is modeled by a series of five 1-μm thick cylindrical heat sources of decreasing intensity. The total heat generated is equal to the incident optical power adjusted by the measured reflectivity of 2 μm of thermal oxide on silicon at 640 nm (R = 0.24). The heat is divided among the five heating regions with a decaying exponential corresponding to the penetration depth of 640 nm light in silicon.[296] The volume of silicon heated by the laser is approximately 10 μm^3, given by the product of the spot size and penetration depth in silicon (3.3 μm). Small changes in the size distribution of the heat sources were found to contribute only minor variations to calculated thermal properties. Resonance shifts

are calculated from the equilibrium temperature of the silica rim, which is found to be highly uniform with the pump beam centered on the toroid. The thermal expansion of silica is an order of magnitude smaller than the thermo-optic effect[297] and was neglected in these calculations. In the low-power regime the thermo-optic coefficient of the silica can be assumed to be constant, with a value of 8.5×10^{-6} K^{-1}.[113] At greater shifts the temperature dependence of the thermo-optic coefficient had to be accounted for (see Figure 37).

9.4 Mapping of single MWCNTs

Single multi-walled nanotubes were modelled as cylinders with dimensions and locations extracted from SEM images. Nanotubes were treated as boundary heat sources. Steady-state solutions to the conductive heat equation are solved for using a software-defined extra-fine mesh. As before, both radiative and convective heat transfer were found to have negligible (< 0.1%) effect on the calculated temperature rise. From the heat transfer solution, two-dimensional slices of the mode area of the toroid are taken at regularly-spaced azimuthal intervals (5°) and overlapped with the known mode profile of the toroidal microresonator.[117] The resulting resonance shift is averaged over every azimuthal position, and the simulated resonance shift is compared to the experimentally-measured resonance shift. The inputted heat flow required from the nanotube is adjusted until the simulated resonance shift matches the measured shift. Knowledge of this heat flow is necessary for calculating the per-atom absorption cross-section, as described in section 4 of the Supporting Information to the JPCL manuscript. Note that in later generations of the code (used for example in the work in Chapter 6) a more sophisticated treatment of the overlap between the optical mode and the temperature is developed (Sections 9.5-9.6).

The time to reach the equilibrium resonance shift was also simulated. The simulated resonance shift as a function of time is plotted in Figure 61. Simulations in COMSOL are used to plot the temperature

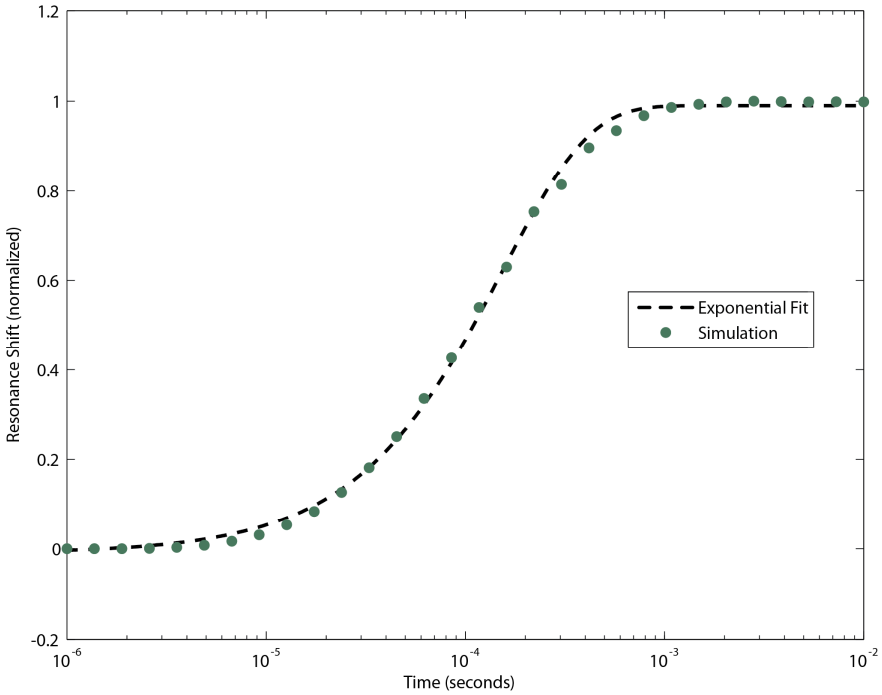

Figure 61: Time dependence of resonance shift (simulated).

The resonance wavelength shift of the toroid as a function of time increases (fit to the form, 1-exp(-t/ τ)) with an rise time of τ= 154 μs (1-1/e).

distribution at each time point, and the resonance shift of the toroid is calculated just as in the equilibrium calculations. Assuming only conductive heat transfer, thermal equilibration should follow a mono-exponential time dependence (this is the solution to the Helmholtz equation, which describes heat conduction). An exponential fit closely matches the simulated time dependence. The calculated 1/e rise time (154 μs) is similar to that experimentally measured for a bare toroid pumped at the center of the toroid (τ = 240 μs).[132] This agreement is not unexpected—in one experiment the heat is deposited at the rim of the toroid and must reach the center for equilibration, and in the other it is deposited at the center and must reach the rim of the toroid to affect the propagating mode.

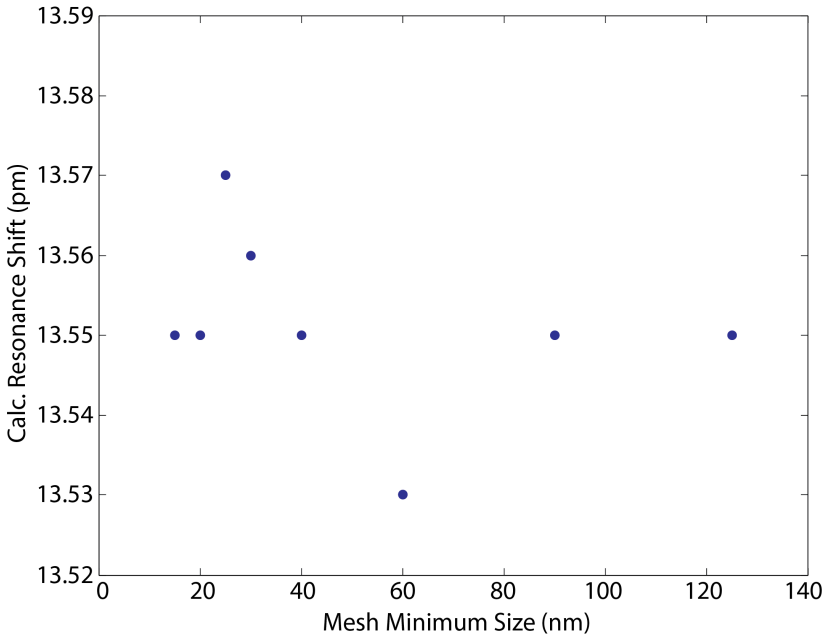

Figure 62 Effect of meshing size on the simulation's accuracy.

The minimum allowed edge length for a tetrahedral meshing of the nanotube-decorated toroidal microresonator is varied from 15 nm to 125 nm. No systematic effect on the calculated resonance shift under pump beam illumination is found.

The effect of varying the smallest allowable element size in the tetrahedral meshing of the modeled microresonator-nanotube system was investigated. Figure 62 shows that large changes in mesh size have minimal (<0.5%) effect on calculated resonance shifts.

The effect of varying the distance between the nanotube and the surface of the resonator was also investigated. Figure 63 demonstrates that shifting the vertical position of the nanotube over tens of nanometers, either by raising it above the microresonator surface or by lowering it below the surface, also has a minimal effect (<0.5%) on the calculated resonance shift. One of the conclusions that can be drawn from this result concerns that magnitude of interfacial thermal resistance. Several groups have endeavored[225,298-301] to experimentally determine the interfacial thermal resistance between a nanotube and various surfaces, with a large range of values observed. While such an interfacial resistance was not

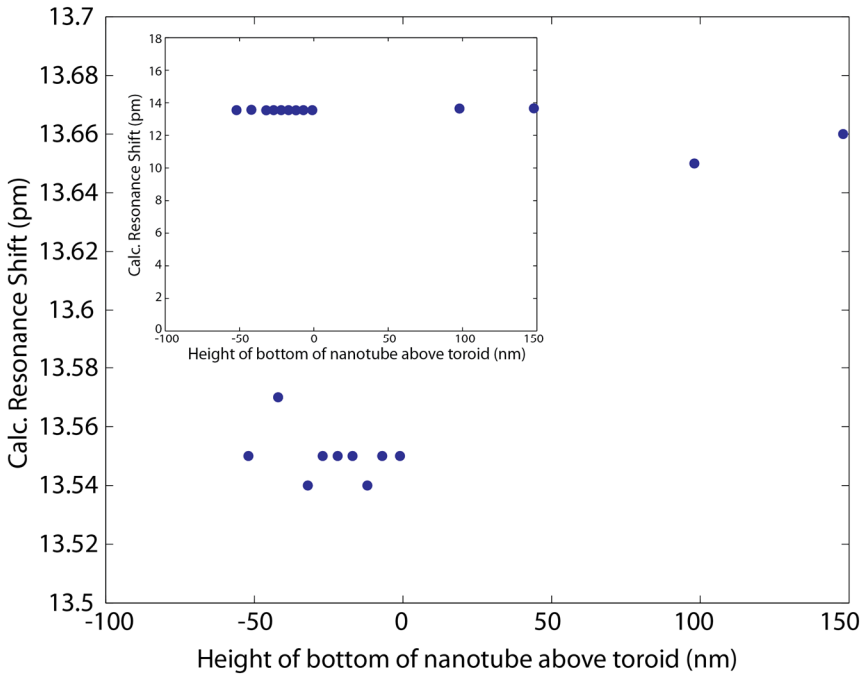

Figure 63 Effect of nanotube-microresonator interfacial contact distance on calculated resonance shift.

The distance between the bottom edge of the nanotube and the top of the silica surface of the microresonator is varied and the effect on the calculated resonance shift measured. The nanotube is 52 nm in radius, and so the nanotube is 50% "immersed" in the resonator at x =-52 nm; conversely, at x = 150 nm the nanotube is suspended in air more than 1 diameter above the surface. Larger, more positive values along the x-axis correspond to less contact area between the nanotube and the resonator. No significant trend is observed, implying that this simulation is tolerant of large uncertainty in the nanotube-silica interfacial thermal resistance. **Inset:** Calculated resonance shift with the entire axis range, demonstrating that the variations observed in the main figure are negligible compared to the total resonance shift.

explicitly included in our calculation, the opening up of a highly insulating thin air layer between the tube and the resonator surface can indirectly probe this possibility. This situation has little effect on the resonance shift, likely due to the extremely small heat capacity of the nanotube relative to the microresonator. Since the inclusion of this layer had only extremely minor influence on the microresonator equilibrium temperature distribution and resulting photothermal shift, we infer that not explicitly including an interfacial thermal resistance is a reasonable approximation.

The simulation is also highly insensitive to the thermal conductivity of the nanotube. Various reports have placed this conductivity in the range of 3000 W/mK to 42 W/mK, depending on the measurement method and the concentration of defects in the MWCNT.[302-307] Changing the conductivity in the model from 3000 to 3 W/mK changed the predicted resonance shift by only 1 part in 10,000. Therefore, we conclude that the wide range of possible values for the thermal conductivity of the nanotubes used in this study does not affect the accuracy of the calculation.

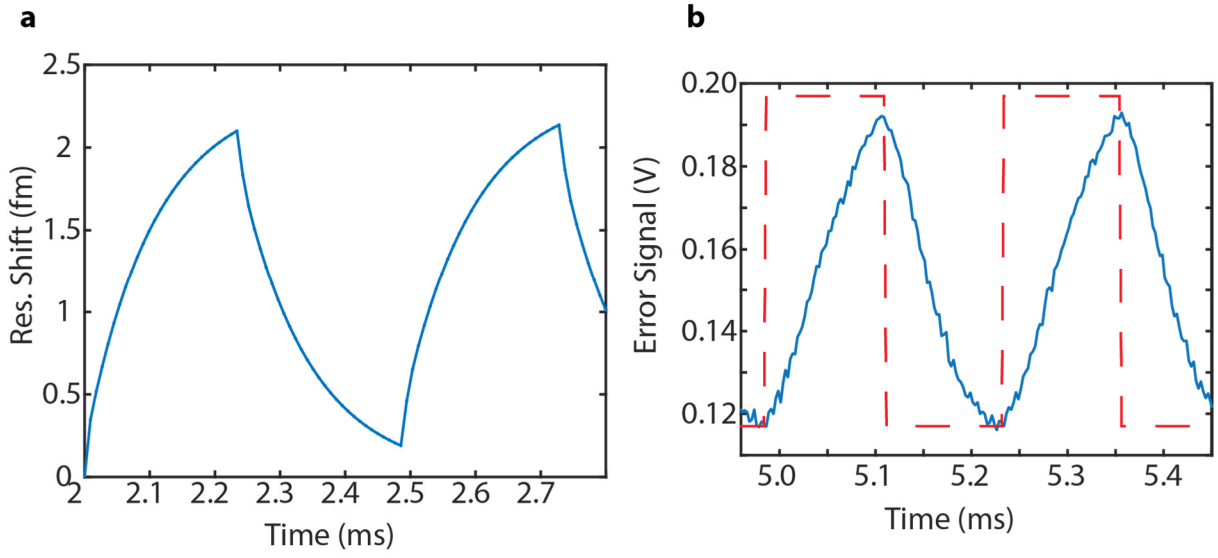

Figure 64 Timescale of resonance shift.

(a) Theoretical resonance shift from a single molecule dissipating 10 nW of heat under excitation modulated at 4 kHz. A characteristic exponential rising and falling behavior is observed, reminiscent of the charge on a capacitor as it undergoes charging and discharging. (b) Experimental error signal when a single organic nanoparticle is pumped with a 4kHz modulated beam. The timescale for equilibration may differ slightly between theoretical and experimental data since the thermal relaxation time is sensitive to the details of the geometry of the particular toroid (Chapter 4).

9.5 Single gold nanorods with amplitude-modulated pumping

In Chapter 6, I described the use of an amplitude-modulated PDH error signal for single-particle spectroscopy. Because the amplitude modulation frequency (either 2 kHz or 4 kHz) was comparable to the thermal equilibration time for the toroid (~4-5 kHz, Chapter 4), the stationary state solved for in earlier generations of the code is insufficient. I switched the code to a time-dependent heating source and solved with a series of 90 time steps. Figure 64 shows that the resulting simulation (panel a) clearly captures the rising and falling exponential behavior of resonance shift as a function of time that is experimentally observed (panel b).

In simulations and analysis of the experimental result I neglected the effects of heating on the AuNRs. While photothermal annealing and melting of AuNRs is a well-characterized phenomenon at higher optical intensity,[262,269,281] at the powers used in the experiments of Chapter 6 the AuNR is not significantly heated. When the AuNR is pumped at the maximum level applied in this experiment, the AuNR will shift the WGM frequency by approximately 12 MHz, corresponding to a heat dissipation of 500 nW. In finite-element simulations, the highest temperature reached by the point heat source modelling the AuNR at 500 nW dissipation is 670 mK above room temperature. There are two complications with interpreting this simulation. First, the nanoscale details of the thermal contact between the AuNR, the CTAB capping bilayer on the AuNR, and the silica surface are neglected. This interfacial resistance would likely increase the actual temperature on the AuNR. Conversely, modeling the AuNR as a point source ignores the effect of having substantial surface contact with the resonator, which would increase heat conduction to the silica and therefore cool the AuNR. We can then regard this sub-Kelvin heating as an estimate and seek for additional methods of estimating the AuNR temperature.

A very different method of measuring optical absorption by single AuNRs was demonstrated by Ma et al.[269] that enables measurement of the exact temperature of the AuNR. After rescaling the temperatures

reported in this work to the lower optical intensity and higher absorption cross-section that we employ, we find a worst-case temperature rise of ~ 420 mK. This determination is in reasonable agreement with the temperature rise calculated by finite-element simulations. In either case, the heating of an AuNR to < 1 K above ambient temperature will not have any significant effect on the LSP linewidth, LSP frequency, or refractive index. Geometrical effects on the LSP wavelength from laser-induced lattice heating of AuNRs are minimal[308] and can be safely neglected here.

9.6 Details of how resonance shift is calculated in the time-dependent photothermal code

I will now describe in detail how the time-dependent photothermal code operates. Parameter values and names are accurate as of the time of writing of this thesis. This code was written and deployed with COMSOL v4.3. It is not advisable to read this section without a copy of the code open on your monitor.

Heating is simulated by a point source at a user-defined location with heat flow defined by the parameter *pheat3*. For example, a heating source switching between 10 nW (pump beam on) and 0 nW (beam off) would be given by the following definition: 1e-8*wave1(t[s])+0.5e-8 . The frequency of modulation is given under “Waveform 1 (wave1)” where a linear frequency of 2.01 kHz is specified as an angular frequency of 2π*2010. The amplitude is 0.5 and phase is zero (the phase is irrelevant). Because the modulation frequency is many orders of magnitude shorter than the excited state lifetime of any reasonable molecule at room temperature, approximation of photothermal heating with a square wave is valid.

The WGM field is simulated in a different COMSOL code and import as a .txt file. Specifically, the total |D-field|^2 is output from the WGM simulations (Equation 9.1). This is necessary because the refractive index changes between the toroid and its surroundings. The thermal simulation is not programmed with a refractive index so it must be imported. The D-field is imported under the "function" section, where the function name is *oxmode* and the position in the file is 1, interpolation is linear and extrapolation is constant. There are no arguments, and the function is referred to as *com* elsewhere in the code. The txt file of the WGM (at the time of writing I was using "CorrectDField_25nm_air_46um_axmode2.txt") is a 3 x N file where the columns (in order) are r, z, |D|^2 (electric displacement field). R is radial position and z is height (this code was written by Mark Oxborrow with 2-dimensional azimuthal symmetry). The actual exported data comes from the file "Mode profile of toroid for AuNR.mph". In the WGM simulation, the total D-field is defined by (Equation 9.1) on a regular grid in spreadsheet format with 452 points each for r and z values. Unsurprisingly, if the geometry of the toroid is modified (for example to simulate larger toroids or all-glass toroids) then it must be changed in both the thermal code and the WGM code equally.

The thermal code should take roughly 20 minutes to run on a fast 2011-vintage desktop computer. A crude estimate of resonance shift comes from a line average along the toroid's outer rim of the data in Solution 3, which is then multiplied by (9.5*(T-293.15)) with units set to mK. This provides a sense check on the resonance shift in units of femtometers, where 9.5 is equal to λ/n *dn/dT. To obtain a more accurate measure of resonance shift, several steps must be taken in postprocessing. First, right click on data sets and make a Function 2D. For function, select Interpolation 1 (oxmode). The first parameter should be y, with a range of e.g. 17 to 29, and the second is x, e.g. 16.5 to 28.5. These coordinates define a sampling grid that fully includes the rim of the toroid, with units in microns, and should be modified if the toroid geometry changes. Next, right click on data sets and create a parametrized surface. Choose *Solution* 3 for the data set. The first parameter is called *s1* with a range of 17 to 29, and second parameter is *s2* with range of 16.5 to 28.5. As before, these values are functions of geometry. In the expression

section, x should be *s2* and y is *s1*, while z is 0. Next make a Revolution 2D with *ModeSlice* as the data set. The axis entry method should be Point and Direction. For point, both x and y are zero; for Direction, y is 1 and x is 0. Make another Revolution 2D where the data set is *ModeSlice*. This should have the same settings as the other Revolution 2D. Then make a Join called "*AzimuthOverlap*". For Data 1, the Data field is *ModeSlice* and Solutions should be set to 1. For Data 2, the data is *ThermalSlice* and Solutions is All., while the method is explicit. Next make a Join called "*Overlap3D*". For Data select Revolution 2D 1 and Solutions One. For Data 2, Data Solution 3 and for Solutions pick All. The method is Explicit. Finally, make a Solution of Solver 1. The Model is Model 1 (*mod1*) and the frame is Material (x, y, z). Choose the solution at angle (phase) 0 with scale factor 1.

The next processing step is a computationally expensive volume integration of 1 with dataset set to *Overlap3D,* evaluated for all time points. The Expression is "data2(T-293.15)*data1(oxmode(x,y))*(8.6e-6)*1.08e9/(5.31e17)". The first term in the expression, data2(T-293.15), is the temperature increase field in units of Kelvin (temperature rise above 293.15 K). The other term *Data1(oxmode(x,y))* is an unnormalized D-field distribution imported from the WGM code. 8.6e-6 is the thermo-optic coefficient of silica (this assumes the surrounding medium is air). The factor of 1.08e9 involves unit conversion (specifically, it's equal to 1550 nm / 1.44 *(10^6 fm/nm)) and is a function of the probe wavelength (1550 nm) and toroid material (n = 1.44). The final term 5.31e17 is an integration constant that comes from "Volume Integration" of "Revolution 2D 1" of Expression "oxmode(x,y)". This integration constant must be recalculated if the toroid geometry, probe wavelength or surrounding medium is changed. When the surrounding medium is not air, it cannot be neglected, and is accounted for by the following. The photothermal shift from the thermal oxide volume is "data2(1*(dom-4)/2)*data1(oxmode(root.x,root.y))*(data2(T-293.15))*(0.86e-5)*1.08e9/(6.78e17)" where the *dom* terms are used to specify a domain index. The specific algebra picks out the toroid rim, as COMSOL decides automatically on domain indices. The integration constant has changed here because some of the D-field

is in the surrounding medium; specifically, this number assumes H_2O (n = 1.33). The contribution from the surrounding medium is calculated from "data2(-1*(dom-6)/2)*data1(oxmode(root.x,root.y))*(data2(T-293.15))*(-9e-5)*1.08e9/(6.78e17)" . The same integration constant is used because the term data2(-1*(dom-6)/2) selectively picks out the mode fraction propagating in the surrounding medium. Note that the thermo-optic coefficient of water is more than 10x larger than that of silica, so even a small amount of D-field extending into the water has an outsize effect. More importantly, the sign of resonance tuning is flipped so it counteracts resonance shift in the silica from photothermal heating. Simply summing the two contributions gives the overall resonance shift. The results of this volume integration are the final data in units of femtometers of resonance shift.

9.7 Known bugs and tips for new users

I will now list and explain a series of problems that can charitably be described as "quirks" of the code. Some are related to the specifics of the model, and some appear to be outright bugs.

The time-dependent thermal simulation cannot be evaluated immediately after opening the code. Every time the file is opened, the user must go into Study 1→solver configurations→ solver 3 and right click on solver 3 and select compile equations. The second field, use study step, must be changed so it shows "Step 1: Time Dependent" instead of a blank slot. The Oxborrow code for solving toroid WGMs in version 4.3 of COMSOL has a bug. It has to do with the assignment of dielectric constants to each region. The simulation only sees two regions: silica (region 1) and surroundings (region 2). It is possible to use this simulation for a toroid immersed in a different medium (for example, water) without further changes. However, the code divides the complicated termin in Equations: Weak Form PDE by e1 (ε_1, defined in Variables 2). Although the parameter e2 (dielectric constant of surrounding medium) is defined in Variables 3, it is not actually used in the Weak Form PDE equations. Thus, changing the value of e2 does

nothing. E1 and e2 also exist in the parameters section. Nominally e2 is the relative permittivity of air but can be redefined at will. This bug can be fixed by going to Model → PDE→ Weak Form PDE 2→ the first line of "weak expressions" should be

(-(Haziz*M*test(Haxi))+Hazir*test(Hazi)+Hazi*test(Hazir)-Hrad*M*test(Hazir)-Haxi*M*test(Haziz)-Hazir*M*test(Hrad)+(Haxi*M^2*test(Haxi)+(Hazi-Hrad*M)*(test(Hazi)-M*test(Hrad)))/r+r*((Haxir-Hradz)*test(Haxir)+Hazir*test(Hazir)+Haziz*test(Haziz)-Haxir*test(Hradz)+Hradz*test(Hradz)))/e2

In a different vein, consider the surrounding medium from the point of view of data visualization. In simulation (and in real life), the toroid is surrounded by either air or water. By default this makes the toroid impossible to see, which is hardly useful. To hide the air/water domain, specify a view and then hide geometric entities and geometric objects. Hiding entities is more helpful. To make a nice visual representation of your simulation, make a 3D surface plot. Under "Hide geometric entities", select boundaries instead of domains and pick out the outer air/water boundary. Add spotlights and play around with the location and orientation to get the lighting correct. First click on the surface plot, then click on the spotlight in the views section and adjust the spotlight (position, orientation, and specularity; specularity is how "shiny").

In terms of setting up a parametric sweep or a time-dependent simulation, it is possible to generate a parametric list inside COMSOL. For example, if you want a simple linear or logarithmic set of time points there is built-in functionality. Sometimes, however it might prove useful to generate a list of parameters in MATLAB, perhaps because the parameters are a non-regular set or are otherwise arbitrary. A vector generated in MATLAB can be exported to Microsoft Excel and then exported from Excel as a .csv file. Copying and pasting from the csv file (as opened in the program Notepad) into COMSOL allows you to input an arbitrary set of parameters for a parametric sweep or time-dependent simulation. The

circuitous route to exporting is a result of strict and unclear formatting requirements for parametric lists in COMSOL.

The most baffling error I encountered involved negative relative temperatures in time-dependent simulations. Specifically, I found that with a time-dependent heating source the region of the toroid nearest the toroid would actually dip below room temperature after the heating source was turned off. This is particularly bizarre because the outer boundaries of the simulation are fixed at room temperature (defined here as 293.15 K). It should be thermodynamically impossible for a region right next to a former heat source to go below that value. Based on my reading of posts by the user Ivar Kjelberg on the COMSOL forums, I attribute this result to spatial aliasing. Because of the low thermal conductivity of silica, the insufficient mesh density and the short time steps (few microseconds) in the simulation caused problems analogous to aliasing in audio recording. Turning off the heat source instantly implies a broadband frequency content (analogous to the Fourier spectrum of an impulse). Because heat spreads slowly through silica, the timescale for diffusion across a single mesh element can be similar to the time step. By not catching the high-frequency components of this impulse, there is an aliasing effect that locally perturbs the gradients calculated by COMSOL to determine conductive heat transfer. Contemporary versions of the code have a mesh with sufficiently high density to overcome this problem.

Incidentally, meshing at high density for micron-scale geometries can be an exercise in frustration. Meshing has been described as “an art, not a science.” Repeated tweaking of growth rate and minimum element size parameters are necessary to mesh sometimes. This problem seems to originate with the confluence of two factors. First, the toroid rim is highly curved, especially given that the simulation bounds are a few hundred microns in size. Second, the mesh density must be high because of the rapid spatial variation in temperature near the point heat source.

Finally, the thermal code will often crash when you try to plot the data as a line graph. You should always save after the code runs (if it's successful), and then go to the volume integration under derived values and, on the table, click Copy Table and Headers to Clipboard. Then you can paste the data into MATLAB and plot/save at your convenience. If you click "table graph" it will reliably crash, without saving data from the simulation run. This is unique to the photothermal code and not a bug intrinsic to all COMSOL files.

Appendix 2

10. Unfinished Experiments

10.1 Overview

The physicist Richard Feynman began his Nobel lecture with the following observation:[309]

"We have a habit in writing articles published in scientific journals to make the work as finished as possible, to cover all the tracks, to not worry about the blind alleys or to describe how you had the wrong idea first, and so on. So there isn't any place to publish, in a dignified manner, what you actually did in order to get to do the work, although, there has been in these days, some interest in this kind of thing."

In this spirit I will briefly report here the unsuccessful avenues of research that I pursued during the course of my Ph.D. The first sample I tried to measure photothermally was a thin film of CoPc, at a time when the detection limit for resonance shift was ~ 10 pm (since improved to ~ 1 am). One advantage of this method of sample preparation is that the film is (in theory) homogeneous. With 1320 nm excitation I have tried to detect single molecules of an IR-absorbing fused porphyrin-pyrene molecule.[310] With the high-power, widely-tunable laser soon arriving from Radiantis this molecule will again be tested on the 1st-generation setup. On the conjugated polymer front, I had trouble preparing a doped sample of MEH-PPV (Poly[2-methoxy-5-(2-ethylhexyloxy)-1,4-phenylenevinylene]). Doping with a Sb_6^- salt may have succeeded, although the resulting powder was fluffy and poorly soluble. On a different front, I explored detachment and midair manipulation[194] of toroids as a means of defeating photothermal background form silicon. The success of all-glass toroids[245] made this work irrelevant. Other abandoned materials include single-walled carbon nanotubes (SWCNTs) and films of the nonfluorescent dye Fast Green FCF. Both of these targets

are now too strongly absorbing to be a useful challenge for the toroid spectrometer, and there are easy methods to study anything that fits that category e.g. spatial modulation spectroscopy.

10.2 CoPc thin film

I identified CoPc (cobalt phthalocyanine) as a good molecule for example calculations in Chapter 1, owing to its modest optical parameters and structural similarity to a lot of important biological chromophores. It also has the virtue of being cheap, air-stable, and excitable with a 640 nm pump laser. Our very first photothermal measurements were taken of a film of CoPc on a toroid. I initially tried spincoating from solution, whereupon giant crystallites formed on the toroid. It was impossible to even couple into these toroids. A next step was controlled deposition using thermal evaporation (Figure 65a,b). This required first sublimating CoPc to remove trapped impurities. Without this step, the ~1% residual solvent trapped in the CoPc powder would damage the high-vacuum pump inside the evaporator. CoPc is difficult to sublimate. Heating to above 450 °C with a sand bath was necessary. Even while pulling vacuum down to 50 mT using a Schlenk line and heating at this temperature, evaporation of ~50 mg took several hours. This temperature was empirically determined to be close to the softening point of the glass the sublimator was made from. As a result, it was necessary to closely monitor the temperature to avoid disaster. A heating mantle was destroyed during the process as well. A high-temperature heater with a sand bath and a dry ice/acetone cooled Schlenk line vacuum worked well. I tried using a dry ice/IPA bath-cooled sublimator, but the extreme temperature of the sublimator made this require refilling every 15 minutes. A cold-water condenser did not require this constant attention. Sublimation of a nominal 15 nm film of CoPc, calibrated using atomic force microscopy of a test film deposited on a silicon wafer piece, produces a roughly even coating on the toroid. The power dependence of photothermal signal was, as

expected, linear (Figure 65c) and far above the level of a bare toroid. Photothermal linescans (Figure 65d) reveal a sharply increasing resonance shift as the position of the pump beam is moved from the center of the toroid to the edge, as expected from simulations (Figure 60). I thank Greg Eyer and Nick Myllenbeck for their help in sublimation of CoPc and Yuelin Peng for her excellent training on thermal evaporation as well as Prof. Trisha Andrew for helping me with this project. Another possible direction with CoPc is derivatization. Sunil Upadhyay prepared a CoPc derivate with t-butyl groups to solubilize it. This is another possible future target.

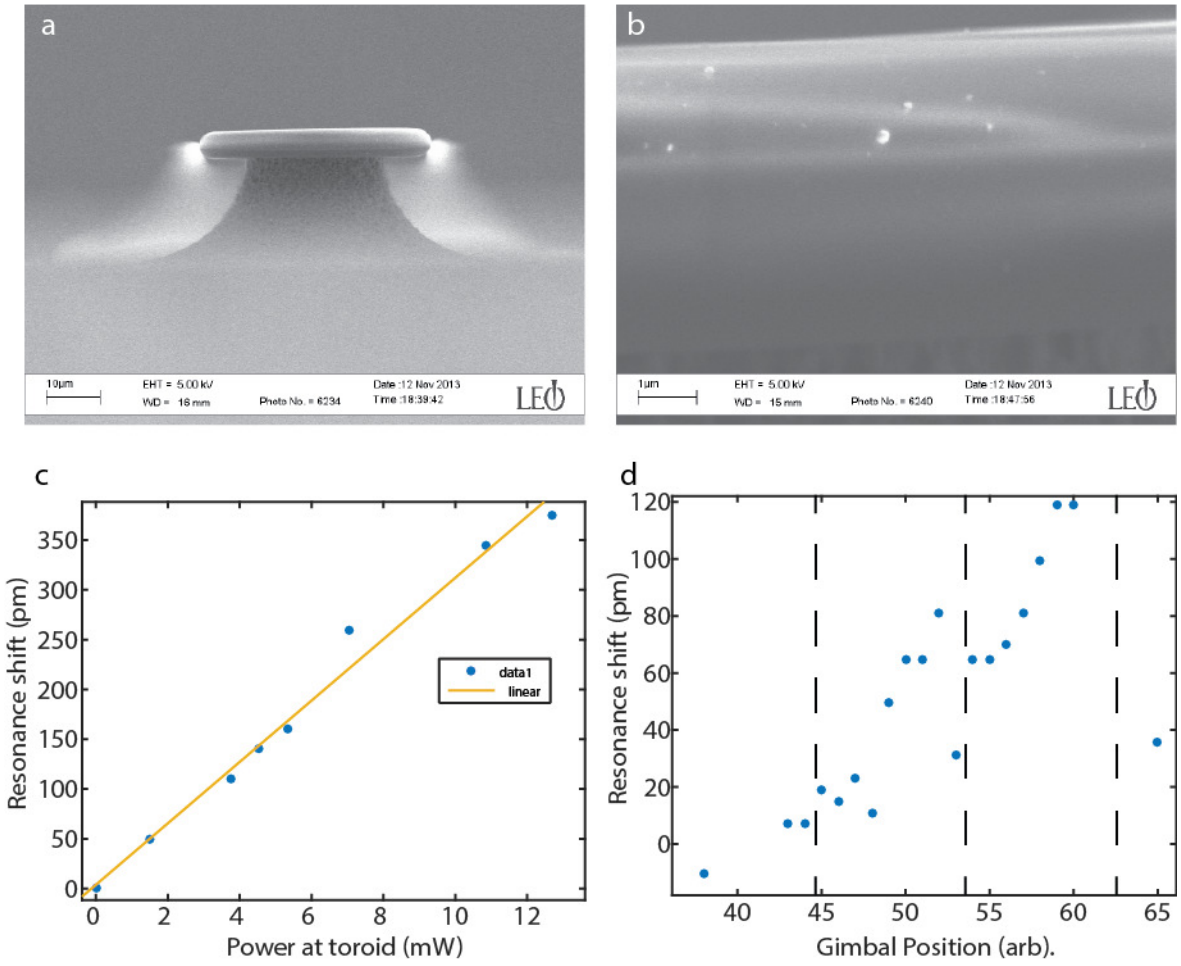

Figure 65: CoPc film on toroid.

(a) SEM image of toroid with nominal 15 nm of CoPc deposited via thermal evaporation. The "streetlamp glow" effect is unique to coated toroids. (b) Zoomed-in SEM showing the tendency of CoPc to form nanocrystallites instead of a homogeneous film. (c) The first photothermal data, plotting the dependence of resonance shift as a function of pump power. The dependence is linear, as expected from Equation 1. (d) Photothermal linescan on a CoPc-coated toroid. The x-axis is scan mirror position (arbitrary) and y-axis is resonance shift in picometers. The dashed lines mark, from left to right, the edge of the silicon pillar, the inner edge of the silica rim, and the outer edge of the silica rim.

10.3 Fused Zn porphyrin:pyrene

The group of Mark Thompson at USC has synthesized molecules with large extinction cross-sections near 1320 nm,[310] within the range of our tunable pump laser, and provided us with several mg.

Molecules with an electronic absorption feature this red are simply not available commercially and are not easy to synthesize. In particular, the fused porphyrin:pyrene molecule with Zn in the coordination site has favorable optical properties. Because of the exceptionally low energy of the LUMO state, this molecule is rapidly oxidized by ambient oxygen and must be carefully handled. Upon receiving the dark green powder Zn porphyrin:pyrene, I immediately divided the 7 mg into 10 different stocks. I purged the flask under argon, then filled 10 vials with argon-sparged dichloromethane (DCM). I then dissolved the original vial with argon-sparged DCM and aliquoted it out into each of the 10 vials. Then I blew down each vial with dry nitrogen until all the solvent evaporated, backfilled with argon, and sealed with a septum and parafilm. Half of the samples are kept in a glovebox for long-term storage. The other working stocks are kept as powder under argon, and when ready for deposition are re-dissolved in sparged DCM before being diluted into toluene. Depositing directly form DCM leaves ruinous amounts of residue on toroid chips. Aggregation is another challenge with this large, highly planar molecule. I employed pyridine and anthracene to help with this issue. The pyridine coordinates to the Zn and helps prevent aggregation; the anthracene intercalates between molecules as they try to stack, also disrupting aggregation. The actual solution used to spincoat molecules onto toroids included 5% pyridine, 1% anthracene, and 10 µg/mL PMMA. PMMA helps to seal the dye from air since it is extremely sensitive to oxidation. Without PMMA, a large majority of molecules will oxidize in the first few hours after deposition (Figure 66b,c). I tried photothermal mapping after waiting overnight for oxidation to lower the concentration of absorbing molecules to near single-molecule levels. Figure 66a shows a series of photothermal maps taken at a full range of linear polarization angles, showing very strong modulation in the photothermal signal. The peak resonance shift of 400 attometers is consistent with only ~5 molecules absorbing under optimized conditions (transition dipoles parallel to pump polarization, λ_{max} at 1320 nm). This molecule is the most likely candidate for us to first demonstrate room-temperature absorption spectroscopy on a single molecule.

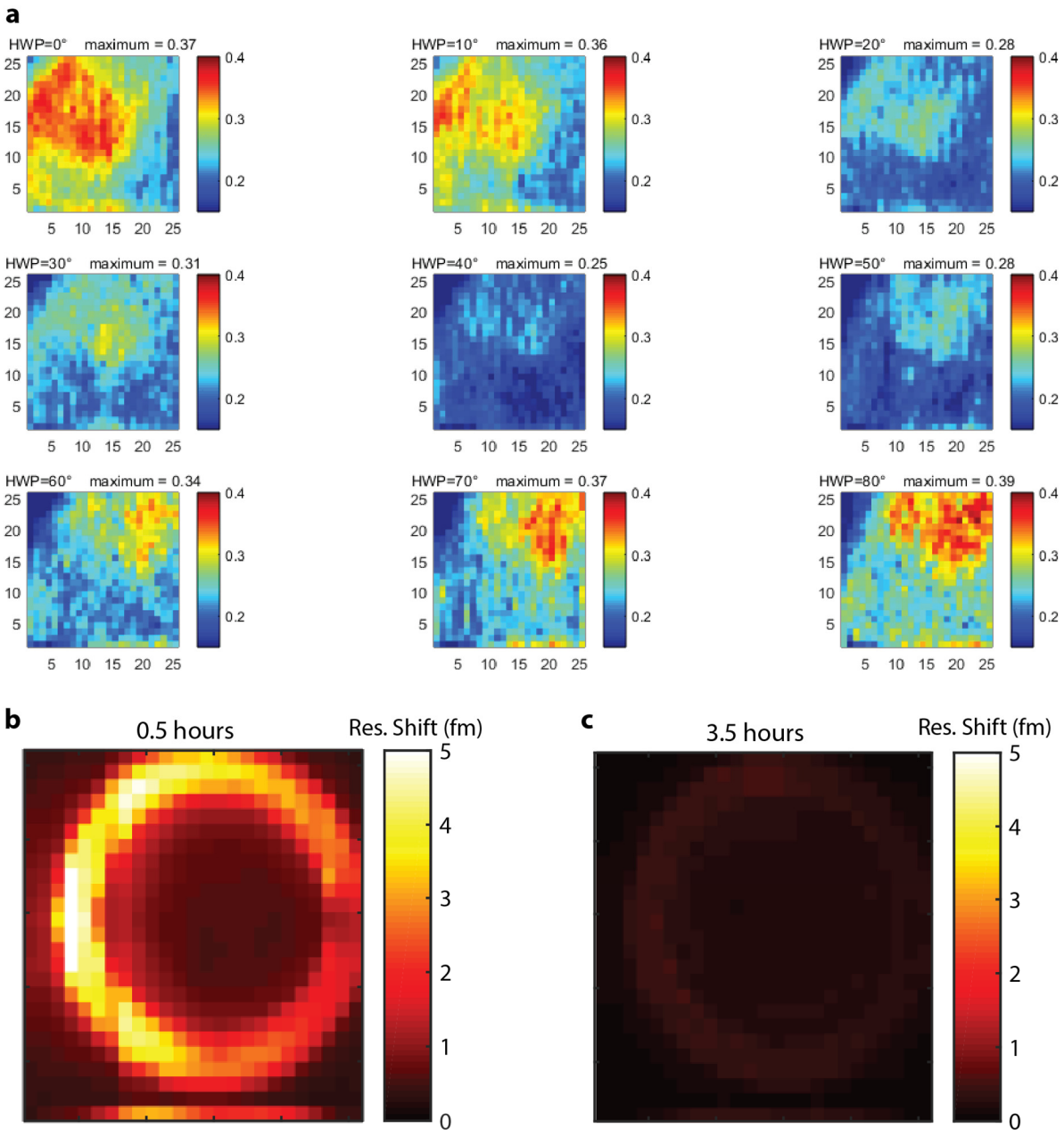

Figure 66: Fused Porphyrin:Pyrene

(a) Photothermal mapping at a full range of polarizations reveals striking fluctuations in the photothermal signal. The color axis is resonance shift in fm. Each map is the average of four individual maps, taken at 0.25 µm/pixel resolution and 1320 nm. (b) Photothermal mapping of a toroid 0.5 hours after deposition without PMMA coating. (c) Photothermal mapping of the same toroid, 3.5 hours after deposition, showing a huge decrease in the number of absorbing molecules.

10.4 MEH-PPV

MEH-PPV is the most widely studied conjugated polymer in single-molecule experiments[212] and probably the most commonly used in organic light-emitting devices. Pristine MEH-PPV is fluorescent and lacks an absorption feature near 1320 nm, making it a difficult target for the early toroid absorption spectrometer. However, p-doping of MEH-PPV will create polarons or bipolarons with near-IR absorption features and quench emission, making the doped form the molecule an attractive test molecule (in addition to the numerous scientific questions surrounding it). In the literature, doping is often reported with I_2 or $FeCl_3$. $FeCl_3$ doping is easy, since it's soluble in DCM and can be dropcast on a film. Iodine doping is accomplished through sublimation by putting the MEH-PPV film and a few iodine crystals. As seen in Figure 67, neither of these approaches led to the growing in of a near-IR absorption feature. This is likely because of a lack of stability of the counter-ion ($FeCl_4^-$ and I_3^-, respectively). With the suggestion of Professor Trisha Andrew, I tried a more sophisticated doping route using the salt triethyloxonium antimony hexachloride. This must be handled very carefully, as antimony pentachloride is easily formed, which is a highly corrosive and oxidizing molecule. Small aliquots (~50 mg) are massed out in a glovebox and transferred into a septum covered, copper wire closed round bottom flask and stored under nitrogen. Using a Schlenk line, a few mL of anhydrous dichloromethane is added to a different round bottom flask (I used DCM from a solvent system that I knew to be dry). The flask was rinsed with acetone and dried in a 200 °C oven before use; the stirbar was treated the same way. For 50 mg of oxidant I added approximately 19 mg of MEH-PPV to the flask before addition of the antimony. The antimony salt is added after cooling the flask to 0 °C. The solution turned dark blue immediately upon addition of MEHPPV to the solution of oxidant in DCM. I reacted the mixture for 1 hour with stirring. Then the flask was cooled to ~ -20 °C with a salty icewater bath. I repeatedly washed the precipitate with dry diethyl ether, and then let the wet precipitate wait for 3 days in a sealed flask after backfilling the flask with nitrogen. I tried filtering

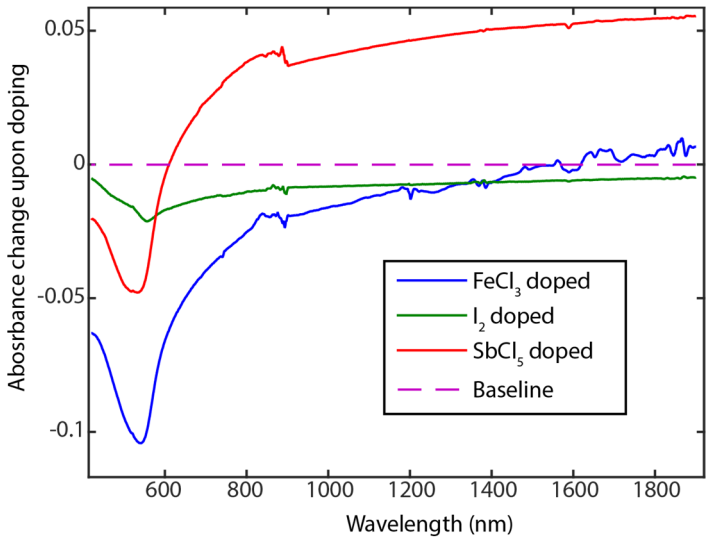

Figure 67: Doping of MEH-PPV.

Thin-film differential absorption spectra of MEH-PPV after doping with $FeCl_3$ (blue), I_2 (green), and $SbCl_5$ (red). The spectrum of pristine MEH-PPV is subtracted from the doped film spectrum. Only $SbCl_6$ doping gives an increase in NIR absorption.

with HPLC grade MeOH, H_2O, and DCM without success. It does however dissolve in o-dichlorobenzene after 30 minutes of sonication (I have yet to find a molecule that is not dissolved by this solvent). The resulting solution is very pale yellow and clear. Waste must be treated specially because of the antimony content. I thank Sunil Upadhyay for teaching me this procedure and making sure that I carried it out safely. One issue is that because of its low solubility, it is really hard to make a dropcasted or spincoated film from antimony hexachloride doped MEH-PPV. I never progressed to the point of depositing MEH-PPV on toroids, partly because I discovered an easier alternative molecule—PEDOT:PSS—while operating under a limited timeframe. The $SbCl_6$ doping test shows that this is a possible route forward.

10.5 Free toroids

After characterizing the silicon substrate-induced background absorption in Chapter 4 we explored various options for reducing it. One pathway, to move to a wavelength range where silicon is transparent, was successfully implemented in Chapter 6. Another direction, fabricating a new type of all-oxide toroid microresonator, was disclosed by my colleague Kassandra Knapper.[245] A third option that was of interest earlier on was the free toroid of Hossein-Zadeh and Vahala.[194] In this work, the toroid is etched again after reflow until the silicon support pillar is but a thread (Figure 68a). At this point a tungsten microprobe (Ted Pella) is brought into contact with the top of the toroid, away from the rim. Cyclically exerting pressure with the microprobe will eventually cause the silicon pillar to break. The silica portion of the microresonator, which is at this point stuck to the microprobe, can be freely manipulated in midair. Coupling into a mid-air toroid is surprisingly easy (Figure 68b) with a tapered fiber. Note that at if the tungsten microprobe is rammed into the substrate it becomes a tungsten microhook, which may be more effective at picking up toroids.

One important caveat with free toroids is that residual silicon can be attached to the center of the silica disk after the pillar is broken. The toroid visible in (Figure 68a) broke at the narrowest part of the pillar, leaving a few µm sized chunk of silicon that caused a huge photothermal background. With the pillar gone, heat builds up very quickly in the toroid after photothermal excitation. Mid-air photothermal mapping of this toroid was not promising. However, mid-air photothermal mapping of the toroid in panel b was more successful, although the extremely low Q-factor limits quantitative evaluation of the background level.

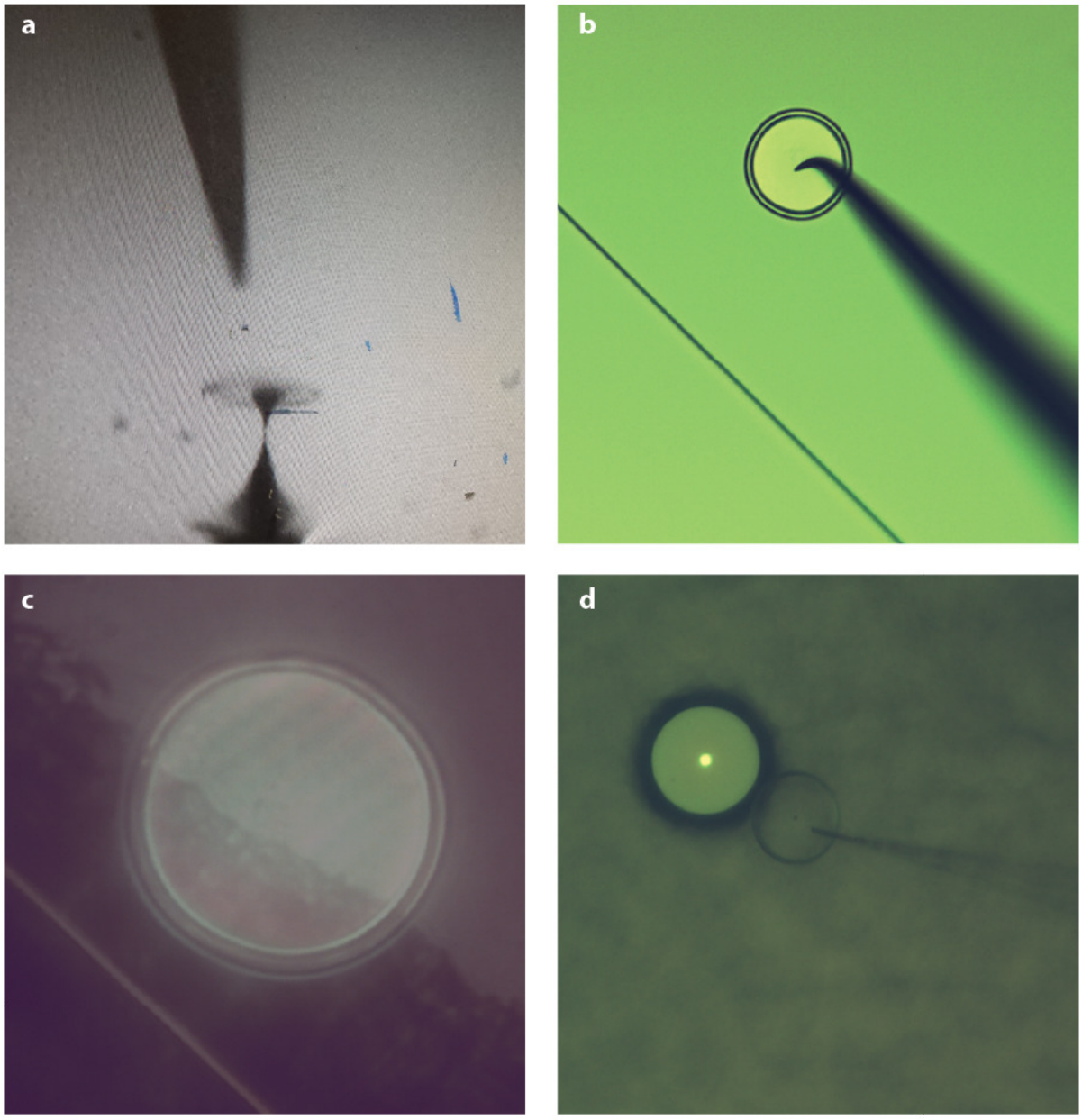

Figure 68: Free toroids

(a) A tungsten microprobe is brought towards the top surface of a toroid that has been re-etched until the silicon pillar is ~ 1 µm thick at its thinnest point. (b) A detached toroid attached to a bent tungsten microprobe, being aligned with a taper for midair coupling. The microprobe was inadvertently bent by ramming into the substrate. (c) A free toroid deposited onto a quartz wafer and a tapered fiber attempting to couple into WGMs. No WGMs were measurable because of coupling into the substrate. (d) Two microdisks, one free and one attached, brought into coupling range.

Placing toroids on new substrates, for example to couple them together, is an integral aspect of the work of Hossein-Zadeh.[194] I initially tried placing a free toroid onto a fused silica wafer (Figure 68c). The free toroid was deposited at the edge of the wafer piece to enable access with the coupling fiber. However, I was not able to observe any resonances. In hindsight, the reason is obvious. The refractive index of thermal oxide and of fused silica are essentially identical, so the total internal reflection condition is not observed at their boundary. Therefore, the toroid deposited onto a silica substrate is not a resonator. This particular toroid is notable as lacking any residual silicon, however. Free toroids or microdisks could also be coupled to regular toroids/microdisks to produce Fano resonance (Figure 68d),[184] potentially enhancing their sensing ability (Chapter 7); however, we did not pursue this avenue of research more closely.

While working with free toroids, with phototolithography I manufactured pillars made from SU-8 photoresist that were approximately 25 μm tall and 25 μm in diameter, and landed free toroids on them (not pictured). SU-8 is an interesting choice because its visible transparency is high enough to use as a low-loss waveguide material, large structures can be made without a single etching step, and its low thermal conductivity enhances the photothermal signal. In closing I would like to emphasize that a chip-scale approach to removing the silicon background has been much more successful.[245] However, free toroids are fascinating because of the much looser process constraints.

Appendix 3

11. Photothermal Microresonator Absorption Microscopy with Backscatter Detection[6]

11.1 Abstract

The extreme temperature sensitivity of whispering-gallery-mode (WGM) microresonators holds great promise as a detection strategy for single-particle photothermal microscopy and spectroscopy. The detection limit is currently partially constrained by frequency noise from the laser used to probe the cavity resonance wavelength. We present a measurement technique capable of simultaneously detecting backscattered and transmitted light from a wavelength-locked optical microresonator, with laser intensity noise and frequency noise partitioned into the two independent detection channels. Photothermal mapping of single absorbing nano-objects demonstrates that both methods are capable of high signal/noise, exceeding 30,000:1 in the backscattering channel for a photothermally-induced microresonator resonance shift of 93 fm.

Keywords: Photothermal Microscopy, Nanospectroscopy, Single-Particle Imaging, Absorption Spectroscopy, Photothermal Mapping, Optical Microresonator

11.2 Introduction

Single-particle photothermal spectroscopy is a powerful tool for live-cell imaging,[311] characterizing carbon nanotubes,[133,226] and probing individual inorganic nanoparticles[22,312] Optical

[6] The material in this chapter was originally published as:

absorption by the target nano-object results in a local temperature increase through thermal dissipation of excitation energy via non-radiative relaxation. Typically, photothermal detection is performed by scattering a second beam from the region of perturbed refractive index caused by the temperature rise. Achieving high sensitivity, down to the single-molecule limit, requires immersing the sample in glycerol to access a higher thermo-optic coefficient[51],[51] limiting the possible range of applications. Here we present a new detection scheme for microresonator photothermal absorption microscopy.[133] The high signal/noise achieved suggests an ultimate detection limit well within the range of individual chromophores.

Whispering-gallery mode (WGM) toroidal optical microresonators[106] possess a powerful combination of ultrahigh optical quality factors (10^8) and small mode volume (~ 200 μm^3).[135] The narrow linewidths (typically sub-pm full-width at half-maximum) of whispering gallery resonances in toroids allows for the measurement of subtle changes in the optical path length of the resonator. The resonance wavelength is determined solely by the optical path length, and varies with temperature through the thermo-optic coefficient of the material (silica). Precise measurements with WGM microresonators have demonstrated nK temperature sensitivity with 1s time resolution.[55]

The resonance condition as a function of temperature is given by Equations 1.2, 1.3. The dependence of the refractive index on temperature makes the resonator highly sensitive to local heat sources. While this sensitivity results in significant drift in the resonance position at longer timescales, it can be exploited for single-particle photothermal sensing as well. In particular, our photothermal signal is amplitude modulated at a frequency ω, effectively separating long time scale temperature drift from the single-particle signal.

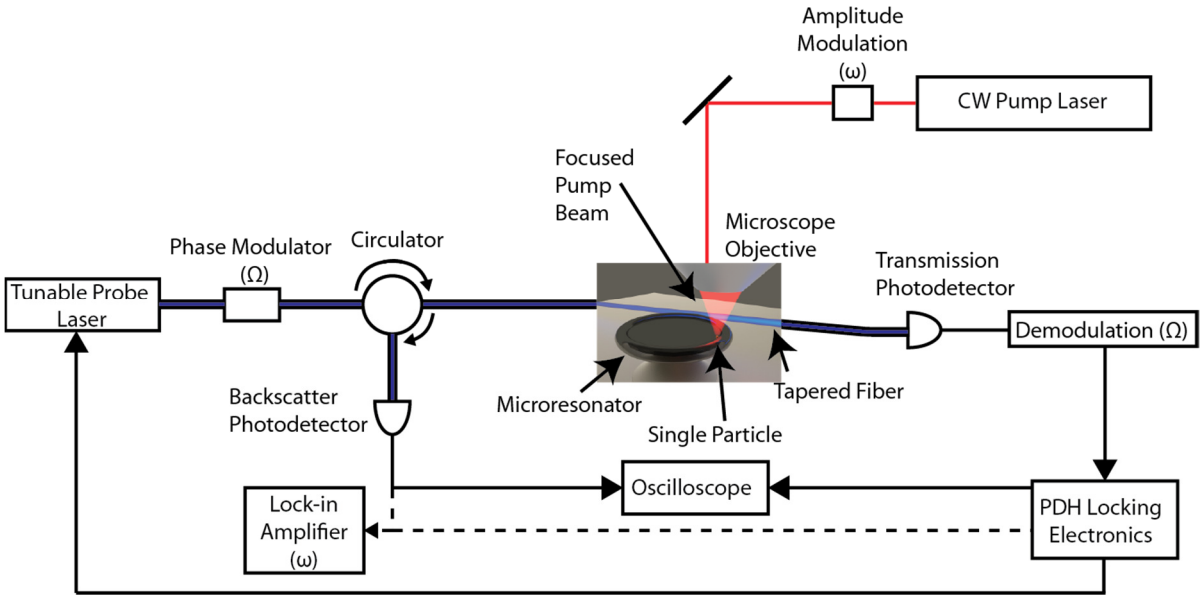

Figure 69: Microresonator photothermal microscope with backscattered detection.

Resonance wavelengths of the microresonator are probed with a fiber-coupled tunable diode laser (black and blue). Phase modulation at a frequency Ω generates the optical sidebands necessary for actively locking the wavelength of the laser to the toroid resonance. Transmission past the microresonator is monitored with a photodetector and demodulated at Ω, yielding an error signal that is used for feedback to the laser and for sensing perturbations in the toroid resonance wavelength. A fiber-optic circulator and a second photodetector collects light backscattered from the propagating mode in the toroid. Single nano-objects are optically pumped with a focused, free-space laser (red) that is amplitude modulated at frequency ω. The demodulated transmission signal and the backscattered signal are measured on an oscilloscope or optionally (dashed line) a lock-in amplifier for the magnitude of the signal at ω, which is directly proportional to the extinction coefficient of the absorbing nano-object.

To perform single-particle absorption microscopy, we optically pump individual nanoparticles on the surface of the microresonator with a tightly-focused, free-space pump laser (Figure 69). As in conventional photothermal experiments, optical excitation of an absorbing nano-object results in a local temperature rise as the absorber dissipates energy to its surroundings. This nanoscale heat source locally increases the refractive index of the microresonator. A second fiber-coupled tunable laser is used to probe the shifting resonance wavelength of the toroid.

Toroidal microresonators are commonly observed to support two optical resonances at each azimuthal mode number[106,313] corresponding to optical modes propagating in a clockwise and counterclockwise direction. Light is initially coupled into a single mode, but any scattering centers in the toroid can couple light between the two modes. Light propagating in the reverse direction (backscattered) will re-couple into the tapered optical fiber in the opposite direction it was launched from. By employing a fiber-optic circulator, this backscattered light can be separated from the initial probe beam and detected with a low-noise photodiode (Figure 69).[95] Backscattered light is observed from whispering-gallery mode resonances in the absence of a photothermal signal. However, the time-dependent local change in refractive index induced by photothermal microscopy serves to scatter additional light into the counter-propagating WGM. By modulating the amplitude of the pump beam while focused onto an absorbing nanoparticle, we observe a synchronous modulation in the intensity of backscattered light, demonstrating that local heating of the microresonator is visible in the backscattered detection channel.

11.3 Experimental

High-frequency amplitude modulation of the pump beam (necessary to minimize the effect of low-frequency noise on the measurement) requires a fast readout on the toroid resonance wavelength. Sweeping of the probe laser wavelength is limited to sub-kHz rates by the 1.2 kHz mechanical resonance of the piezo used to tune the laser. Instead, the probe laser can be forced to actively track the exact center of the resonance through the Pound-Drever-Hall (PDH) wavelength-locking technique.[161] In PDH, the wavelength of a tunable laser is actively locked to an optical cavity, and although this technique is often used to stabilize laser operating wavelength, it can also be used to track perturbations in an optical cavity.[162] In this experiment, the PDH technique is used to lock the probe laser wavelength to the toroid resonance wavelength, giving a sensitive, high-bandwidth readout of the resonance position. The locking

feedback loop requires a dispersive error signal, which is implemented by phase-modulating the laser at RF frequencies (in this experiment, Ω = 200 MHz) and measuring the transmitted light. Modulation creates optical sidebands on the carrier. When the carrier is precisely resonant with the microresonator, the upper and lower sidebands are equal in magnitude and opposite in phase, and thus cancel completely. Detuning in wavelength changes this phase relationship and consequently the sign and magnitude of the voltage recorded by the photodetector. This error signal, after demodulation, is used as feedback to lock the probe laser wavelength to the microresonator. Periodic perturbations in the resonant wavelength—caused by amplitude modulation of the pump beam and the resulting modulation of the photothermal signal—are readily observed in the error signal. A lock-in amplifier is used to increase the signal/noise by rejecting all fluctuations in the toroid resonance except in a narrow bandwidth at the pump modulation frequency.

While the probe laser is locked to the microresonator, single absorbing nanoparticles are imaged by scanning the position of the pump beam across the surface of the microresonator and measuring the change in resonance wavelength[133] [133] (Figure 70). Identical images are obtained with both imaging methods, verifying the fidelity of the backscattered detection channel. Importantly, backscattered detection works while the PDH locking loop is engaged, allowing for simultaneous and independent detection of resonance shift and thus single-particle absorption via the two different detection channels.

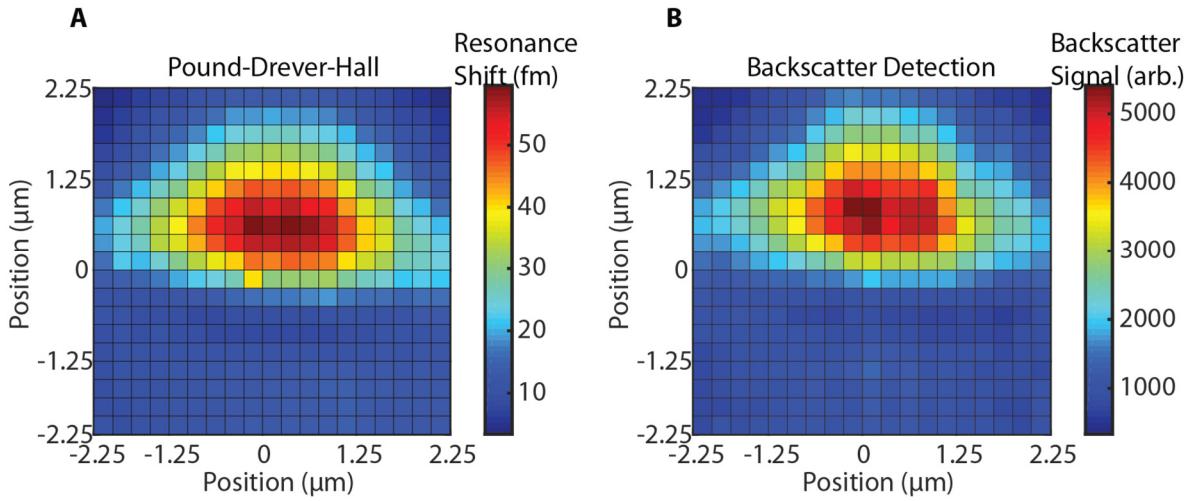

Figure 70: Photothermal mapping with the PDH and backscattered channels.

A single nanoparticle is mapped using the transmitted light channel (the PDH error signal) and backscattered channel. Each image was acquired at 10 mW pump power at λ = 1320 nm, at 0.25 μm/pixel resolution, with a lock-in time constant = 100 ms.

We typically detect 10-50 nW of backscattered light with ~ 5 μW of light impinging on the transmission photodetector. Part of the low yield for backscattered light is attributed to the high losses in bare fiber splices between the backscatter detector and the tapered fiber. Use of a fusion splicer would significantly increase the signal intensity in the backscatter channel. Because the lock-in amplifier is only sensitive to backscattered photons with a frequency component at the pump beam modulation frequency, and the pump beam is only coupled to the probe beam through photothermal single-particle absorption, an increase in collection efficiency should directly improve the signal/noise ratio.

11.4 Discussion

The photothermal signal from an individual absorbing nano-object that produces a resonance shift of 93 fm is resolved with very high signal/noise. A normalized power spectrum of the PDH and backscattered channels (Figure 71) reveals an extremely sharp peak at the amplitude modulation frequency (ω = 4.05 kHz). The signal/noise ratio can be calculated by comparing the ratio of the signal at

4.05 kHz to the baseline at a slightly detuned frequency. The ratio in signal between 4.05 kHz and the baseline at 100 Hz detuning is 200,000:1 for the PDH signal, and slightly lower for the backscattered signal, 30,000:1. Low-frequency noise is also substantially higher in the backscattered signal, along with a prominent set of 60 Hz sidebands on the photothermal signal, indicating that reduction in technical noise and a lower-noise photodetector could further improve the signal/noise ratio, along with improvements to the signal level from decreased losses in the probe beam's optical path.

We believe that higher technical noise in the less-optimized backscattered channel explains the contrast in our findings with previous work on backscattered detection in toroids,[95] where PDH sensing was found to be substantially noisier at low frequencies. Additionally, we believe that a major source of noise is vibration and drift in the position of the tapered fiber used to couple light into and out of the toroid. This noise can be in principle eliminated through active[169] or passive stabilization of the fiber's position[314] at critical coupling, as proposed in earlier work with backscattered detection[95].[95] Coupling noise quadratically affects the strength of the backscattered signal, because a decrease in taper-toroid coupling lowers the circulating intensity in the resonator as well as the outcoupling rate into the backscattered channel. The PDH signal is affected by coupling fluctuations in several ways. The PDH error signal is proportional to the resonator Q-factor, which is nonlinearly degraded by overcoupling of the tapered fiber. Changes in coupling also contribute detection noise from light that is not coupled into the resonator. We do not employ active stabilization of the tapered fiber's position, degrading the relative signal/noise of the backscattered channel and explaining the difference in relative performance to ref. [95].

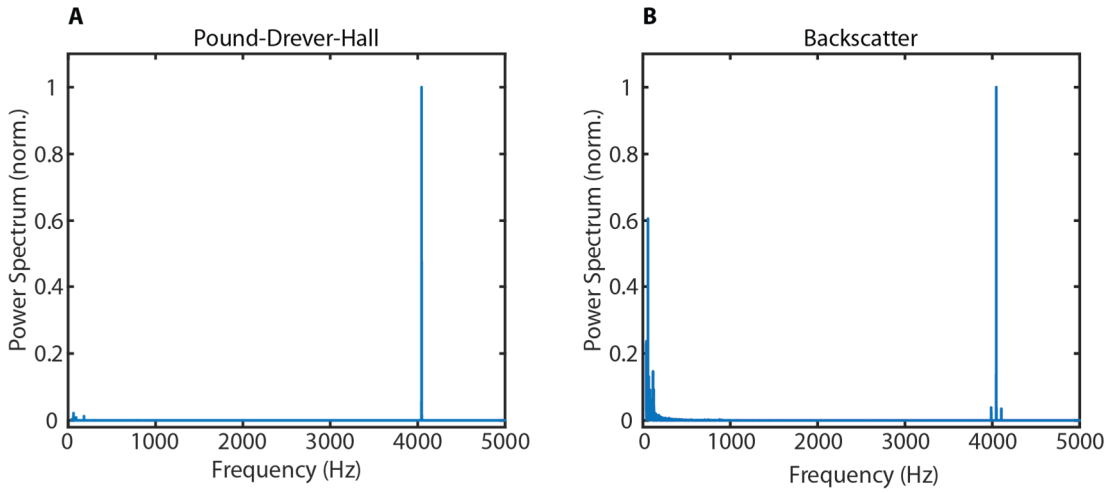

Figure 71: Normalized power spectra of the Pound-Drever-Hall (A) and backscattered (B) channels.

Photothermal signal from a single abosrbing nanoparticle (93 fm resonance shift) is visible with high signal/noise at the pump beam modulation frequency (ω = 4.05 kHz). Simultaneous acquisition of both channels reveals high signal/noise ratio on both channels.

PDH and backscatter detection are in some sense complementary techniques because PDH is (to first order) insensitive to laser intensity noise and backscatter detection is insensitive to frequency noise (to first order). Although low-frequency noise is most relevant to typical biosensing experiments,[72,73,104] microresonator absorption microscopy is immune to drift in laser frequency or intensity outside of the 1 Hz measurement bandwidth of the lock-in amplifier. The modulation frequency (ω) is a free parameter, and the exact choice of frequency will determine whether laser intensity noise or laser frequency noise is greater in magnitude, thus determining whether transmitted or backscattered light is most appropriate. This is in contrast to sensing through the reactive shift of the toroid's resonant frequency from a stochastic binding event,[73,315] where the signal is inherently DC and cannot be modulated. The high signal/noise ratio reported in Figure 71 does not take into account the more significant experimental limitation of drift in the position of the tapered coupling fiber, which in practice is a much larger limitation than noise within the lock-in amplifier's bandwidth. However, as reported above, techniques have already been demonstrated for greatly reducing fluctuations in the fiber's position.

11.5 Conclusion

Microresonator absorption microscopy is a powerful tool for characterizing individual nanoparticles, with a sensitivity projected to reach single-chromophore sensitivity. Backscattered detection is used to measure small shifts in the resonant wavelength of the microresonator, and is immune to frequency noise in the probe laser, a concern with diode lasers. Backscattered detection faces different noise sources than detection via the PDH error signal, allowing for greater flexibility in adapting the experimental setup to technical noise sources. Looking forward, a resonance shift of 2 fm is achievable for a single chromophore pumped at its maximum absorption wavelength,[133] suggesting that the technique presented here is well-positioned to reach single-chromophore sensitivity.

11.6 Acknowledgments

Funding was provided by the NSF through the University of Wisconsin Materials Research Science and Engineering Center (UW-MRSEC, DMR-1121288) and by the Defense Advanced Research Projects Agency (N6601-12-1-4215).

Appendix 4

12. Photothermal Imaging of Individual Carbon Nanofibers with Optical Microresonators[7]

12.1 Abstract

A new method is described for measuring the absorption of light by single non-emissive nanoparticles. Individual carbon nanofibers are imaged using a photonic transducer to quantify the heat dissipated after the electronic energy is thermalized. Leveraging the high sensitivity of ultrahigh-quality-factor optical microresonators as photothermal transducers provides high sensitivity. Polarization-resolved measurements indicate that the orientation of the absorption dipole of a nanofiber matches the long axis of the fiber. The per-atom absorption cross-section is determined to be (2.9×10^{-18} cm^2/carbon atom), in close agreement with the value for bulk graphite.

Keywords: Photothermal Microscopy, Single-Particle Spectroscopy, Carbon Nanofibers, Nanophotonics

12.2 Introduction

Optical measurements on single nanoparticles provide a wealth of information that is lost in ensemble averaging, including the distribution of single-particle electronic structures. One important application requiring thorough understanding of the electronic properties of individual nano-components is the design of next-generation computer interconnects using single carbon nanofibers.[316] Carbon nanofibers are a promising alternative material to copper for interconnects owing to their low thermal

[7] The material in this chapter was originally published as:

and electrical resistivity, and high chemical stability.[317] Nanofiber circuits are well-suited for non-contact optical characterization. Additional information about the orientation and electronic structure of the nanofiber can be found by incorporating wavelength- and polarization-resolved absorption spectroscopy. Typically, single-particle spectroscopy is performed with luminescence or scattering. Luminescence is only applicable to a small subset of systems, and is blind to plasmonic nanoparticles, carbon nanofibers/tubes, and a wide variety of other important targets. Detecting scattered light bypasses this obstacle, but scattering cross-sections scale unfavorably(αV^2) with decreasing particle size compared to absorption (αV).[21] Another approach, photothermal detection of optical absorption, has been used in a far-field geometry to image plasmonic nanoparticles,[227] carbon nanotubes,[226] and under favorable conditions, single molecules.[51] Photothermal detection is achieved by measuring the heat dissipated after non-radiative relaxation of a single nanoparticle upon optical pumping. The amount of heat is proportional to the absorption coefficient of the nano-object. We have recently shown that the sensitivity of this measurement can be greatly increased by using toroidal optical microresonators as the detection apparatus instead of quantifying the scattered light in the far-field.[133] Toroidal optical microresonators offer a unique combination of ultranarrow resonant line widths[106] and small mode volumes.[135] The wavelength of the microcavity resonance varies with temperature due to the thermooptic coefficient (dn/dT) of silica shifting the optical path length, and is highly sensitive to the presence of local perturbations in temperature. The extension of photothermal single-particle imaging to optical microresonators enables more sensitive measurements to be made, potentially allowing for substantially lower detection limits than existing methods of photothermal imaging. Previously, we used this approach to determine the absolute absorption cross-section of multi-walled carbon nanotubes.[133] Carbon nanofibers provide an interesting target system as their optical properties have not been explored at the single particle level.

12.3 Experimental

The experimental setup combines photothermal excitation with an optical microresonator as a sensing element (Figure 72). Single nanofibers are deposited randomly on the top surface of the microresonator by spincoating from HPLC-grade ethanol. A fiber-coupled tunable diode laser (Newport) centered at 1550 nm is used to probe the resonant wavelengths of the toroid. Nanofibers are photoexcited with a pump beam (640 nm) focused by a microscope objective (60×, 0.95 NA) to a near-diffraction-limited spot (780 nm $1/e^2$ diameter). The position of the focused pump beam in the sample plane is controlled via a servo mirror at a plane conjugate to the objective back aperture (Figure 72a). Polarization optics (a polarizer and half-wave plate) are used to tune the linear polarization angle at the target nanofiber. Photothermal maps at variable resolution are taken by scanning the pump beam across the top surface of the resonator and measuring the dissipated heat via the shift in resonant wavelength.

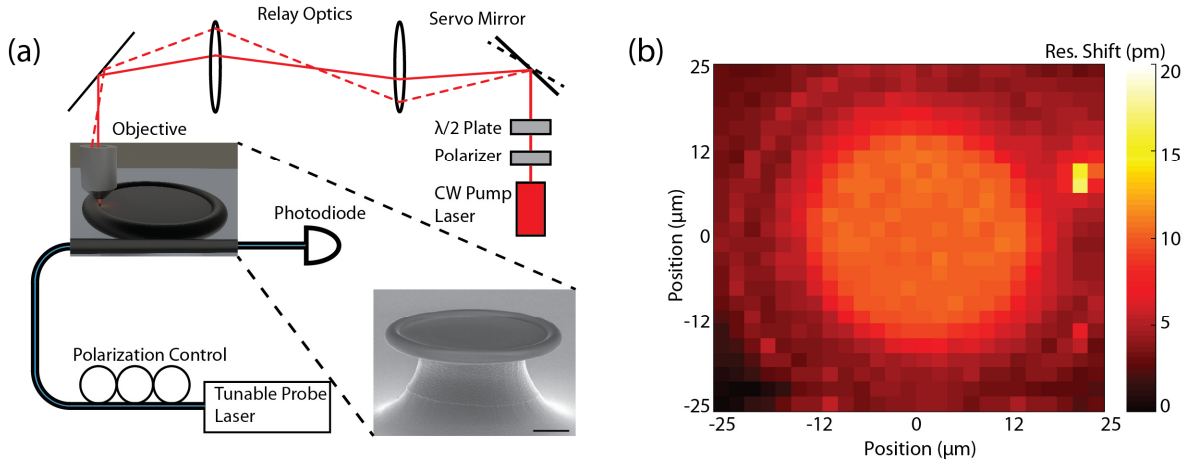

Figure 72: Apparatus for photothermal mapping of carbon nanofibers.

(a) Block diagram of instrument. A tunable-wavelength, fiber-coupled laser (black and blue) is used to couple into the resonator and its transmission is detected with a photodiode. A free-space pump beam (red) is focused onto the surface of the resonator. A half-wave plate is used to control the excitation polarization while the position of the excitation spot in the sample plane is controlled with a servo mirror and relay optics. (Inset) SEM of a toroidal optical microresonator with a 10 µm scale bar. (b) Coarse-resolution photothermal map of a microresonator. The bright set of pixels on the top right side is a single absorbing nanofiber, significantly stronger than the background arising from substrate absorption.

Wide-area maps (50 μm × 50 μm) at low resolution (2 μm/pixel) are taken to characterize the location of single absorbers (Figure 72b, Figure 73a). The shape of the nanofiber is defined with a high-resolution map (3 μm × 3 μm at 0.25 μm/pixel) (Figure 73b). At every pixel, the resonance wavelength is measured with the pump beam off and on, correcting for ambient temperature drift. Individual particles are observable as "hot spots" of resonance shift, easily distinguished from the background from absorption by the silicon substrate.[132] Scanning electron micrographs (SEMs) taken of the resonator's surface provide information about the size and orientation of particular nanofibers (Figure 73d).

12.4 Discussion

An individual carbon nanofiber is imaged via photothermal mapping and SEM (Figure 73). The SEM image of this nanofiber (Figure 73d) yields dimensions of 775 nm length and 90 nm diameter. The nanofiber was located on the resonator by photothermally scanning the entire microresonator (Figure 73a) until a signal was observed in the lower-right corner. A high-resolution photothermal map (Figure 73b) reflects the nanofiber's size, but is convoluted with the dimensions of the near-diffraction-limited excitation beam. The absorption coefficient is strongly dependent on the polarization of the pump light (Figure 73c). The maximum absorption is observed with the pump beam polarized parallel to the long axis of the nanofiber. Using this technique, the orientation of nanofibers can be determined even when the image resolution is insufficient to resolve the orientation.

Calculating the absorption cross-section from the measured resonance shift requires finite-element simulations, which were performed using COMSOL Multiphysics. These simulations have been previously demonstrated to correctly model the thermal physics of toroidal microresonators.[132] The local increase in temperature resulting from the heat dissipated by the nanofiber increases the refractive index of the microresonator. An overlap integral between the electric field distribution of the propagating mode

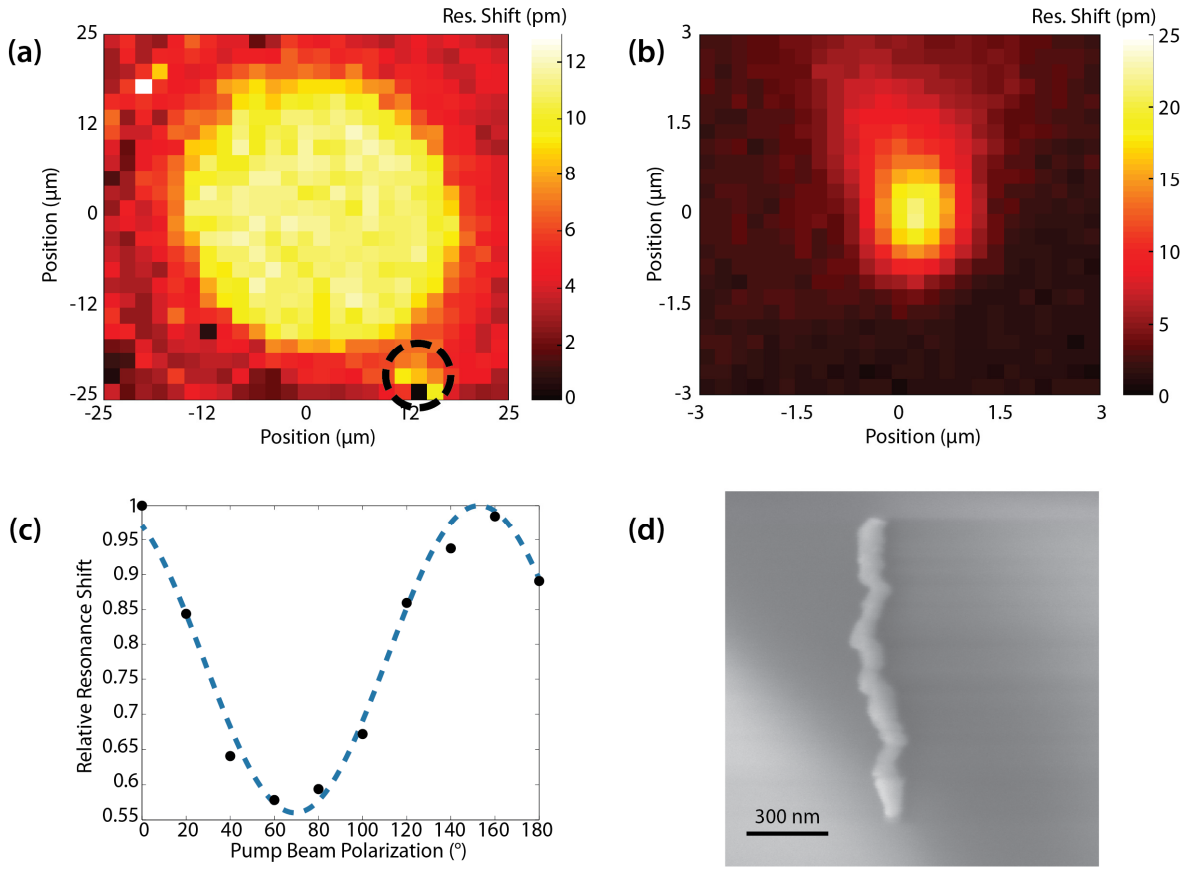

Figure 73: Representative data set with carbon nanofibers.

(a) Large-area, low-resolution photothermal map of an entire microresonator. A single nanofiber is visible in the marked region to the lower right. (b) High-resolution photothermal map of the nanofiber. (c) Polarization-dependence of the absorption of the nanofiber. The maximum of photothermal signal is coincident with the long axis of the nanofiber. (d) SEM of the same nanofiber, giving the physical dimensions. The observed image is elongated by sin (45°) in the vertical direction because of stage tilt.

in the microresonator and the change in refractive index is used to calculate the resonance shift. This simulated resonance shift can be compared to the experimental value and used to determine the amount of dissipated heat necessary to produce the observed resonance shift. The absorption cross-section of the single nanoparticle is equal to the heat dissipated divided by the incident optical pump intensity, weighted by the overlap integral of the focused pump beam spot and the physical dimensions of the nanofiber.

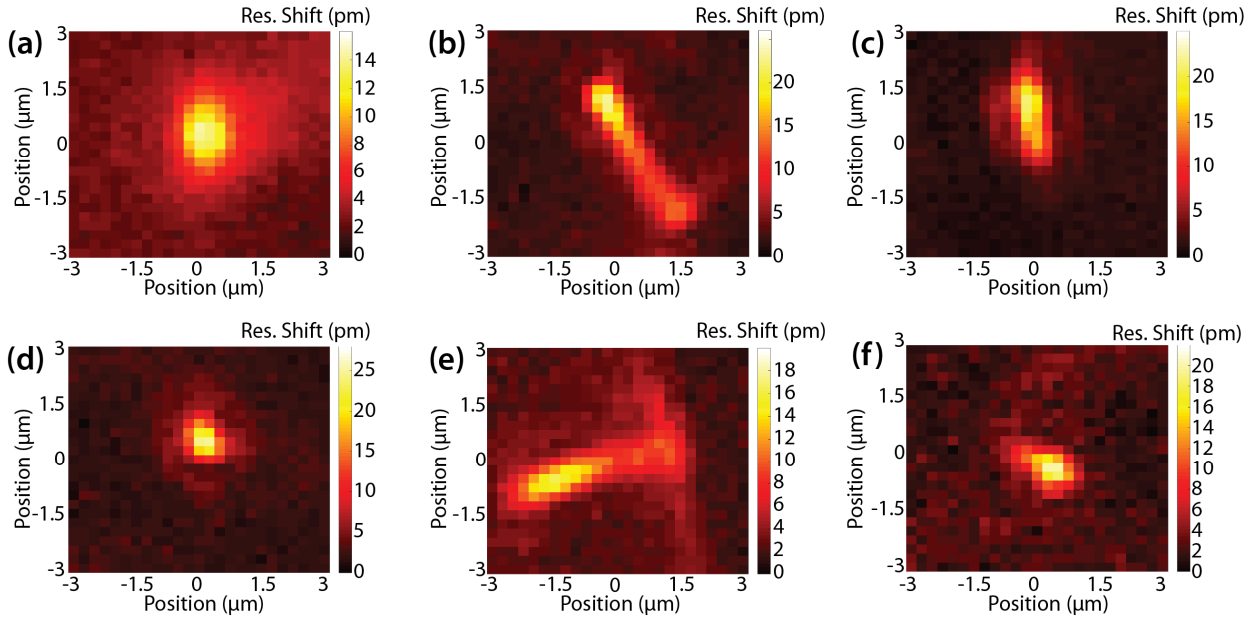

Figure 74: Representative photothermal maps of single carbon nanofibers.

(a)-(f) are taken at a resolution of 0.25 μm/pixel. The intensity axis is the shift in resonant wavelength of the toroid.

Because the SEM provides exact physical dimensions for the nanofiber the per-atom absorption cross section can be reported. The observed value (2.9 x 10^{-18} cm^2/atom) agrees well with that of multi-walled carbon nanotubes[133] (2.3 x 10^{-18} cm^2/atom) and bulk graphite (2.5-2.8 x 10^{-18} cm^2/atom).[230] This is physically reasonable, as the internal lattice of the carbon nanofiber is identical to graphite.[318]

The size, shape, and orientation of carbon nanofibers varies greatly from particle to particle, as illustrated in Figure 74a-f. Small fibers (Figure 74a, d) appear as circular spots, mapping out the point-spread function of the microresonator photothermal microscope. Longer nanowires (Figure 74b, e) show a definite resolved orientation.

12.5 Conclusion

In summary, a method has been demonstrated for imaging single nanoparticles using the heat dissipated upon optical pumping. The absolute absorption cross-section of an individual carbon nanofiber was determined. This method is not uniquely applicable to carbon nanofibers, but can be applied to a wide variety of nano-systems. In particular, hyperspectral imaging can be readily incorporated by measuring the wavelength dependence of the photothermal signal using a tunable-wavelength pump laser. This type of single-particle spectroscopy offers great promise as a tool for characterizing nanoscopic systems.

12.6 Acknowledgments

Support was provided by the Defense Advanced Research Projects Agency (N66001-12-1-4215) and the University of Wisconsin Materials Research Science and Engineering Center (UW-MRSEC, DMR-1121288).

List of Publications

1. **Heylman, K.D.**, Rea, M., et al. “Tunable Photonic-Plasmonic Resonance with Toroidal Microresonators and Fisher Information Theory on Fano Resonance Spectra.” *In Preparation* (2016).
2. **Heylman, K.D.**, et al. “Optical Microresonators for Sensing: A Materials Perspective.” *Invited Progress Report, Advanced Materials* (2016).
3. **Heylman, K.D.,** Thakkar, N., Horak, E. H., Quillin, S.C., Cherqui, C., Knapper, K.A., Masiello, D.J., Goldsmith, R.H. “Optical Microresonators as Single-Particle Absorption Spectrometers.” *Nature Photonics* (2016).
4. Knapper, K. A., **Heylman, K. D.,** Horak, E. H. & Goldsmith, R. H. “Chip-Scale Fabrication of High-Q All-Glass Toroidal Microresonators for Single-Particle Label-Free Imaging.” *Advanced Materials* **28**, 2945-2950 (2016).
5. Horak, E. H., Knapper, K. A., **Heylman, K. D** & Goldsmith, R. H. “Cleaning Procedure for Improved Photothermal Background of Toroidal Optical Microresonators.” *SPIE Nanoscience+ Engineering.* 99230Z-99230Z-99236 (2016).
6. **Heylman, K. D.,** Horak, E. H., Knapper, K. A. & Goldsmith, R. H. “Photothermal Microresonator Absorption Microscopy with Backscatter Detection.” *SPIE Nanoscience+ Engineering.* 95540U-95540U-95546 (2015).
7. **Heylman, K. D.,** Knapper, K. A. & Goldsmith, R. H. Photothermal Microscopy of Nonluminescent Single Particles Enabled by Optical Microresonators. *Journal of Physical Chemistry Letters* **5**, 1917-1923 (2014).

8. **Heylman, K. D.,** Knapper, K. A., Horak, E. H. & Goldsmith, R. H. “Phothermal Imaging of Individual Carbon Nanofibers with Optical Microresonators.” *SPIE BiOS.* 93310G-93310G-93315 (2015).
9. **Heylman, K. D**. & Goldsmith, R. H. Photothermal mapping and free-space laser tuning of toroidal optical microcavities. *Applied Physics Letters* **103** (2013).

References

1 Kirchoff, G. B., Robert. Chemical analysis by spectrum-observations.—Second memoir. *The London, Edinburgh, and Dublin Philosophical Magazine and Journal of Science* **22**, 329-349 (1861).

2 Colaprete, A. *et al.* Detection of Water in the LCROSS Ejecta Plume. *Science* **330**, 463-468 (2010).

3 Moerner, W. E. & Kador, L. Optical-Detection and Spectroscopy of Single Molecules in a Solid. *Phys Rev Lett* **62**, 2535-2538 (1989).

4 Konopacky, Q. M., Barman, T. S., Macintosh, B. A. & Marois, C. Detection of Carbon Monoxide and Water Absorption Lines in an Exoplanet Atmosphere. *Science* **339**, 1398-1401 (2013).

5 Yu, Z. H. & Barbara, P. F. Low-temperature single-molecule spectroscopy of MEH-PPV conjugated polymer molecules. *J Phys Chem B* **108**, 11321-11326 (2004).

6 English, B. P. *et al.* Ever-fluctuating single enzyme molecules: Michaelis-Menten equation revisited. *Nat Chem Biol* **2**, 87-94 (2006).

7 Groenendaal, L., Jonas, F., Freitag, D., Pielartzik, H. & Reynolds, J. R. Poly (3, 4‐ethylenedioxythiophene) and its derivatives: past, present, and future. *Adv Mater* **12**, 481-494 (2000).

8 Kim, Y. H. *et al.* Highly conductive PEDOT: PSS electrode with optimized solvent and thermal post‐treatment for ITO‐free organic solar cells. *Advanced Functional Materials* **21**, 1076-1081 (2011).

9 Bubnova, O. *et al.* Optimization of the thermoelectric figure of merit in the conducting polymer poly (3, 4-ethylenedioxythiophene). *Nature materials* **10**, 429-433 (2011).

10 Takano, T., Masunaga, H., Fujiwara, A., Okuzaki, H. & Sasaki, T. PEDOT Nanocrystal in Highly Conductive PEDOT:PSS Polymer Films. *Macromolecules* **45**, 3859-3865 (2012).

11 Noriega, R., Salleo, A. & Spakowitz, A. J. Chain conformations dictate multiscale charge transport phenomena in disordered semiconducting polymers. *Proceedings of the National Academy of Sciences* **110**, 16315-16320 (2013).

12 Noriega, R. *et al.* A general relationship between disorder, aggregation and charge transport in conjugated polymers. *Nature materials* **12**, 1038-1044 (2013).

13 Hu, D. H. *et al.* Collapse of stiff conjugated polymers with chemical defects into ordered, cylindrical conformations. *Nature* **405**, 1030-1033 (2000).

14 Van Dijk, M. A., Lippitz, M. & Orrit, M. Far-field optical microscopy of single metal nanoparticles. *Accounts Chem Res* **38**, 594-601 (2005).

15 Debrabander, M., Geuens, G., Nuydens, R., Moeremans, M. & Demey, D. J. Microtubule-Dependent Intracellular Motility Investigated with Nanometer Particle Video Ultramicroscopy (Nanovid Ultramicroscopy). *Ann Ny Acad Sci* **466**, 666-668 (1986).

16 Arbouet, A. *et al.* Direct measurement of the single-metal-cluster optical absorption. *Phys Rev Lett* **93** (2004).

17 Sonnichsen, C. *et al.* Spectroscopy of single metallic nanoparticles using total internal reflection microscopy. *Appl Phys Lett* **77**, 2949-2951 (2000).

18 Klar, T. *et al.* Surface-plasmon resonances in single metallic nanoparticles. *Phys Rev Lett* **80**, 4249-4252 (1998).

19 Lindfors, K., Kalkbrenner, T., Stoller, P. & Sandoghdar, V. Detection and spectroscopy of gold nanoparticles using supercontinuum white light confocal microscopy. *Phys Rev Lett* **93** (2004).

20 Boyer, D., Tamarat, P., Maali, A., Lounis, B. & Orrit, M. Photothermal imaging of nanometer-sized metal particles among scatterers. *Science* **297**, 1160-1163 (2002).

21 Cognet, L., Berciaud, S., Lasne, D. & Lounis, B. Photothermal methods for single nonluminescent nano-objects. *Anal Chem* **80**, 2288-2294 (2008).

22 Yorulmaz, M. *et al.* Single-Particle Absorption Spectroscopy by Photothermal Contrast. *Nano Lett* **15**, 3041-3047 (2015).

23 Li, Z. M., Mao, W. Z., Devadas, M. S. & Hartland, G. V. Absorption Spectroscopy of Single Optically Trapped Gold Nanorods. *Nano Lett* **15**, 7731-7735 (2015).

24 Muskens, O. L. *et al.* Quantitative absorption spectroscopy of a single gold nanorod. *J Phys Chem C* **112**, 8917-8921 (2008).

25 Baida, H. *et al.* Ultrafast Nonlinear Optical Response of a Single Gold Nanorod near Its Surface Plasmon Resonance. *Phys Rev Lett* **107** (2011).

26 Yu, K., Zijlstra, P., Sader, J. E., Xu, Q. H. & Orrit, M. Damping of Acoustic Vibrations of Immobilized Single Gold Nanorods in Different Environments. *Nano Lett* **13**, 2710-2716 (2013).

27 Heylman, K. D. *et al.* Optical microresonators as single-particle absorption spectrometers. *Nat Photon* **advance online publication** (2016).

28 Moerner, W. E. & Fromm, D. P. Methods of single-molecule fluorescence spectroscopy and microscopy. *Rev Sci Instrum* **74**, 3597-3619 (2003).

29 Celebrano, M., Kukura, P., Renn, A. & Sandoghdar, V. Single-molecule imaging by optical absorption. *Nat Photonics* **5**, 95-98 (2011).

30 Maser, A., Gmeiner, B., Utikal, T., Gotzinger, S. & Sandoghdar, V. Few-photon coherent nonlinear optics with a single molecule. *Nat Photonics* **10**, 450-+ (2016).

31 Orrit, M. & Bernard, J. Single Pentacene Molecules Detected by Fluorescence Excitation in a Para-Terphenyl Crystal. *Phys Rev Lett* **65**, 2716-2719 (1990).

32 Zheng, Q. *et al.* Ultra-stable organic fluorophores for single-molecule research. *Chem. Soc. Rev.* **43**, 1044-1056 (2014).

33 Bolinger, J. C., Traub, M. C., Adachi, T. & Barbara, P. F. Ultralong-Range Polaron-Induced Quenching of Excitons in Isolated Conjugated Polymers. *Science* **331**, 565-567 (2011).

34 Schindler, F., Lupton, J. M., Feldmann, J. & Scherf, U. A universal picture of chromophores in pi-conjugated polymers derived from single-molecule spectroscopy. *P Natl Acad Sci USA* **101**, 14695-14700 (2004).

35 Yu, Z. & Barbara, P. F. Low-temperature single-molecule spectroscopy of MEH-PPV conjugated polymer molecules. *The Journal of Physical Chemistry B* **108**, 11321-11326 (2004).

36 Piatkowski, L., Gellings, E. & van Hulst, N. F. Broadband single-molecule excitation spectroscopy. *Nat Commun* **7** (2016).

37 Stopel, M. H. W., Blum, C. & Subramaniam, V. Excitation Spectra and Stokes Shift Measurements of Single Organic Dyes at Room Temperature. *J Phys Chem Lett* **5**, 3259-3264 (2014).

38 Chong, S. S., Min, W. & Xie, X. S. Ground-State Depletion Microscopy: Detection Sensitivity of Single-Molecule Optical Absorption at Room Temperature. *J Phys Chem Lett* **1**, 3316-3322 (2010).

39 Millard, R. R. & Greene, B. I. Direct Determination of Nonradiative Relaxation Rates in Nonfluorescent Metallophthalocyanines. *J Phys Chem-Us* **89**, 2976-2978 (1985).

40 Goldoni, A. Porphyrins: fascinating molecules with biological significance. *Elettra highlights* **2001**, 64-65 (2002).

41 Ortega-Arroyo, J. & Kukura, P. Interferometric scattering microscopy (iSCAT): new frontiers in ultrafast and ultrasensitive optical microscopy. *Phys Chem Chem Phys* **14**, 15625-15636 (2012).

42 Piliarik, M. & Sandoghdar, V. Direct optical sensing of single unlabelled proteins and super-resolution imaging of their binding sites. *Nat Commun* **5** (2014).

43 Arroyo, J. O. *et al.* Label-Free, All-Optical Detection, Imaging, and Tracking of a Single Protein. *Nano Lett* **14**, 2065-2070 (2014).

44 Spindler, S. *et al.* Visualization of lipids and proteins at high spatial and temporal resolution via interferometric scattering (iSCAT) microscopy. *J Phys D Appl Phys* **49** (2016).

45 Betzig, E. & Chichester, R. J. Single Molecules Observed by near-Field Scanning Optical Microscopy. *Science* **262**, 1422-1425 (1993).

46 Betzig, E. & Trautman, J. K. Near-Field Optics - Microscopy, Spectroscopy, and Surface Modification Beyond the Diffraction Limit. *Science* **257**, 189-195 (1992).

47 Le Ru, E. C. & Etchegoin, P. G. Single-molecule surface-enhanced Raman spectroscopy. *Annu Rev Phys Chem* **63**, 65-87 (2012).

48 Sharma, B., Frontiera, R. R., Henry, A.-I., Ringe, E. & Van Duyne, R. P. SERS: materials, applications, and the future. *Materials today* **15**, 16-25 (2012).

49 Kneipp, K. *et al.* Single molecule detection using surface-enhanced Raman scattering (SERS). *Phys Rev Lett* **78**, 1667 (1997).

50 Nie, S. & Emory, S. R. Probing single molecules and single nanoparticles by surface-enhanced Raman scattering. *Science* **275**, 1102-1106 (1997).

51 Gaiduk, A., Yorulmaz, M., Ruijgrok, P. V. & Orrit, M. Room-Temperature Detection of a Single Molecule's Absorption by Photothermal Contrast. *Science* **330**, 353-356 (2010).

52 Berciaud, S., Cognet, L., Blab, G. A. & Lounis, B. Photothermal heterodyne imaging of individual nonfluorescent nanoclusters and nanocrystals. *Phys Rev Lett* **93**, 257402 (2004).

53 Narayana, S. & Sato, Y. Compact Miniature High-Resolution Thermometer. *Ieee T Appl Supercon* **20**, 2402-2405 (2010).

54 Sergatskov, D. A. *et al.* New paramagnetic susceptibility thermometers for fundamental physics measurements. *Aip Conf Proc* **684**, 1009-1013 (2003).

55 Weng, W. L. *et al.* Nano-Kelvin Thermometry and Temperature Control: Beyond the Thermal Noise Limit. *Phys Rev Lett* **112** (2014).

56 Abbott, B. P. *et al.* Observation of Gravitational Waves from a Binary Black Hole Merger. *Phys Rev Lett* **116** (2016).

57 Ma, Q. L., Rossmann, T. & Guo, Z. X. Whispering-gallery mode silica microsensors for cryogenic to room temperature measurement. *Measurement Science & Technology* **21**, 025310 (2010).

58 Dong, C.-H. *et al.* Fabrication of high-Q polydimethylsiloxane optical microspheres for thermal sensing. *Appl Phys Lett* **94**, 231119 (2009).

59 Maker, A. J. & Armani, A. M. Nanowatt threshold, alumina sensitized neodymium laser integrated on silicon. *Opt Express* **21**, 27238-27245 (2013).

60 He, L. N., Ozdemir, S. K. & Yang, L. Whispering gallery microcavity lasers. *Laser Photonics Rev* **7**, 60-82 (2013).

61 Min, B. *et al.* Ultralow threshold on-chip microcavity nanocrystal quantum dot lasers. *Appl Phys Lett* **89**, 191124 (2006).

62 Rayleigh, L. CXII. The problem of the whispering gallery. *The London, Edinburgh, and Dublin Philosophical Magazine and Journal of Science* **20**, 1001-1004 (1910).

63 Corning. Corning SMF-28e+ Optical Fiber (Corning Incorporated, 2014).

64 Tong, Z., Jakubinek, M., Wright, A., Gillies, A. & Loock, H.-P. Fiber-loop ring-down spectroscopy: a sensitive absorption technique for small liquid samples. *Rev Sci Instrum* **74**, 4818-4826 (2003).

65 Richtmyer, R. Dielectric resonators. *J Appl Phys* **10**, 391-398 (1939).

66 Braginsky, V. B., Gorodetsky, M. L. & Ilchenko, V. S. Quality-Factor and Nonlinear Properties of Optical Whispering-Gallery Modes. *Phys Lett A* **137**, 393-397 (1989).

67 Benner, R., Barber, P., Owen, J. & Chang, R. Observation of structure resonances in the fluorescence spectra from microspheres. *Phys Rev Lett* **44**, 475 (1980).

68 Taylor, M. A. *et al.* Cavity optoelectromechanical regenerative amplification. *Opt Express* **20**, 12742-12751 (2012).

69 Grudinin, I. S., Lee, H., Painter, O. & Vahala, K. J. Phonon Laser Action in a Tunable Two-Level System. *Phys Rev Lett* **104** (2010).

70 Verhagen, E., Deleglise, S., Weis, S., Schliesser, A. & Kippenberg, T. J. Quantum-coherent coupling of a mechanical oscillator to an optical cavity mode. *Nature* **482**, 63-67 (2012).

71 Bahl, G., Zehnpfennig, J., Tomes, M. & Carmon, T. Stimulated optomechanical excitation of surface acoustic waves in a microdevice. *Nat Commun* **2**, 403 (2011).

72 Dantham, V. R. *et al.* Label-Free Detection of Single Protein Using a Nanoplasmonic-Photonic Hybrid Microcavity. *Nano Lett* **13**, 3347-3351 (2013).

73 Baaske, M. D., Foreman, M. R. & Vollmer, F. Single-molecule nucleic acid interactions monitored on a label-free microcavity biosensor platform. *Nat Nanotechnol* **9**, 933-939 (2014).

74 Li, B. B. *et al.* Single nanoparticle detection using split-mode microcavity Raman lasers. *P Natl Acad Sci USA* **111**, 14657-14662 (2014).

75 Ozdemir, S. K. *et al.* Highly sensitive detection of nanoparticles with a self-referenced and self-heterodyned whispering-gallery Raman microlaser. *P Natl Acad Sci USA* **111**, E3836-E3844 (2014).

76 Mader, M., Reichel, J., Hansch, T. W. & Hunger, D. A scanning cavity microscope. *Nat Commun* **6** (2015).

77 Vallance, C., Trichet, A. A. P., James, D., Dolan, P. R. & Smith, J. M. Open-access microcavities for chemical sensing. *Nanotechnology* **27** (2016).

78 Wang, J. *et al.* High-Q lithium niobate microdisk resonators on a chip for efficient electro-optic modulation. *Opt Express* **23**, 23072-23078 (2015).

79 Arnold, S., Khoshsima, M., Teraoka, I., Holler, S. & Vollmer, F. Shift of whispering-gallery modes in microspheres by protein adsorption. *Opt Lett* **28**, 272-274 (2003).

80 Swaim, J. D., Knittel, J. & Bowen, W. P. Detection limits in whispering gallery biosensors with plasmonic enhancement. *Appl Phys Lett* **99** (2011).

81 Shopova, S., Rajmangal, R., Holler, S. & Arnold, S. Plasmonic enhancement of a whispering-gallery-mode biosensor for single nanoparticle detection. *Appl Phys Lett* **98**, 243104 (2011).

82 Foreman, M. R. & Vollmer, F. Theory of resonance shifts of whispering gallery modes by arbitrary plasmonic nanoparticles. *New J Phys* **15** (2013).

83 Dantham, V., Holler, S., Kolchenko, V., Wan, Z. & Arnold, S. Taking whispering gallery-mode single virus detection and sizing to the limit. *Appl Phys Lett* **101**, 043704 (2012).

84 Yu, W. Y., Jiang, W. C., Lin, Q. & Lu, T. Cavity optomechanical spring sensing of single molecules. *Nat Commun* **7** (2016).

85 Matsko, A. B., Savchenkov, A. A., Yu, N. & Maleki, L. Whispering-gallery-mode resonators as frequency references. I. Fundamental limitations. *JOSA B* **24**, 1324-1335 (2007).

86 Shao, L. *et al.* Detection of Single Nanoparticles and Lentiviruses Using Microcavity Resonance Broadening. *Adv Mater* (2013).

87 Nishimura, J., Kobayashi, M., Saito, R. & Tanabe, T. NaCl ion detection using a silica toroid microcavity. *Appl Optics* **54**, 6391-6396 (2015).

88 Li, M., Wu, X., Liu, L., Fan, X. & Xu, L. Self-referencing optofluidic ring resonator sensor for highly sensitive biomolecular detection. *Anal Chem* **85**, 9328-9332 (2013).

89 Schliesser, A., Anetsberger, G., Riviere, R., Arcizet, O. & Kippenberg, T. J. High-sensitivity monitoring of micromechanical vibration using optical whispering gallery mode resonators. *New J Phys* **10** (2008).

90 Lu, T. *et al.* High sensitivity nanoparticle detection using optical microcavities. *P Natl Acad Sci USA* **108**, 5976-5979 (2011).

91 Charlebois, M. *et al.* Toward Automatic Label-Free Whispering Gallery Modes Biodetection with a Quantum Dot-Coated Microsphere Population. *Nanoscale Res Lett* **5**, 524-532 (2010).

92 Weng, W. L., Anstie, J. D. & Luiten, A. N. Refractometry with Ultralow Detection Limit Using Anisotropic Whispering-Gallery-Mode Resonators. *Phys Rev Appl* **3** (2015).

93 Alnis, J. *et al.* Thermal-noise-limited crystalline whispering-gallery-mode resonator for laser stabilization. *Phys Rev A* **84**, 011804 (2011).

94 Swaim, J. D., Knittel, J. & Bowen, W. P. Detection of nanoparticles with a frequency locked whispering gallery mode microresonator. *Appl Phys Lett* **102** (2013).

95 Knittel, J., Swaim, J. D., McAuslan, D. L., Brawley, G. A. & Bowen, W. P. Back-scatter based whispering gallery mode sensing. *Sci Rep-Uk* **3** (2013).

96 Maker, A. J. & Armani, A. M. Heterodyned toroidal microlaser sensor. *Appl Phys Lett* **103** (2013).

97 R Ali, A., Ioppolo, T., Ötügen, V., Christensen, M. & MacFarlane, D. Photonic electric field sensor based on polymeric microspheres. *Journal of Polymer Science Part B: Polymer Physics* **52**, 276-279 (2014).

98 Martin, L. *et al.* High pressure tuning of whispering gallery mode resonances in a neodymium-doped glass microsphere. *JOSA B* **30**, 3254-3259 (2013).

99 Barnes, J. *et al.* Loss determination in microsphere resonators by phase-shift cavity ring-down measurements. *Opt Express* **16**, 13158-13167 (2008).

100 Barnes, J. A., Gagliardi, G. & Loock, H. P. Absolute absorption cross-section measurement of a submonolayer film on a silica microresonator. *Optica* **1**, 75-83 (2014).

101 Boyd, R. W. & Heebner, J. E. Sensitive disk resonator photonic biosensor. *Appl Optics* **40**, 5742-5747 (2001).

102 Weiss, D. *et al.* Splitting of high-Q Mie modes induced by light backscattering in silica microspheres. *Opt Lett* **20**, 1835-1837 (1995).

103 Zhu, J. G. *et al.* On-chip single nanoparticle detection and sizing by mode splitting in an ultrahigh-Q microresonator. *Nat Photonics* **4**, 46-49 (2010).

104 He, L. N., Ozdemir, K., Zhu, J. G., Kim, W. & Yang, L. Detecting single viruses and nanoparticles using whispering gallery microlasers. *Nat Nanotechnol* **6**, 428-432 (2011).

105 Ganta, D., Dale, E. B. & Rosenberger, A. T. Measuring sub-nm adsorbed water layer thickness and desorption rate using a fused-silica whispering-gallery microresonator. *Meas Sci Technol* **25** (2014).

106 Armani, D. K., Kippenberg, T. J., Spillane, S. M. & Vahala, K. J. Ultra-high-Q toroid microcavity on a chip. *Nature* **421**, 925-928 (2003).

107 Riviere, R. *et al.* Optomechanical sideband cooling of a micromechanical oscillator close to the quantum ground state. *Phys Rev A* **83**, 063835 (2011).

108 Pinnow, D. A., Rich, T. C., Ostermayer, F. W. & Didomenico, M. Fundamental Optical Attenuation Limits in Liquid and Glassy State with Application to Fiber Optical Waveguide Materials. *Appl Phys Lett* **22**, 527-529 (1973).

109 Kippenberg, T. J. A. *Nonlinear optics in ultra-high-Q whispering-gallery optical microcavities*, California Institute of Technology, (2004).

110 Armani, A. M., Armani, D. K., Min, B., Vahala, K. J. & Spillane, S. M. Ultra-high-Q microcavity operation in H2O and D2O. *Appl Phys Lett* **87** (2005).

111 Gorodetsky, M. L., Savchenkov, A. A. & Ilchenko, V. S. Ultimate Q of optical microsphere resonators. *Opt Lett* **21**, 453-455 (1996).

112 Rokhsari, H., Spillane, S. M. & Vahala, K. J. Loss characterization in microcavities using the thermal bistability effect. *Appl Phys Lett* **85**, 3029-3031 (2004).

113 Leviton, D. B. & Frey, B. J. Temperature-dependent absolute refractive index measurements of synthetic fused silica - art. no. 62732K. *Optomechanical Technologies for Astronomy, Pts 1 and 2* **6273**, K2732-K2732 (2006).

114 Fernandes, L. A., Grenier, J. R., Herman, P. R., Aitchison, J. S. & Marques, P. V. S. Stress induced birefringence tuning in femtosecond laser fabricated waveguides in fused silica. *Opt Express* **20**, 24103-24114 (2012).

115 Gorodetsky, M. L. & Grudinin, I. S. Fundamental thermal fluctuations in microspheres. *J Opt Soc Am B* **21**, 697-705 (2004).

116 Labrador-Paez, L. *et al.* Optical humidity sensor based on a liquid whispering-gallery mode resonator. *arXiv preprint arXiv:1602.03322* (2016).

117 Oxborrow, M. Traceable 2-D finite-element simulation of the whispering-gallery modes of axisymmetric electromagnetic resonators. *Ieee T Microw Theory* **55**, 1209-1218 (2007).

118 Schunk, G. *et al.* Identifying modes of large whispering-gallery mode resonators from the spectrum and emission pattern. *Opt Express* **22**, 30795-30806 (2014).

119 Carmon, T. & Vahala, K. J. Visible continuous emission from a silica microphotonic device by third-harmonic generation. *Nat Phys* **3**, 430-435 (2007).

120 Tomes, M., Vahala, K. J. & Carmon, T. Direct imaging of tunneling from a potential well. *Opt Express* **17**, 19160-19165 (2009).

121 Vahala, K. J. Optical microcavities. *Nature* **424**, 839-846 (2003).

122 Savchenkov, A. A., Matsko, A. B., Ilchenko, V. S. & Maleki, L. Optical resonators with ten million finesse. *Opt Express* **15**, 6768-6773 (2007).

123 Savchenkov, A. A., Ilchenko, V. S., Matsko, A. B. & Maleki, L. Kilohertz optical resonances in dielectric crystal cavities. *Phys Rev A* **70**, 051804 (2004).

124 Farca, G., Shopova, S. & Rosenberger, A. Cavity-enhanced laser absorption spectroscopy using microresonator whispering-gallery modes. *Opt Express* **15**, 17443-17448 (2007).

125 Rosenblum, S., Lovsky, Y., Arazi, L., Vollmer, F. & Dayan, B. Cavity ring-up spectroscopy for ultrafast sensing with optical microresonators. *Nat Commun* **6** (2015).

126 Carey, C. R. *et al.* Imaging and Absolute Extinction Cross-Section Measurements of Nanorods and Nanowires through Polarization Modulation Microscopy. *J Phys Chem C* **114**, 16029-16036 (2010).

127 Zhu, J. G. *et al.* Interfacing whispering-gallery microresonators and free space light with cavity enhanced Rayleigh scattering. *Sci Rep-Uk* **4** (2014).

128 Ganta, D., Dale, E., Rezac, J. & Rosenberger, A. Optical method for measuring thermal accommodation coefficients using a whispering-gallery microresonator. *The Journal of chemical physics* **135**, 084313 (2011).

129 Schietinger, S. & Benson, O. Coupling single NV-centres to high-Q whispering gallery modes of a preselected frequency-matched microresonator. *Journal of Physics B: Atomic, Molecular and Optical Physics* **42**, 114001 (2009).

130 Schietinger, S., Schröder, T. & Benson, O. One-by-one coupling of single defect centers in nanodiamonds to high-Q modes of an optical microresonator. *Nano Lett* **8**, 3911-3915 (2008).

131 Götzinger, S. *et al.* Confocal microscopy and spectroscopy of nanocrystals on a high-Q microsphere resonator. *Journal of Optics B: Quantum and Semiclassical Optics* **6**, 154 (2004).

132 Heylman, K. D. & Goldsmith, R. H. Photothermal mapping and free-space laser tuning of toroidal optical microcavities. *Appl Phys Lett* **103** (2013).

133 Heylman, K. D., Knapper, K. A. & Goldsmith, R. H. Photothermal Microscopy of Nonluminescent Single Particles Enabled by Optical Microresonators. *J Phys Chem Lett* **5**, 1917-1923 (2014).

134 Burzo, M. G., Komarov, P. L. & Raad, P. E. Thermal transport properties of gold-covered thin-film silicon dioxide. *Ieee T Compon Pack T* **26**, 80-88 (2003).

135 Kippenberg, T. J., Spillane, S. M. & Vahala, K. J. Demonstration of ultra-high-Q small mode volume toroid microcavities on a chip. *Appl Phys Lett* **85**, 6113-6115 (2004).

136 Borselli, M., Johnson, T. J. & Painter, O. Measuring the role of surface chemistry in silicon microphotonics. *Appl Phys Lett* **88** (2006).

137 Yi, X. *et al.* Multiple-Rayleigh-scatterer-induced mode splitting in a high-Q whispering-gallery-mode microresonator. *Phys Rev A* **83** (2011).

138 He, L. N., Ozdemir, S. K., Zhu, J. G. & Yang, L. Ultrasensitive detection of mode splitting in active optical microcavities. *Phys Rev A* **82** (2010).

139 Spillane, S. M. *et al.* Ultrahigh-Q toroidal microresonators for cavity quantum electrodynamics. *Phys Rev A* **71** (2005).

140 Il'chenko, V. S. & Gorodetskii, M. L. Thermal Nonlinear Effects in Optical Whispering Gallery Microresonators. *Laser Phys* **2**, 1004-1009 (1992).

141 Inagawa, H. *et al.* Reflecting microscope system with a 0.99 numerical aperture designed for three-dimensional fluorescence imaging of individual molecules at cryogenic temperatures. *Sci Rep-Uk* **5** (2015).

142 Optics, O. Tapered and Lensed Fibers.

143 Vogelsang, J., Brazard, J., Adachi, T., Bolinger, J. C. & Barbara, P. F. Watching the Annealing Process One Polymer Chain at a Time. *Angew Chem Int Edit* **50**, 2257-2261 (2011).

144 Delay, M. Practical Aspects of Mirror Usage in Optical Systems for Biology. (Semrock, Inc., Semrock, Inc.).

145 Stone, J. & Walrafen, G. E. Overtone Vibrations of Oh Groups in Fused-Silica Optical Fibers. *J Chem Phys* **76**, 1712-1722 (1982).

146 Asay, D. B. & Kim, S. H. Evolution of the adsorbed water layer structure on silicon oxide at room temperature. *J Phys Chem B* **109**, 16760-16763 (2005).

147 Henze, R. *et al.* Fine-tuning of whispering gallery modes in on-chip silica microdisk resonators within a full spectral range. *Appl Phys Lett* **102** (2013).

148 Armani, D., Min, B., Martin, A. & Vahala, K. J. Electrical thermo-optic tuning of ultrahigh-Q microtoroid resonators. *Appl Phys Lett* **85**, 5439-5441 (2004).

149 Zhu, J. G., Ozdemir, S. K., He, L. N. & Yang, L. Optothermal spectroscopy of whispering gallery microresonators. *Appl Phys Lett* **99** (2011).

150 Hobbs, P. C. *Building electro-optical systems: making it all work*. Vol. 71 (John Wiley & Sons, 2011).

151 Xiao, Y. F. *et al.* Tunneling-induced transparency in a chaotic microcavity. *Laser Photonics Rev* **7**, L51-L54 (2013).

152 Yang, Q. F., Jiang, X. F., Cui, Y. L., Shao, L. B. & Xiao, Y. F. Dynamical tunneling-assisted coupling of high-Q deformed microcavities using a free-space beam. *Phys Rev A* **88** (2013).

153 Knight, J. C., Cheung, G., Jacques, F. & Birks, T. A. Phase-matched excitation of whispering-gallery-mode resonances by a fiber taper. *Opt Lett* **22**, 1129-1131 (1997).

154 Kippenberg, T., Spillane, S., Armani, D. & Vahala, K. Fabrication and coupling to planar high-Q silica disk microcavities. *Appl Phys Lett* **83**, 797-799 (2003).

155 Spillane, S. *Fiber-coupled ultra-high-Q microresonators for nonlinear and quantum optics* Ph.D. thesis, California Institute of Technology, (2004).

156 Zhang, X. M. & Armani, A. M. Silica microtoroid resonator sensor with monolithically integrated waveguides. *Opt Express* **21**, 23592-23603 (2013).

157 Hoffman, J. E. *et al.* Ultrahigh transmission optical nanofibers. *Aip Adv* **4** (2014).

158 Fang, Z. *et al.* Fabrication of a microresonator-fiber assembly maintaining a high-quality factor by CO 2 laser welding. *Opt Express* **23**, 27941-27946 (2015).

159 Song, J., Lin, J., Tang, J., Qiao, L. & Cheng, Y. Integration of an optical fiber taper with an optical microresonator fabricated in glass by femtosecond laser 3D micromachining. *arXiv preprint arXiv:1402.1356* (2014).

160 Rokhsari, H. & Vahala, K. J. Ultralow loss, high Q, four port resonant couplers for quantum optics and photonics. *Phys Rev Lett* **92** (2004).

161 Drever, R. W. P. *et al.* Laser Phase and Frequency Stabilization Using an Optical-Resonator. *Appl Phys B-Photo* **31**, 97-105 (1983).

162 Black, E. D. An introduction to Pound-Drever-Hall laser frequency stabilization. *Am J Phys* **69**, 79-87 (2001).

163 Carmon, T. *et al.* Feedback control of ultra-high-Q microcavities: application to micro-Raman lasers and microparametric oscillators. *Opt Express* **13**, 3558-3566 (2005).

164 Lee, K. H., McRae, T. G., Harris, G. I., Knittel, J. & Bowen, W. P. Cooling and Control of a Cavity Optoelectromechanical System. *Phys Rev Lett* **104** (2010).

165 Pound, R. V. Electronic frequency stabilization of microwave oscillators. *Rev Sci Instrum* **17**, 490-505 (1946).

166 Minicircuits. *Minicircuits Applications Notes*, <http://www.minicircuits.com/applications/applications_notes.html> (

167 Black, E. (Laser Interferometer Gravitational Wave Observatory, 1998).

168 O'Shea, D., Rettenmaier, A. & Rauschenbeutel, A. Active frequency stabilization of an ultra-high Q whispering-gallery-mode microresonator. *Appl Phys B-Lasers O* **99**, 623-627 (2010).

169 Chow, J. H. *et al.* Critical coupling control of a microresonator by laser amplitude modulation. *Opt Express* **20**, 12622-12630 (2012).

170 Armani, D. K. *Ultra-high-Q planar microcavities and applications*, California Institute of Technology, (2005).

171 Jager, J.-B. *Fabrication et étude optique de microcavités à modes de galerie intégrées sur silicium*, Université de Grenoble, (2012).

172 Zhang, X. M., Choi, H. S. & Armani, A. M. Ultimate quality factor of silica microtoroid resonant cavities. *Appl Phys Lett* **96** (2010).

173 MicroChemicals. Lithography Trouble Shooter: Questions and Answers Around the Most Common Problems in Micro-Structuring. (2012).

174 Linde, H. & Austin, L. Wet Silicon Etching with Aqueous Amine Gallates. *J Electrochem Soc* **139**, 1170-1174 (1992).

175 Lee, H. *et al.* Chemically etched ultrahigh-Q wedge-resonator on a silicon chip. *Nat Photonics* **6**, 369-373 (2012).

176 Jager, J.-B. *et al.* High-Q silica microcavities on a chip: from microtoroid to microsphere. *Appl Phys Lett* **99**, 181123 (2011).

177 Ward, J. M., Maimaiti, A., Le, V. H. & Chormaic, S. N. Contributed Review: Optical micro- and nanofiber pulling rig. *Rev Sci Instrum* **85** (2014).

178 Ding, L., Belacel, C., Ducci, S., Leo, G. & Favero, I. Ultralow loss single-mode silica tapers manufactured by a microheater. *Appl Optics* **49**, 2441-2445 (2010).

179 Zhang, E. J., Sacher, W. D. & Poon, J. K. S. Hydrofluoric acid flow etching of low-loss subwavelength-diameter biconical fiber tapers. *Opt Express* **18**, 22593-22598 (2010).

180 Ward, J. M. *et al.* Heat-and-pull rig for fiber taper fabrication. *Rev Sci Instrum* **77** (2006).

181 Connolly, E. W. *Experiments with toroidal microresonators in cavity QED* Ph.D. thesis, California Institute of Technology, (2009).

182 Fujiwara, M., Toubaru, K. & Takeuchi, S. Optical transmittance degradation in tapered fibers. *Opt Express* **19**, 8596-8601 (2011).

183 Aoki, T. *et al.* Observation of strong coupling between one atom and a monolithic microresonator. *Nature* **443**, 671-674 (2006).

184 Li, B.-B. *et al.* Experimental controlling of Fano resonance in indirectly coupled whispering-gallery microresonators. *Appl Phys Lett* **100**, 021108 (2012).

185 Harker, A., Mehrabani, S. & Armani, A. M. Ultraviolet light detection using an optical microcavity. *Opt Lett* **38**, 3422-3425 (2013).

186 Savchenkov, A. A. *et al.* Narrowband tunable photonic notch filter. *Opt Lett* **34**, 1318-1320 (2009).

187 Baaske, M. & Vollmer, F. Optical resonator biosensors: molecular diagnostic and nanoparticle detection on an integrated platform. *ChemPhysChem* **13**, 427-436 (2012).

188 Washburn, A. L., Gunn, L. C. & Bailey, R. C. Label-free quantitation of a cancer biomarker in complex media using silicon photonic microring resonators. *Anal Chem* **81**, 9499-9506 (2009).

189 Soteropulos, C. E., Zurick, K. M., Bernards, M. T. & Hunt, H. K. Tailoring the protein adsorption properties of whispering gallery mode optical biosensors. *Langmuir* **28**, 15743-15750 (2012).

190 Zhu, J., Özdemir, Ş. K., He, L., Chen, D.-R. & Yang, L. Single virus and nanoparticle size spectrometry by whispering-gallery-mode microcavities. *Opt Express* **19**, 16195-16206 (2011).

191 Kippenberg, T. J., Spillane, S. M. & Vahala, K. J. Kerr-nonlinearity optical parametric oscillation in an ultrahigh-Q toroid microcavity. *Phys Rev Lett* **93**, 083904 (2004).

192 Armani, A. M., Kulkarni, R. P., Fraser, S. E., Flagan, R. C. & Vahala, K. J. Label-free, single-molecule detection with optical microcavities. *Science* **317**, 783-787 (2007).

193 Cheema, M. I. *et al.* Simultaneous measurement of quality factor and wavelength shift by phase shift microcavity ring down spectroscopy. *Opt Express* **20**, 9090-9098 (2012).

194 Hossein-Zadeh, M. & Vahala, K. J. Free ultra-high-Q microtoroid: a tool for designing photonic devices. *Opt Express* **15**, 166-175 (2007).

195 Pan, J. *et al.* Aligning microcavity resonances in silicon photonic-crystal slabs using laser-pumped thermal tuning. *Appl Phys Lett* **92**, 103114 (2008).

196 Peng, B., Ozdemir, S. K., Zhu, J. G. & Yang, L. Photonic molecules formed by coupled hybrid resonators. *Opt Lett* **37**, 3435-3437 (2012).

197 Savchenkov, A. A., Ilchenko, V. S., Handley, T. & Maleki, L. Ultraviolet-assisted frequency trimming of optical microsphere resonators. *Opt Lett* **28**, 649-650 (2003).

198 Topolancik, J. & Vollmer, F. All-optical switching in the near infrared with bacteriorhodopsin-coated microcavities. *Appl Phys Lett* **89**, 184103 (2006).

199 Tapalian, H. C., Laine, J. P. & Lane, P. A. Thermooptical switches using coated microsphere resonators. *Ieee Photonic Tech L* **14**, 1118-1120 (2002).

200 Carmon, T., Yang, L. & Vahala, K. J. Dynamical thermal behavior and thermal self-stability of microcavities. *Opt Express* **12**, 4742-4750 (2004).

201 Curtis, J. E., Koss, B. A. & Grier, D. G. Dynamic holographic optical tweezers. *Optics Communications* **207**, 169-175 (2002).

202 Nirmal, M. *et al.* Fluorescence intermittency in single cadmium selenide nanocrystals. *Nature* **383**, 802-804 (1996).

203 Banin, U. *et al.* Evidence for a thermal contribution to emission intermittency in single CdSe/CdS core/shell nanocrystals. *J Chem Phys* **110**, 1195-1201 (1999).

204 Empedocles, S. A., Neuhauser, R., Shimizu, K. & Bawendi, M. G. Photoluminescence from single semiconductor nanostructures. *Adv Mater* **11**, 1243-1256 (1999).

205 Slaughter, L., Chang, W. S. & Link, S. Characterizing Plasmons in Nanoparticles and Their Assemblies with Single Particle Spectroscopy. *J Phys Chem Lett* **2**, 2015-2023 (2011).

206 Fernee, M. J., Tamarat, P. & Lounis, B. Spectroscopy of single nanocrystals. *Chem Soc Rev* **43**, 1311-1337 (2014).

207 Staleva, H. & Hartland, G. V. Transient absorption studies of single silver nanocubes. *J Phys Chem C* **112**, 7535-7539 (2008).

208 Link, S. & El-Sayed, M. A. Shape and size dependence of radiative, non-radiative and photothermal properties of gold nanocrystals. *Int Rev Phys Chem* **19**, 409-453 (2000).

209 Sfeir, M. Y. *et al.* Probing electronic transitions in individual carbon nanotubes by Rayleigh scattering. *Science* **306**, 1540-1543 (2004).

210 Freitag, M., Martin, Y., Misewich, J. A., Martel, R. & Avouris, P. H. Photoconductivity of single carbon nanotubes. *Nano Lett* **3**, 1067-1071 (2003).

211 Gliboff, M. *et al.* Direct Measurement of Acceptor Group Localization on Donor–Acceptor Polymers Using Resonant Auger Spectroscopy. *The Journal of Physical Chemistry C* **118**, 5570-5578 (2014).

212 Barbara, P. F., Gesquiere, A. J., Park, S. J. & Lee, Y. J. Single-molecule spectroscopy of conjugated polymers. *Accounts Chem Res* **38**, 602-610 (2005).

213 Kaake, L. G., Barbara, P. F. & Zhu, X. Y. Intrinsic Charge Trapping in Organic and Polymeric Semiconductors: A Physical Chemistry Perspective. *J Phys Chem Lett* **1**, 628-635 (2010).

214 Palacios, R. E., Fan, F. R. F., Bard, A. J. & Barbara, P. F. Single-molecule spectroelectrochemistry (SMS-EC). *J Am Chem Soc* **128**, 9028-9029 (2006).

215 Vollmer, F. & Arnold, S. Whispering-gallery-mode biosensing: label-free detection down to single molecules. *Nat Methods* **5**, 591-596 (2008).

216 Washburn, A. L., Luchansky, M. S., Bowman, A. L. & Bailey, R. C. Quantitative, Label-Free Detection of Five Protein Biomarkers Using Multiplexed Arrays of Silicon Photonic Microring Resonators. *Anal Chem* **82**, 69-72 (2010).

217 Farca, G., Shopova, S. I. & Rosenberger, A. T. Cavity-enhanced laser absorption spectroscopy using microresonator whispering-gallery modes. *Opt Express* **15**, 17443-17448 (2007).

218 Serpenguzel, A., Arnold, S. & Griffel, G. Excitation of Resonances of Microspheres on an Optical-Fiber. *Opt Lett* **20**, 654-656 (1995).

219 Arnold, S., Shopova, S. I. & Holler, S. Whispering gallery mode bio-sensor for label-free detection of single molecules: thermo-optic vs. reactive mechanism. *Opt Express* **18**, 281-287 (2010).

220 Kim, W. *et al.* Detection and size measurement of individual hemozoin nanocrystals in aquatic environment using a whispering gallery mode resonator. *Opt Express* **20**, 29426-29446 (2012).

221 Blancon, J. C. *et al.* Direct measurement of the absolute absorption spectrum of individual semiconducting single-wall carbon nanotubes. *Nat Commun* **4** (2013).

222 Kukura, P., Celebrano, M., Renn, A. & Sandoghdar, V. Single-Molecule Sensitivity in Optical Absorption at Room Temperature. *J Phys Chem Lett* **1**, 3323-3327 (2010).

223 Kim, H., Sheps, T., Collins, P. G. & Potma, E. O. Nonlinear Optical Imaging of Individual Carbon Nanotubes with Four-Wave-Mixing Microscopy. *Nano Lett* **9**, 2991-2995 (2009).

224 Tsen, A. W., Donev, L. A. K., Kurt, H., Herman, L. H. & Park, J. Imaging the electrical conductance of individual carbon nanotubes with photothermal current microscopy. *Nat Nanotechnol* **4**, 108-113 (2009).

225 Wang, D., Carlson, M. T. & Richardson, H. H. Absorption Cross Section and Interfacial Thermal Conductance from an Individual Optically Excited Single-Walled Carbon Nanotube. *Acs Nano* **5**, 7391-7396 (2011).

226 Berciaud, S., Cognet, L., Poulin, P., Weisman, R. B. & Lounis, B. Absorption spectroscopy of individual single-walled carbon nanotubes. *Nano Lett* **7**, 1203-1207 (2007).

227 Chang, W. S., Ha, J. W., Slaughter, L. S. & Link, S. Plasmonic nanorod absorbers as orientation sensors. *P Natl Acad Sci USA* **107**, 2781-2786 (2010).

228 Rezac, J. P. & Rosenberger, A. T. Locking a microsphere whispering-gallery mode to a laser. *Opt Express* **8**, 605-610 (2001).

229 Kim, S. H., Mulholland, G. W. & Zachariah, M. R. Density measurement of size selected multiwalled carbon nanotubes by mobility-mass characterization. *Carbon* **47**, 1297-1302 (2009).

230 Djurisic, A. B. & Li, E. H. Optical properties of graphite. *J Appl Phys* **85**, 7404-7410 (1999).

231 Stagg, B. J. & Charalampopoulos, T. T. Refractive-Indexes of Pyrolytic-Graphite, Amorphous-Carbon, and Flame Soot in the Temperature-Range 25ºC to 600ºC. *Combust Flame* **94**, 381-396 (1993).

232 Greenawa.Dl, Harbeke, G., Bassani, F. & Tosatti, E. Anisotropy of Optical Constants and Band Structure of Graphite. *Physical Review* **178**, 1340-1348 (1969).

233 Wang, X. F., Chen, Y. P. & Nolte, D. D. Strong anomalous optical dispersion of graphene: complex refractive index measured by Picometrology. *Opt Express* **16**, 22105-22112 (2008).

234 Pokrass, M., Burshtein, Z., Gvishi, R. & Nathan, M. Saturable absorption of multi-walled carbon nanotubes/hybrid-glass composites. *Optical Materials Express* **2**, 825-838 (2012).

235 Oudjedi, L., Parra-Vasquez, A. N. G., Godin, A. G., Cognet, L. & Lounis, B. Metrological Investigation of the (6,5) Carbon Nanotube Absorption Cross Section. *J Phys Chem Lett* **4**, 1460-1464 (2013).

236 Islam, M. F., Milkie, D. E., Kane, C. L., Yodh, A. G. & Kikkawa, J. M. Direct measurement of the polarized optical absorption cross section of single-wall carbon nanotubes. *Phys Rev Lett* **93**, 037404 (2004).

237 Christofilos, D. *et al.* Optical Imaging and Absolute Absorption Cross Section Measurement of Individual Nano-objects on Opaque Substrates: Single-Wall Carbon Nanotubes on Silicon. *J Phys Chem Lett* **3**, 1176-1181 (2012).

238 Zijlstra, P., Paulo, P. M. R. & Orrit, M. Optical detection of single non-absorbing molecules using the surface plasmon resonance of a gold nanorod. *Nat Nanotechnol* **7**, 379-382 (2012).

239 Wade, J. H. & Bailey, R. C. Applications of Optical Microcavity Resonators in Analytical Chemistry. *Annu Rev Anal Chem* **9**, 1-25 (2016).

240 Kador, L., Latychevskaia, T., Renn, A. & Wild, U. P. Absorption spectroscopy on single molecules in solids. *J Chem Phys* **111**, 8755-8758 (1999).

241 Gerhardt, I. *et al.* Strong extinction of a laser beam by a single molecule. *Phys Rev Lett* **98** (2007).

242 Rezus, Y. L. A. *et al.* Single-Photon Spectroscopy of a Single Molecule. *Phys Rev Lett* **108** (2012).

243 Xiao, Y. F. *et al.* Strongly enhanced light-matter interaction in a hybrid photonic-plasmonic resonator. *Phys Rev A* **85** (2012).

244 Link, S. & El-Sayed, M. A. Spectral properties and relaxation dynamics of surface plasmon electronic oscillations in gold and silver nanodots and nanorods. *J Phys Chem B* **103**, 8410-8426 (1999).

245 Knapper, K. A., Heylman, K. D., Horak, E. H. & Goldsmith, R. H. Chip-Scale Fabrication of High-Q All-Glass Toroidal Microresonators for Single-Particle Label-Free Imaging. *Adv Mater* **28**, 2945-2950 (2016).

246 Keng, D., Tan, X. & Arnold, S. Whispering gallery micro-global positioning system for nanoparticle sizing in real time. *Appl Phys Lett* **105** (2014).

247 Fano, U. Effects of configuration interaction on intensities and phase shifts. *Phys Rev A* **124**, 1866 (1961).

248 Anderson, P. W. Localized magnetic states in metals. *Physical Review* **124**, 41 (1961).

249 Miroshnichenko, A. E., Flach, S. & Kivshar, Y. S. Fano resonances in nanoscale structures. *Rev Mod Phys* **82**, 2257-2298 (2010).

250 Li, B. B. *et al.* Experimental observation of Fano resonance in a single whispering-gallery microresonator. *Appl Phys Lett* **98** (2011).

251 Barclay, P. E., Santori, C., Fu, K. M., Beausoleil, R. G. & Painter, O. Coherent interference effects in a nano-assembled diamond NV center cavity-QED system. *Opt Express* **17**, 8081-8097 (2009).

252 Kroner, M. *et al.* The nonlinear Fano effect. *Nature* **451**, 311-314 (2008).

253 Stern, L., Grajower, M. & Levy, U. Fano resonances and all-optical switching in a resonantly coupled plasmonic-atomic system. *Nat Commun* **5** (2014).

254 Giannini, V., Francescato, Y., Amrania, H., Phillips, C. C. & Maier, S. A. Fano Resonances in Nanoscale Plasmonic Systems: A Parameter-Free Modeling Approach. *Nano Lett* **11**, 2835-2840 (2011).

255 Foreman, M. R. & Vollmer, F. Level repulsion in hybrid photonic-plasmonic microresonators for enhanced biodetection. *Phys Rev A* **88** (2013).

256 Zhang, Y. *et al.* Coherent anti-Stokes Raman scattering with single-molecule sensitivity using a plasmonic Fano resonance. *Nat Commun* **5** (2014).

257 Zhang, Y., Wen, F., Zhen, Y. R., Nordlander, P. & Halas, N. J. Coherent Fano resonances in a plasmonic nanocluster enhance optical four-wave mixing. *P Natl Acad Sci USA* **110**, 9215-9219 (2013).

258 Gallinet, B. & Martin, O. J. F. Analytical Description of Fano Resonances in Plasmonic Nanostructures. *Fourth International Workshop on Theoretical and Computational Nanophotonics (Tacona-Photonics 2011)* **1398** (2011).

259 Langbein, D. Non-Retarded Dispersion Energy between Macroscopic Spheres. *J Phys Chem Solids* **32**, 1657-& (1971).

260 Wiersig, J. Structure of whispering-gallery modes in optical microdisks perturbed by nanoparticles. *Phys Rev A* **84** (2011).

261 Zhang, S. P., Bao, K., Halas, N. J., Xu, H. X. & Nordlander, P. Substrate-Induced Fano Resonances of a Plasmonic: Nanocube: A Route to Increased-Sensitivity Localized Surface Plasmon Resonance Sensors Revealed. *Nano Lett* **11**, 1657-1663 (2011).

262 Link, S., Burda, C., Nikoobakht, B. & El-Sayed, M. A. Laser-induced shape changes of colloidal gold nanorods using femtosecond and nanosecond laser pulses. *J Phys Chem B* **104**, 6152-6163 (2000).

263 Willets, K. A. & Van Duyne, R. P. Localized surface plasmon resonance spectroscopy and sensing. *Annu Rev Phys Chem* **58**, 267-297 (2007).

264 Jana, N. R., Gearheart, L. & Murphy, C. J. Wet chemical synthesis of high aspect ratio cylindrical gold nanorods. *J Phys Chem B* **105**, 4065-4067 (2001).

265 DeSantis, C. J. *et al.* Laser-Induced Spectral Hole-Burning through a Broadband Distribution of Au Nanorods. *The Journal of Physical Chemistry C* (2015).

266 Ng, K. C. & Cheng, W. Fine-tuning longitudinal plasmon resonances of nanorods by thermal reshaping in aqueous media. *Nanotechnology* **23**, 105602 (2012).

267 Petrova, H. *et al.* On the temperature stability of gold nanorods: comparison between thermal and ultrafast laser-induced heating. *Phys Chem Chem Phys* **8**, 814-821 (2006).

268 Link, S., Wang, Z. L. & El-Sayed, M. A. How Does a Gold Nanorod Melt?#. *The Journal of Physical Chemistry B* **104**, 7867-7870 (2000).

269 Ma, H., Bendix, P. M. & Oddershede, L. B. Large-scale orientation dependent heating from a single irradiated gold nanorod. *Nano Lett* **12**, 3954-3960 (2012).

270 Zijlstra, P., Chon, J. W. & Gu, M. White light scattering spectroscopy and electron microscopy of laser induced melting in single gold nanorods. *Phys Chem Chem Phys* **11**, 5915-5921 (2009).

271 Taylor, A. B., Chow, T. T. & Chon, J. W. Alignment of gold nanorods by angular photothermal depletion. *Appl Phys Lett* **104**, 083118 (2014).

272 Taylor, A. B., Siddiquee, A. M. & Chon, J. W. Below melting point photothermal reshaping of single gold nanorods driven by surface diffusion. *Acs Nano* **8**, 12071-12079 (2014).

273 Boulais, E. t., Lachaine, R. m. & Meunier, M. Plasma-mediated nanocavitation and photothermal effects in ultrafast laser irradiation of gold nanorods in water. *The Journal of Physical Chemistry C* **117**, 9386-9396 (2013).

274 Albrecht, W. *et al.* Single Particle Deformation and Analysis of Silica-Coated Gold Nanorods before and after Femtosecond Laser Pulse Excitation. *Nano Lett* **16**, 1818-1825 (2016).

275 Kuhlicke, A., Schietinger, S., Matyssek, C., Busch, K. & Benson, O. In Situ Observation of Plasmon Tuning in a Single Gold Nanoparticle during Controlled Melting. *Nano Lett* **13**, 2041-2046 (2013).

276 Santiago-Cordoba, M. A., Boriskina, S. V., Vollmer, F. & Demirel, M. C. Nanoparticle-based protein detection by optical shift of a resonant microcavity. *Appl Phys Lett* **99**, 073701 (2011).

277 Min, B. K. *et al.* High-Q surface-plasmon-polariton whispering-gallery microcavity. *Nature* **457**, 455-U453 (2009).

278 Kippenberg, T. J. & Vahala, K. J. Cavity optomechanics: Back-action at the mesoscale. *Science* **321**, 1172-1176 (2008).

279 Carmon, T., Rokhsari, H., Yang, L., Kippenberg, T. J. & Vahala, K. J. Temporal behavior of radiation-pressure-induced vibrations of an optical microcavity phonon mode. *Phys Rev Lett* **94**, 223902 (2005).

280 Baaske, M. D. & Vollmer, F. Optical observation of single atomic ions interacting with plasmonic nanorods in aqueous solution. *Nat Photonics* (2016).

281 Kennedy, W. J. *et al.* High-Resolution Mapping of Thermal History in Polymer Nanocomposites: Gold Nanorods as Microscale Temperature Sensors. *ACS applied materials & interfaces* **7**, 27624-27631 (2015).

282 Fisher, R. A. Two new properties of mathematical likelihood. *Proceedings of the Royal Society of London. Series A, Containing Papers of a Mathematical and Physical Character* **144**, 285-307 (1934).

283 Sheikholeslami, S. N., García-Etxarri, A. & Dionne, J. A. Controlling the interplay of electric and magnetic modes via Fano-like plasmon resonances. *Nano Lett* **11**, 3927-3934 (2011).

284 Clerk, A., Waintal, X. & Brouwer, P. Fano resonances as a probe of phase coherence in quantum dots. *Phys Rev Lett* **86**, 4636 (2001).

285 Arnold, S. *et al.* Whispering gallery mode carousel–a photonic mechanism for enhanced nanoparticle detection in biosensing. *Opt Express* **17**, 6230-6238 (2009).

286 Badieirostami, M., Lew, M. D., Thompson, M. A. & Moerner, W. E. Three-dimensional localization precision of the double-helix point spread function versus astigmatism and biplane. *Appl Phys Lett* **97**, 161103 (2010).

287 Matsko, A. B. *Practical applications of microresonators in optics and photonics*. (CRC Press, 2009).

288 Dobrindt, J. *Bio-sensing using toroidal microresonators & theoretical cavity optomechanics*, lmu, (2012).

289 Shao, L. *et al.* Detection of single nanoparticles and lentiviruses using microcavity resonance broadening. *Adv Mater* **25**, 5616-5620 (2013).

290 Havard, N., Li, Z. M., Murthy, V., Lo, S. S. & Hartland, G. V. Spatial modulation spectroscopy of graphene sheets. *J Chem Phys* **140** (2014).

291 Muskens, O. L. *et al.* Single metal nanoparticle absorption spectroscopy and optical characterization. *Appl Phys Lett* **88** (2006).

292 Billaud, P. *et al.* Absolute optical extinction measurements of single nano-objects by spatial modulation spectroscopy using a white lamp. *Rev Sci Instrum* **81** (2010).

293 Richter, J., Nezhad, M. P. & Witzens, J. in *Opto-Electronics and Communications Conference (OECC), 2015.* 1-3 (IEEE).

294 Jiang, X. F. *et al.* Highly Unidirectional Emission and Ultralow-Threshold Lasing from On-Chip Ultrahigh-Q Microcavities. *Adv Mater* **24**, Op260-Op264 (2012).

295 Devadas, M. S. *et al.* Detection of single gold nanoparticles using spatial modulation spectroscopy implemented with a galvo-scanning mirror system. *Appl Optics* **52**, 7806-7811 (2013).

296 Green, M. A. Self-consistent optical parameters of intrinsic silicon at 300 K including temperature coefficients. *Sol. Energy Mater.* **92**, 1305-1310 (2008).

297 Berthold, J., Jacobs, S. & Norton, M. Dimensional stability of fused silica, invar, and several ultra-low thermal expansion materials. *Metrologia* **13**, 9 (1977).

298 Kim, P., Shi, L., Majumdar, A. & McEuen, P. L. Thermal transport measurements of individual multiwalled nanotubes. *Phys. Rev. Lett.* **87**, 215502 (2001).

299 Maune, H., Chiu, H. Y. & Bockrath, M. Thermal resistance of the nanoscale constrictions between carbon nanotubes and solid substrates. *Appl. Phys. Lett.* **89**, 013109 (2006).

300 Shi, L. *et al.* Thermal probing of energy dissipation in current-carrying carbon nanotubes. *J. Appl. Phys.* **105**, 104306 (2009).

301 Pop, E. The role of electrical and thermal contact resistance for Joule breakdown of single-wall carbon nanotubes. *Nanotechnology* **19**, 295202 (2008).

302 Pettes, M. T. & Shi, L. Thermal and Structural Characterizations of Individual Single-, Double-, and Multi-Walled Carbon Nanotubes. *Adv Funct Mater* **19**, 3918-3925 (2009).

303 Kim, P., Shi, L., Majumdar, A. & McEuen, P. Thermal transport measurements of individual multiwalled nanotubes. *Phys Rev Lett* **87**, 215502 (2001).

304 Samani, M. K. *et al.* Thermal conductivity of individual multiwalled carbon nanotubes. *Int J Therm Sci* **62**, 40-43 (2012).

305 Choi, T. Y., Poulikakos, D., Tharian, J. & Sennhauser, U. Measurement of thermal conductivity of individual multiwalled carbon nanotubes by the 3-omega method. *Appl. Phys. Lett.* **87**, 013108 (2005).

306 Choi, T. Y., Poulikakos, D., Tharian, J. & Sennhauser, U. Measurement of the thermal conductivity of individual carbon nanotubes by the four-point three-omega method. *Nano Lett.* **6**, 1589-1593 (2006).

307 Yang, J. K. *et al.* Measurement of the Intrinsic Thermal Conductivity of a Multiwalled Carbon Nanotube and Its Contact Thermal Resistance with the Substrate. *Small* **7**, 2334-2340 (2011).

308 Hartland, G. V. Coherent vibrational motion in metal particles: Determination of the vibrational amplitude and excitation mechanism. *The Journal of chemical physics* **116**, 8048-8055 (2002).

309 Feynman, R. P. (1965).

310 Diev, V. V., Hanson, K., Zimmerman, J. D., Forrest, S. R. & Thompson, M. E. Fused Pyrene‐Diporphyrins: Shifting Near‐Infrared Absorption to 1.5 μm and Beyond. *Angewandte Chemie International Edition* **49**, 5523-5526 (2010).

311 Lasne, D. *et al.* Single nanoparticle photothermal tracking (SNaPT) of 5-nm gold beads in live cells. *Biophys J* **91**, 4598-4604 (2006).

312 Giblin, J., Syed, M., Banning, M. T., Kuno, M. & Hartland, G. Experimental Determination of Single CdSe Nanowire Absorption Cross Sections through Photothermal Imaging. *Acs Nano* **4**, 358-364 (2010).

313 Kippenberg, T. J., Spillane, S. M. & Vahala, K. J. Modal coupling in traveling-wave resonators. *Opt Lett* **27**, 1669-1671 (2002).

314 Monifi, F., Friedlein, J., Ozdemir, S. K. & Yang, L. A Robust and Tunable Add-Drop Filter Using Whispering Gallery Mode Microtoroid Resonator. *J Lightwave Technol* **30**, 3306-3315 (2012).

315 Vollmer, F. *et al.* Protein detection by optical shift of a resonant microcavity. *Appl Phys Lett* **80**, 4057-4059 (2002).

316 Saito, T. *et al.* Improved contact for thermal and electrical transport in carbon nanofiber interconnects. *Appl Phys Lett* **93** (2008).

317 Ngo, Q. *et al.* Structural and electrical characterization of carbon nanofibers for interconnect via applications. *Ieee T Nanotechnol* **6**, 688-695 (2007).

318 Chambers, A., Park, C., Baker, R. T. K. & Rodriguez, N. M. Hydrogen storage in graphite nanofibers. *J Phys Chem B* **102**, 4253-4256 (1998).